Alma Mater Studiorum - Università di Bologna

DOTTORATO DI RICERCA IN

NANOSCIENZE PER LA MEDICINA E PER L'AMBIENTE

Ciclo 34

Settore Concorsuale: 03/B1 - FONDAMENTI DELLE SCIENZE CHIMICHE E SISTEMI INORGANICI

Settore Scientifico Disciplinare: CHIM/03 - CHIMICA GENERALE E INORGANICA

PHOTOACTIVE (SUPRA)MOLECULAR DEVICES IN DOUBLE LAYER MEMBRANES

Presentata da: Erica Paltrinieri

Coordinatore Dottorato

Dario Braga

Supervisore

Alberto Credi

Co-supervisore

Serena Silvi

Esame finale anno 2022

Table of contents

Abstract

Biological systems are complex and highly organized architectures governed by non-covalent interactions responsible for the regulation of essential tasks such as molecular recognition, self-assembly, molecular transport, signal transmission. These systems are a constant source of inspiration for supramolecular chemists aiming to design multicomponent molecular assemblies able to perform elaborated tasks, thanks to the role and action of the components that constitute them. The properties of the supramolecular assemblies are far beyond the simple addition of the individual features of their components, as the assembled systems exhibit novel and elaborate functions that cannot be performed by each component alone. Artificial supramolecular systems exploit non-covalent interactions to mimic naturally occurring events and design life-like synthetic materials. In this context, stimuli-responsive supramolecular systems have attracted an increasing amount of attention due to the possibility to control macroscopic effects through modifications at the nanoscale. Particular relevance has been given to photo-operated systems, as the use of light as an external stimulus allows these devices to function in a clean and time- and space-controlled way.

Chapter 1 provides a general overview on biological and artificial compartmentalized systems, focusing on their functionalization to achieve specific functions. Particular attention is given to biomimetic systems such as artificial vesicles and their use in medicinal chemistry. Finally, the incorporation of artificial molecular machines as guests to carry out targeted tasks, such as substrate transport or release is carefully reviewed.

Chapter 2 regards the investigation of liposomes functionalized by a photoactive molecule such as azobenzene and the influence that such molecule has on their characteristics. The aim is to outline experimental procedures making use of a commercially available compound and understand the influence and the behavior of this photochrome on vesicles characteristic such as size, charge surface, membrane stability and viscosity.

Chapter 3 reports the synthesis and study of two photoactive molecules tailored to be intercalated in a liposome membrane. Thanks to these characteristics, such compounds could potentially be used as components for a light-activated molecular machine capable of directionally pumping substrates across the membrane. In the first part, the synthesis and characterization of the molecules is reported. Characterized by a rod-like structure, the two molecules **C10** and **C12** present hydrophilic endgroups delimiting a central region that comprises an azobenzene unit, an ammonium recognition site for a macrocycle substrate

and a lipophilic spacer of different length for each compound. Such molecules have been investigated *via* UV-vis spectroscopy both in homogeneous solution and when intercalated in liposomes, exhibiting in the latter case, a marked influence on the properties of the vesicles. Specifically, the functionalized liposome suspension showed a photoinduced and reversible aggregation-disaggregation behaviour that depends on the guest molecule configuration. In the second part, the role of the guest structure in the functionalised liposomes has been investigated through the use of model molecules structurally related to the axle **C12**. In particular, the influence of the hydrophilic endgroups has been examined in three model molecules that have been conceived by systematically removing the hydrophilic endgroups, leading to threads having only one hydrophilic chain attached to one of the two ends or devoid of any ethylene glycol fragment. The analyses performed on liposomes functionalized with such molecules displayed aggregation processes that are dependent on the number and position of ethylene glycol chains. Finally, preliminary computational studies provided further support to the mechanism through which the reversible aggregation phenomenon takes place.

Chapter 4 regards the design and investigation of the [3]rotaxane system **Rot**H_2^{3+} that comprises two dibenzo-24-crown-8 (DB24C8) rings, interlocked with an axle containing one permanent triazolium station and two dibenzylammonium stations that can be deactivated by deprotonation. The system is able to change the ratio between the recognition sites and the crown ethers according to acid-base inputs. The rotaxanes containing a number of recognition sites respectively larger, equal or lower than the number of interlocked macrocyclic rings are connected by a network of acid-base reactions that lead to the differentiation of the chemically equivalent acidic sites. In the first part of the chapter, the rotaxanes originating from the base-induced switching were investigated by means of NMR and UV-vis spectroscopy. Deprotonation of one ammonium station of **Rot**H_2^{3+} led to the formation of the dicationic species **Rot**H^{2+}, that exist in two non-equivalent isomeric forms. Due to the presence of the rings, such isomers that differ for the position of the ammonium site (and of its surrounding macrocycle) with respect to the central triazolium station, exhibited a slow proton exchange between them, thus enabling their studies. The analyses performed on the two forms of **RotH**$^{2+}$ highlighted a peculiar effect of the moving rings on the acidity of the ammonium sites. The complete deprotonation of **Rot**H^{2+} led to the monocationic species **Rot**$^+$. Such rotaxane comprising the triazolium site shared by two rings is a ‘frustrated' species and displayed interesting co-conformational dynamics. In the

last part, further investigations of such rotaxanes by means of computational calculations are reported.

1. Introduction

1.1 Biological membranes

Biological membranes are effective constituents of all cells, whether eukaryotic or prokaryotic, and act as the boundary between the cells surroundings and their interior. Besides providing structural support and spatial compartmentalization to the cell, the membrane also regulates many essential cellular activities, such as material transport, signal transduction, cell–cell interaction, and enzymatic reactions. The first representation of the membrane structure depicted as a lipid bilayer was proposed in 1925 and later, in 1972, Singer and Nicolson proposed the *fluid mosaic model* that best describes the supramolecular structure of biological membranes. The membrane is a very complicated supramolecular structure composed of lipids, proteins, and carbohydrates (**Figure 1.1**). Lipids are the major component of cell membranes and three types of them can be found in biomembranes: phospholipids, glycolipids and sterols. These molecules are amphiphilic, meaning they have one polar hydrophilic head and at least one apolar lipophilic tail. The lipids amphiphilic nature determines their arrangement in solution, for example in water they adopt the most thermodynamically stable molecular structure forming bilayers, positioning all of the polar heads in contact with the polar solvent and all of the hydrocarbon tails close together creating an hydrophobic environment. Another important component of the membranes are intramembrane proteins, that have various functions and characteristics, indeed they are responsible for transport, reactions catalysis (for example *oxidoreductases*, *transferases* and *hydrolases*), for recognition activities and some of them are natural molecular machines that allow the passage of substances through the membrane.[1] They can be divided into integral and peripheral proteins, which depending on their location, embedded in the whole bilayer or located in the inner or outer surface of the phospholipid bilayer, respectively. Finally, carbohydrates are found only on one side of the bilayers and are covalently bound to lipids and proteins. This optimal organization of different components with specific relative ratios and compositions contributes to the structural complexity and functional distinctiveness of the cell membrane. However, the intrinsic high dynamicity that characterizes the membrane makes it difficult to study.

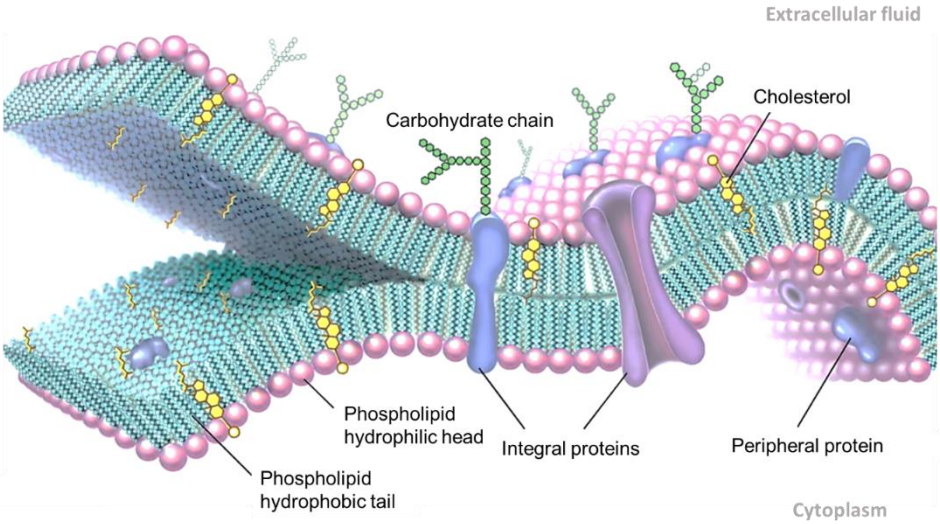

Figure 1.1. Structural representation of a cell membrane.[2]

1.1.1 Transmembrane transport

One of the most studied processes regarding membrane functions is the transport of substrates across the bilayer. Biomembranes are selectively permeable, so they are able to regulate the passage of solutes such as ions and small molecules according to their charge, size and other chemical properties. Membrane proteins are involved in the transport of material across the membrane, and without them the phospholipid membrane would be an impenetrable barrier for many types of molecules. Indeed, while small and neutral molecules, including water, can simply diffuse through membranes *via* non-mediated transport, charged or large molecules usually require a mediator.[3] This differentiation leads to the classification of passive and active transport, as shown in **Figure 1.2**.

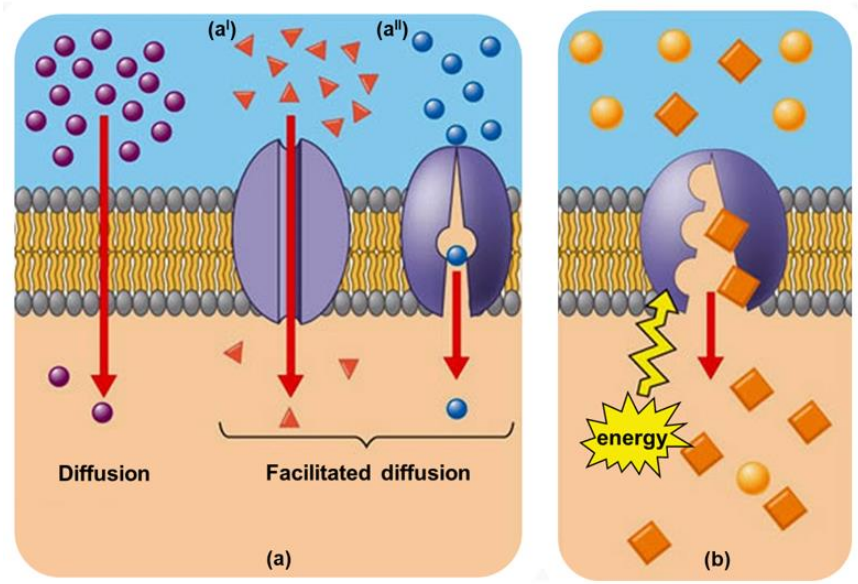

Figure 1.2. Schematic representation of a) diffusion and passive transport and b) active transport mechanisms.

In passive transport, a concentration gradient exists that allows ions and molecules to diffuse across cell membranes in order to reach an equilibrium state, which can also be facilitated by a transporter. Since substances diffuse from a more concentrated solution toward a more diluted one, this type of process does not require external energy inputs to occur. Passive transporters are for example ion channels (**Figure 1.2a^{I}**) and carriers (**Figure 1.2a^{II}**).
If transport is mediated by a channel, the selectivity is determined by the size and the charge of the pore. Otherwise, carrier proteins can facilitate passive transport; this mechanism is more selective but also slower since it involves conformational changes in the proteins.
On the contrary, in active transport mechanism (**Figure 1.2b**) ions and molecules flow through the transporter against a concentration gradient exploiting the energy provided by external sources such as ATP hydrolysis or electrochemical gradients. According to the energy being used, active transport can be classified in two categories: i) primary active transport, that takes place when proteins use ATP hydrolysis to pump species from a lower concentration area to a higher concentration one; ii) secondary active transport, that requires an electrochemical gradient of ions to drive the uphill movement of another species, either in the same direction (symport) or in an opposite direction (antiport).[4]

1.2 Liposomes

Liposomes are artificial vesicles of spherical shape composed of surfactants, block copolymers, natural or synthetic (phospho)lipids. Initially discovered in the 1960s by the hematologist A.D. Bangham and collaborators,[5] they are widely studied thanks to their similarity with biological membranes, easy preparation, biocompatibility, biodegradability and promising applicability in areas such as cosmetics, pharmaceutics, and food and farming industries.[6,7]

In aqueous solution, amphiphilic compounds are able to assemble due to the hydrophobic effect. When their concentration is above the critical aggregation concentration (CAC) aggregation occurs, giving rise to a variety of three-dimensional structures. A simple model for the aggregation of phospholipids has been proposed, based on the packing parameter (p) that is related to the geometry of the molecules.[8] Considering the surface area of the head-group (a) and the volume and length of the hydrocarbon chain (v and l, respectively), the packing parameter can be defined as:

$$p = \frac{v}{l \times a}$$

With increasing values of p, the amphiphilic aggregates pass from being organized in spherical micelles ($p < 1/3$), to non-spherical micelles ($1/3 < p < 1/2$), bilayer vesicles ($1/2 < p < 1$), planar bilayers ($p = 1$) and inverted micelles ($p > 1$) as shown in **Figure 1.3**.

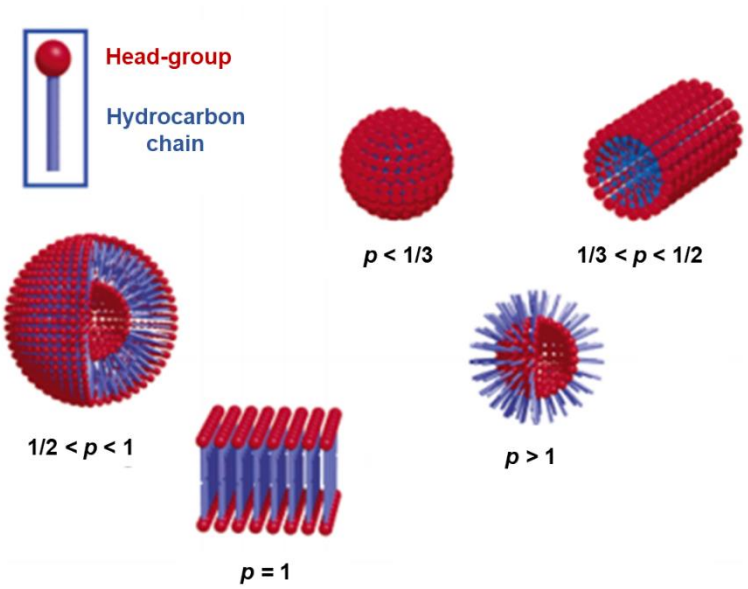

Figure 1.3. Different aggregates morphologies as a function of the packing parameter p.

Liposomes can be defined as artificial vesicles of diameter ranging from 30 nm up to several micrometers, suspended in aqueous solution and containing an inner aqueous core surrounded by one or more lipid double layer. Thanks to their structure they can trap hydrophilic molecules in the inner aqueous compartment, hydrophobic guests in the lipid bilayer and substances with intermediate lipophilicity in both, thus becoming perfect carriers for numerous substrates.[9]

Liposomes can be obtained from many types of cholesterols and phospholipids, and the nature of the constituents of the bilayer determines the surface properties, size and rigidity of the vesicles. This remarkable feature makes liposomes a flexible platform for medical applications, specifically for drugs and gene delivery.[10]

1.2.1 Classification

Liposomes can be classified on the basis of their *structural parameters* and *composition.*

According to their *structure*, liposomes are categorized on the basis of their size and number of lipid bilayers (lamellae).[10] The vesicle size is a useful parameter to determine the stability and circulation half-life of liposomes in the blood stream.[9] Moreover both size and number of bilayers affect the amount of guest encapsulated in the liposomes.

Based on their lamellarity, liposomes can be classified as:

- *Unilamellar* (ULV), all size range
- *Multilamellar* (MLV), > 0.5 μm
- *Multivescicular* (MVV), > 1.0 μm

and ULVs can be further divided in:

- *Small unilamellar vesicles* (SUVs), 20-100 nm
- *Large unilamellar vesicles* (LUVs),100 nm-1 μm
- *Giant unilamellar vesicles* (GUVs), > 1 μm

The amphiphilic nature of phospholipids allows liposomes to encapsulate both hydrophilic and hydrophobic guests, thus distributing the first homogeneously in the aqueous core, while the last is retained inside the lipid bilayer.

In *unilamellar vesicles* the aqueous core is surrounded by a single phospholipid bilayer, with a greater capacity for the encapsulation of hydrophilic compounds.

Multilamellar vesicles present two or more concentric lipid bilayers organized by an onion-like structure, and because of this they excel in encapsulating lipophilic compounds.

On the other end, *multivescicular vesicles* have several small non-concentric vesicles entrapped within a single lipid bilayer, and are efficient for the encapsulation of voluminous hydrophilic compounds.[11]

The second classification parameter evaluates liposome composition, and divides them into the following categories:[12,13]

- *Conventional liposomes*, composed of cationic, anionic, or neutral (phospho)lipids and cholesterol. Such liposomes are mainly used for vaccine administration and macrophage targeting and since they are rapidly captured by mononuclear phagocyte systems, they are characterised by a short blood circulation time (**Figure 1.4a**);
- *Long-circulating liposomes*, also known as "stealth" or "sterically stabilized" liposomes, whose external surface is modified with poly(ethylenglycole) (PEG) to improve their stability and increase their longevity in circulation (**Figure 1.4b**);
- *Ligand-targeted liposomes*, in which the external surface is decorated with ligands (e.g., antibodies, peptides, and carbohydrates) attached directly to it or to the terminal end of the external PEG chains. This allows liposomes to bind specific targets (**Figure 1.4c**);
- *Theranostic liposomes*, that consist of a single system composed of a targeting element, an imaging component, and a therapeutic component (**Figure 1.4d**).

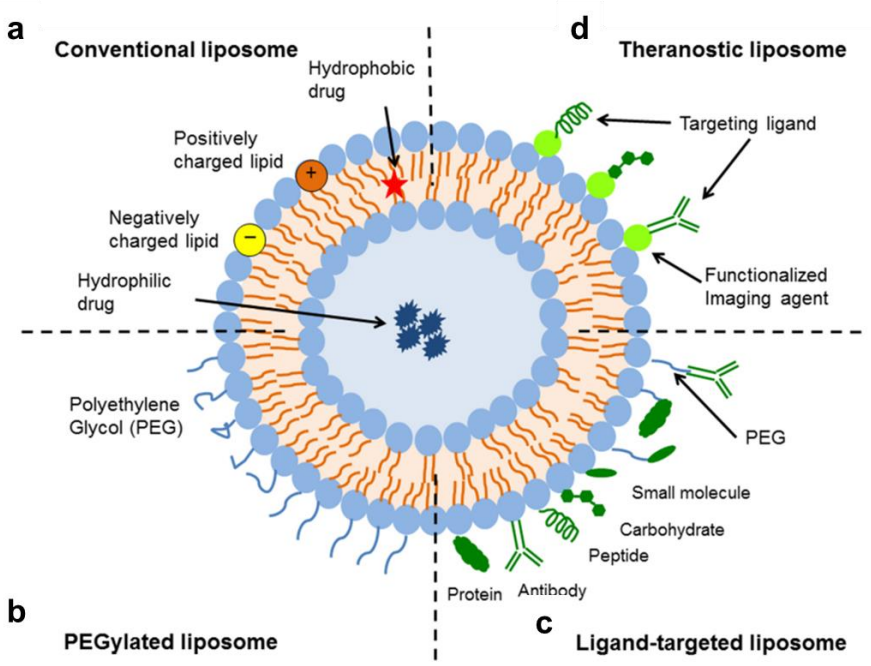

Figure 1.4. Schematic representation of the four main types of liposomes, according to the composition of their membranes. Reproduced with permission [13].

1.3 Molecular machines

Molecular machines can be defined as an assembly of a discrete number of molecular components that exhibit a mechanical movement in response to an external stimulus. In all living organisms molecular machines are essential to life, as a great number of such devices are responsible of performing essential tasks that include movement, locomotion, energy conversion, transport and regulating functions.[14,15,16]

1.3.1 Natural transmembrane molecular machines

Several examples of sophisticated and engineered membrane-spanning molecular machines are present in living organism, and one of the most studied class is represented by ATP (synth)ase rotary motors (**Figure 1.5**). ATP (synth)ase is composed of: the rotary motor complex F_0 embedded in the membrane, the second motor and catalytic complex F_1 responsible of ATP synthesis and positioned in the cytosol, and a peripheral stator b_2 that connects them together and prevents rotation of the catalytic subunits F_1. The central axle, constituted by δ, γ, and ε subunits, is part of F_1 and its rotation is coupled to that of the membrane rotor F_0.

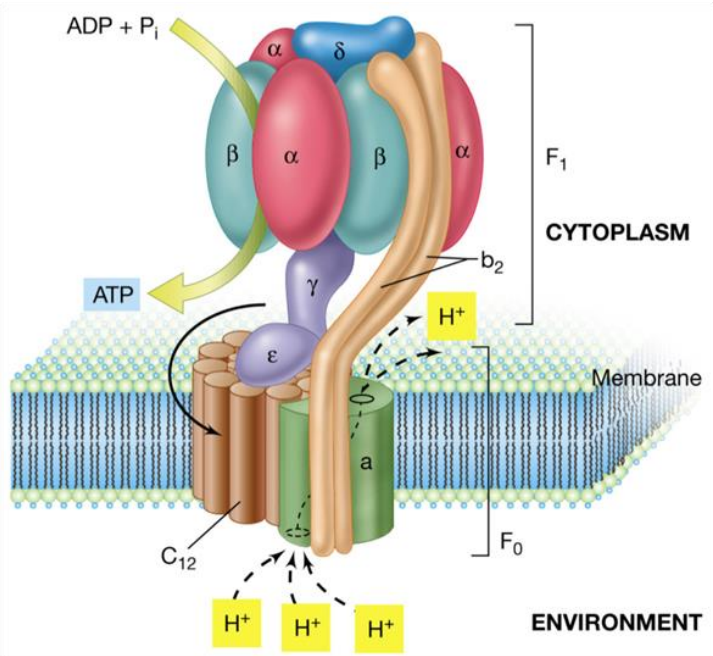

Figure 1.5. Schematic representation of the ATP (synth)ase rotary motor.[17]

This rotary motor can operate in two reciprocal modes. In the ATP synthesis mode, protons flow through the F_0 motor down a transmembrane gradient that leads to the unidirectional rotation of the F_0 subunit coupled with the rotation of the axle, that induces conformational changes in the F_1 subunit. Due to these movements, F_1 is able to bind ADP (adenosine diphosphate) and P_i (inorganic phosphate) to catalyse the reaction between them and release ATP. Conversely, in the reciprocal mode, the hydrolysis of ATP is exploited to generate a transmembrane proton gradient.[18,19] ATP (synth)ase combines an enzyme, two molecular motors and an ion pump in a single complex bio-machine.

Indeed, in nature molecular machines are incredibly complex and are formed spontaneously by self-assembly of programmed molecules. Natural biomachines are a constant source of inspiration to chemists that in the last thirty yers have made extensive research efforts with the aim to create artificial molecular-scale devices able to mimic the sophisitcated machines found in natural systems. In the prospective of design and construction of artificial molecular devices and machines, the knowledge regarding the working principles of biological systems is of great importance. Moreover, by studying such systems it becomes evident that molecular machines are not a simple “shrunken” version of their macroscopic analogous. Indeed, it is important to remembrer that at molecular level some properties of the entities are quite different from those of the macroscopic object; specifically, molecules are floppy, they must operate at a constant temperature (due to the rapid heat flows at that scale), are subjected to constant collision due to kinetic energy (Brownian motion) and operate at a scale where viscous forces dominate.

1.3.2 Mechanically interlocked molecules as artificial molecular machines

In the last decades chemists have developed systems with impressive and diverse machine-like behaviours and with this aim, several types of mechanically interlocked molecules (MIMs) have been designed, taking advantage of the ability of the spatially constrained subcomponents to undergo large amplitude relative motions.[20] MIMs are multicomponent compounds held together by mechanical bonds or entanglements.[21,22,23] J. F. Stoddart, Nobel prize laureate in 2016 for his work on molecular machines, defined mechanical bonds as “*an entanglement in space between two or more molecular entities such that they cannot be separated without breaking or distorting chemical bonds between atoms*”.[24] Taking aside

molecular knots, which lack independent subcomponents, the two archetypal examples of MIMs are catenanes (**Figure 1.6a**) and rotaxanes (**Figure 1.6b**).

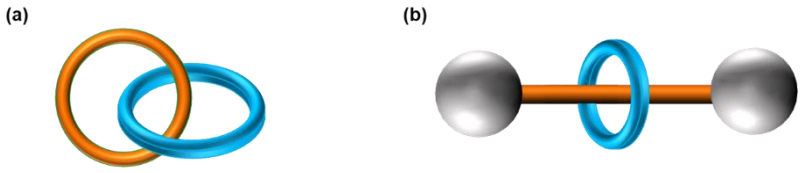

Figure 1.6 Graphical representation of a catenane (a) and a rotaxane (b).

Catenanes are systems with two or more interlocked ring-shaped molecular components. Instead, rotaxanes comprise one or more ring-shaped molecules threaded by a dumbbell possessing bulky endgroups, called “stoppers”, that prevent the rings from dethreading.[25] When at least one of the bulky groups is not present or the kinetics of threading/dethreading is fast enough, the species is called pseudorotaxane. Such systems do not strictly abide to the definition of MIMs since they lack the mechanical bond, nevertheless they contain the fundamental structural information and interactions (*e.g.* π-electron donor-acceptor interactions, hydrogen bonding) of MIMs and, for this reason, they can be used as precursors for the synthesis of rotaxanes and catenanes (**Figure 1.7**).

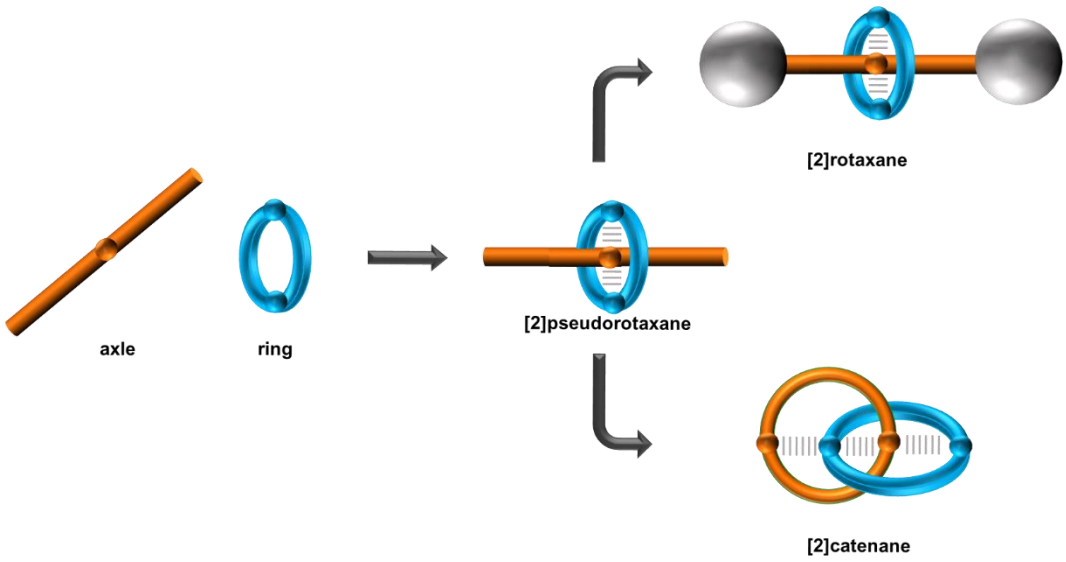

Figure 1.7. Schematic representation of the use of pseudorotaxanes as MIMs precursors.

At the molecular level, random fluctuations caused by thermal energy are the predominant form of motion. Natural bio-machines have developed different mechanisms to overcome

and modulate this random motion by following a strategy called rectified Brownian motion (RBM).[26] Such devices use external energy sources to make a certain direction more favoured than others, thus leading to a directional and controlled motion. Even though the artificial construction of nanomachines is far from reaching the complexity of their biological counterparts, the fundamentals of what should be their functioning principle is progressively propagating in the chemical community. In particular, molecular machines can be divided in two main categories: switches and motors.[15,15] Molecular switches are bistable (or multistable) entities which can be actuated back and forth upon external stimulation (e.g., optical, electrical, or chemical) and due to the principle of microscopic reversibility the returning to the original position of the submolecular components leads to the cancellation of any work done during the forward motion. Differently, molecular motors move their subcomponents following a non-reversible pathway; moreover, a motor can repeat its motion by processing with a full directional rotation of 360° and can even possibly cycle autonomously when supplied with a constant source of external energy.[27]

To achieve movement an energy input is needed. In this context, the choice of the energy source is very important and must be considered in the design of a molecular device. Most commonly, biomolecular machines, like macroscopic ones, make use of exergonic processes for their functioning. However, by considering an artificial molecular device or motor, addition of fresh “fuel” (reactant) would be needed at every step of the working cycle, implying the possible formation of waste products which can be accumulated over repeated cycles and consequently compromise the device efficiency. For these reasons, endergonic and reversible processes such as isomerization or redox reactions are those mainly studied for the operation of molecular machines. Among the employed energy sources, light can be used to power nanoscale machines, providing a renewable, clean and widely available energy supply. A photochemical stimulus can for example induce large structural changes as in isomerization processes; as such, a common strategy is to include a photoswitchable double bond as C=C, N=N or C=N in the device. Additionally, the use of light as an energy source allows to control the amount of energy transferred to the chemical systems by regulating its wavelength and intensity in relation to the absorption spectrum of the species. Such energy can be transferred to the molecules without any physical connection to the source, the only requirement being the transparency of the matrix at the excitation wavelength. Nonetheless, in those circumstances in which light has to be delivered at specific locations such as inside an instrument or in the human body, the use of optical fibre can provide solutions.[28]

1.3.3 Artificial transmembrane molecular machines

Among the extensive research efforts on molecular machines, an attractive application is their use in biological systems. One of the major roles of cell membranes is the regulation of chemical potential gradients between the inner and outer environments of the cell. For this reason, artificial molecules such as molecular carriers and channels able to control material transport across the membrane has been investigated with much interest in the last decade.[29] In this context, the use of liposomes has been extensively employed, whit the aim to better understand cellular organization and transmembrane transport phenomena in a simplified biomimetic system.[30,31]

In nature, there are several membrane-spanning systems with specific tasks, such as stimuli-responsive channels that work at equilibrium or active transmembrane proteins that operate far from equilibrium condition, and they are characterized by different levels of complexity. In the same way, artificial transmembrane machines mirror this progression in complexity, with numerous examples reported in literature, from passive channels to light-driven transmembrane devices.

Artificial transmembrane channels are involved in the passive transport of ions, allowing the passage of the solute following a concentration gradient. They can be simply formed by cyclic peptides that self-assemble in lipid bilayers forming nanopores[32] or by helical foldamers. In recent report, foldamers composed of pyridine-oxadiazole repeating units were adopted, giving rise to a highly selective transmembrane K^+ transporter channel and to a Na^+ preferential channel (**Figure 1.8a**).[33] Alternatively, amphiphilic linear molecules with lengths comparable to that of the membrane can act as passive channels for ions, such as Na^+, K^+, Cl^-.[34] In a recent work, Chen and co-workers reported a rotaxane system that, when intercalated in a lipid bilayer, is able to promote passive ion transport through its stochastic shuttling motion (**Figure 1.8b**). Such a system is composed of an amphiphilic axle with three binding stations, which is interlocked with a double macrocycle that can shuttle along the axle while binding a potassium ion.[35]

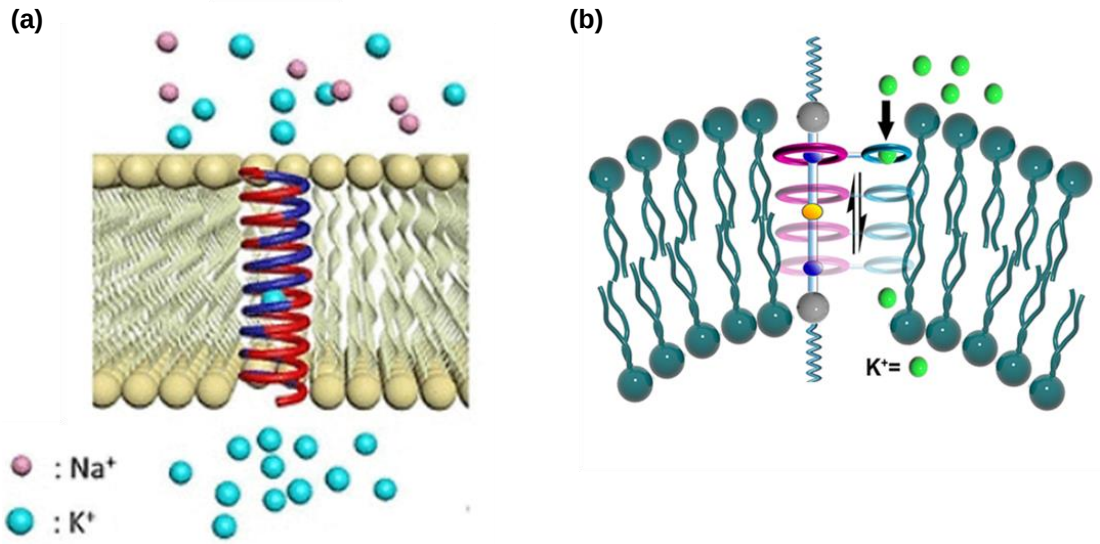

Figure 1.8. Lipid bilayers functionalized with (a) an artificial ion channel or (b) a molecular shuttle. Reproduced with permission.[33,35]

Light-driven artificial transmembrane channels are systems that use light as an external stimulus or as an energy source to drive and facilitate transmembrane processes. Synthetic photoactive functionalities able to undergo configurational changes have been employed to achieve an optical control over the membrane transport. Following the study on the rotaxane molecular shuttle reported in **Figure 1.8b**, the same group developed a second transmembrane molecular shuttle that presents a photoactive azobenzene unit embedded in the rotaxane axle (**Figure 1.9a**).[36] In such system, due to the geometrical transformation of the azobenzene moiety, the shuttle motion can be controlled by light. The rotaxane shuttle performs transmembrane cation transport when the azobenzene is in its linear *E* form, while it is able to interrup it upon isomerization to the *Z* form as a consequence of UV light irradiation, thus realizing a light-gated ion transport.

In a third recent report, Giuseppone and co-workers developed an artificial ion channel based on 18-crown-6 macrocycles linked to a light-driven rotary molecular motor. Upon actuation of the motor component with UV light irradiation, such a system exhibits a strong increase in the transmembrane ion transport activity compared to that recorded in the dark (**Figure 1.9b**).[37]

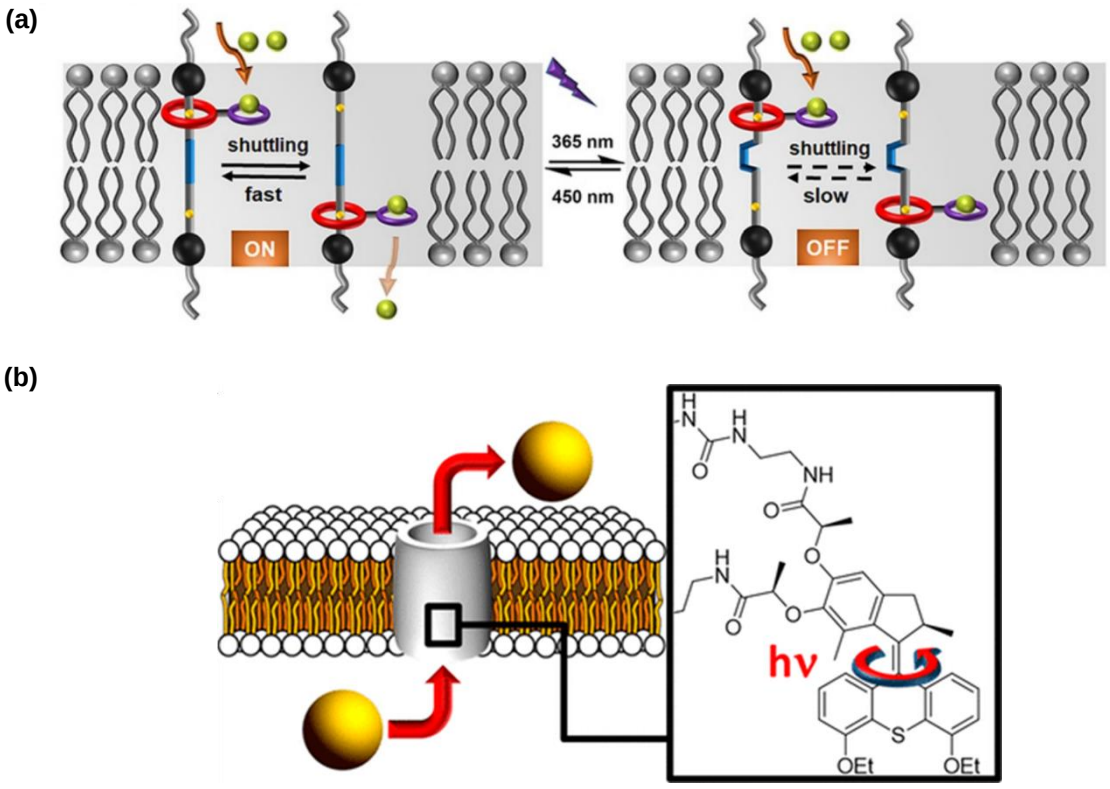

Figure 1.9. Examples of (a) azobenzene based molecular shuttle and (b) light boosted ions channel in lipid bilayer. Reproduced with permission.[36,37]

These works provide a brief description of the use of photoswitchable molecular machines to realize transmembrane ion transport, demonstrating the value of molecular machines embedded in biomembranes.

1.4 Azobenzene in molecular machines

As already observed, great interest regards the integration of photoactive units in molecular machines, in order to control their structural and functional properties with light. In this context, one of the most studied photoactive molecules that has been incorporated in a wide variety of molecular machines is azobenzene. The preference toward this molecule with respect to other photoactive units relies on its easy preparation and functionalization, on the neat photophysical behaviour that allows fast *E/Z* isomerization, and additionally on the large geometrical rearrangement that accompanies the isomerization process.[38] Azobenzene is a chemical compound formed by two phenyl rings linked by a N=N double bound that can undergo $E \rightarrow Z$ isomerization under UV light irradiation, as shown in **Figure 1.10**. The

isomerization reaction is reversible, fast and efficient, not leading to the formation of byproducts. The Z → *E* interconversion may occur through the absorption of visible light, but because the *Z* isomer is metastable, it can also spontaneously back-isomerize to *E* isomer in the dark.

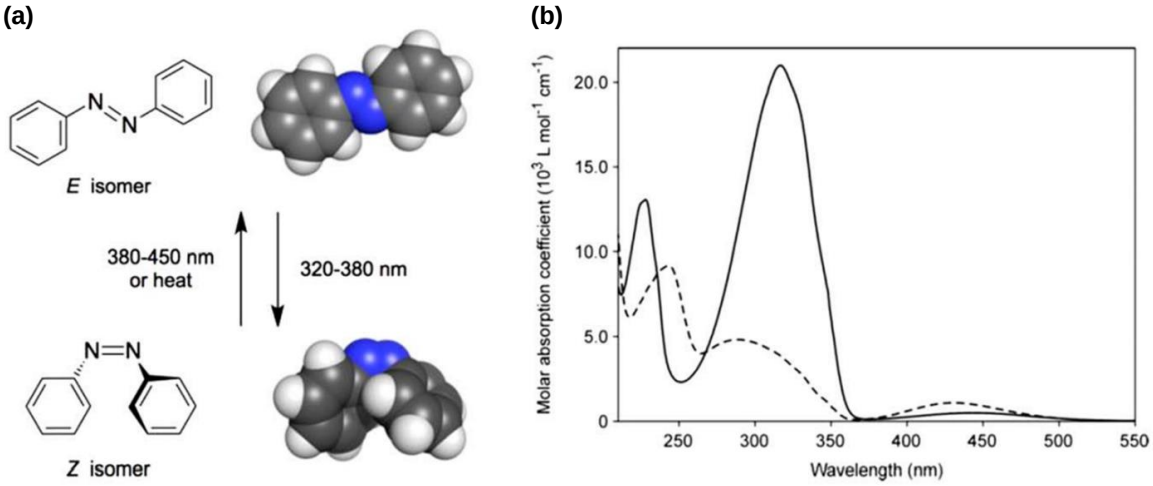

Figure 1.10 a) Photo- and thermally-induced interconversion between *E* and *Z* azobenzene isomers, b) absorption spectra of *E*-azobenzene (bold line) and *Z*-azobenzene (dashed line); acetonitrile, 298 K.[39]

Both azobenzene isomers present different physical properties such as geometry, dipole moment and absorption spectrum. The *E* → *Z* photoisomerization, which turns the structure from planar to non-planar, brings the aromatic phenyl rings closer, reducing the distance between the 4 and 4' carbon atoms of the aryl groups from 9 Å to 5.5 Å. Moreover, while the *E* form has no dipole moment, that of the *Z* isomer is 3.0 Debye.[40] During photoisomerization, relevant changes in the UV-vis absorption spectrum also occur: *E*-azobenzene exhibits an intense band in the near UV region corresponding to the symmetry allowed $\pi \rightarrow \pi^*$ transition[41] and a weaker band in the visible region arises from the symmetry forbidden $n \rightarrow \pi^*$ transition,[42] while the spectrum of *Z*-azobenzene is characterized by a lower intensity of the $\pi \rightarrow \pi^*$ transition band with a concomitant hypsochromic shift and an increase in intensity of the $n \rightarrow \pi^*$ transition band (**Figure 1.10b**).

The isomerization mechanism can take place according to four pathways such as inversion, rotation, concerted inversion and inversion-assisted rotation. However, relaxation from all four transition states can lead to both isomers, so all mechanisms predict photostationary states consisting of both *E*- and *Z*-azobenzene. [43]

Due to its characteristics, the use of azobenzene as photoactive molecular switch have been exploited to develop molecular memories[44] and devices.[45]

Avellini and co-workers reported a molecular switch in the form of a [2]rotaxane composed of a π-electron-deficient ring cyclobis(paraquat-p-phenylene) ($CBPQT^{4+}$) interlocked in a dumbbell axle that comprises two π-electron-donating recognition sites, a primary tetrathiafulvalene (TTF) and a secondary, 1,5-dioxynaphthalene (DNP), and a photoactive 3,5,3',5'-tetramethylazobenzene functionality (TMeAB) located in between the two sites (**Figure 1.11**). Since the TTF unit is more electron-rich than the DNP, the ring prefers to encircle it when the rotaxane is in its ground state co-conformation (GSCC). Upon chemical or electrochemical oxidation of the TTF unit to its radical cation form ($TTFC^{\bullet+}$), the ring shuttles to the DNP site on account of the Coulombic repulsion between the ring and the $TTFC^{\bullet+}$ unit. Successively, upon isomerization of the TMeAB unit to its *Z* configuration, followed by $TTFC^{\bullet+}$ unit reduction back to its neutral state TTF, the ring resides on the DNP recognition site for some time before its relaxation from the metastable state co-conformation (MSCC) to the ground state co-conformation is completed. The lifetime of the metastable state co-conformation can be controlled by isomerization of the TMeAB unit from its *Z* to *E* configuration. In this system the ring cannot move from the DNP to the TTF site over the *Z*-TMeAB unit, and the relaxation rate from the metastable state co-conformation to the ground state co-conformation is determined by the rate of the thermal opening of the gate, unless isomerization from the *Z* to the *E* isomer upon light stimulus is provided. This process is able to affect the free-energy barrier for the shuttling of the ring along the dumbbell component due to the larger steric hindrance of the *Z* azobenzene unit with respect to the *E* one. The system thus designed is able to act as a bistable memory element under kinetic control. The data can be written on the rotaxane by an oxidation stimulus and locked by UV light irradiation. After the writing session, the oxidized species can be reduced back to the original form without losing the written data for a time. The data are stored until the thermal opening of the azobenzene gate occurs. Such system presents sophisticated functionalities that can be accessed through convenient and reversible processes under mild conditions, thus representing a promising step forward toward real world applications in many fields of nanotechnology.

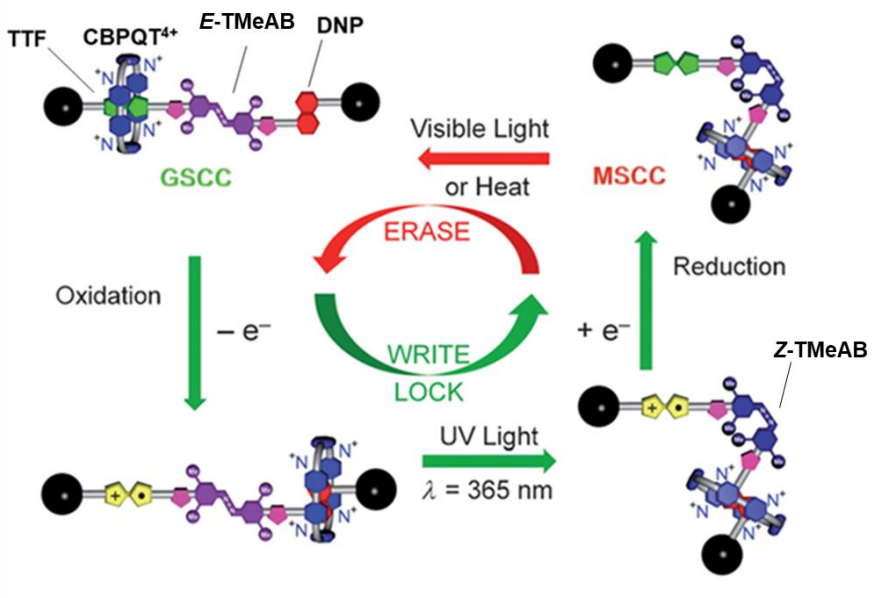

Figure 1.11 Chemically and photochemically triggered memory switching cycle of the [2]rotaxane.[44]

Alternatively, the photoisomerization of azobenzene combined with the self-assembly of a pseudorotaxane species, was recently exploited to obtain an autonomous supramolecular pump powered by light.[45] In such molecular device, azobenzene photoisomerization enables the supramolecular system to cyclically operate due to the relative unidirectional transit of a non-symmetric molecular axle through a macrocycle, requiring light as the only energy input (**Figure 1.12**).

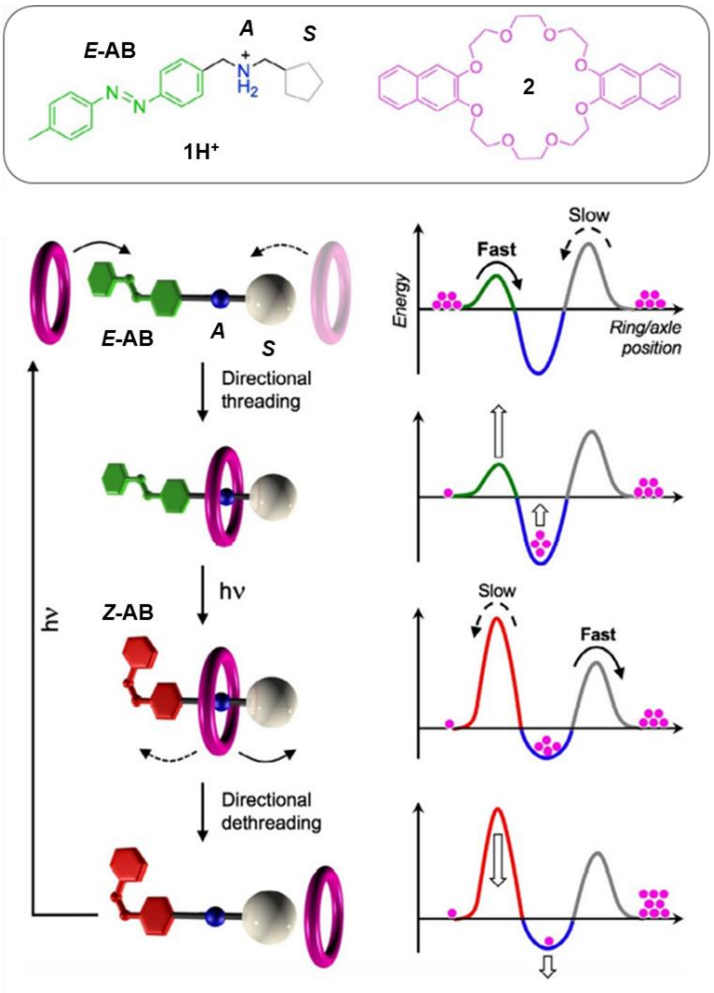

Figure 1.12 Operation cycle of light-powered artificial molecular pump.[28,45]

The system is composed of a non-symmetrical molecular axle **1H$^+$** comprising an azobenzene unit (AB) on one side, a central ammonium station (A) as recognition site for the macrocycle and a photoinactive cyclopentyl unit (S) on the other side, and a macrocycle **2**. In dichloromethane solution at room temperature, there is a driving force for the assembly of the pseudorotaxane in which the macrocyclic component encircles the ammonium site because of hydrogen bonding interactions. When the azobenzene unit is in the *E* form, it presents a smaller hindrance compared to the cyclopentyl end, and for this reason the threading of the macrocycle through the photoactive moiety is kinetically preferred, dictating the direction of the first step. The absorption of a photon in the UV or blue region causes the azobenzene to isomerize from the *E* isomer to the *Z* one. Such transformation destabilizes the system, leading to the macrocycle ejection and since *Z*-azobenzene is bulkier than the *E* isomer, such transit is kinetically preferred at the pseudo-stopper side. Because azobenzene is photoactive in both its isomeric forms, that moreover absorb in the same

spectral region, by supplying another photon identical to the first one the transformation from *Z* to *E* isomer is achieved thus resulting in the closing of the switching cycle. The resulting pseudorotaxane uses photons to rectify Brownian fluctuations and can be defined as an autonomous system, since it is able to repeat its operation under photostationary conditions, that is under the action of a single optical stimulus with constant wavelength and intensity, without the need for additional energy inputs, and moreover as a dissipative system considering that it operates away from equilibrium. This device represents the first example of an autonomous artificial molecular pump driven by light. However, while it is true that ring is withdrawn from the solution to form the pseudorotaxane, it is also true that upon photoisomerization it is directionally released in the same medium. For such reason, compartmentalization of the reaction medium would be required to exploit the molecular pump to its fullest and achieve effective substrate pumping across or against a concentration gradient. This observation lays the foundation for the experimental work described in this thesis.[46,47,48,49]

1.5 Aim of the work

This thesis is divided in three experimental chapters, characterized by a progressive increase in molecular complexity.

Initially, the preparation and studies of liposomes functionalized with a photoactive guest such as azobenzene in the bilayer were tackled, in order to establish appropriate synthetic and characterization procedures and to evaluate the effect of such photochrome on the vesicles properties (**Chapter 2**).

Subsequently, the synthesis and studies of thread-like molecules comprising an azobenzene functionality and an ammonium recognition site for a macrocycle (pump module) are reported. Such molecules were conceived to be intercalated in the bilayer membrane of liposomes and interact with light, with the aim to be used as components for transmembrane molecular pumps (**Figure 1.13**, **Chapter 3**).

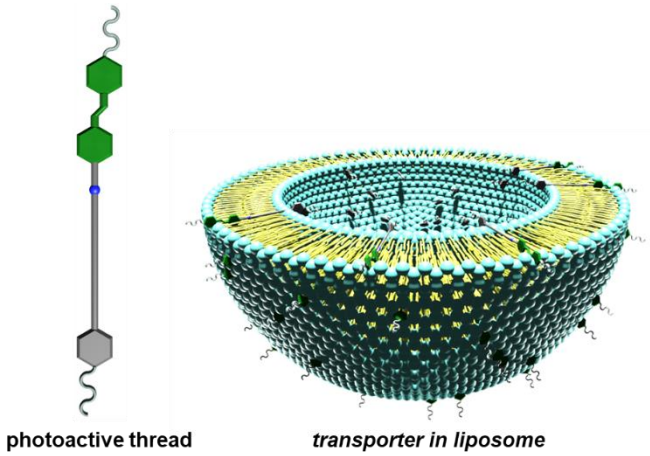

Figure 1.13 Liposome functionalised with photoactive thread molecules.

Finally, a [3]rotaxane was developed and studied in solution. This system is composed of two crown ether rings interlocked with an axle containing three recognition sites for the macrocycles, i.e. two acid-base-switchable ammonium stations and a permanent triazolium station. Such molecule was designed to achieve a change in the ratio between the recognition sites and the crown ethers as a consequence of acid-base inputs, thus leading to the formation of rotaxanes containing a number of recognition sites respectively larger, equal or lower than the number of interlocked rings and connected by a network of acid-base reactions (**Scheme 1.14**, **Chapter 4**)[50].

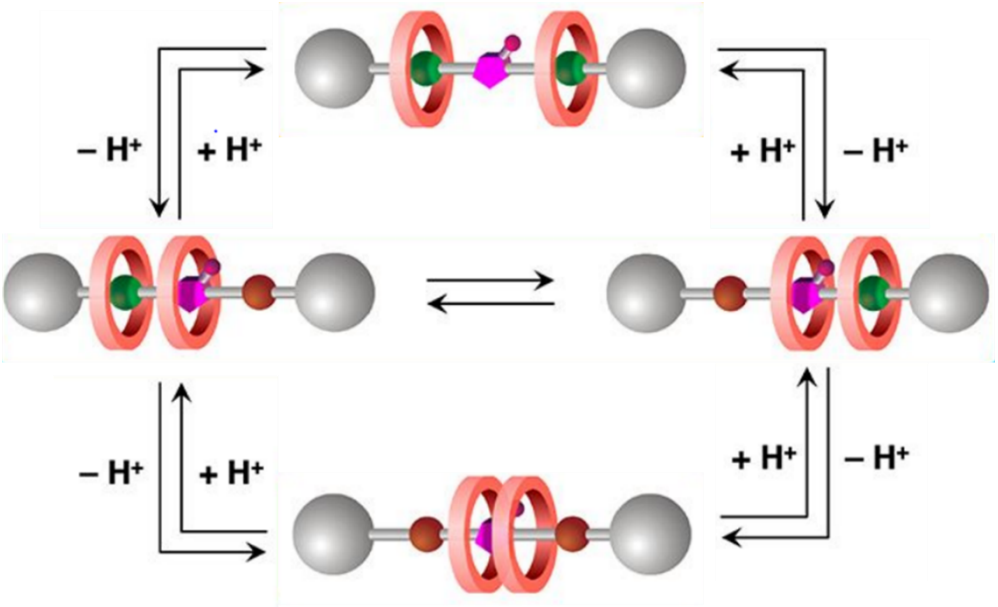

Figure 1.14 Acid-base triggered interconversion in the [3]rotaxane system.

[1] Almén, M. A.; Nordström, K. J.; Fredriksson, R.; Schiöth, H. B., *BCM Biology*, **2009**, *7*, 50.

[2] Britannica, T. Editors of Encyclopaedia. "cell membrane." Encyclopedia Britannica, **2019**.

[3] Cooper G.M., The Cell: A Molecular Approach, Sinauer Associates, Sunderland (MA), **2000**.

[4] Albers, R. W.; Siegel, G. J.; JianXie, Z., Chapter 3 - Membrane Transport. *Basic Neurochemistry*, eighth edition; New York, **2012**.

[5] Bangham, A. D.; Horne, R. W., *J. Mol. Biol*. **1964**, *8*, 660.

[6] Barenholz, Y., *Curr. Opin. Colloid Interface Sci.* **2001**, *1*, 66.

[7] Liu, L.; Kost, J.; Fishman, M. L.; Hicks, K. B., *ACS Symposium Series* **2008**, *992*, 14, 265.

[8] Israelachvili, J. N.; Marcelja, R. G.; Horn, R. G., *Q. Rev. Biophys*. **1980**, *2*, 121.

[9] Akbarzadeh, A.; Razaei-Sadabady, R.; Davaran, S.; Joo, S. W.; Zarghami, N.; Hanifehpour, Y.; Samiei, M.; Kouhi, M.; Nejati-Koshki, K., *Nanoscale Res. Lett*. **2013**, *8*, 102.

[10] Samad, A.; Sultana, Y.; Aqil, M., *Curr. Drug. Deliv*. **2007**, *4*, 297-305.

[11] Emami, S.; Azadmard-Damirchi, S.; Peighambardoust, S. H.; Valizadeh, H.; Hesari, J., *J. Exp. Nanosci.*, 11, 9, 737.

[12] Immordino, M. L.; Dosio, F.; Cattel, L., *Int. J. Nanomed*. **2006**, *3*, 297.

[13] Sercombe, L.; Veerati, T.; Moheimani, F.; Wu S. Y.; Sood, A. K.; Hua, S.; Front. Pharmacol., **2015**, 6, 286.

[14] Balzani, V.; Credi, A.; Venturi, M.; Molecular Devices and Machines-Concepts and Perspectives for the Nanoworld, Wiley-VCH, Weinheim, **2008**.

[15] a) Balzani, V.; Credi, A.; Raymo, F. M.; Stoddart, J. F.; *Angew. Chem. Int. Ed*., **2000**, 39, 3348; b) Erbas-Cakmak, S.; Leigh, D. A.; McTernan, C. T.; Nussbaumer, A. L.; *Chem. Rev.,* **2015**, 115, 10081.

[16] Schliwa, M.; Molecular Motors, Wiley-VCH, Weinheim, **2003**.

[17] Madigan, M. T.; Martinko, J. M.; Brock, T. D., *Brock biology of microorganisms*, Upper Saddle River, NJ, Pearson Prentice Hall, **2006**

[18] Watson, M. A., Cockroft, S. L., *Chem. Soc. Rev.*, **2016**, 45, 6118

[19] Weber, J., *Nat. Chem. Biol*., **2010**, *6*, 794.

[20] Heard W. A.; Goldup S. M., *ACS Cent. Sci.,* **2020**, *6*, 117.

[21] Sauvage, J. P.; Dietrich-Buchecker, C., *Molecular Catenanes, Rotaxanes and Knots*; Wiley: New York, **1999**.

[22] Bruns, C. J.; Stoddart, J. F. *The Nature of the Mechanical Bond: From Molecules to Machines*; Wiley: Hoboken, **2016**.

[23] Balzani V.; Credi A.; Raymo F. M.; Stoddart J. F., Angew. Chem. Int. Ed., **2000**, 39, 3348.

[24] Stoddart, J. F., *Angew. Chem. Int. Ed*. **2017**, *56*, 11094.

[25] Bruns, C. J.; Stoddart, J. F. The Nature of the Mechanical Bond: From Molecules to Machines. John Wiley and Sons, Hoboken, **2016**.

[26] Parisi, G.; *Nature*, **2005**, vol. 433, 221.

[27] Dattler, D.; Fuks, G.; Heiser, J.; Moulin, E.; Perrot, A.; Yao, X.; Giuseppone, N.; Chem. Rev., 2020, 120, 1, 310.

[28] Baroncini, M.; Casimiro, L.; De Vet, C.; Groppi, J.; Silvi, S.; Credi, A., ChemistryOpen, 2018, 7 (2), 169.

[29] Ariga, K., *Chem. Sci*., **2020**,11, 10594.

[30] Loose, M.; Schwille, P., *J. Struct. Biol*., **2009**, *1*, 143.

[31] Kinoshita, T., *Prog. Polym. Sci*. **1995**, *20*, 527.

[32] Ghadiri, M. R.; Granja, J. R.; Buehler, L. K., *Nature* **1994**, *369*, 301.

[33] Qi, S.; Zhang, C.;Yu, H.; Zhang, J.;Yan, T.;Lin, Z.; Yang, B.; Dong, Z., *J. Am. Chem. Soc.,* **2021**, 143, 9, 3284.

[34] Wang, W.; Li, R.; Gokel, G. W., *Chem. Eur. J*. **2009**, *15*, 10543.

[35] Chen, S.; Wang, Y.; Nie, T.; Bao, C.; Wang, C.; Xu, T.; Lin, Q.; Qu, D. H.; Gong, X.; Yang, Y.; Zhu, L.; Tian, H., *J. Am. Chem. Soc*., **2018**, *140*, 17992.

[36] Wang, C.; Wang, S.;Yang, H.;Xiang, Y.; Wang, X.; Bao C.; Zhu, L.; Tian, H.; Qu, D. H., *Angew. Chem. Int. Ed*., **2021**, 60, 27, 14836

[37] Wang, W. Z.; Huang, L. B.; Zheng, S. P.; Moulin, E.; Gavat, O.; Barboiu, M.; Giuseppone, N., J. Am. Chem. Soc., **2021**, 143, 38, 15653.

[38] Tecilla, P.; Bonifazi, D., *Chemistry Open*, **2020**, 9, 5, 538.

[39] Baroncini, M.; Ragazzon, G.; Silvi, S.; Venturi, M.; Credi, A.; *Photochemistry*, **2017**, 44, 296.

[40] Hartley, G. S., *Nature* **1937**, *140*, 281.

[41] Forber, C. L.; Kelusky, E. C.; Bunce, N. J.; Zerner, M. C., *J. Am. Chem., Soc*. **1985**, *107*, 5884.

[42] Cusati, T.; Granucci, G.; Persico, M.; Spighi, G., *J. Chem. Phys.,* **2008**,*128*, 194312.

[43] Bandara, D. H. M.; Burdette, S. C., *Chem. Soc. Rev*., **2012**, *41*, 1809.

[44] Avellini, T.; Li, H.; Coskun, A.; Barin, G.; Trabolsi, A.; Basuray, A. N.; Dey, S. K.; Credi, A.; Silvi, S.; Stoddart, J. F.; Venturi, M., *Angew. Chem. Int. Ed*. **2012**, *7*, 1611.

[45] Ragazzon, G.; Baroncini, M.; Silvi, S.; Venturi, M.; Credi, *Nature Nanotechnol*., **2015**, *10*, 70.

[46] Coskun, A.; Banaszak, M.; Astumian, R. D.; Stoddart, J. F.; Grzybowski, B. A., *Chem. Soc. Rev*., **2012**, *41*, 19.

[47] Chatterjee, M. N.; Kay, E. R.; Leigh, D. A., *J. Am. Chem. Soc.* **2006**, *128*, 4058.

[48] Zang, H.; Hou, X.; Zeng, L.; Yang, F.; Li, L.; Yan, D.; Tian, Y.; Jiang, L., *J. Am. Chem. Soc*., **2013**, *135*, 16102.

[49] Steinberg-Yfrach, G.; Liddell, P. A.; Hung, S.-C.; Moore, A. L.; Gust, D.; Moore, T. A, *Nature,* **1997**, *385*, 239.

[50] Curcio, M.; Nicoli, F.; Paltrinieri, E.; Fois, E.; Tabacchi, G.; Cavallo, L.; Silvi, S.; Baroncini, M.; Credi, A., *J. Am. Chem. Soc.*, **2021**, 143, 21, 8046.

2. Azobenzene intercalation in phospholipidic bilayer membrane

2.1 Introduction

Azobenzene is a widely used and well known stimuli-responsive molecule. In recent years this photoactive compound, has been applied in the field of supramolecular chemistry for the development of many light-modulated supramolecular systems[1,2,3] as well as of strategies for manufacturing molecular machines.[4,5] Prior to the intercalation and study in the liposomes membrane of more complex systems comprising azobenzene functionalities, this chapter regards studies performed on the sole azobenzene molecule intercalated in 1-palmitoyl-2-oleyl-*sn*-glycero-3-phosphocholine (POPC) liposomes, with the aim to outline experimental procedures and understand the influence and the behavior of this photochrome on the vesicles size, charge surface, membrane stability and viscosity.

2.2 Synthesis and study of azobenzene fuctionalised liposomes

Liposomes functionalized with azobenzene were prepared according to the method described in **Section 2.4.1** by addition of a chloroform solution of **azobenzene** (5% mol/mol) to a chloroform solution containing the phospholipids POPC (1-palmitoyl-2-oleoyl-*sn*-glycero-3-phosphocholine) and by removal of the solvent under reduced pressure to obtain a homogeneous film. Rehydration of the film with a phosphate buffer solution (PBS, 121.5 M NaCl, 25.2 mM Na_2HPO_4, 4.8 mM KH_2PO_4, pH = 7.4) and extrusion through a porous polycarbonate membrane placed in a hand-held extrusion device (100 nm pore size) provided the functionalized vesicles. However, upon analysis of the final liposomes suspension via UV-vis spectroscopy, a lower amount of guest was detected compared to the amount of azobenzene added. In order to quantify the loss and define its origin, liposomes doped with different amounts of azobenzene were prepared and analyzed by UV-vis absorption spectroscopy. The screening led to the identification of a systematic 4% loss of loaded guest (**Table 2.1**), likely caused by the nanopore filtration through the extruder

membranes responsible of material retention,[6] and potentially worsened by the small size of the guest molecule.

Table 2.1. Retention of intercalated **azobenzene** in liposome vesicles; [POPC] = $6.5 \cdot 10^{-3}$ M, PBS pH = 7.4, 298 K.

Experiment	Azobenzene loaded (mol%)	Azobenzene in liposomes (mol%)	Azobenzene loss (mol%)
1	8	4.5	3.5
2	10	5.8	4.2
3	30	25.3	4.7

This investigation enabled to proceed in the preparation of azobenzene-functionalized vesicles and perform the analysis required for their characterization. The absorption spectrum of POPC liposomes containing 5% of *E*-**azobenzene** is reported in **Figure 2.1**: it exhibits an intense band in the near UV region corresponding to the $\pi \rightarrow \pi^*$ transition and a weaker band in the visible region arising from $n \rightarrow \pi^*$ transition. Upon irradiation at λ = 365 nm for 1 h, $E \rightarrow Z$ isomerization of the chromophore occurs, obtaining the absorption spectrum of the *Z*-**azobenzene** functionalised liposomes (**Figure 2.1**, red line). Such spectrum is characterized by a lower intensity of the $\pi \rightarrow \pi^*$ transition band accompanied by a small increase in the intensity of the $n \rightarrow \pi^*$ transition band, confirming that the photoisomerization of the guest is possible even when intercalated in the membrane. The physicochemical characterization of liposomes was performed analyzing particle size and size distribution, surface Z-potential, membrane stability and viscosity.

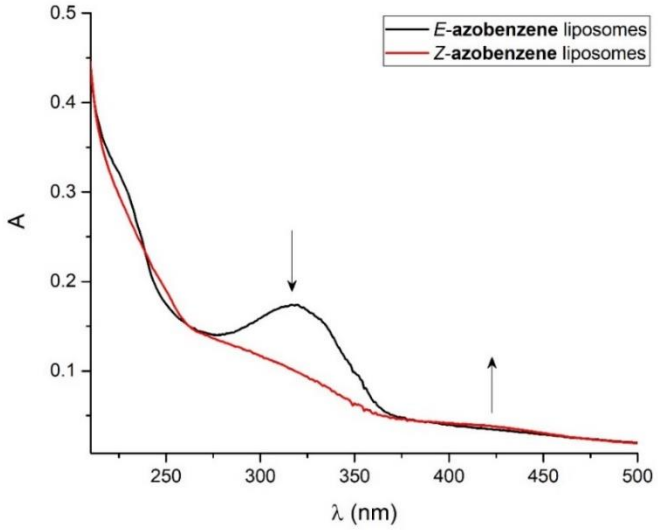

Figure 2.1. Absorption spectra of an aqueous suspension of liposomes functionalised with *E*-**azobenzene** (black line) or after irradiation at λ = 365 nm for 1 h to *Z*-**azobenzene** (red line); [POPC] = $1.5 \cdot 10^{-4}$ M; **azobenzene** 5% mol/mol, PBS pH = 7.4, 298 K.

2.2.1 Dynamic Light Scattering characterization

Information on the size distribution of liposomal vesicles was obtained by means of dynamic light scattering (DLS). Liposomes composed of pure POPC phospholipids analysed by DLS displayed a monodisperse population with an average diameter of 125 nm (**Table 2.2**). The measurement performed on 5% *E*-**azobenzene** functionalized liposomes showed the presence of a single population with a diameter of 121 nm, that remained unvaried upon azobenzene $E \rightarrow Z$ isomerization by irradiation at λ = 365 nm for 1 h (**Figure 2.2**). Overall, comparing functionalized liposomes with pristine ones did not highlight any influence from the presence of the azobenzene guest in the bilayer in any of its configuration.

Table 2.2. Hydrodynamic diameter of aqueous suspensions of liposomes containing only POPC, functionalized with *E*-**azobenzene** or after irradiation at λ = 365 nm for 1 h to *Z*-**azobenzene**; **azobenzene** 5% mol/mol, [POPC] = $3.2 \cdot 10^{-4}$ M, PBS pH = 7.4, 298K.

Liposomes sample	Hydrodynamic diameter (nm)
POPC	125
E-**azobenzene**	121
Z-**azobenzene**	123

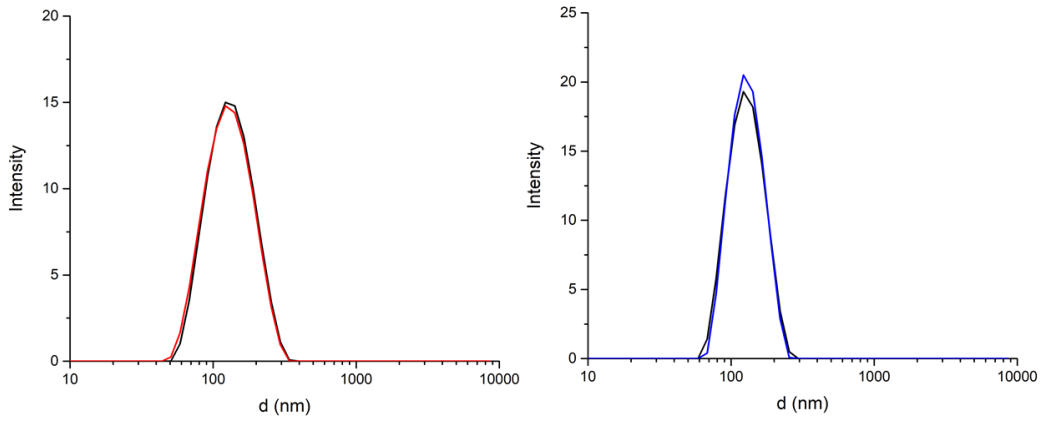

Figure 2.2. DLS graphs of aqueous suspensions of liposomes functionalized with *E*-**azobenzene** (left) or after irradiation at λ = 365 nm for 1 h to *Z*-**azobenzene** (right); **azobenzene** 5% mol/mol, [POPC] = $3.2 \cdot 10^{-4}$ M, PBS, pH = 7.4, 298K.

2.2.2 Surface zeta potential analysis

Zeta potential analysis is performed to gain an indirect measurement of particles surface charge and information regarding the stability of the colloidal system. Focusing on POPC-derived liposomes, the phospholipid 1-palmitoyl-2-oleoyl-*sn*-glycero-3-phosphocholine is a zwitterionic molecule and in such lipids the origin of the sign of the zeta potential is a matter of discussion. The zeta potential value is related to the microscopic arrangement of liposomes surface functional groups and water at the interphase, and its sign and value are ascribed to the orientation of the polar head groups in the plane of the membrane, with the orientation that changes by varying the temperature and the ionic strength of the medium. At low ionic strength, the choline groups are located below the phosphate groups (negative zeta potential), whereas at high ionic strength the situation is reversed.[7,8] Therefore, the Z-

potential analysis performed on pure POPC liposomes in a low ionic strength medium, such as a 10 mM NaCl solution, provides a negative and close to zero Z-potential value (**Table 2.3**).

Similarly to what observed for DLS measurements, Z-potential analysis carried out on liposomes containing 5% **azobenzene** in its *E* or *Z* forms did not show substantial variations compared to the unfunctionalized sample, suggesting that the relatively small and neutrally charged guest does not affect the liposomal surface organization and thus its surface potential.

Table 2.3. Z-potential value of aqueous suspensions of liposomes containing only POPC**,** functionalized with *E*-**azobenzene** or after irradiation at λ = 365 nm for 1 h to *Z*-**azobenzene**; **azobenzene** 5% mol**/**mol, [POPC] = $1.32 \cdot 10^{-5}$ M, 10 mM NaCl, 298K.

Liposomes sample	**ζ (mV)**
POPC	– 4.0
E-**azobenzene**	– 6.4
Z-**azobenzene**	– 6.2

2.2.3 Photoinduced carboxyfluorescein leakage

To evaluate the effect of the intercalated guest on the membrane stability, a commonly used experimental approach makes use of the photophysical properties of selected fluorescent dyes. Among them, 5(6)-carboxyfluorescein (CF^{3-}) is widely used due to its low membrane permeability and its pH- and concentration-dependent photophysical properties.[9,10] Initially, the dye is loaded in the liposomal core at a high concentration that induces the self-quenching of its fluorescence due to energy transfer to non-fluorescent dimers.[11] Subsequently, the efflux from liposomes results in the dilution of the dye in the extravesicular medium with the concomitant recovery of its fluorescence.[12] Taking advantage of this release, the time dependent increase of CF^{3-} fluorescence is recorded and the resulting kinetic constant used to evaluate the liposomal membrane permeability.

Liposomes containing self-quenched CF^{3-} in their aqueous core and functionalized with 5% mol/mol of **azobenzene** in the bilayer membrane were prepared following the procedure in **Section 2.4.2.** The absorption spectrum of the *E*-**azobenzene** functionalized liposomes loaded with CF^{3-} is reported in black in **Figure 2.3**. Upon irradiation of the sample with 365

nm light for 1h, the typical spectral variations associated to the *E* to *Z* azobenzene photoisomerization are displayed.

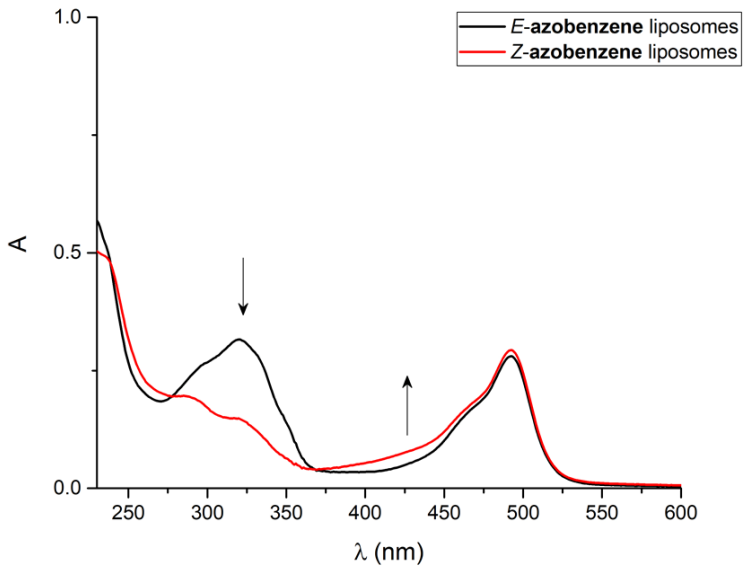

Figure 2.3 Absorption spectra of aqueous suspensions of liposomes containing CF^{3-} and functionalized with *E*-**azobenzene** (black) and after irradiation at λ = 365 nm for 1 h to *Z*-**azobenzene** (red); **azobenzene** 5 % mol/mol, [CF^{3-}] = 50 mM, [POPC] = $2.6 \cdot 10^{-4}$ M, PBS pH = 7.4, 298 K.

The membrane stability of liposomes composed of pure POPC or functionalized with 5% mol/mol of *E* or *Z* **azobenzene** was evaluated by monitoring the increase in emission caused by the efflux of the entrapped dye. Fitting the experimental data provided a kinetic constant for each set of experiments, which was used to quantify the level of permeabilization achieved as a consequence of the presence of the guest in the bilayer – the higher the kinetic constant was, the more are the defects that the intercalated guest induces in the membrane. The time-dependent release of the dye encapsulated in *E*-**azobenzene** functionalized liposomes kept in the dark was compared with that obtained from the sample functionalized with *Z*-**azobenzene** and to the spontaneous release obtained from pure POPC liposomes.

A typical kinetic profile consists of a curve in which the time-dependent increase of carboxyfluorescein fluorescence is reported. This profile is consistent with a first order kinetic mechanism and usually an apparent first order rate constant k_{obs} can be determined according to the following equation:

$$\frac{d[CF^{3-}]}{dt} = k_{obs}\,[CF^{3-}]$$

By comparing the kinetic constant value arising from CF^{3-} leakage, it is possible to verify whether the presence of azobenzene in its *E* or *Z* isomer has an influence on the efflux of the dye from the liposomal core to the extravesicular medium. However, while the kinetic profile of the CF^{3-} release from pure POPC liposomes is in accordance with the first order kinetic equation, those resulting from vesicles functionalised with *E*- or *Z*-**azobenzene** molecules require two first order contributions to be described, thus providing two k_i values weighted by two pre-exponential factors (A_i) (**Figure 2.4, Table 2.5**). It can be hypothesised that, because of the relatively small size of azobenzene, such molecules are able to organize themselves in the membrane, leading to a non-homogeneous functionalization. In this context, the CF^{3-} efflux experiences different environments in the bilayer giving rise to two different kinetics, of which one presents a higher kinetic constant (k_{obs1}) while the other presents a lower kinetic constant (k_{obs2}) of the same order of magnitude as that observed for the pristine POPC liposomes leakage. Moreover, the experimental data suggest that the membrane permeability is not affected by the different isomers of the guest, as the values of the kinetic constants are similar for both *E*- and *Z*-**azobenzene** (**Table 2.5**). Analogously, also the analysis performed to determine the vesicles size and size distribution did not display changes as a consequence of the presence of the intercalated guest in the bilayer, even after its photoisomerization (**Table 2.6**).

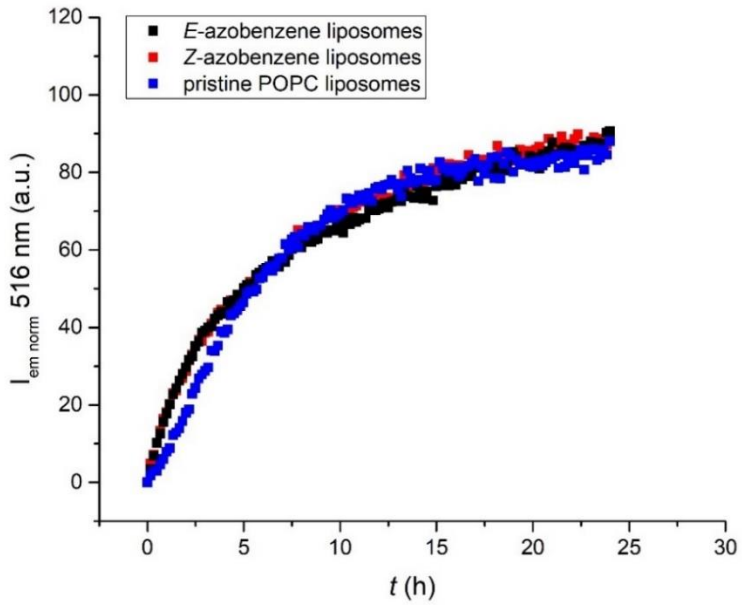

Figure 2.4. Kinetic profile of the release of CF^{3-} loaded in unfunctionalized liposomes (blue), or liposomes functionalized with *E*-**azobenzene** (black) or *Z*-**azobenzene** (red); **azobenzene** 5% mol/mol, [POPC] = $1.32 \cdot 10^{-5}$ M, PBS pH = 7.4, 298 K.

Table 2.5. Kinetic constants related to the release of CF^{3-} from unfunctionalized liposomes, or liposomes functionalized with *E*-**azobenzene** or *Z*-**azobenzene**; **azobenzene** 5% mol/mol, [POPC] = $1.32 \cdot 10^{-5}$ M, PBS pH = 7.4, 298 K.

Liposomes sample	k_{obs1} **(s^{-1})**	k_{obs2} **(s^{-1})**	**Pre-exponential factor A_1 (%)**	**Pre-exponential factor A_2 (%)**
POPC	$(4.71 \pm 0.07) \times 10^{-5}$	-	-	-
E-**azobenzene**	$(2.6 \pm 0.2) \times 10^{-4}$	$(3.2 \pm 0.3) \times 10^{-5}$	45	55
Z-**azobenzene**	$(1.5 \pm 0.5) \times 10^{-4}$	$(1.9 \pm 0.2) \times 10^{-5}$	50	50

Table 2.6. Hydrodynamic diameter of aqueous suspensions of liposomes containing CF^{3-} in the inner core and composed of POPC only, functionalized with *E*-**azobenzene,** or after irradiation at λ = 365 nm for 1 h to *Z*-**azobenzene**; **azobenzene** 5% mol/mol, [CF^{3-}] = 50mM, [POPC] = $2.6 \cdot 10^{-4}$ M, PBS pH=7.4, 298 K.

CF^{3-} loaded liposomes sample	**Hydrodynamic diameter (nm)**
POPC	90
E-**azobenzene**	84
Z-**azobenzene**	83

2.2.4 Membrane microviscosity analysis

An additional parameter to get information about the organisation between phospholipids and guest molecules is viscosity. The most diffused approach to determine liposomal membrane microviscosity takes advantage of a fluorescent lipophilic probe, such as pyrene, and its aptitude to form excimers.[13] This technique assumes that, because of its hydrophobicity, the probe is distributed exclusively in the phospholipid bilayer. The formation of excimers implies a high mobility of the probe in the membrane, and this indicates a low viscosity of the environment surrounding pyrene molecules. The ratio between the fluorescence intensity of the pyrene excimer (I_E, λ = 480 nm) and that of the pyrene monomer

(I_M, λ= 395 nm), is used to quantify the translational diffusivity of the probe in the bilayer, which is inversely proportional to the viscosity of the membrane.[14] Emission spectra of POPC vesicles functionalized with *E*-**azobenzene**, recorded upon increasing the amount of pyrene in the sample (see **Section 2.4.3**) exhibit a gradual increase in the fluorescence of the sole band at λ = 395 nm, whereas liposomes containing *Z*-**azobenzene** show an increase at λ = 395 nm combined with the slight increase of the band at λ = 480 nm (**Figure 2.5**). The comparison between the fluorescence intensity ratio I_E/I_M of liposomes functionalized with *E*-**azobenzene**, *Z*-**azobenzene** or pure POPC vesicles, obtained at a precise concentration of pyrene and phospholipids in the sample, allows to determine that the presence of the guest in both its isomeric forms influences the bilayer viscosity. More specifically, *E*-**azobenzene** increases the membrane viscosity even more compared to the *Z*-isomer (**Table 2.7**). This could arise from the apolar nature of the *E*-**azobenzene** isomer which induces a greater increase in the viscosity when located in the lipophilic bilayer, than the *Z*-isomer, which locates itself closer to the polar head of the phospholipids due to its higher dipole moment.

Table 2.7. I_E/I_M ratio and hydrodynamic diameter of aqueous suspensions of unfunctionalized liposomes, or liposomes functionalized with *E*-**azobenzene**, or *Z*-**azobenzene**; **azobenzene** 5% mol/mol, [POPC] = $2.65 \cdot 10^{-3}$ M, PBS pH = 7.4, 298 K.

Sample	**I_E/I_M**	**Hydrodynamic diameter (nm)**
POPC	0.35	125
E-**azobenzene**	0.11	123
Z-**azobenzene**	0.17	123

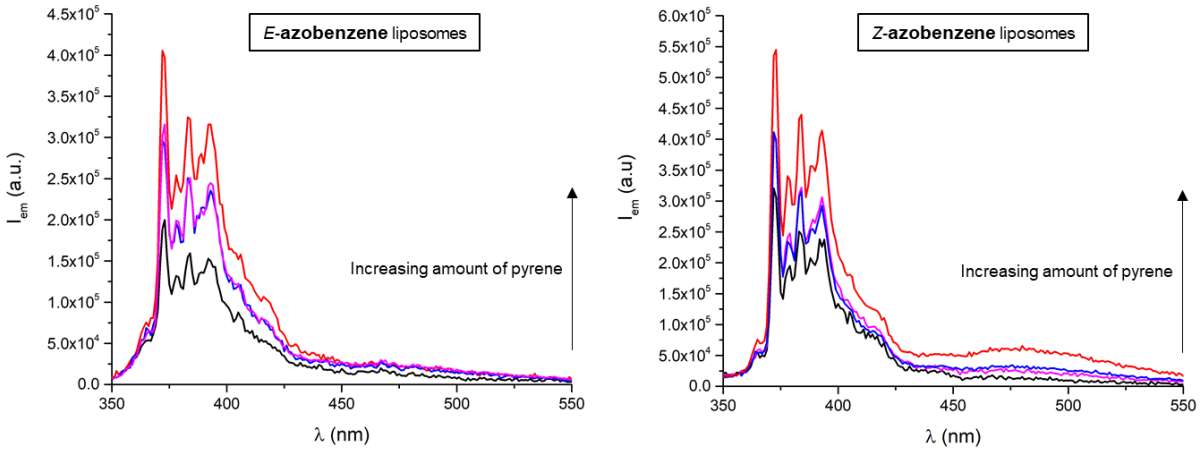

Figure 2.5. Emission spectra of aqueous suspensions of liposomes functionalized with *E*-**azobenzene** (left) or *Z*-**azobenzene** (right); **azobenzene** 5% mol/mol, [POPC] = $2.65 \cdot 10^{-3}$ M, PBS pH = 7.4, 298 K.

2.3 Conclusions

A set of experimental procedures was developed to characterize liposomes presenting a guest molecule in the bilayer. The use of azobenzene as the guest provided the opportunity to analyse the effect of the photoactive compound in the bilayer, both in the *E* form and upon photoisomerization of the guest to the *Z* isomer. From the analyses carried out to evaluate vesicles diameter, surface charge and membrane permeability it can be concluded that, upon intercalation of azobenzene, the properties of the bilayer remain mostly unaltered compared to the unfunctionalized vesicles. Conversely, the introduction of the chromophore guest has an influence on the membrane viscosity, modifying the phospholipids packing and increasing the net viscosity of the membrane. Moreover, the two isomeric forms of the guest impact differently the viscosity, with *E*-**azobenzene** providing a higher increase compared to the *Z*-isomer.

The establishment of accurate procedures to analyse complex systems such as liposomal vesicles enabled the development and characterization of systems embedding more complex photoresponsive guests, which will be described in the following chapter.

2.4 Instruments and methods

POPC was purchased from Avanti Polar Lipids (Alabaster, AL). CF^{3-} (95% purity), Sephadex G-25 and pyrene (99% purity) were purchased from Merck.

2.4.1 Preparation of vesicles

An appropriate amount of azobenzene solution in $CHCl_3$ was added to a POPC solution in $CHCl_3$ (25 mg/mL) to give required guest/lipid ratio. The mixture was evaporated under reduced pressure at 30°C to form a thin phospholipid film on the inside wall of a flask that was dried under vacuum for 1 h, then stored for 18h at 4°C before rehydration with 1 mL of the appropriate buffered solution. The resulting heterogeneous liposomal suspension was extruded 25 times through polycarbonate membrane (pore size 100 nm) mounted on an Avanti Polar Lipids (Alabaster, AL, USA) mini-extruder, extrusion was performed at room temperature. The POPC concentration of liposomal suspension after extrusion was 6.5×10^{-3} M. Prior to be used, the extruded suspension was diluted with the appropriate buffer to give a final concentration of POPC equal to 2.64×10^{-3} M for viscosity measurements, 3.25×10^{-4} M for DLS analysis, 1.32×10^{-5} M for Z-potential analysis and stability measurements. For DLS analysis liposomes were suspended in PBS composed of 121.5 mM NaCl, 25.2 mM Na_2HPO_4, 4.8 mM KH_2PO_4, (pH=7.4) while for Z-potential measurements liposomes were suspended in NaCl 10 mM aqueous solution.

2.4.2 Carboxyfluorescein permeation experiment

For quenching/dequenching carboxyfluorescein (CF^{3-}) measurements, the rehydration of the lipidic film was performed by using 50 mM CF^{3-} buffered aqueous solution (121.5 mM NaCl, 25.2 mM Na_2HPO_4, 4.8 mM KH_2PO_4, 50 mM CF^{3-}). To get rid of non-entrapped dye the liposomes were purified via size exclusion chromatography making use of Sephadex G-25 resin. Extrusion and gel permeation column chromatography were performed at room temperature. Prior to use, the liposomal solutions were diluted with the appropriate buffer (isosmotic to the one used during the rehydration step) to give a final concentration of POPC equal to 1.32×10^{-5} M for stability measurements, assuming 100% elution of the lipid during the gel filtration process. The buffer used for the stability measurements was made of PBS composed of 121.5 mM NaCl, 25.2 mM Na_2HPO_4, 4.8 mM KH_2PO_4, (pH=7.4). The

fluorescence intensity was measured at an emission wavelength of 516 nm using 490 nm as the excitation wavelength.

2.4.3 Microviscosity analysis

The viscosity of the liposomal membranes was determined by using pyrene as the fluorescent probe. A 5×10^{-3} M solution of pyrene in MeOH was added portion-wise to the 2.64×10^{-3} M liposomes suspension to reach a final concentration of POPC and pyrene in the suspension of 2.64×10^{-3} M and 5×10^{-5} M respectively. The fluorescence intensity ratio, I_E/I_M, was used for membrane microviscosity estimates (where I_E is fluorescence intensity of the pyrene excimer at 480 nm and I_M is fluorescence intensity of the pyrene monomer at 395 nm). Fluorescence emission spectra were taken at the excitation wavelength l_{ex}=335 nm. The buffer solution used for the dilution of the extruded liposomes suspension to perform viscosity measurements was made of 121.5 mM NaCl, 25.2 mM Na_2HPO_4, 4.8 mM KH_2PO_4.

2.4.4 Liposomes characterization

The absorption spectra in the 800-200 nm range were recorded using a PerkinElmer Lambda 750 double beam spectrophotometer. All the acquisitions were carried out at room-temperature on air-equilibrated solutions of the samples contained in spectrophotometric quartz cuvettes of 1 cm optical path length. The precision on the wavelength values was ± 1 nm. Emission spectra were recorded using Perkin-Elmer LS 50.

Irradiation of samples was performed using a medium pressure Hg lamp (200 W) with constant stirring. The irradiation wavelength was selected using interference filters. All photoisomerizations were carried out by irradiating the samples for defined intervals of time and recording variations in the absorption spectra with the spectrophotometer until the photostationary state (PSS) was reached.

The liposomes were characterized on a Malvern Instruments DLS ZetaSizer Nano-ZS to estimate their size and zeta potential. For size measurements single-use PMMA cuvettes were used, containing 1 mL of diluted liposomal suspension; for zeta potential determination, disposable folded capillary cells containing 1 mL of diluted liposomal suspension in NaCl 10 mM (pH 7.4) were used.

- **DLS technique**

Dynamic light scattering is a useful technique to determine particle size having submicrometric dimensions.[15] The particles size is expressed in terms of hydrodynamic diameter, $d(H)$, which is derived from the translational diffusion coefficient (D) using the *Stokes-Einstein equation*:

$$d(H) = \frac{K_B T}{3\pi\eta D}$$

where K_B is the Boltzmann constant, T is the temperature and η expresses the medium viscosity. Since particles are in solution, the $d(H)$ is defined as the diameter of a spherical rigid particle having the same diffusion coefficient and the same diffusion speed as the measured one.

- **Z-potential analysis**

The zeta potential (ζ) is a physical property exhibited by particles in suspension that indicates the colloidal stability of the system. When a particle bears a net charge on its surface and it is suspended in a solution, the liquid layer that surrounds it exists as two regions: the *Stern layer*, in which ions having opposite charge are strongly bound to the surface of the particle and the *diffuse layer*, where ions are less firmly associated. Within this layer, a theoretical boundary layers exists, in which ions and particles form a stable entity: when the particle moves, ions within this layer move with it, whereas ions beyond this layer stay whit the bulk dispersant. Zeta potential is defined as the potential at this surface of hydrodynamic shear, as shown in **Figure 2.6**.

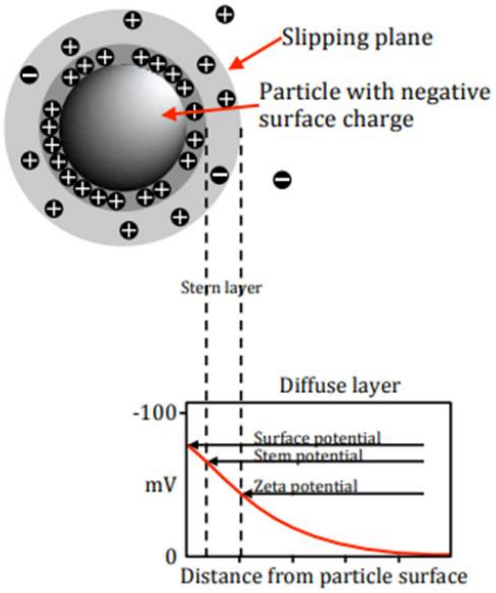

Figure 2.6 Schematic representation of the zeta potential.[16]

Zeta potential depends on pH, ionic strength and conductivity of the dispersing medium and on the superficial charge of the particle. The main consequence of having a colloidal system, in which the dispersed particles are charged, is that they interact with an applied electric field. The electrophoresis method is widely used and the *Henry equation* correlates the electrophoretic mobility (U_E) and the zeta potential (z):

$$U_E = \frac{2\varepsilon z f(ka)}{3\eta}$$

Where ε is the dielectric constant, η is the viscosity and $f(ka)$ is the Henry's function. Electrophoretic mobility is measured by using the Laser Doppler Electrophoresis Technique together with a combination of Laser Doppler velocimetry and Phase Analysis Light Scattering. As a consequence of the applied electric field, motion of particles caused a fluctuation of the light scattered by the sample and the fluctuation frequency is proportional to the particle speed, allowing the zeta potential to be derived. Generally, values below –10 mV indicate negatively charged particles, zeta potentials above +10 mV describe positive particles, while intermediate values denote particles with neutral surfaces.[17]

[1] Qu, D. H.; Wang, Q. C.; Zhang, Q. W.; Tian, X. Ma, H., *Chem. Rev.,* **2015**, 115, 7543.

[2] Baroncini, M.; Bergamini G., *Chem. Rec.*, **2017**, 17, 700.

[3] Kamiya, Y.; Asanuma, H., *Acc. Chem. Res.,* **2014**, 47, 1663.

[4] Dattler, D.; Fuks, G.; Heiser, J.; Moulin, E.; Perrot, A.; Yao, X.; Giuseppone, N., *Chem. Rev.*, **2020**, 120, 310.

[5] Cheng, H. B.; Zhang, S.; Qi, J.; Liang, X. J.; Yoon, J., *Adv. Mater*. **2021**, 2007290.

[6] Guo, P.;Huang, J.; Zhao, Y.; Marti,n C. R.; Zare, R. N.; Moses M. A., *Small* **2018**, 170349.

[7] Disalvo, A.; Frias, M. A., *Membranes*, **2021**, 11, 821.

[8] Kassem, A. M.; Mowafy, H. A. A.; Abu-Elyazid, S. K.; Samy, A. M.; Okuhira, K., *Az. J. Pharm Sci*. **2021**, 63.

[9] Cohen-Kashi, M.; Deutsch, M.; Tirosh, R.; Rachmani, H.; Weinreb, A., *Spectrochim. Acta*, **1997**, 53, 1655.

[10] Aschi, M.; D'Archivio, A.; Fontana, A.; Formiglio, A., *J. Org. Chem*., **2008**, 73, 3411.

[11] Chen, R. F.; Knutson, J. R., *Anal. Biochem.*, **1988**, 172, 61.

[12] Weistein, J. N.; Yoshikami, S.; Henkart, P.; Blumenthal, R.; Hagins, W. A.; *Science*, **1977**, 195, 489.

[13] a) Pownall, H. J.; Smith, L. C.; *J. Am. Chem. Soc*., **1973**, 95, 3136. b) Galla, H. J.; Sackmann, E.; *Biochim. Biophys. Acta*, **1974**, 339, 103.

[14] a) Vanderkooi, J. M.; Callis, J.B.; *Biochemistry*, **1974**, 13, 4000 b) Han, S. K.; Lee, Y. S.; Kim, M.; *Arch. Pharm. Res*., **1990**, 13, 192.

[15] Pecora, R., *J. Nanoparticle Res*., **2000**, *2*, 121.

[16] Malvern Instrument Technical Note.

[17] Smith, M. C.; Crist, R. M.; Clogston, J. D.; McNeil, S. E., *Anal. Bioanal. Chem.,* **2017**, *24*, 409-417.

3. Intervesicular interactions promoted by intercalated photoactive threads

3.1 Introduction

The compartmentalization of space provided by biological membranes is one of the foundational elements of life.[1] The membrane provides a barrier that defines and protects cellular or subcellular structures, but at the same time the passage of ions and polar molecules needs to be allowed to maintain the operation of the cell. Such transport across cell membranes is performed by species embedded in the bilayer in accordance to passive or active mechanisms. In light of the importance of those species in nature, the development of synthetic molecular devices capable of regulating ion transport across membranes is a growing research area in supramolecular chemistry, motivated by the high basic science value and the potential for therapeutic applications.[2] While synthetic molecular machines able to achieve a passive transport have been reported,[36,37] artificial systems capable of performing active transport across the bilayer are still missing. In addition, the prospective of exploiting an external source of energy like light to power such synthetic molecular pumps is an inspiring ambition.

The first things to evaluate when designing a molecule to be intercalated in a phospholipid bilayer are the characteristics that such a molecule must possess. The most important property required in a compound with this purpose is the amphiphilicity. Wang and co-workers reported a list of criteria to follow to design molecules having a transmembrane conformation. Essential factors are the molecule length, which must be membrane-spanning; the presence of a residue with central relay functions; polar groups localised at both extremities of the molecule to improve amphiphilicity, and finally, a straightforward and modular synthetic approach. [3] Based on this, the synthetic route proposed for our axles has been devised to access common intermediates, such as the polar tails and the dibenzylamine moiety. A modular approach allows for a more efficient synthesis of molecules sharing a similar chemical structure.

This chapter regards the synthesis and the study of two molecular axles able to interact with light that, once intercalated in a compartmentalized structure such as the lipid bilayer membrane of a liposome, could be used as components for molecular pumps. The axles, presented in **Figure 3.1**, contain an ammonium station that can act as a recognition site for a macrocycle, an azobenzene photoactive unit, able to undergo reversible *E/Z* photoisomerization, an alkyl chain with the function of hydrophobic spacer and two hydrophilic ethylene glycol chains at the extremities. The two molecules differ only in the length of the alkyl chain: in the axle named **C10**, the alkyl chain contains ten carbon atoms, while in the other, labelled **C12**, it includes twelve carbon atoms (**Figure 3.2**). In the following paragraphs, we will refer to a *head section* to indicate the portion of the molecule where the ethylene glycol chain is attached to the azobenzene group and to a *tail section* to indicate the portion of the molecule where the ethylene glycol chain is linked to the hydroquinone portion.

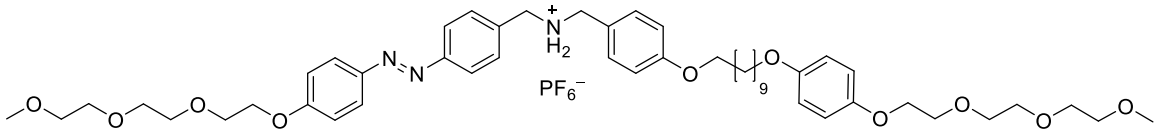

E-**C10**

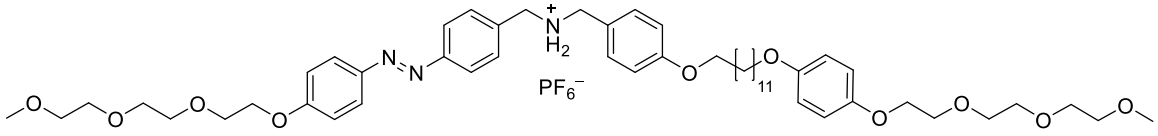

E-**C12**

Figure 3.1. Chemical structures of the molecular axles *E*-**C10** and *E*-**C12**.

These molecular axles have been designed to allow their intercalation in lipid bilayers, indeed, they are amphiphilic and have a length comparable with the thickness of the POPC double layer membrane. The length of *E*-**C12** is the same as that of the POPC bilayer membrane, while *E*-**C10** is slightly shorter. Due to the hydrophilic chains placed at both ends, both axles can arrange themselves linearly inside the lipid bilayer so that the two ends are on opposite sides placed in the membrane polar interfacial region (**Figure 3.2**).

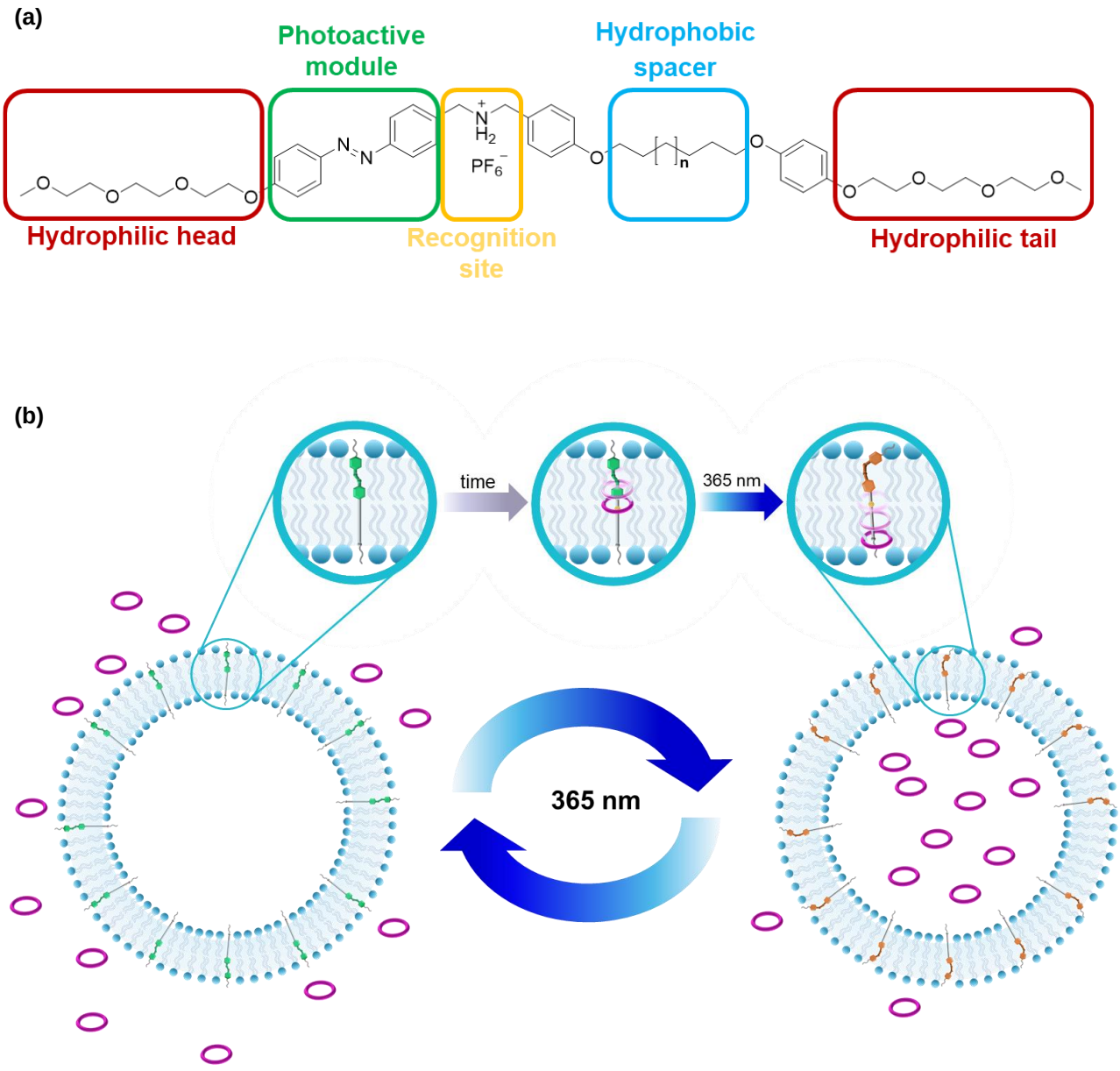

Figure 3.2. a) Highlight of the subunits that compose the axles **C10** and **C12**. b) Schematic representation of the pumping process: the macrocycles initially located in the bulk solution (left) are pumped across the membrane towards the core compartment (right) through *E*↔*Z* isomerization cycles upon light irradiation (central insets).

3.2 Synthesis and characterization of the C10 molecular axle

The first fragment synthesized contains the aliphatic chain and was obtained from the reaction of hydroquinone monobenzyl ether **2** and the amphiphilic ethylene glycol derivative **1** to provide the thread "tail". Subsequent debenzylation and substitution with 1,10-dibromodecane afforded intermediate **5**. In order to synthesize the precursor of the

recognition site module, a reductive amination between *tert*-butyl(4-formylphenyl)carbamate and 4-hydroxybenzylamine was carried out, leading ultimately to the formation of the dibenzylamine derivative **6**. The latter was successively protected to provide the carbamate **7** in an overall 95% yield.

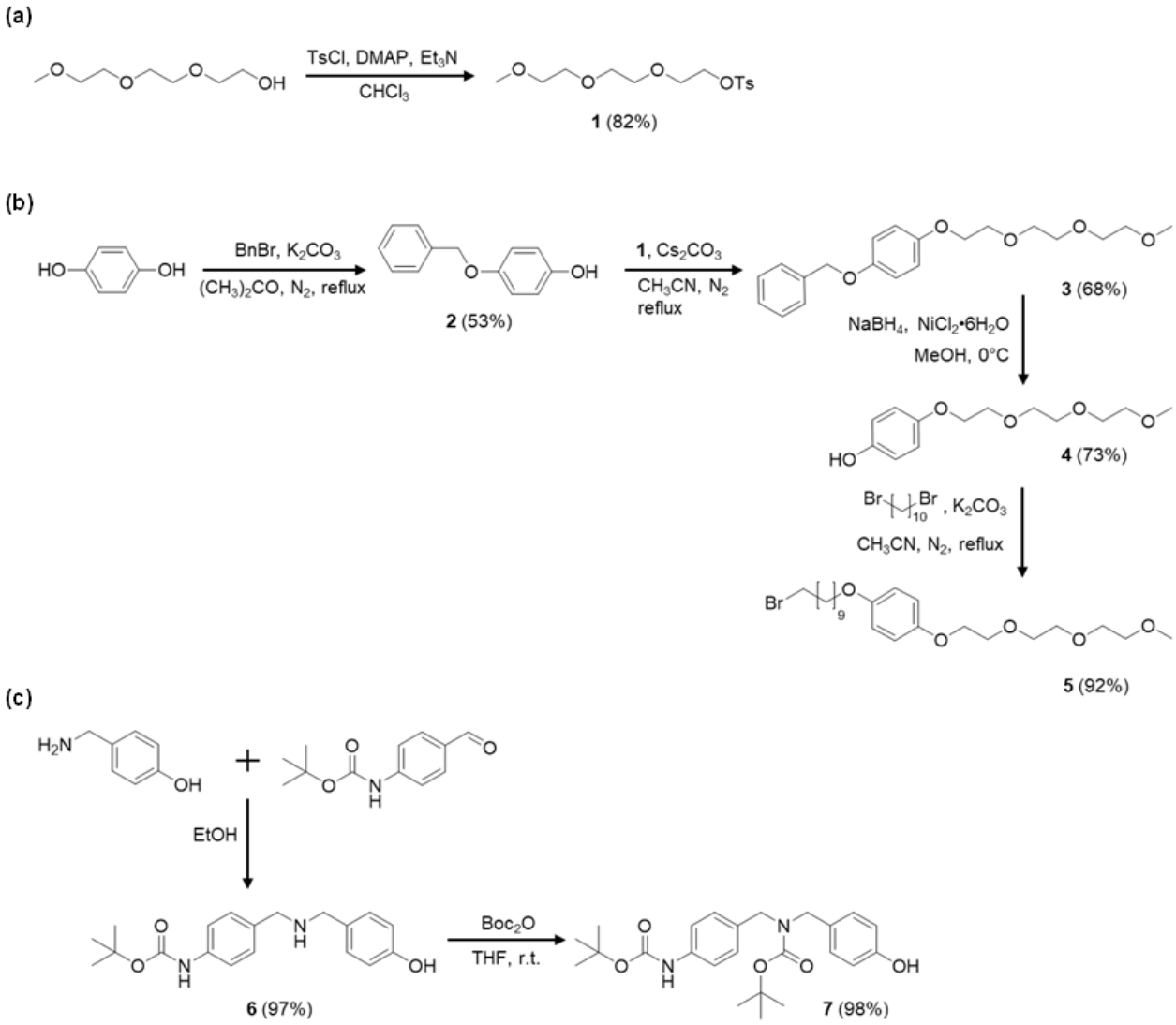

Scheme 3.1. Synthetic route to intermediates **1** (a), **5** (b), **7** (c).

The reaction between the precursor of the recognition site module **7** and intermediate **5** gave compound **8** in 75% yield. The latter was deprotected on both amine and aniline groups and used in a diazocopulation reaction to access the photoactive azobenzene derivative **10**. Starting from **10**, a protection-substitution protocol provided the carbamate thread **12**. The final step involved the removal of the amine protecting group and the simultaneous

protonation to dibenzylammonium salt to obtain the axle *E*-**C10** in quantitative yield (**Scheme 3.2**).

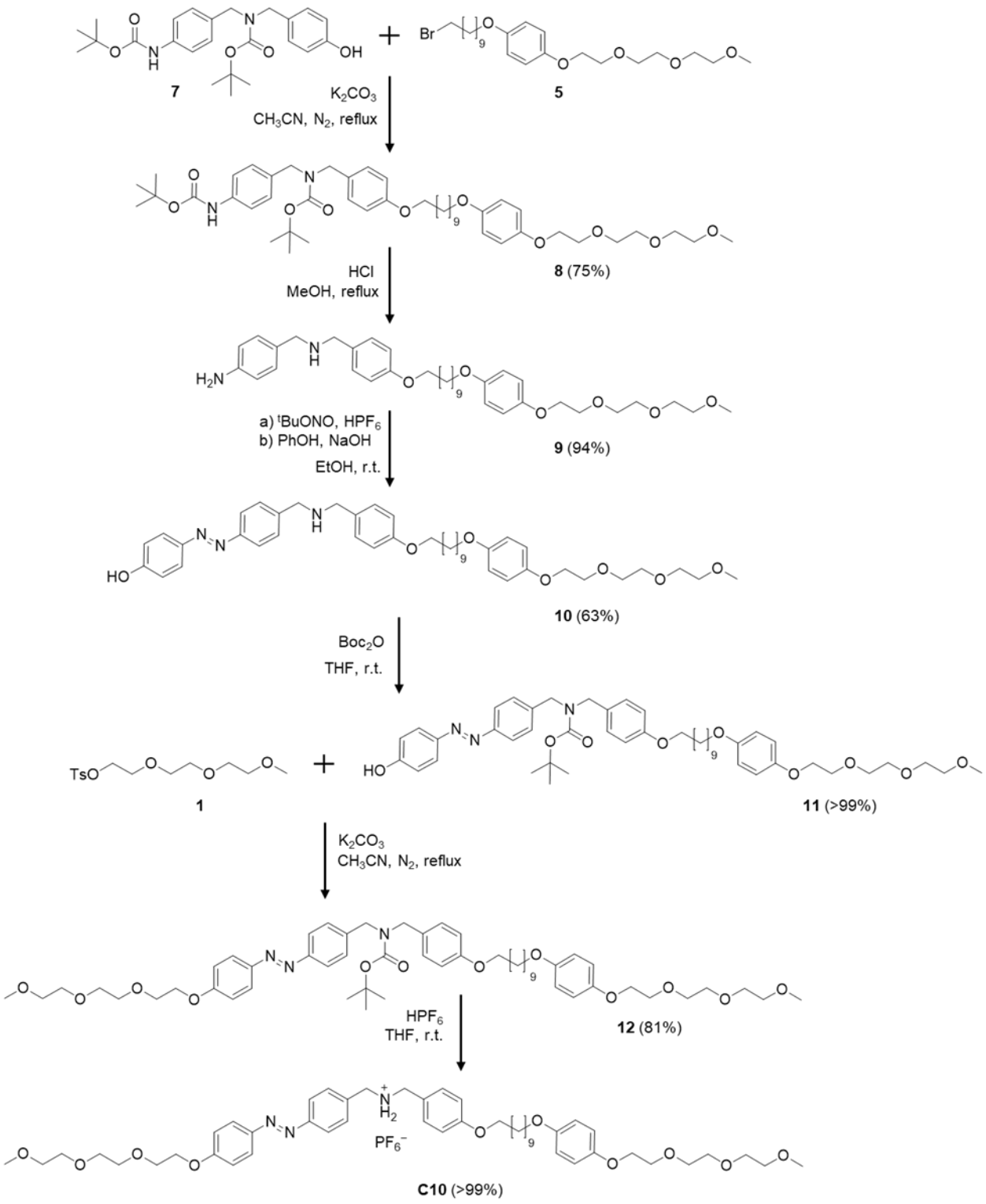

Scheme 3.2. Synthetic route to the molecular axle E-**C10**.

A preliminary investigation of the molecular axle *E*-**C10** involved its characterization by ^{1}H NMR spectroscopy. During initial studies in dichloromethane, a peculiar behavior was observed, with spectra of the same solution recorded days apart showing clear shifts of some resonances (**Figure 3.3**). In particular, the broad singlet assigned to the ammonium protons is overlapped with the peak at 7.88 ppm when the solution is freshly prepared, while over time it shifts to lower fields reaching 8.96 ppm after 4 days (**Figure 3.3**, yellow dot).

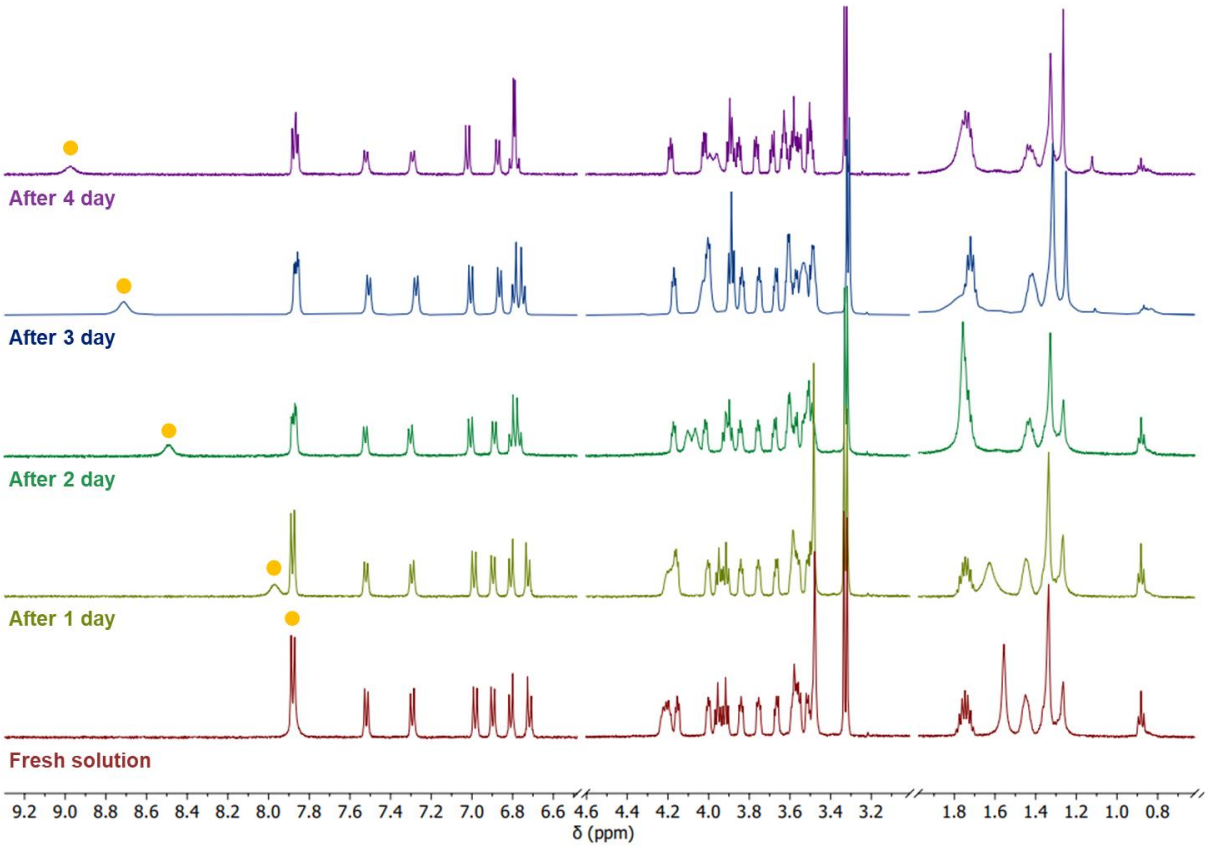

Figure 3.3 Monitoring of *E*-**C10** over time; 500 MHz, CD_2Cl_2, 298 K.

This behavior is likely caused by the rearrangement and aggregation of molecules in solution. In order to stabilize the solute and disfavor the aggregation, a small amount of methanol was added and the experiment repeated. The addition of 1% v/v of methanol efficiently prevented aggregation, providing stable ^{1}H NMR spectra (**Figure 3.4**).

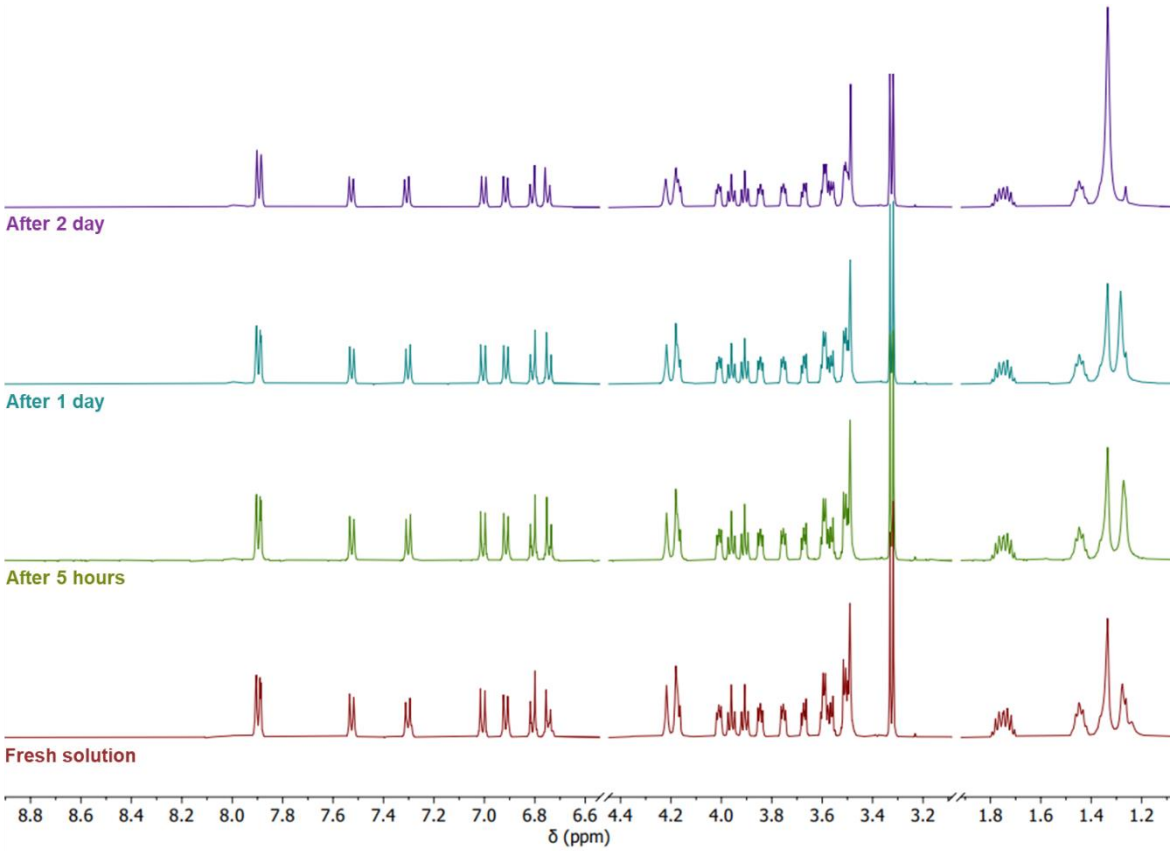

Figure 3.4. Partial ^{1}H NMR spectrum of *E*-**C10** monitored over time following methanol addition; 500 MHz, CD_2Cl_2/CD_3OD 99:1 v/v, 298 K.

In light of this, all the following experiments and characterizations were carried out in dichloromethane/methanol mixtures (99:1 v/v).

The *E*-**C10** axle was fully characterized by ^{1}H and ^{13}C NMR (**Section 3.7.2**). The ^{1}H NMR spectrum of *E*-**C10** is reported in **Figure 3.5**.

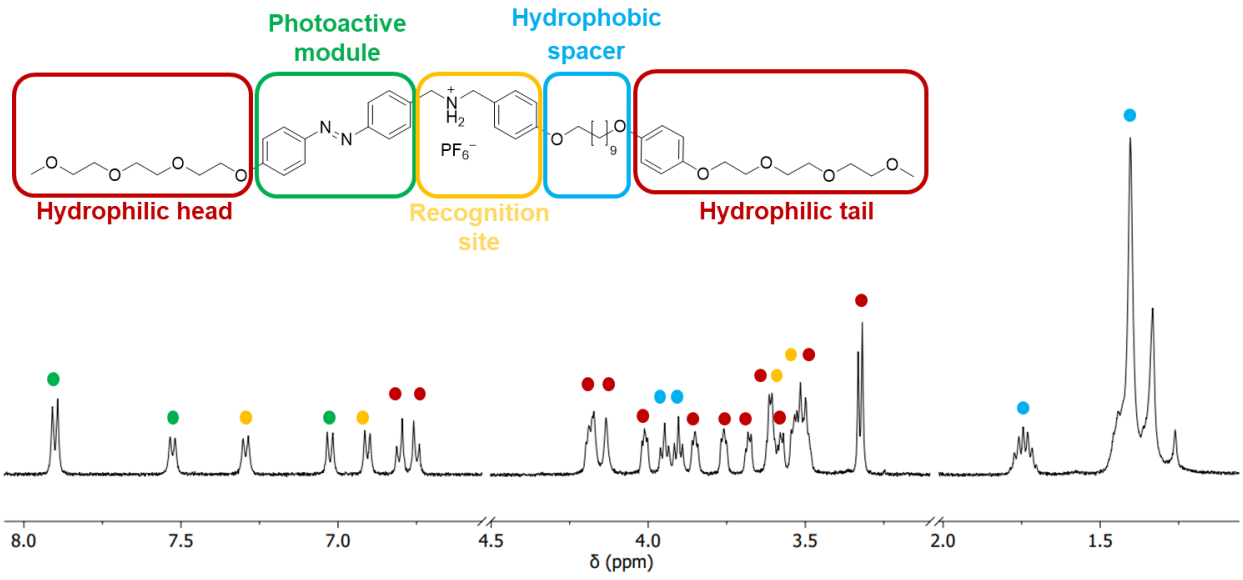

Figure 3.5. ^{1}H NMR spectrum of *E*-**C10**; 500 MHz, CD_2Cl_2/CD_3OD 99:1 v/v, 298 K.

3.2.1 Photophysical and photochemical characterization of the molecular axle C10

Further characterization of **C10** involved photochemical measurements. The absorption spectrum of *E*-**C10**, reported in **Figure 3.6** , shows a band structure typical of the *E*-azobenzene unit, where the intense band at λ_{max} = 355 nm (ε_{max} = 26500 M^{-1} cm^{-1}) is characteristic of the symmetry allowed $\pi \rightarrow \pi^*$ transition and the weaker band at λ_{max} = 443 nm (ε_{max} = 1000 M^{-1} cm^{-1}) arise from the symmetry forbidden $n \rightarrow \pi^*$ transition.

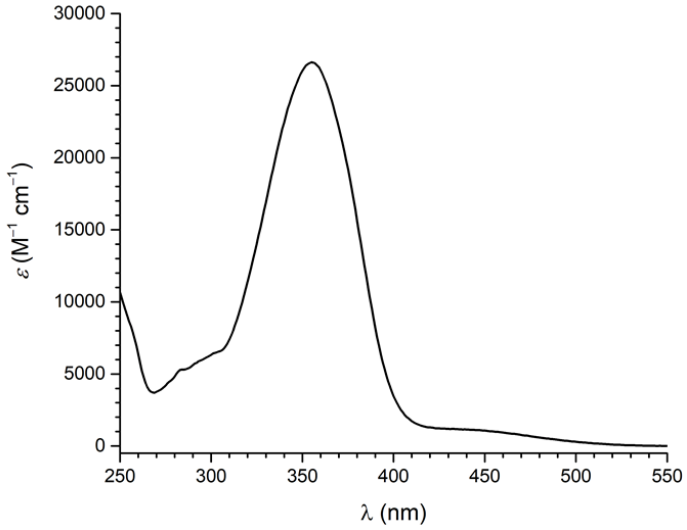

Figure 3.6. Molar absorption spectrum of *E*-**C10;** CH_2Cl_2/CH_3OH 99:1 v/v, 298 K.

The absorption spectrum of *E*-**C10** allowed the identification of a suitable irradiation wavelength (λ = 365 nm, close to λ_{max}) to study the photoisomerization process. The $E \rightarrow Z$ conversion caused a decrease in the intensity of the $\pi \rightarrow \pi^*$ transition band which almost completely disappeared and an increase in the $n \rightarrow \pi^*$ transition band, in line with related azobenzene derivatives. Moreover, a new band appeared in the UV region (λ_{max} = 253 nm, ε_{max} = 12500 M^{-1} cm^{-1}). Irradiation at 365 nm for less than 2 min led to a photostationary state (PSS) indicating an almost complete $E \rightarrow Z$ conversion (**Figure 3.7**).

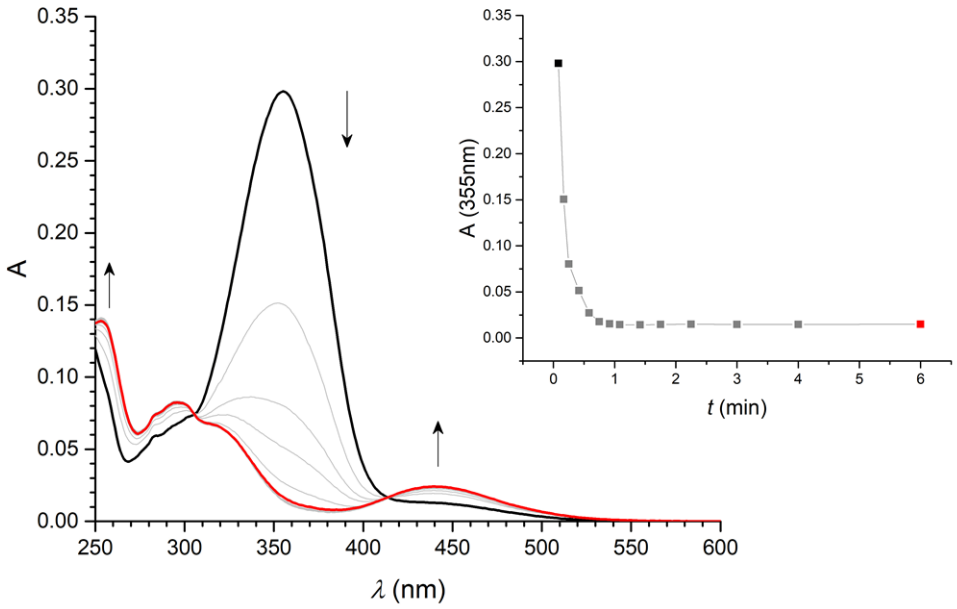

Figure 3.7. Variations in absorption of a solution of *E*-**C10** upon irradiation at λ = 365 nm: *E*-**C10** (black line), PSS_{365nm} (red line); inset: plot of **C10** absorption at λ = 355 nm *vs* time; [**C10**] = 1.12×10^{-5} M, CH_2Cl_2/CH_3OH 99:1 v/v, 298 K.

The thermal $Z \rightarrow E$ back-isomerization was monitored by leaving the solution at the PSS_{365nm} in the dark at room temperature and recording absorption spectra at 15 min intervals (**Figure 3.8**).

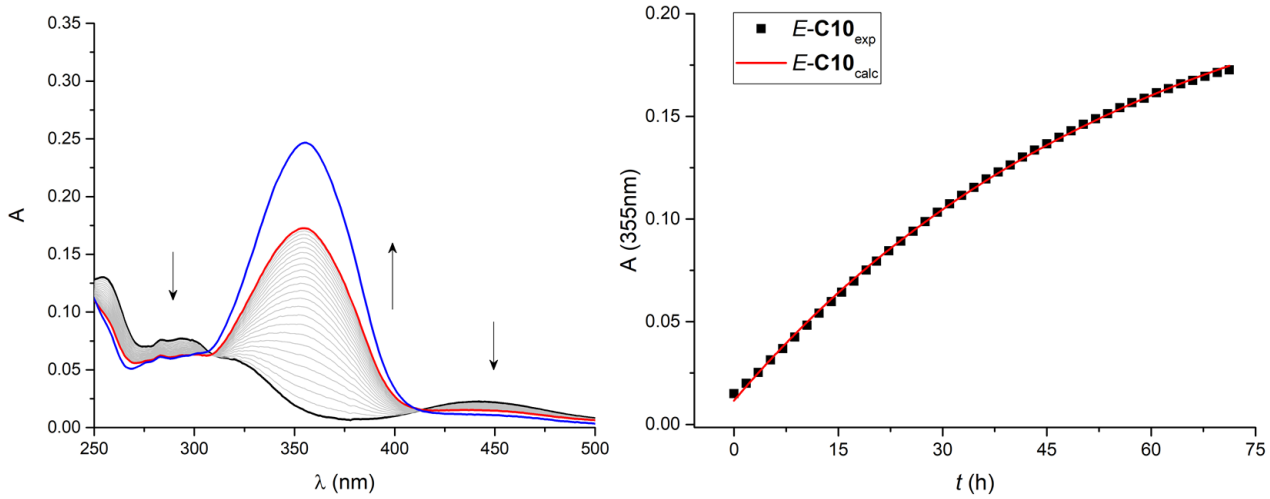

Figure 3.8. Changes in absorption of a solution of *E*-**C10** upon irradiation at 365 nm and subsequent thermal back-isomerization in the dark: (left) *E*-**C10** solution (blue line), $PSS_{365\ nm}$ (black line), absorption spectrum after 71 h in the dark (red line); (right) plot of *E*-**C10** absorption at λ = 355 nm *vs* time: black squares experimental data, red line fitting of the data according to a first order reaction model; [**C10**] = 9.31×10^{-6} M, CH_2Cl_2/CH_3OH 99:1 v/v, 298 K.

The thermal *Z* → *E* isomerization is a very slow process, and after 71 h in the dark at room temperature only the 70% of the *E* isomer is restored (**Figure 3.8a**). The experimental data reported in **Figure 3.8b** were fitted according to a first order reaction to obtain a kinetic constant value of $k = 4.8 \cdot 10^{-6}$ s^{-1} for the thermal back-isomerization process.

In situ NMR photoisomerization experiments are particularly useful to monitor the evolution of the sample in solution upon irradiation in real time, providing an additional insight into the reactivity of the analyte and complementing the results obtained by standard absorption spectroscopy. A solution of *E*-**C10** was therefore irradiated at 365 nm directly inside the NMR spectrometer and the concentrations of the *E* and *Z* isomers measured referencing to TCE (1,1,2,2-tetrachloroethane) as an internal standard both during irradiation and after switching off the light. The ^{1}H NMR spectra of **C10** before irradiation (*E* isomer) and at the PSS_{365} (98:2 *Z*/*E*) are reported in **Figure 3.9**.

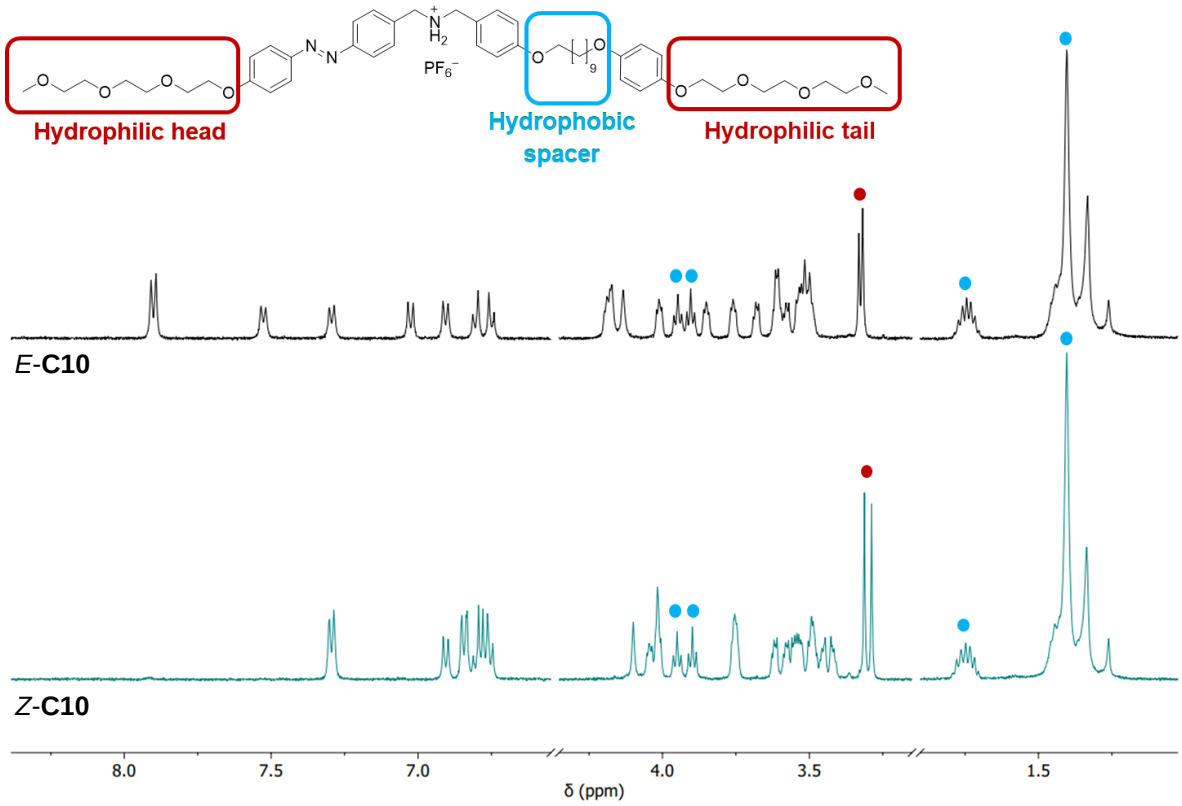

Figure 3.9. ^{1}H NMR spectra of *E*-C10 (black trace) and *Z*-C10 (green trace); 500 MHz, CD_2Cl_2/CD_3OD 99:1 v/v, 298 K.

Upon isomerization, peaks in the NMR spectrum corresponding to the *E* isomer started to decrease in intensity and disappeared almost completely; at the same time, the appearance of new resonances corresponding to the *Z* species and their increase in intensity were

observed. The *Z* isomer spectrum differs considerably from the spectrum of the *E* isomer, even though resonances corresponding to the aliphatic spacer and the methyl group of the polar tails are found unaltered. On the other hand, resonances related to the "head" of the molecule – *i.e*. the azobenzene-containing extremity – display notable variations and shifts, supporting a significant influence of the isomerization of the azobenzene subunit on the head of the molecule, while the chemical environment of the tail remains almost unchanged.

The *E* → *Z* photoisomerization process followed in real time by sequential acquisition of the NMR spectra during irradiation is presented in **Figure 3.9**. Clearly, this is a rapid process, and the PSS_{365} is reached in less than 2 min. After switching off the light, the thermal *Z* → *E* isomerization takes place very slowly, leading only to 4% *E*-**C10** over 60 min.

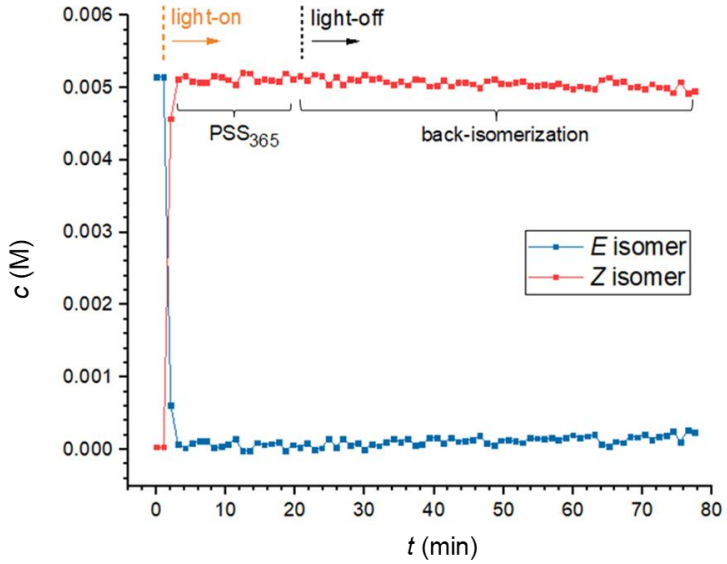

Figure 3.9. Monitoring of the speciation of **C10** under irradiation at λ = 365 nm (light on) and in the dark (light off). Concentrations are calculated from the integrals of the aromatic peaks in the ^{1}H NMR spectra using TCE as an internal standard; 500 MHz, CD_2Cl_2/CD_3OD 99:1 v/v, [TCE] = 6.47×10^{-3} M, 298 K).

Overall, both characterizations by *in situ* irradiation in the NMR and UV-vis absorption spectra gave consistent results: the *E* → *Z* photoisomerization is a very efficient process, irradiating at λ = 365 nm for 2 min is sufficient to reach the PSS and achieve an almost complete conversion from *E*-**C10** to *Z*-**C10**.

The thermal *Z* → *E* isomerisation is very slow, but alternatively it is possible to convert the *Z* isomer in the *E* isomer by irradiating the sample at λ = 546 nm, achieving a back-conversion of 89% (**Figure 3.10**)

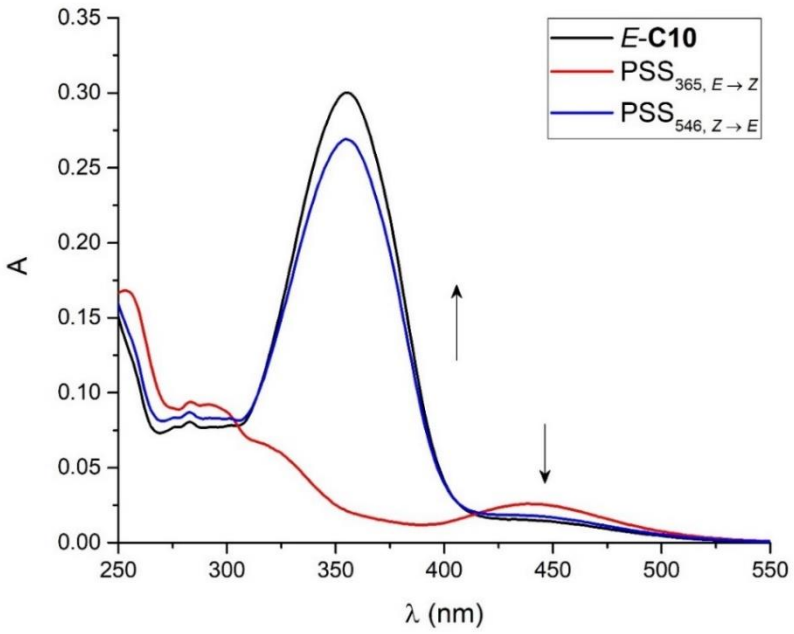

Figure 3.10. Variations in absorption of a solution of *E*-**C10** upon irradiation at 365 nm to the PSS_{365} and subsequent irradiation at λ = 546 nm: *E*-**C10** solution (black line), PSS_{365nm} (red line), PSS_{546nm} (blue line); [**C10**] = 1.13×10^{-5} M, CH_2Cl_2/CH_3OH 99:1 v/v, 298 K.

3.2.2 Preparation and study of liposomes functionalized with the molecular axle C10

Once the spectroscopic and photochemical characterization of the axle **C10** had been completed, the next steps involved its intercalation within liposomal vesicles. The functionalized liposomes were prepared according to the method described in **Section 3.7.1**, by addition of 10% mol/mol of a dichloromethane/methanol (99:1 v/v) solution of *E*-**C10** to a chloroform solution of POPC and obtaining, upon removal of the solvent under reduced pressure, a homogeneous film of phospholipids and guest. In a first attempt, rehydration of the dry film was performed with PBS [NaCl (121.5 mM), Na_2HPO_4 (25.2 mM), KH_2PO_4 (4.8 mM), pH = 7.4], however, agglomerates formed that prevented extrusion, possibly as a consequence of the high ionic strength of the media that favours the aggregation of the guest. Lowering the guest loading to 2% mol/mol allowed the isolation of liposomes containing 0.7% of *E*-**C10**. The effective intercalation of the guest is supported by the absorption spectrum of the functionalized liposomes, which exhibits an absorption band at 355 nm assigned to the $\pi \rightarrow \pi^*$ transition band of the *E*-**C10** axle (**Figure 3.11**).

Moreover, irradiation at λ = 365 nm for 30 s lead to a decrease in the band intensity, suggesting the occurrence of an isomerization process.

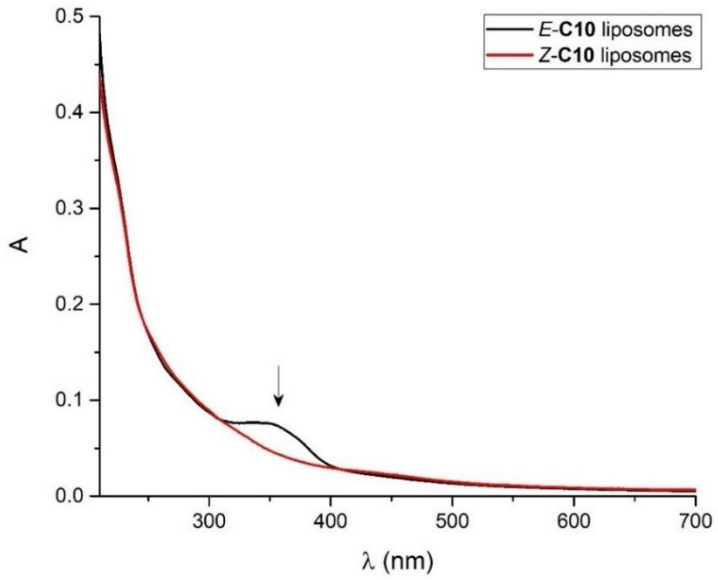

Figure 3.11. Absorption spectrum of liposomes suspension freshly extruded (black line) and after irradiation at λ = 365 nm for 30 s (red line); [POPC] = 6.5×10^{-4} M, **C10** 0.7 % mol, PBS pH = 7.4, 298 K.

To confirm the effective intercalation and discard the simple dissolution of the thread **C10** in the rehydration medium, its solubility in water or PBS was investigated. Such solubility resulted much lower than that required to observe an absorption spectrum comparable to that recorded for the functionalized liposomes suspension (**Figure 3.12**, blue and red dashed lines), thus confirming the effective intercalation of the axle within the bilayer.

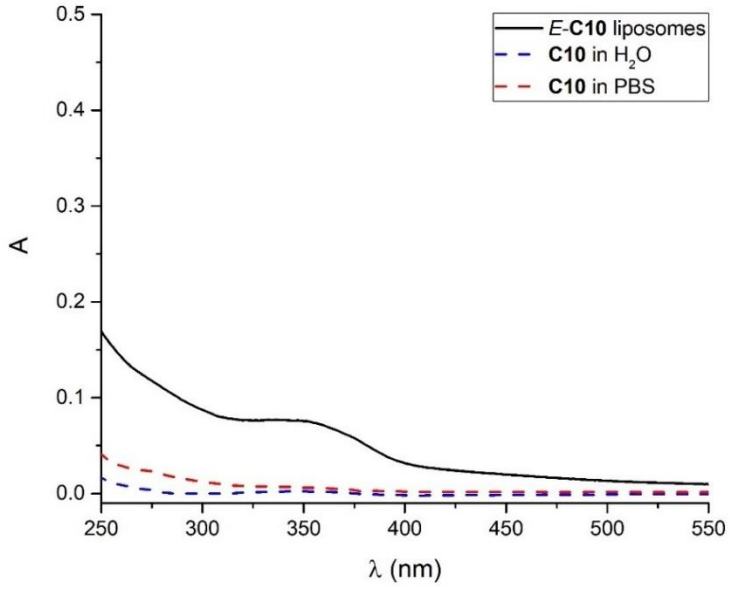

Figure 3.12. Absorption spectra of **C10** in H_2O (blue dashed line), **C10** in PBS (red dashed line) and freshly extruded suspension of liposomes functionalized with *E*-**C10**, (black line), [POPC] = 6.5×10^{-4} M, **C10** 0.7 % mol, PBS pH = 7.4, 298 K.

Once the intercalation has been ascertained, the next step to optimise was the effective guest loading. The guest molecule displayed a low propensity to intercalate in the bilayer when PBS was used to hydrate the film, therefore to decrease the ionic strength of the medium, in a second attempt water was chosen as hydration solvent. A 10% mol/mol *E*-**C10** doped film was rehydrated with ultrapure water, and in these experimental conditions liposomes functionalized with 9% *E*-**C10** were obtained (**Figure 3.13**). In the absorption spectrum of functionalized liposomes the *E*-**C10** band structure can be identified, in particular the intense $\pi \rightarrow \pi^*$ band at λ_{max} = 355 nm and the weaker $n \rightarrow \pi^*$ band at λ_{max} = 443 nm. Despite the successful functionalization, the formed liposomes were not stable, as the corresponding absorption spectrum showed several changes over time even in the dark (**Figure 3.14**). Specifically, the band at λ = 355 nm decreased in intensity and changed shape, exhibiting a hypsochromic shift from 355 nm to 310 nm.

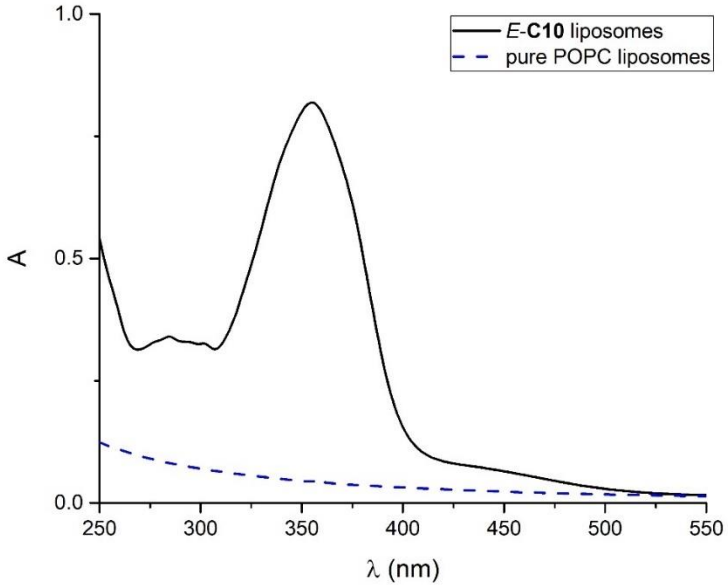

Figure 3.13. Comparison between absorption spectra of an aqueous suspension of liposomes composed of POPC only (blue dashed line), or functionalized with *E*-**C10** (black line); [POPC] = 3.25×10^{-4} M, *E*-**C10** 9% mol/mol, H_2O, 298 K.

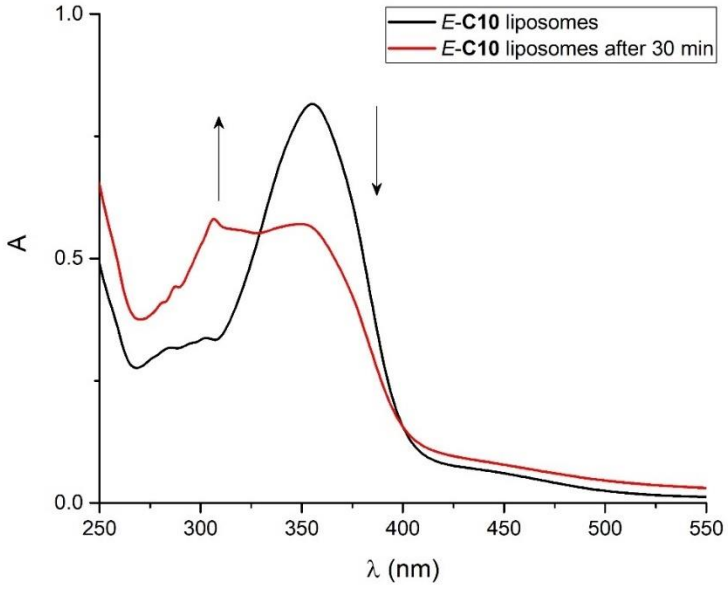

Figure 3.14. Changes in absorbance of an aqueous suspension of liposomes functionalized with *E*-**C10** when freshly extruded (black line) and kept 30 min in the dark (red line); [POPC] = 3.2×10^{-4} M, *E*-**C10** 9% mol/mol, H_2O, 298 K.

Analogous spectroscopic behavior was reported for an azobenzene containing polymer, which in water forms micelles and exhibits a decrease in intensity and a shift toward the blue

region of the band relative to the π → π* transition, as a consequence of the H-stacking between the azobenzene functionalities.[4] The similarity with the spectral changes of the functionalized liposomes suggests that *E*-**C10** azobenzene moieties undergo aggregation. The vesicles suspension was analysed by means of DLS in order to evaluate the particle size and size distribution of the sample. Notably, while the freshly prepared sample showed a population with an average diameter of 100 nm accompanied by minor populations of large diameter (**Figure 3.15a**), the same sample after 30 min appeared polydisperse with several populations having a large diameter (**Figure 3.15b**), suggesting the formation of liposomes aggregates over time. Based on the concomitant occurrence of the UV-vis spectral variations and the size distribution changes observed by DLS analyses, it can be hypotesized that the aggregation process involves inter-liposomal stacking between azobenzene functionalities.

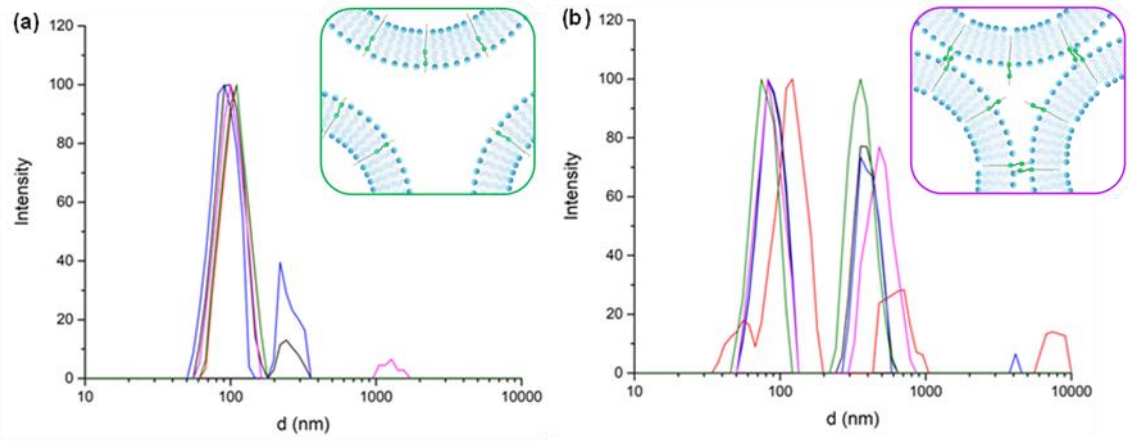

Figure 3.15. DLS graphs of an aqueous suspension of liposomes functionalized with *E*-**C10** (a) freshly extruded and (b) after 30 min in the dark; [POPC] = $3.2 \cdot 10^{-4}$ M; *E*-**C10** 9% mol/mol, H_2O, 298 K. A single DLS analysis includes multiple individual scans, each reported in a different colour. The insets highlight the correlation between the vesicle aggregation state and the inter-liposomal azobenzene stacking.

Irradiation of the aggregated liposomes suspension with 365 nm light produced a time-stable spectrum consistent with the photoisomerization of *E*-**C10** to its *Z* isomer (**Figure 3.16**, red dashed line). However, as soon as the molecular axle returns to the *E* form aggregation occurs, as it can be observed in the spectra obtained by irradiating the sample at 546 nm. In particular, while after 3 min of irradiation the bands related to *E*-**C10** are clearly visible (**Figure 3.16**, green line), proceeding with the irradiation leads to the spectrum corresponding to the aggregated species (**Figure 3.16**, solid blue line). Interestingly, a

second irradiation of the sample at 365 nm restores an absorption spectrum perfectly coherent with the one of the *Z*-**C10** molecule (**Figure 3.16**, dashed blue line).

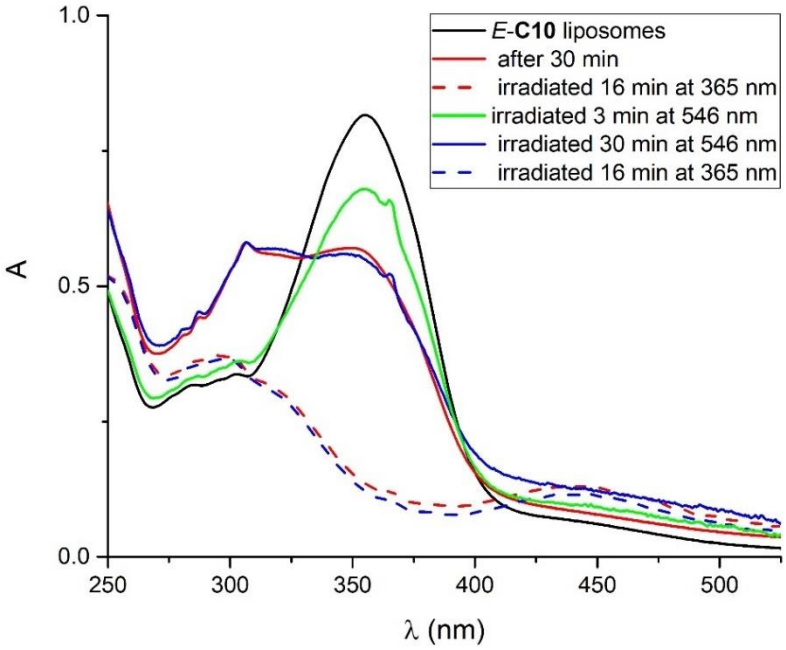

Figure 3.16. Changes in absorbance of an aqueous suspension of liposomes functionalized with *E*-**C10**, freshly extruded (solid black line), after 30 min in the dark (red line), irradiated at λ = 365 nm (dashed red line), irradiated at λ = 546 nm for 3 min (solid green line) or 30 min (solid blue line), irradiated at λ = 365 nm (dashed blue line); [POPC] = $3.2 \cdot 10^{-4}$ M, *E*-**C10** 9% mol/mol, H_2O, 298 K.

The DLS measurements carried out on this sample further support this behavior, as it can be observed from the data reported in **Figure 3.17**. When the molecular axle **C10** is in the *E* form, liposomes tend to aggregate producing a suspension characterized by different populations and a high polydispersity index. Nevertheless, isomerizing *E*-**C10** to its *Z* form, the sample recovers a narrow distribution composed of liposomes with a diameter of 100 nm. This process takes place without showing any sign of degradation and confirms that the phenomenon observed was the formation of aggregates and not fusion between the suspended vesicles. Importantly, as confirmed by both UV-vis and DLS, the procedure can be performed multiple times, thus enabling a reversible photoinduced aggregation-disaggregation of the functionalized liposomes.

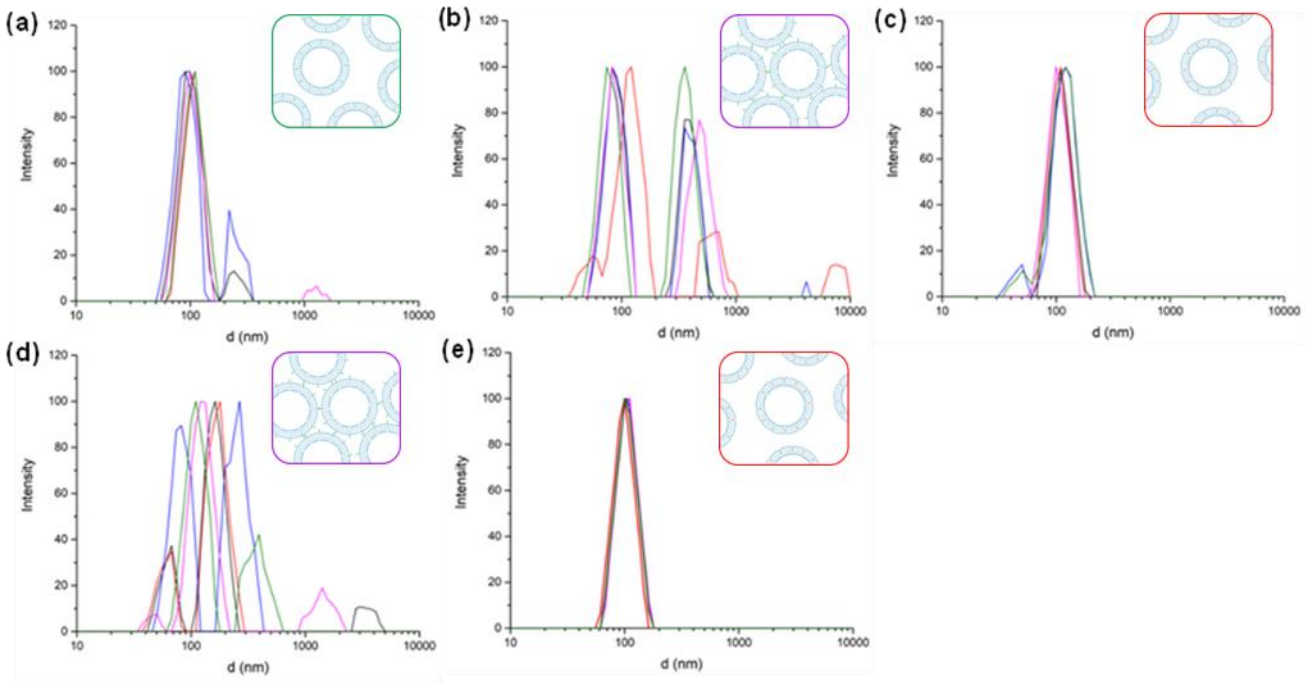

Figure 3.17. DLS graphs of an aqueous suspension of liposomes functionalized with *E*-**C10** (a) freshly extruded, (b) after 30 min in the dark, (c) irradiated 16 min at λ = 365 nm, (d) irradiated 30 min at λ = 546 nm, (e) irradiated 16 min at λ = 365 nm; [POPC] = $3.2 \cdot 10^{-4}$ M; **C10** 9% mol/mol, H_2O, 298 K. A single DLS analysis includes multiple individual scans, each reported in a different colour. The insets report the aggregation-disaggregation behaviour of the functionalised liposomes.

Moreover, *Z*-**C10** liposomes monitored over time did not show changes in the absorption spectrum as long as 365 nm light is provided. Conversely, upon suspension of light irradiation, a very slow aggregation process can be observed monitoring the increase in absorption at 300 nm; a phenomenon likely related to the rising amount of *E*-**C10** formed by thermal back-isomerisation of the initial *Z* isomer (**Figure 3.18**). From the absorption variations reported in **Figure 3.18b** and **3.18c** it can be noticed that, while the absorbance at 355 nm starts increasing as soon as the 365 nm irradiation is suspended, indicating the formation of *E*-**C10** in the membrane, the band at 300 nm exhibits an initial plateau followed by an increase in absorbance, these two different trends can be explained as the formation of a sufficient amount of *E*-**C10** in liposomes able to start the aggregation process.

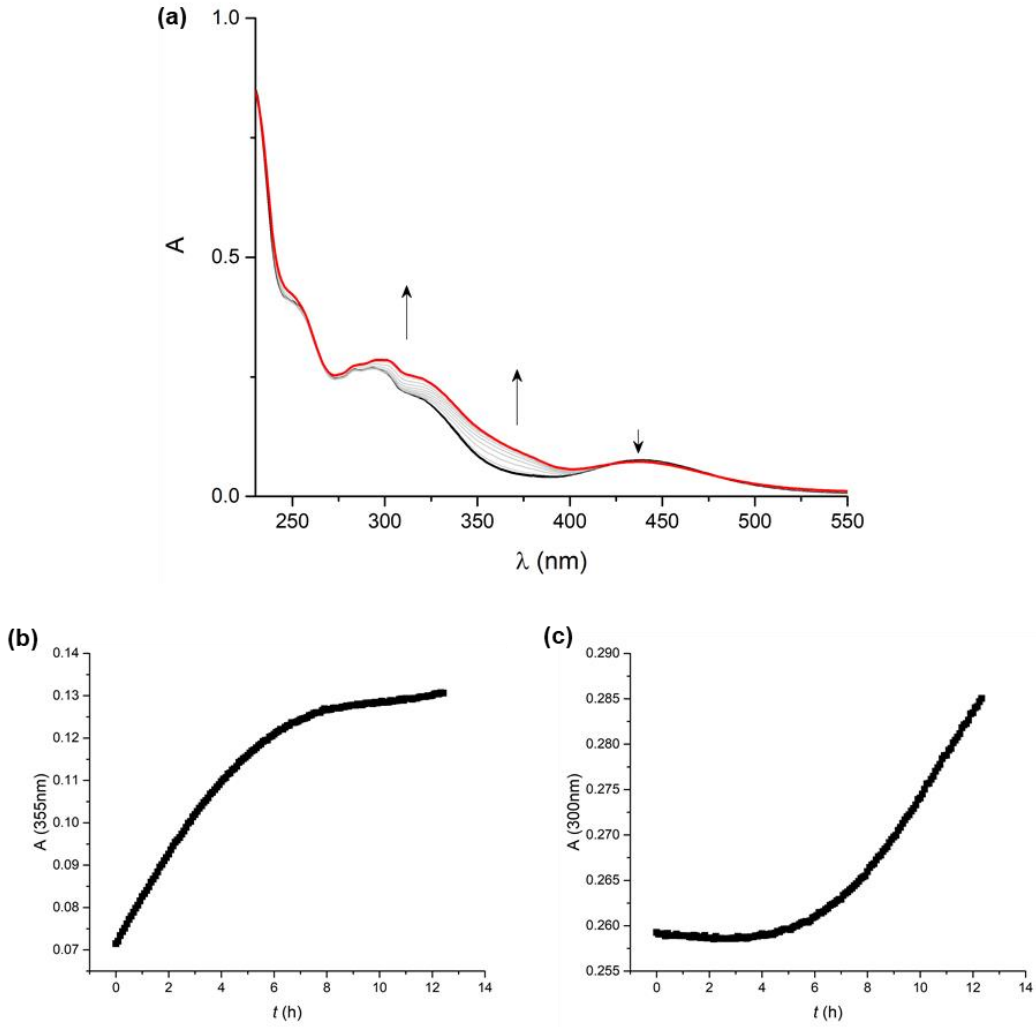

Figure 3.18. Changes in absorbance of an aqueous suspension of liposomes functionalized with the **C10** axle irradiated at λ = 365 nm to the PSS_{365} (black line) and after 12.5 h in the dark (red line) (a), absorbance *vs* time plot at λ = 355 nm (b) and λ = 300 nm (c); **C10** 9% mol/mol, [POPC] = $3.2 \cdot 10^{-4}$ M, H_2O, 298 K.

To further correlate the aggregation process to the sole presence of the guest molecule, a control analysis was carried out on liposomes composed of pure POPC phospholipids, monitoring their stability over time in the experimental conditions employed for the analysis of the functionalized liposomes. The vesicles were prepared according to the method described in **Section 3.7.1** and the obtained suspension was monitored over time *via* DLS and UV-vis and DLS spectrophotometry, confirming their stability in water (**Figure 3.19**). The DLS analysis performed on the freshly prepared vesicles displayed an average diameter of 130 nm unvaried during the whole monitoring process; analogously, the absorption spectrum showed no increase in the sample scattering. Importantly, such results allow to relate the observed aggregation process exclusively to the presence of the **C10** axle in the bilayer membrane.

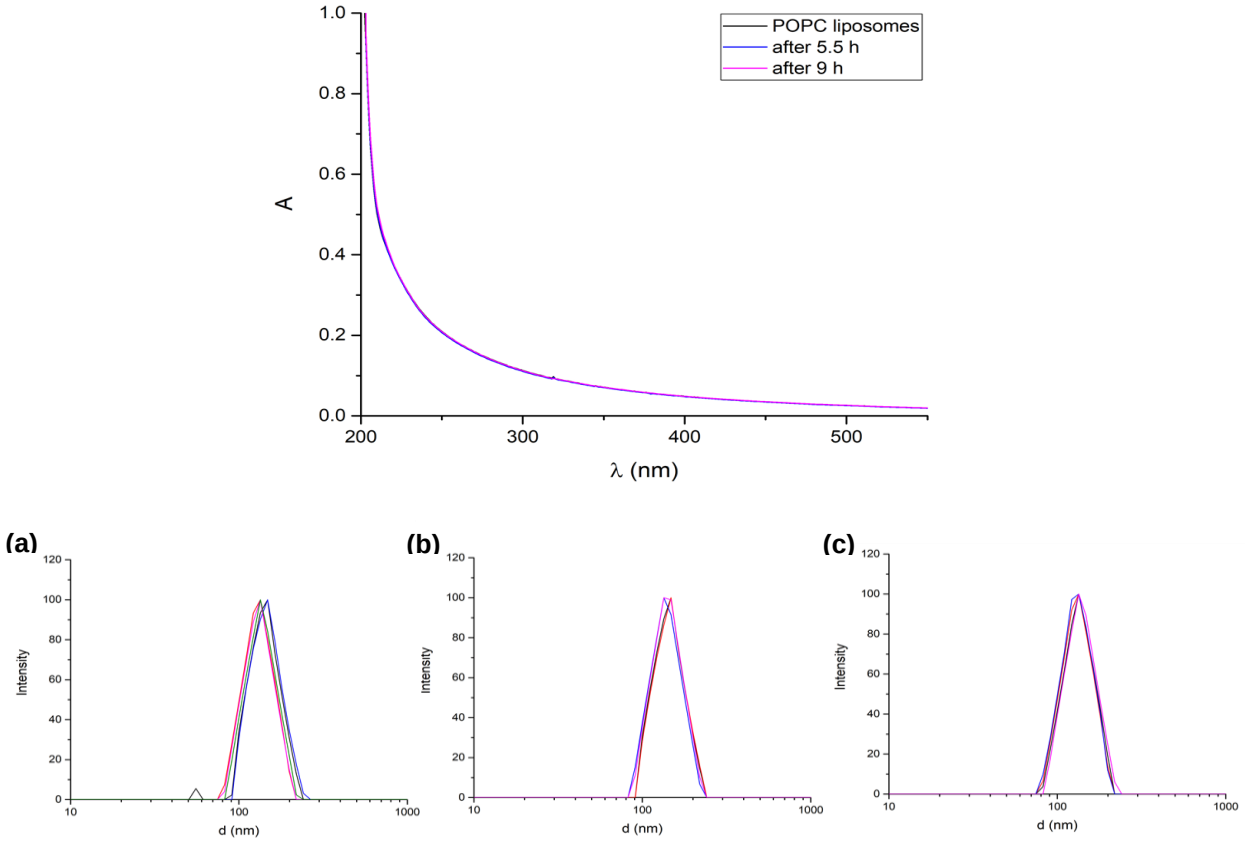

Figure 3.19. Absorption spectrum (top) and DLS graphs of an aqueous suspension of POPC liposomes (a) freshly extruded, (b) after 5.5 h and (c) after 9 h; [POPC] = $3.2 \cdot 10^{-4}$ M, H_2O, 298 K. A single DLS analysis includes multiple individual scans, each reported in a different colour.

3.2.2.1 C10-functionalized liposomes in saline solution

With the aim to prevent or disfavour the aggregation process, the possibility to increase the ionic strenght of the external medium was evaluated. Liposomes functionalized with 9% *E*-**C10** were prepared by addition of a 10% mol/mol of a dichloromethane/methanol (99:1 v/v) solution of *E*-**C10** to a chloroform solution of POPC and obtaining a homogeneous film upon removal of the solvent under reduced pressure. Rehydration of the film with ultrapure water and extrusion, provided the 9% *E*-**C10** functionalized liposomes, that were then suspended in Hepes buffer solution (4-(2-Hydroxyethyl)piperazine-1-ethanesulfonic acid, 10 mM, pH = 7). In these experimental conditions the functionalized liposomes resulted to be more stable with respect to the vesicles in pure water, as by DLS analysis and UV-vis spectroscopy. The absorption spectrum of the vesicles displayed only minor variations over time (**Figure 3.19**), while the DLS analysis on the freshly prepared suspension showed a monodisperse

population with a diameter of 100 nm that remained unvaried (**Figure 3.20**). The increased ionic strength of the extravesicular medium stabilizes the liposomes exposed surface, minimizing inter-liposomal interactions and therefore disfavoring the aggregation process.

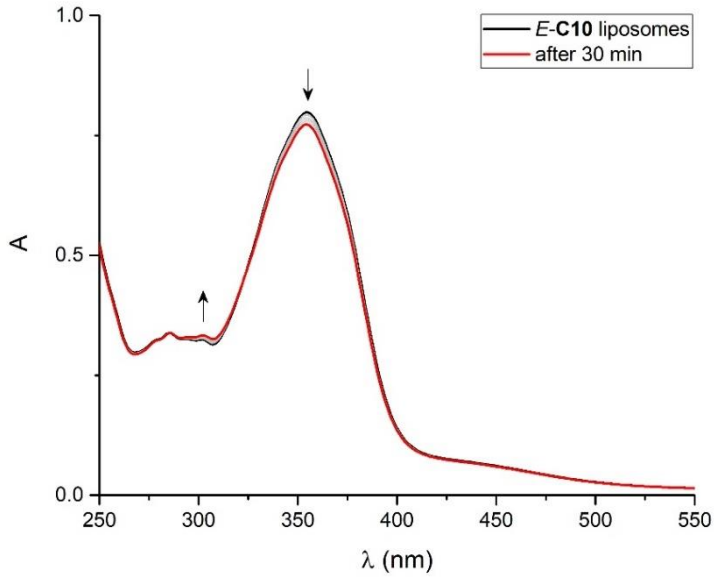

Figure 3.19. Changes in absorbance of an aqueous suspension of liposomes functionalized with *E*-**C10** when freshly extruded (black line), monitored in the dark at 2 min intervals (grey lines) up to 30 min (red line); [POPC] = $3.2 \cdot 10^{-4}$ M, *E*-**C10** 9% mol/mol, Hepes buffer pH = 7, 298 K.

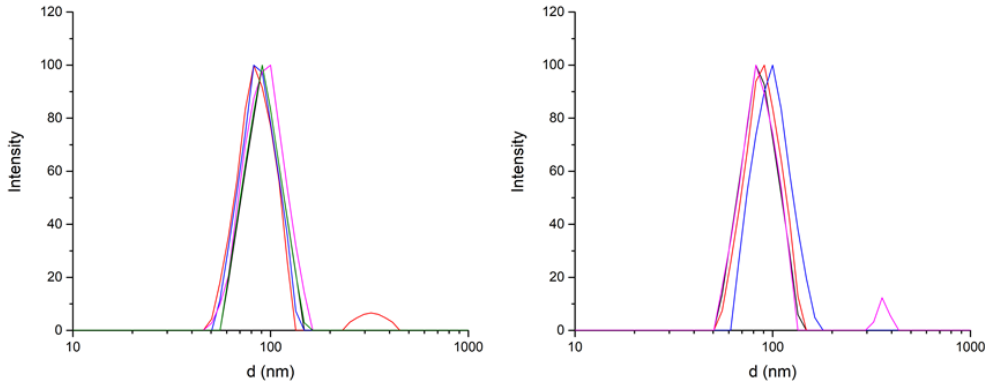

Figure 3.20. DLS graphs of an aqueous suspension of liposomes functionalized with *E*-**C10** when (left) freshly extruded or (right) after 30 min in the dark; [POPC] = $3.2 \cdot 10^{-4}$ M, *E*-**C10** 9% mol/mol, Hepes buffer pH = 7, 298 K. A single DLS analysis includes multiple individual scans, each reported in a different colour.

3.3 Synthesis and characterization of the molecular axle C12

The unique features displayed by **C10**-functionalized liposomes prompted the investigation of the role played by the structure of such molecular axle on the observed aggregation process. For this reason, a second molecule was synthesized. The new axle, namely **C12**, was designed with the same general structure of the **C10** molecule, the only difference being the two carbon atoms longer apolar spacer. This led to an overall length comparable to that of the liposomal bilayer, matching especially in the lipophilic region (approximately 40 Å), in order to achieve an optimal cross-membrane fit.

The synthesis of the **C12** axle started from the reaction between intermediate **7** and 1,12-dibromododecane to connect the lipophilic spacer fragment and quantitatively obtain compound **13** (**Scheme 3.3**). Reaction of **13** with the hydrophilic tail module **4** led to the formation of compound **14** in 80% yield. Upon deprotection and successive diazonium salt coupling, the azobenzene-derived compound **16** was obtained in 58% overall yield. The compound **16** was successively protected to provide the carbamate **17** in 82% yield. The hydrophilic head module was then connected upon reaction between intermediate **17** and precursor **1**, providing compound **18** in 80% yield. The final step involved the removal of the amine protective group and the simultaneous formation of the ammonium cation to access the axle *E*-**C12** in quantitative yield (**Scheme 3.4**). The *E*-**C12** compound was fully characterised by ^{1}H and ^{13}C NMR (**Figure 3.21**).

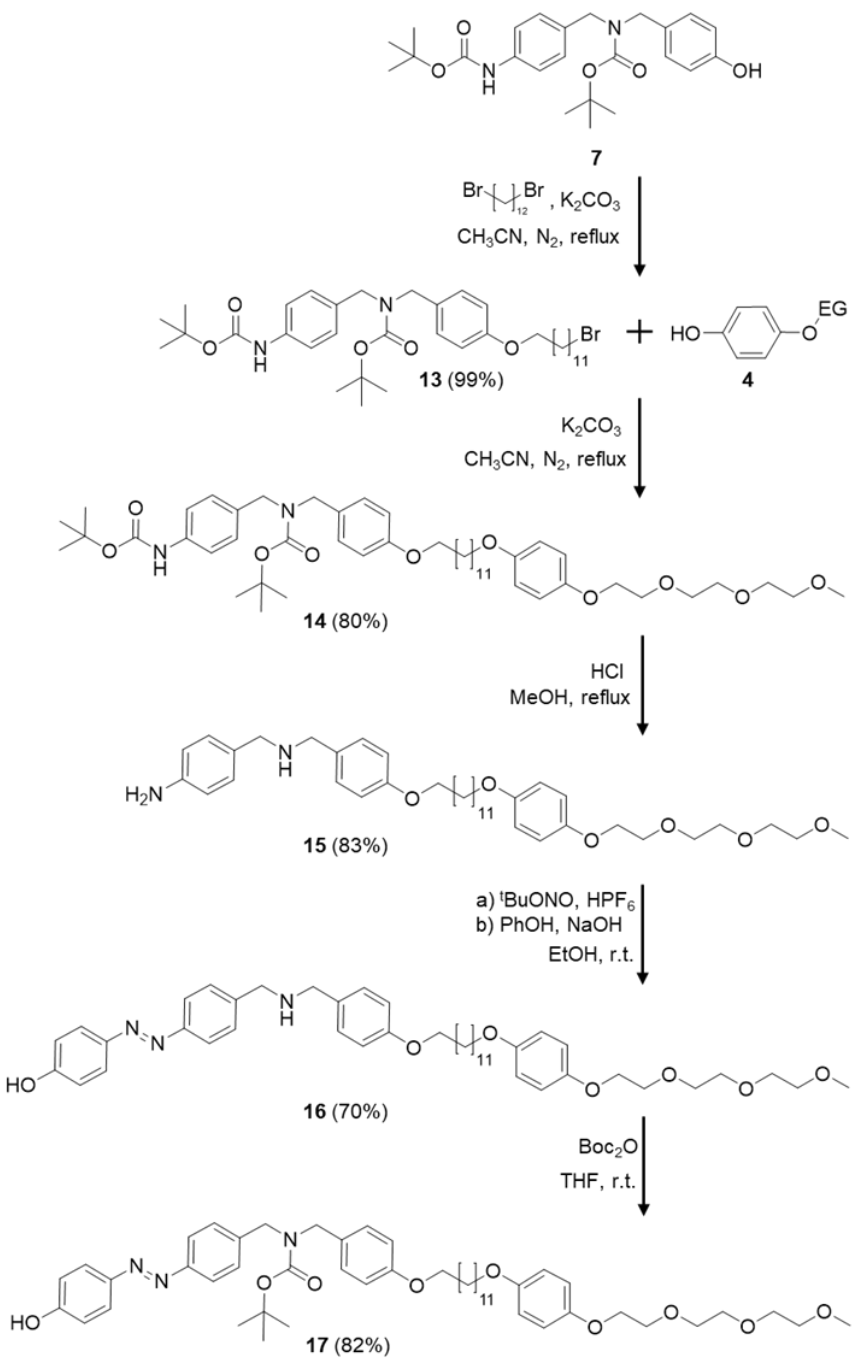

Scheme 3.3. Synthesis of intermediate **17**.

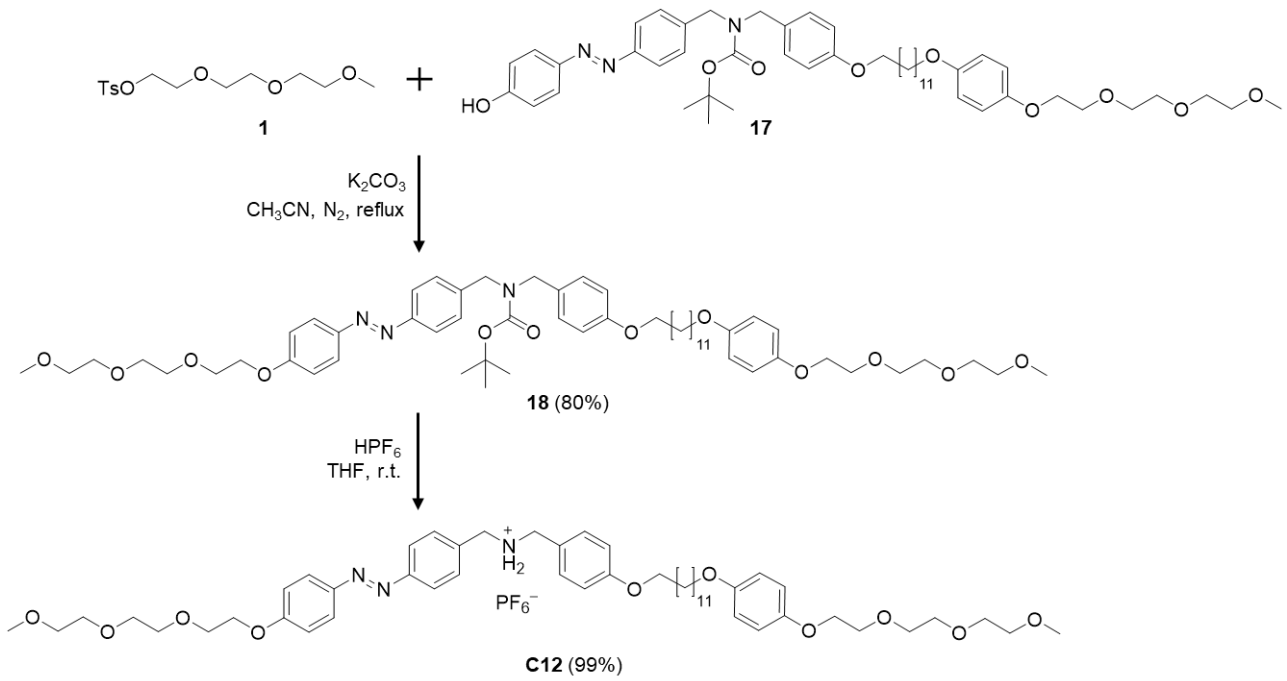

Scheme 3.4. Synthesis of the axle *E*-**C12**.

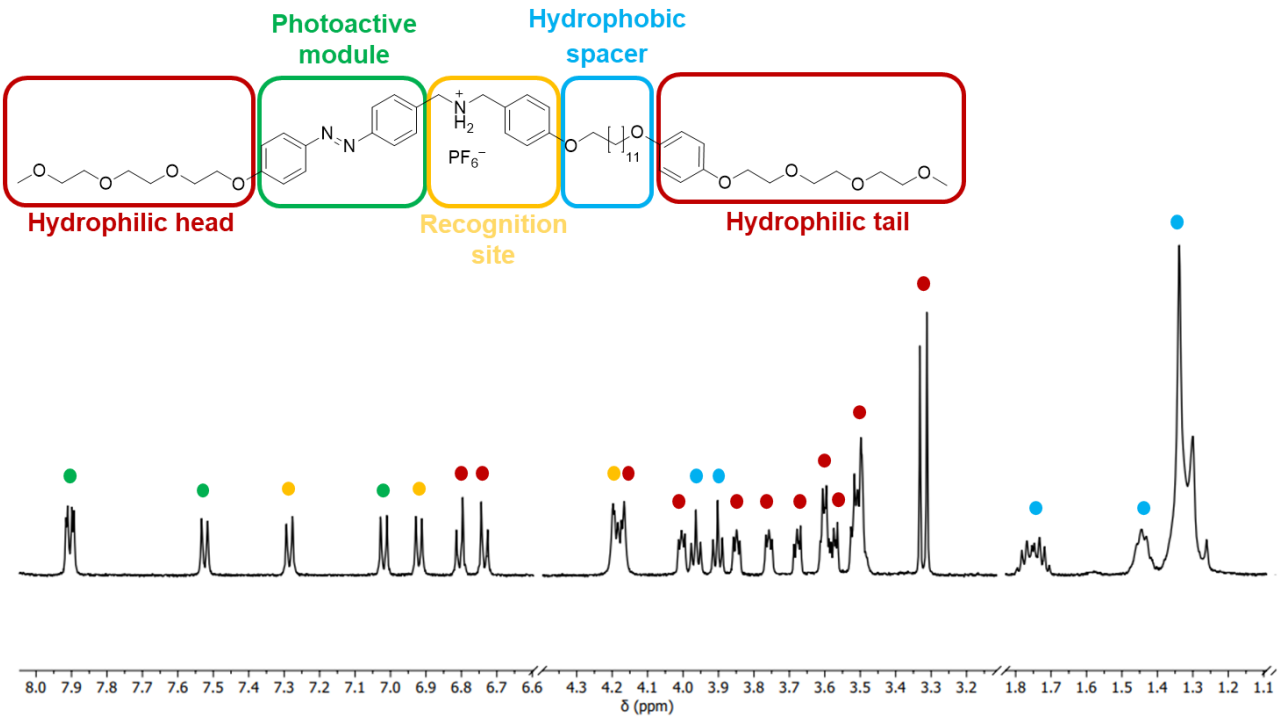

Figure 3.21. ^{1}H NMR spectrum of *E*-**C12**; 500 MHz, CD_2Cl_2/CD_3OD 99:1 v/v, 298 K.

3.3.1 Photophysical and photochemical characterization of the molecular axle C12

The molecular axle **C12** was characterized with the same set of experiments used for the shorter relative **C10**. In order to avoid the aggregation and rearrangement phenomena already verified with the **C10** axle, compound **C12** was studied directly in a dichloromethane/methanol solution (99:1 v/v). The absorption spectrum of *E*-**C12** isomer, reported in **Figure 3.22a**, shows the same band structure of *E*-**C10** molecule: an intense band at λ_{max} = 355 nm (ε_{max} = 27800 M^{-1} cm^{-1}) related to the symmetry allowed $\pi \rightarrow \pi^*$ transition and a weaker band at λ_{max} = 440 nm (ε_{max} = 1400 M^{-1} cm^{-1}) arising from the symmetry forbidden $n \rightarrow \pi^*$ transition.

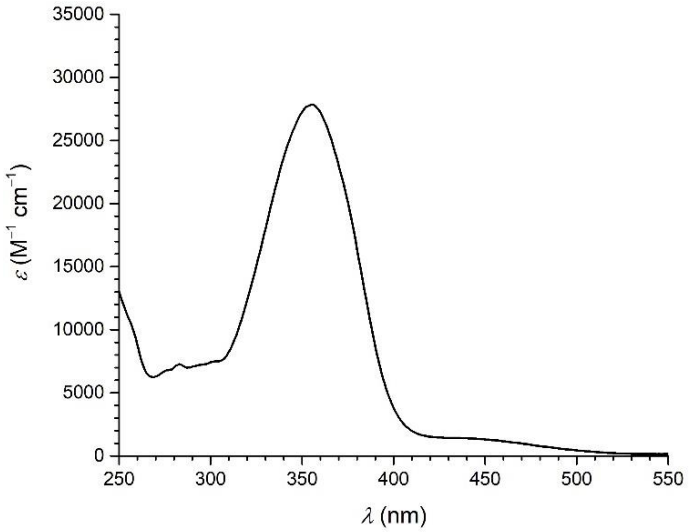

Figure 3.22. Molar absorption spectrum of *E*-**C12**, CH_2Cl_2/CH_3OH 99:1 v/v, 298 K.

Irradiation at λ = 365 nm caused a fast photoisomerization (**Figure 3.23**), the PSS was reached in 1 min achieving an almost complete conversion of the *E* isomer in the *Z* isomer. In the absorption spectrum recorded at the PSS, the $\pi \rightarrow \pi^*$ transition band at λ = 355 nm almost completely disappeared, the $n \rightarrow \pi^*$ transition band at λ_{max} = 442 nm increased and a new band at λ_{max} = 254 nm appeared in the UV region.

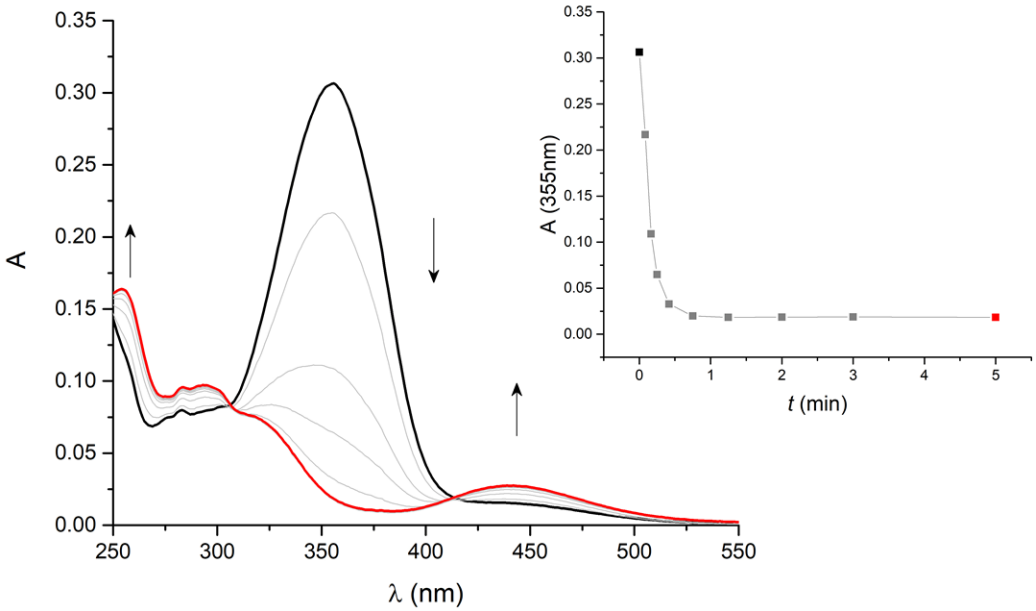

Figure 3.23. Variations in absorption of a *E*-**C12** solution upon irradiation at λ = 365 nm: *E*-**C12** solution (black line), $PSS_{365\ nm}$ (red line); inset: plot of **C12** absorption at λ = 355 nm *vs* time; [**C12**] = 1.10×10^{-5} M**,** CH_2Cl_2/CH_3OH 99:1 v/v, 298 K.

The thermal $Z \rightarrow E$ isomerization is a very slow process, with 65% conversion obtained after 60 h in the dark at room temperature (**Figure 3.24.a**). A small increase in the baseline was recorded during the experiment, which is probably related to the occurrence of a slight aggregation phenomenon that however did not affect the thermal back-isomerization process. The experimental data, reported in **Figure 3.24.b**, were fitted to obtain a kinetic constant value of $k = 4.37\cdot10^{-6}$ s^{-1} for the back-isomerization process.

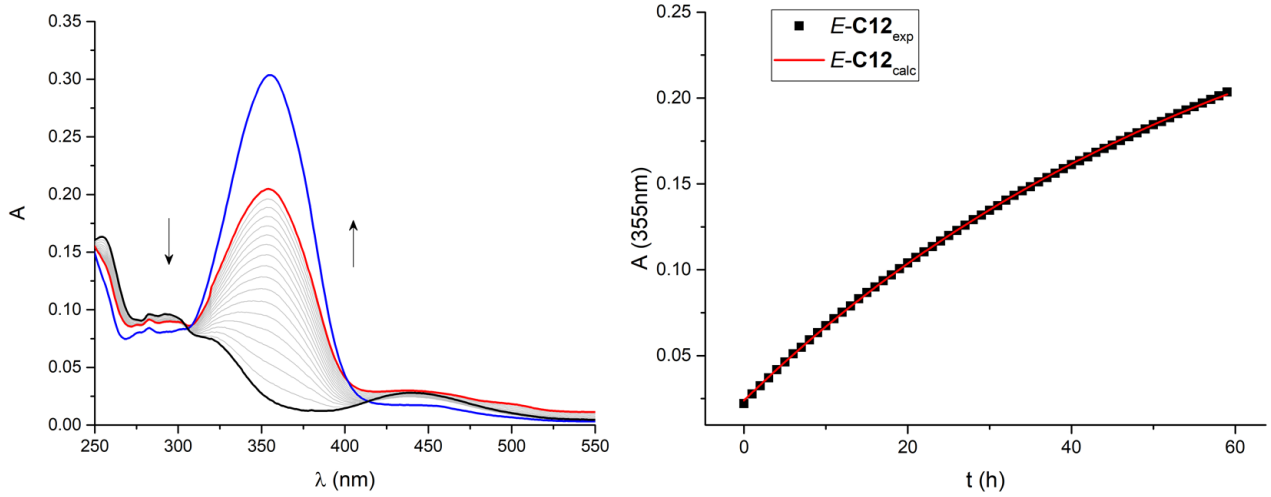

Figure 3.24. Changes in absorption of a solution of *E*-**C12** upon irradiation at 365 nm and subsequent thermal back-isomerization in the dark: (a) *E*-**C12** solution (blue line), $PSS_{365\ nm}$ (black line), absorption spectrum after 60 h (red line); (b) plot of **C12** absorption at λ = 355 nm *vs* time: black squares experimental data, red line fitting of the data according to a first order reaction model; [**C12**] = 1.1×10^{-5} M**,** CH_2Cl_2/CH_3OH 99:1 v/v, 298 K.

As for axle **C10**, isomerization and thermal back-isomerization of **C12** were also investigated by means of NMR spectroscopy. A solution of *E*-**C12** was irradiated at 365 nm directly inside the NMR spectrometer and the concentrations of the *E* and *Z* isomers measured both during irradiation and after switching off the light. The ^{1}H NMR spectra of **C12** before irradiation (*E* isomer) and at the PSS_{365} (*Z* isomer) are reported in **Figure 3.25**. Upon isomerization, the peaks in the NMR spectrum corresponding to the *E* isomer started to decrease in intensity and almost disappear while at the same time the appearance of new peaks corresponding to the formation of the *Z* species and their increase in intensity are observed. The spectrum of the *Z* isomer is highly different from that of the *E* isomer, although the resonances corresponding to the aliphatic spacer does not vary. On the other hand, the resonances related to the 'head' of the molecule show notable changes and shifts, highlighting that the isomerization of the azobenzene subunit significantly affects the 'head' of the molecule, while the chemical environment of the aliphatic 'tail' remains almost unchanged.

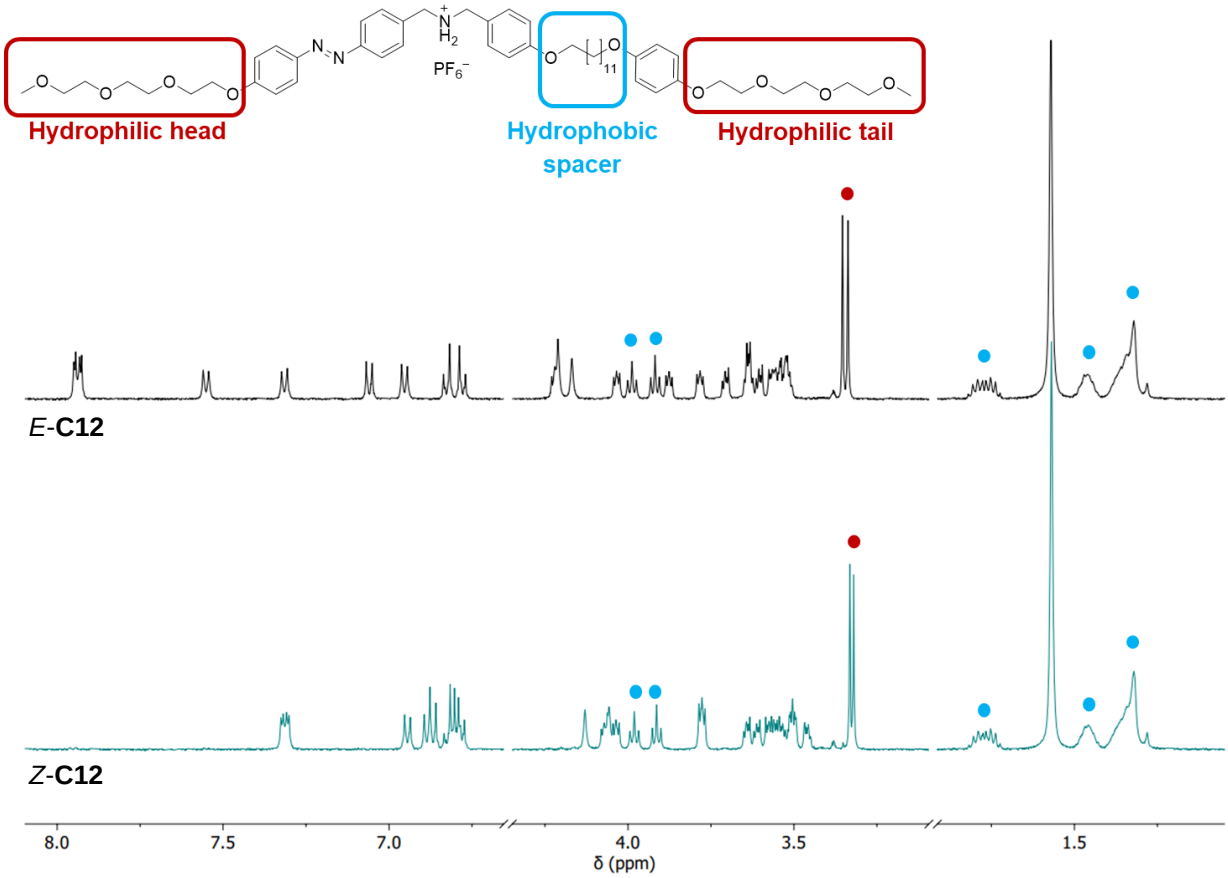

Figure 3.25. ^{1}H NMR spectra of *E*-**C12** (black line) and *Z*-**C12** (green line); 500 MHz, CD_2Cl_2/CD_3OD 99:1 v/v, 298 K.

The *E* → *Z* photoisomerization monitored in real time by sequential acquisition of NMR spectra during the irradiation process and subsequently in the dark is reported in **Figure 3.26**. Upon irradiation at 365 nm a rapid *E* → *Z* photoisomerization occurs, reaching the PSS_{365} composed by a 95:5 *E/Z* in 5 min. After switching off the light, the thermal Z → E isomerisation takes place very slowly, restoring only 8% of *E*-**C12** over 60 min.

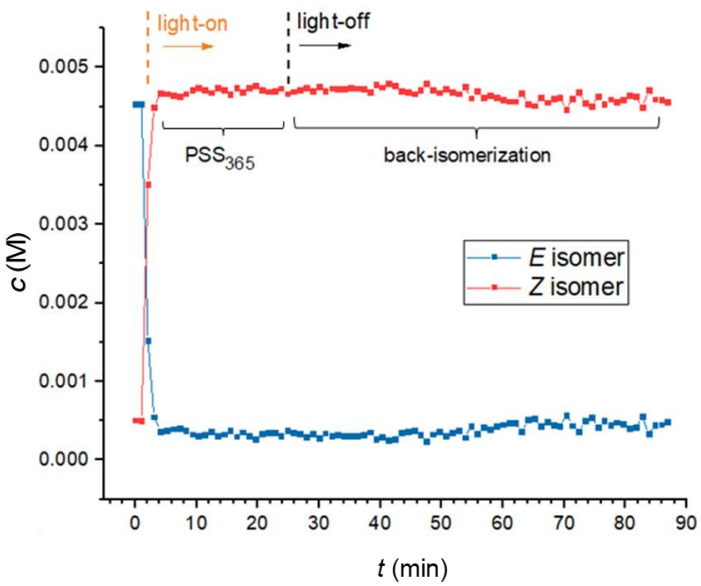

Figure 3.26. Monitoring of the speciation of **C12** under irradiation at λ = 365 nm (light on) and in the dark (light off). Concentrations are calculated from the integrals of the aromatic peaks in the ^{1}H NMR spectra using TCE as the internal standard; 500 MHz, CD_2Cl_2/CD_3OD 99:1 v/v, [TCE] = $7.5 \cdot 10^{-3}$ M, 298 K.

The structural similarity between the two axles **C10** and **C12** provides these compounds with similar photochemical properties. The *E* → *Z* photoisomerization of **C12** is a very rapid process, irradiating at λ = 365 nm for 5 min is sufficient to reach the PSS and achieve an almost complete conversion of *E* to *Z* isomers. The thermal *Z* → *E* isomerisation is very slow, but it is nonetheless possible to convert the *Z* isomer in the *E* isomer by irradiating the sample at λ = 546 nm with a PSS conversion of 86% (**Figure 3.27**)

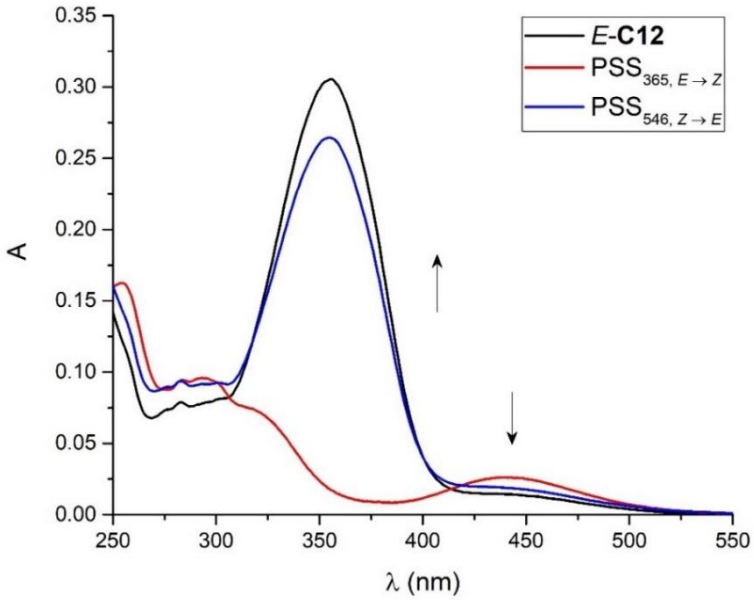

Figure 3.27. Variations in absorption of a solution of *E*-**C12** upon irradiation at 365 nm to the PSS_{365} and subsequent irradiation at λ = 546 nm: *E*-**C12** solution (black line), PSS_{365nm} (red line), PSS_{546nm} (blue line); [**C12**] = 1.1×10^{-5} M, CH_2Cl_2/CH_3OH 99:1 v/v, 298 K.

3.3.2 Preparation and study of liposomes functionalized with the molecular axle C12

The spectroscopic and photochemical characterizaton of the axle **C12** in solution allowed for its use in the functionalization of liposomes. The vesicles were prepared according to the method described in **Section 3.7.1**, by addition of 10% mol/mol of a dichloromethane/methanol (99:1 v/v) solution of *E*-**C12** to a chloroform solution of POPC and obtaining, upon removal of the solvent under reduced pressure a homogeneous film. Rehydration of the film with ultrapure water and extrusion provided the 9% *E*-**C12** functionalized liposomes, whose absorption spectrum is reported in **Figure 3.28**. The solubility of the *E*-**C12** compound in water was also investigated and, as in the previously studied axle **C10**, resulted much lower than that required to observe an absorption spectrum comparable to that recorded for the functionalized liposome suspension (**Figure 3.28**, blue dashed line), thus confirming the effective intercalation of the axle within the bilayer.

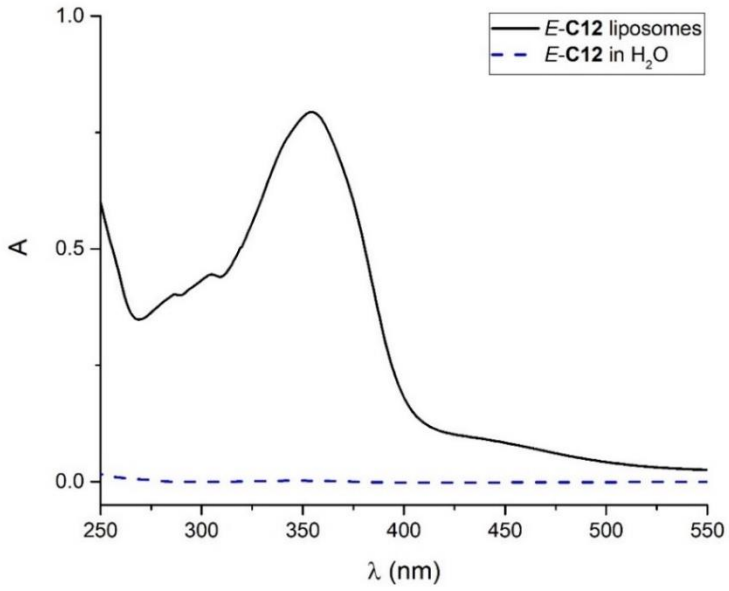

***Figure 3.28*.** Absorption spectra of a freshly extruded aqueous suspension of liposomes functionalized with *E*-**C12**, (black line) and *E*-**C12** in H_2O (blue dashed line); [POPC] = 3.2×10^{-4} M; **C12** 9 % mol/mol, 298 K.

In the absorption spectrum of the functionalized liposomes, the band structure associated to the *E*-**C12** molecule can be identified: the intense band at λ_{max} = 355 nm is assigned to the symmetry allowed $\pi \rightarrow \pi^*$ transition while the weaker band at λ_{max} = 443 nm arises from the symmetry forbidden $n \rightarrow \pi^*$ transition.

Interestingly, also in this case the presence of the molecular axle in the membrane induced the liposomes to interact. The absorption spectrum of the freshly prepared liposomes suspension functionalized with *E*-**C12** displayed several changes over time (**Figure 3.29**), with a trend comparable to that of *E*-**C10** liposomes (**Figure 3.14**). The $\pi \rightarrow \pi^*$ transition band (λ_{max} = 355 nm) of the *E*-**C12** liposomes over time undertakes evident changes, decreasing in intensity and undergoing a blue shift from 355 nm to 310 nm (**Figure 3.29**).

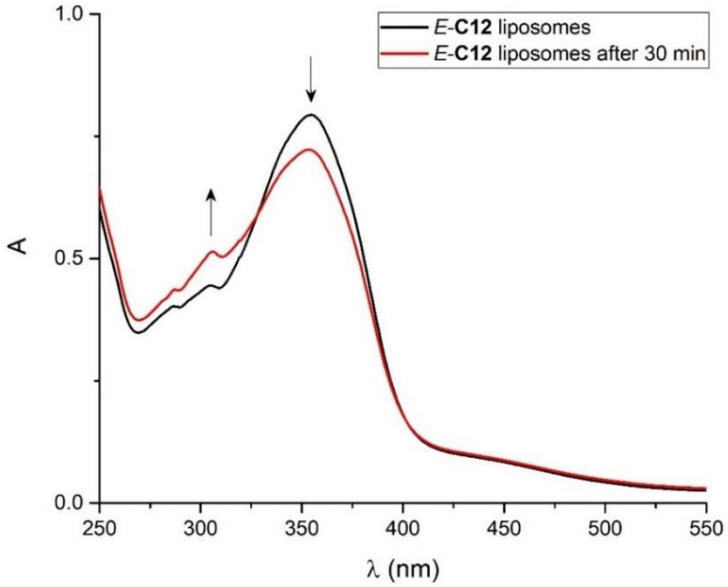

Figure 3.29. Changes in absorbance of an aqueous suspension of liposomes functionalized with *E*-**C12** when freshly extruded (black line) or kept 30 min in the dark (red line); [POPC] = 3.2×10^{-4} M, *E*-**C12** 9% mol/mol, H_2O, 298 K.

DLS analysis performed on the freshly prepared sample showed a narrow population with an average diameter of 100 nm, while the same sample after 30 min resulted more polydisperse with the appearance of several population of larger diameter (**Figure 3.30**).

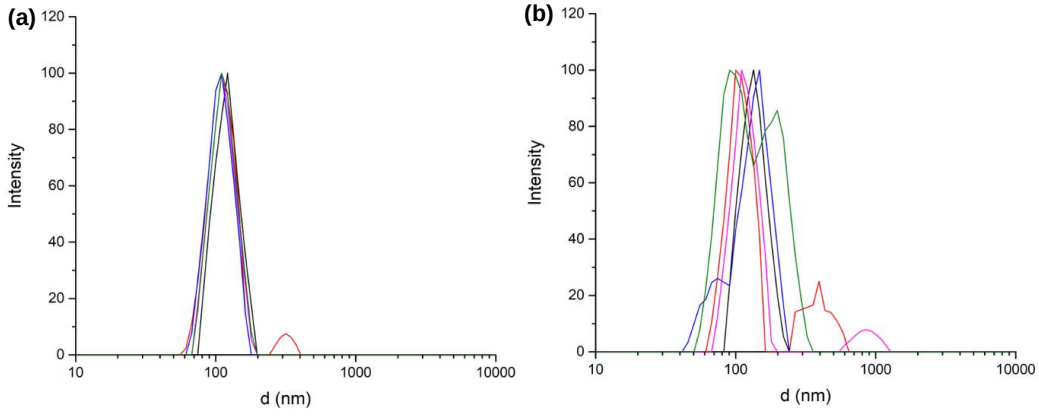

Figure 3.30. DLS graphs of an aqueous suspension of liposomes functionalized with *E*-**C12** (a) freshly extruded and (b) after 30 min in the dark; [POPC] = 3.2×10^{-4} M, *E*-**C12** 9% mol/mol, H_2O, 298 K. A single DLS analysis includes multiple individual scans, each reported in a different colour.

Irradiation of the aggregated liposomes for 15 min with 365 nm light led to the *E* → *Z* photoisomerization of the **C12** axle, as displayed in **Figure 3.31** (red bold line). The sample thus obtained was analysed by means of DLS, showing the recovery of a smaller and monodisperse population having size and size distribution characteristic of the freshly extruded suspension (**Figure 3.32b**). Similarly to what was observed in the **C10** functionalized liposomes, as soon as the **C12** molecular axle returns to the *E* configuration the aggregation process takes place, as it can be observed in the DLS and UV-vis analysis of the sample irradiated at 546 nm (**Figure 3.31**, magenta line and **Figure 3.32c**). Upon a second irradiation at 365 nm and subsequent *E* → *Z* photoisomerization, the vesicles functionalized with the **C12** guest exhibited a reversible disaggregation behaviour. Such a process occurred with no detectable degradation (**Figure 3.31**, green bold line and **Figure 3.32d**), indicating that a reversible and repeatable aggregation-disaggregation process can be realized also with the **C12** functionalized liposomes.

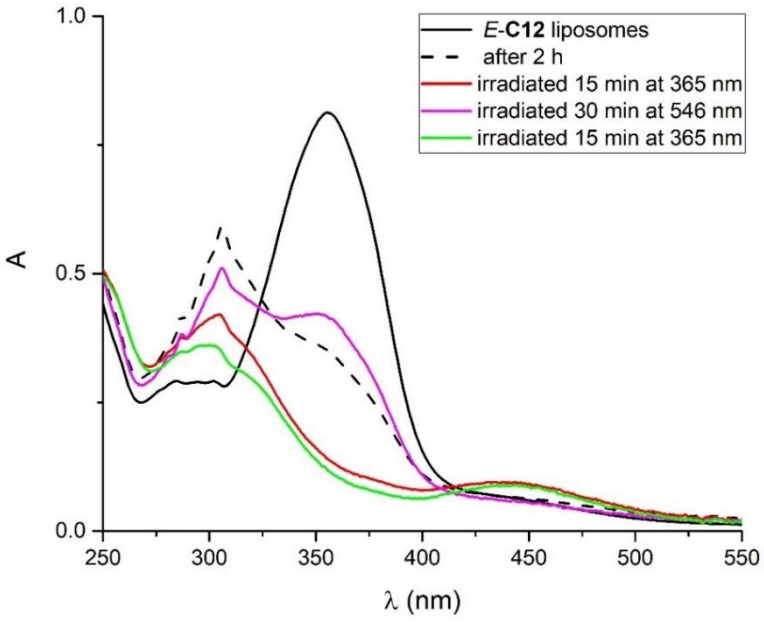

Figure 3.31. Absorption spectra of an aqueous suspension of liposomes functionalized with *E*-**C12**, freshly extruded (solid black line), after 2 h in the dark (dashed black line), irradiated at λ = 365 nm (solid red line), irradiated at λ = 546 nm (solid magenta line), then irradiated at λ = 365 nm (solid green line); [POPC] = 3.2×10^{-4} M, **C12** 9% mol/mol, H_2O, 298 K.

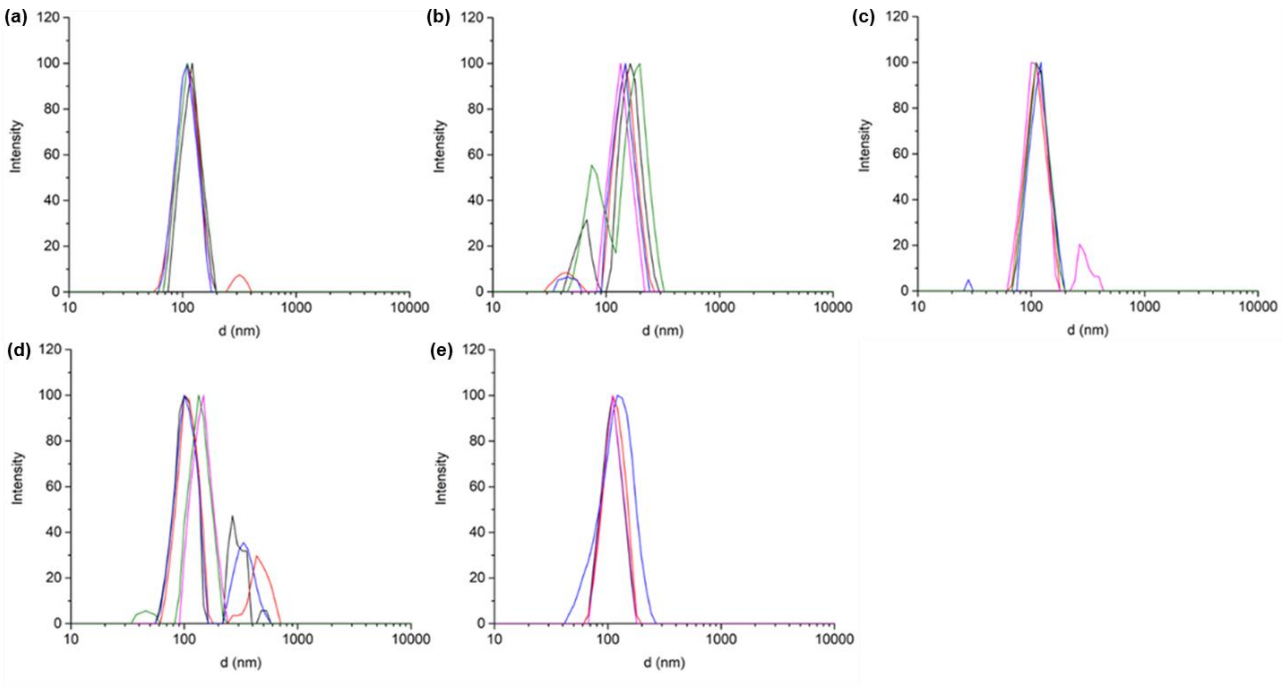

Figure 3.32. DLS graphs of an aqueous suspension of liposomes functionalized with *E*-**C12** (a) freshly extruded (b) after 3.5 h in the dark (c) irradiated 15 min at λ = 365 nm (d) irradiated 30 min at λ = 546 nm (e) irradiated 15 min at λ = 365 nm; [POPC] = 3.2×10^{-4} M, **C12** 9% mol/mol, H_2O, 298 K. A single DLS analysis includes multiple individual scans, each reported in a different colour.

The absorption spectrum of **C12** functionalized liposomes upon irradiation at 365 nm to the PSS, did not show any changes over time as long as light was provided (**Figure 3.33**). Conversely, upon suspension of the irradiation, a very slow aggregation process was observed as indicated by the increase in absorption at 300 nm. This phenomenon is likely related to the minimal amount of *E*-**C12** restored in the bilayer, as a consequence of the thermal back-isomerization of the initial *Z* isomer. As soon as the 365 nm irradiation is interrupted, the absorbance at 355 nm starts to increase (**Figure 3.33b**), supporting the slow formation of *E*-**C12** in the membrane. Analyzing the profile obtained by monitoring the changes in absorbance at 300 nm an initial plateau can be observed, successively followed by an increasing in the absorbance likely concomitant to the presence of a sufficient amount of intercalated *E*-**C12** to start the aggregation process (**Figure 3.33c**).

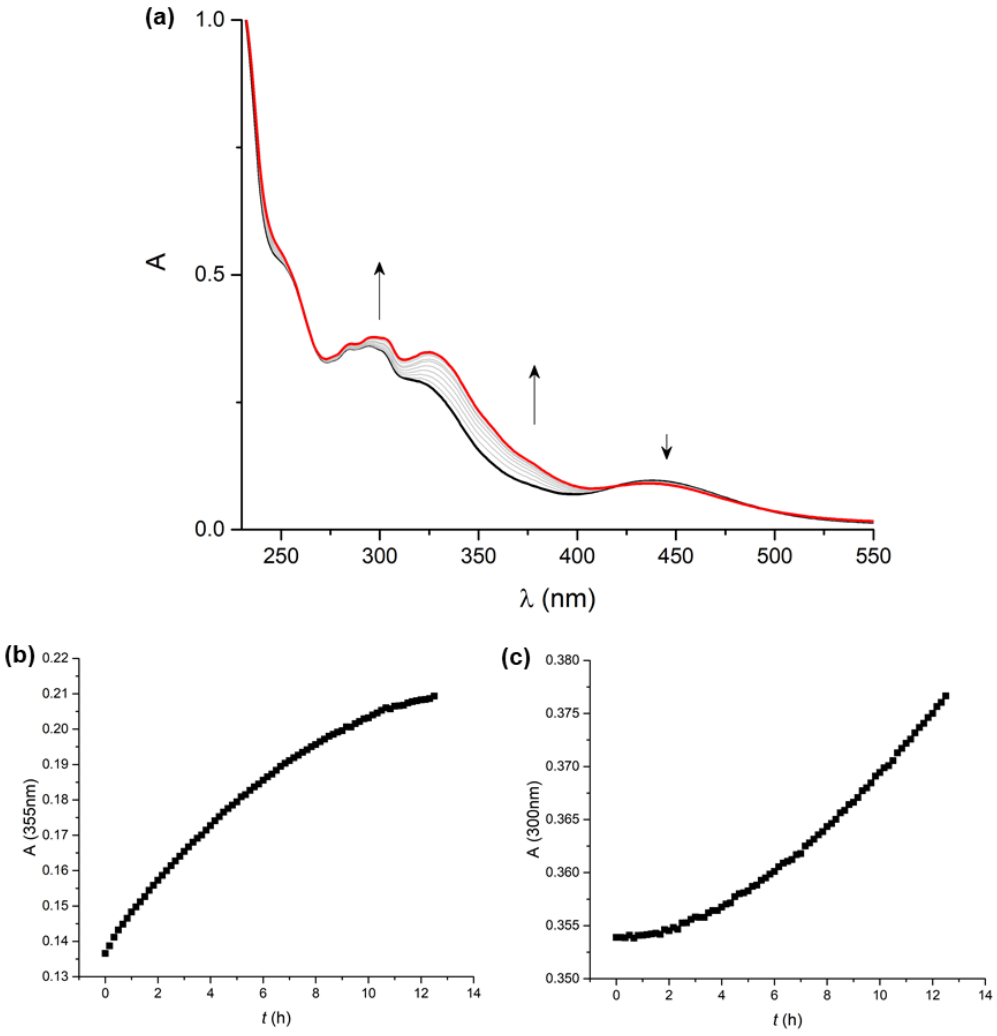

Figure 3.33. Changes in absorbance of an aqueous suspension of liposomes functionalized with the **C12** axle irradiated at λ = 365 nm to the PSS_{365} (black line) and after 12.5 h in the dark (red line) (a), absorbance *vs* time plot at λ = 355 nm (b) and λ = 300 nm (c); **C12** 9% mol/mol, [POPC] = 3.2×10^{-4} M, H_2O, 298 K.

3.3.3 Comparison between liposomes functionalized with C10 or C12

From the experimental data so far discussed, it can be inferred that liposomes functionalized with the molecular axles **C10** or **C12** exhibit the tendency to undertake aggregation when the guests are in the *E* configuration. This propensity was measured over time by recording the changes in the absorption spectra (**Figure 3.34**). Starting from a suspension of freshly extruded functionalized liposomes, which gave the absorption spectrum reported in black in **Figure 3.34**, a gradual decrease and blue shift of the $\pi \rightarrow \pi^*$ transition band was recorded over time, exhibiting the spectrum reported in red in **Figure 3.34** after 2.5 h. The comparison

between the time dependent variations at λ = 300 nm, highlights a different aggregation rate for *E*-**C10** and *E*-**C12** functionalized liposomes with equal guest loading (**Figure 3.35**). Indeed, *E*-**C10** vesicles displayed a faster aggregation process compared to that of liposomes functionalized with *E*-**C12**. This suggest that a difference of two methylene groups (approximately 3 Å) likely impacts the arrangement of the guests within the bilayer. Such information prompted further studies, focused on the role played by the polar extremities, which are important components in the transmembrane guest structure.[3] In order to investigate the influence of the ethylene glycol chains, a family of model axles was developed.

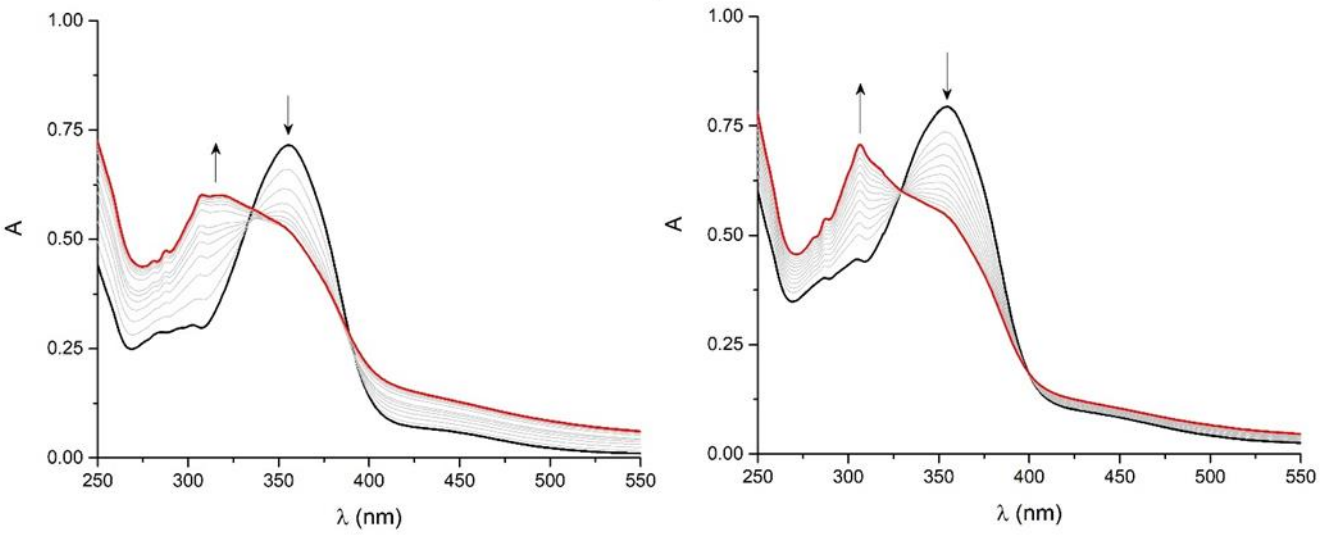

Figure 3.34. Changes in absorbance of aqueous suspensions of liposomes functionalized with (left) *E*-**C10** and (right) *E*-**C12**, freshly extruded (black line) and after 2.5 h (red line); guest 9% mol/mol, [POPC] = 3.2×10^{-4} M, H_2O, 298 K.

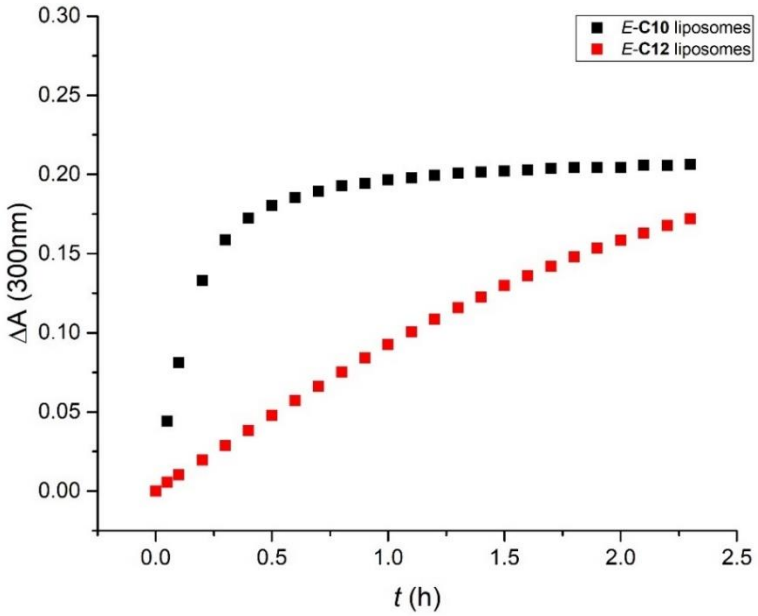

Figure 3.35. Normalized changes in absorbance of aqueous suspension of liposomes functionalized with *E*-**C10** (black squares) or *E*-**C12** (red squares); **guest** 9% mol/mol, [POPC] = 3.2×10^{-4} M, H_2O, 298 K.

3.4 Synthesis and study of model molecules related to the axle C12

Due to the slower aggregation process exhibited by *E*-**C12** functionalized liposomes, further studies focused on such compounds were carried out, with the aim to better understand which functional groups play an active role in the observed aggregation process. For this reason, a family of model molecules was designed, synthesized, and characterized both in solution and intercalated in liposomes. The model axles were conceived by systematically removing the polar chains, leading to threads having: only one ethylene glycol (EG) chain attached to the azobenzene moiety (**C12hEG**, **h** = head), only one EG chain attached at the end of the lipophilic spacer (**C12tEG**, **t** = tail), or no EG chains (**C12noEG**), with the endgroups replaced by methoxy substituents (**Figure 3.36**).

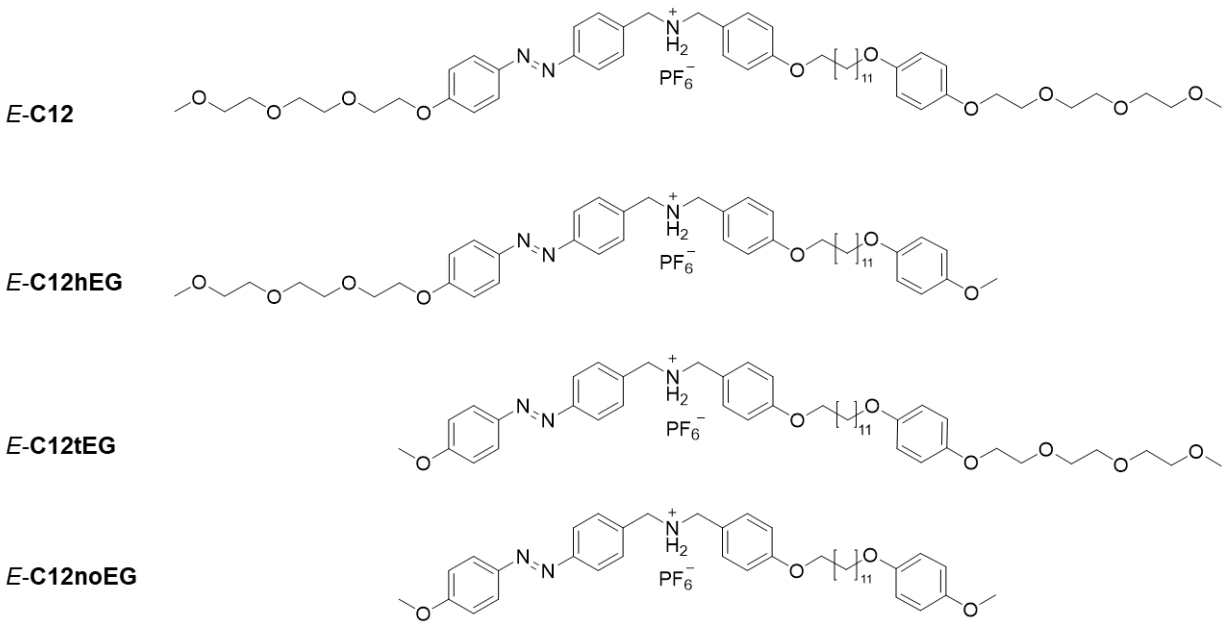

Figure 3.36. Molecular structures of *E*-**C12** and its related model compounds.

3.4.1 Synthesis of the model axles C12hEG, C12tEG and C12noEG

The synthesis of **C12hEG**, **C12tEG** and **C12noEG** was performed taking advantage of the intermediates already synthetized for the molecular axle **C12** (**Schemes 3.5** and **3.6**). The reaction of compound **13** with 4-methoxyphenol led to the formation of compound **19** in 71% yield, that upon deprotection and diazonium salt coupling formed the azobenzene derivative **22** in an overall 50% yield. Reaction of **22** with methyl iodide provided compound **23**, that presents a methoxy functionality in place of the ethylene glycol chain. The removal of the amine protective group with the simultaneous formation of the ammonium recognition site and the successive purification via size exclusion chromatography gave **C12noEG** in an overall 68% yield. Alternatively, reaction of intermediate **22** with **1**, followed by deprotection and protonation provided the axle **C12hEG** in an overall 80% yield.

To access **C12tEG**, compound **17** was reacted with methyl iodide to obtain the protected axle **25**, which was then deprotected and protonated to obtain **C12tEG** in an overall 76% yield. Compounds **C12hEG**, **C12tEG** and **C12noEG** were fully characterized by ^{1}H and ^{13}C NMR (**Section 3.7.2**).

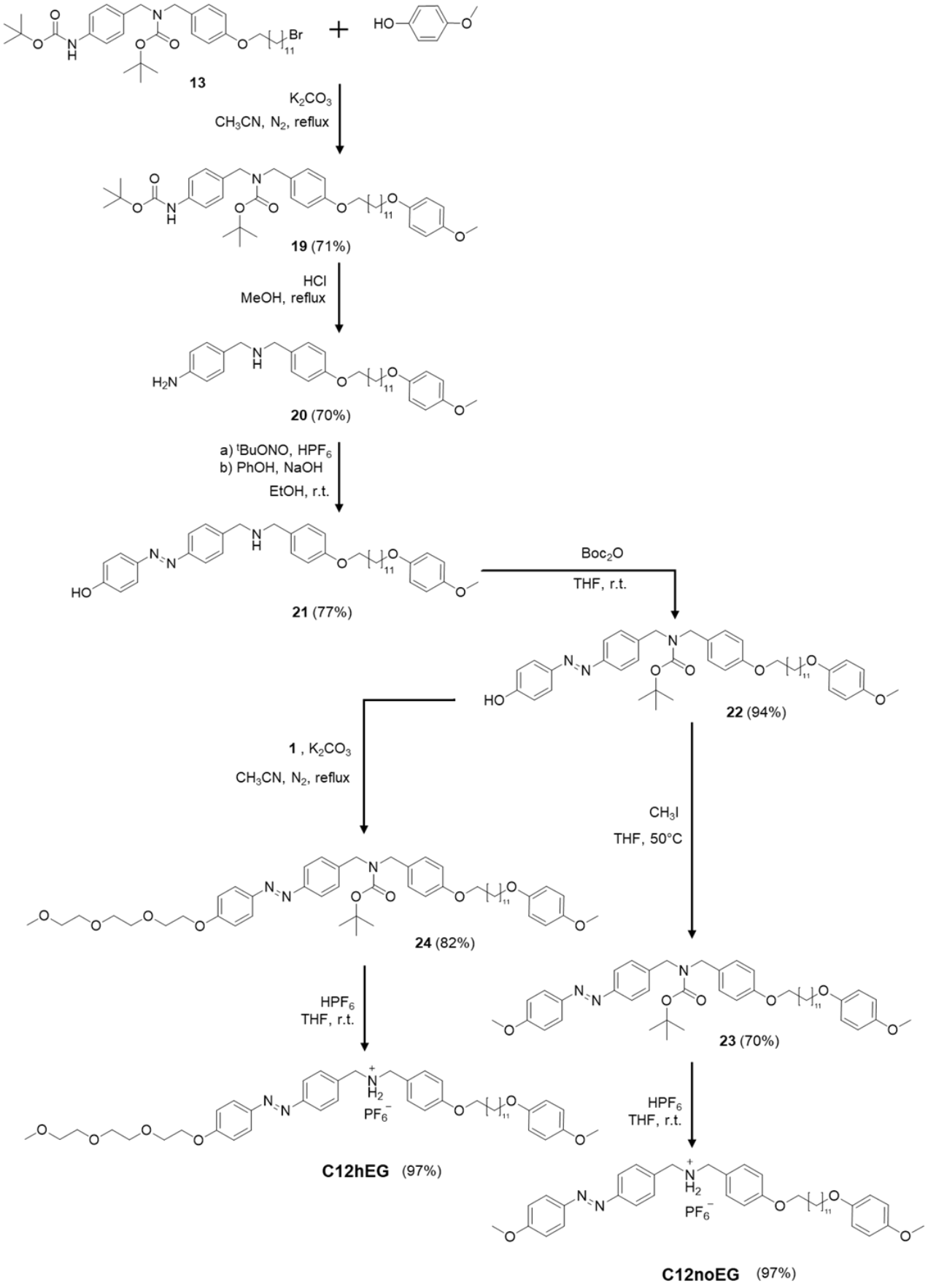

Scheme 3.5. Synthesis of the model axles **C12hEG** and **C12noEG**.

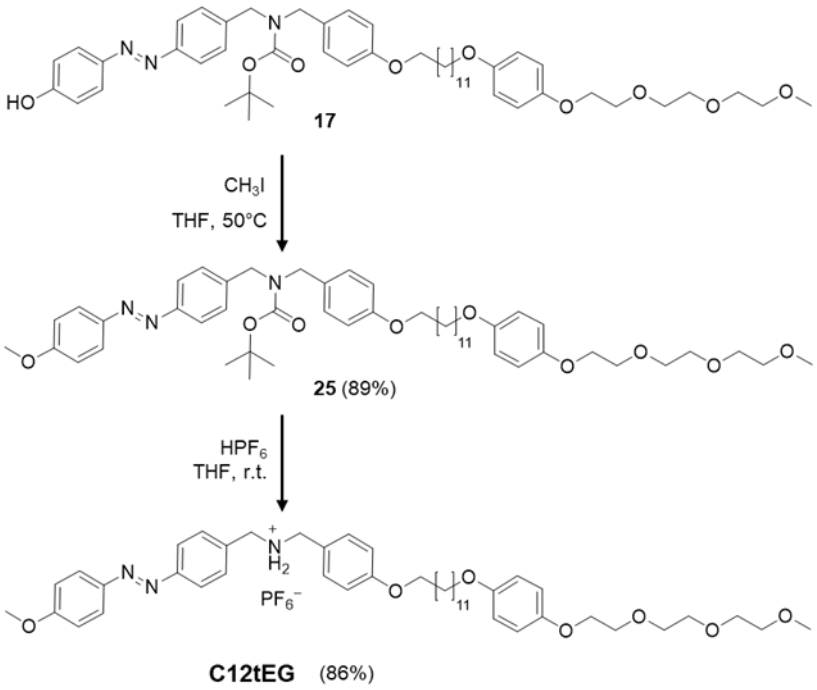

Scheme 3.6. Synthesis of **C12tEG**.

3.4.2 Photochemical characterization of C12hEG, C12tEG, C12noEG molecular axles

The model compounds were studied in dichloromethane/methanol (99:1 v/v) solution thus employing the same experimental condition used for **C10** and **C12** characterization. The absorption spectra of the *E* isomer of **C12hEG**, **C12tEG**, **C12noEG** are reported in black in **Figure 3.37**. In the spectra it is possible to identify the characterisic bands of azobenzene, the intense $\pi \rightarrow \pi^*$ band at λ_{max} = 355 nm and the weaker $n \rightarrow \pi^*$ band at λ_{max} = 440 nm. Upon irradiation with 365 nm light a fast photoisomerization is observed, leading to the *E* → *Z* conversion (**Figure 3.37**, solid red line) and reaching the PSS in 2 min. In the spectrum recorded at the PSS_{365}, the $\pi \rightarrow \pi^*$ transition band at λ = 355 nm almost completely disappeared while the $n \rightarrow \pi^*$ transition band λ_{max} = 442 nm increased and a new band λ_{max} = 254 nm appeared in the UV region. This confirmed that the molecular axles have similar photochemical properties to the parent molecule **C12** and can thus be used as model compounds to investigate the observed liposome aggregation phenomenon.

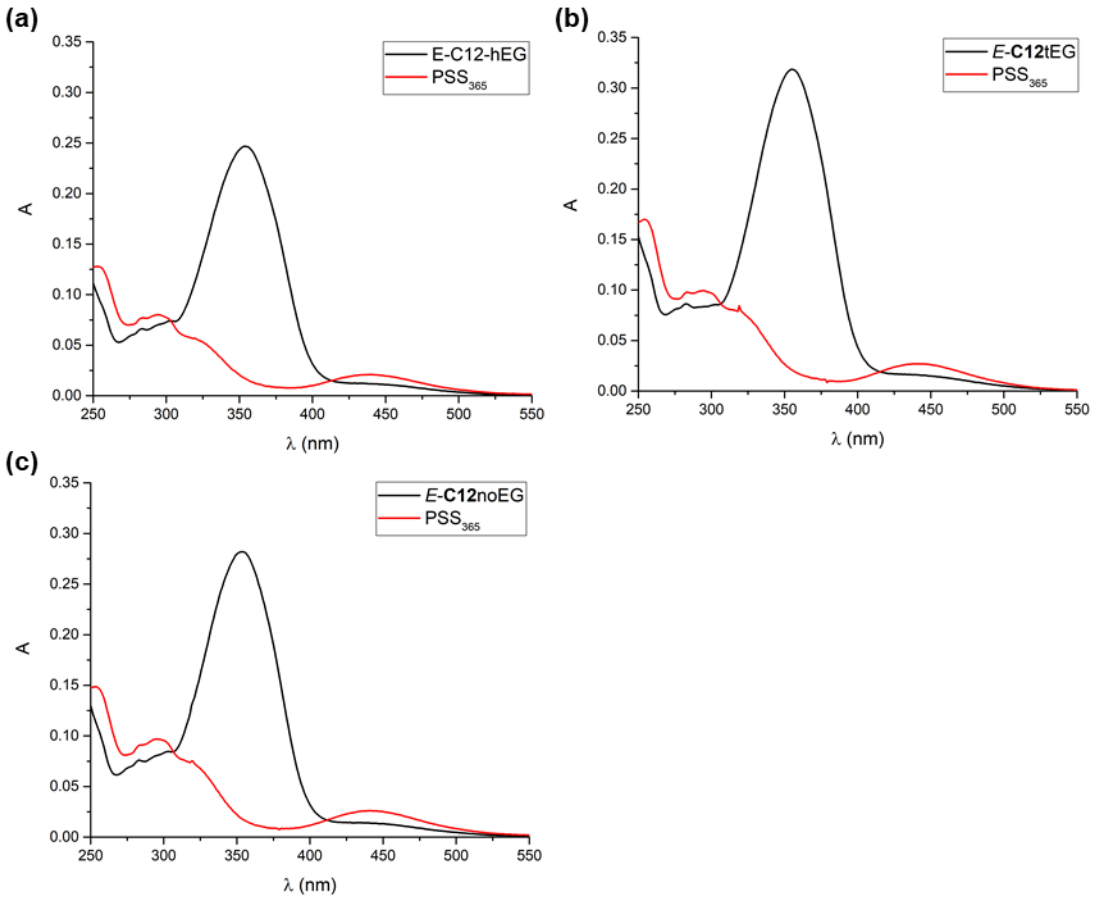

Figure 3.37. Absorption spectra of (a) *E*-**C12hEG**, (b) *E*-**C12tEG**, (c) *E*-**C12noEG** (black line) and absorption spectra at the photostationary state obtained upon irradiation at λ = 365 nm (red line); [**C12hEG**] = 9.0×10^{-6} M, [**C12tEG**] = 1.2×10^{-5} M, [**C12noEG**] = 1.0×10^{-5} M, CH_2Cl_2/CH_3OH 99:1 v/v, 298 K.

3.4.3 Preparation and study of liposomes functionalized with the model axles C12hEG, C12tEG or C12noEG

The efficient photoisomerization of the model compounds in organic solvent solution allowed to proceed with their investigation within the lipid bilayer. Liposomes functionalized with 9% of **C12hEG**, **C12tEG** or **C12noEG** were prepared according to the method reported in **Section 3.7.1** and analysed by UV-vis spectrophotometry obtaining the absorption spectra reported in **Figure 3.38**.

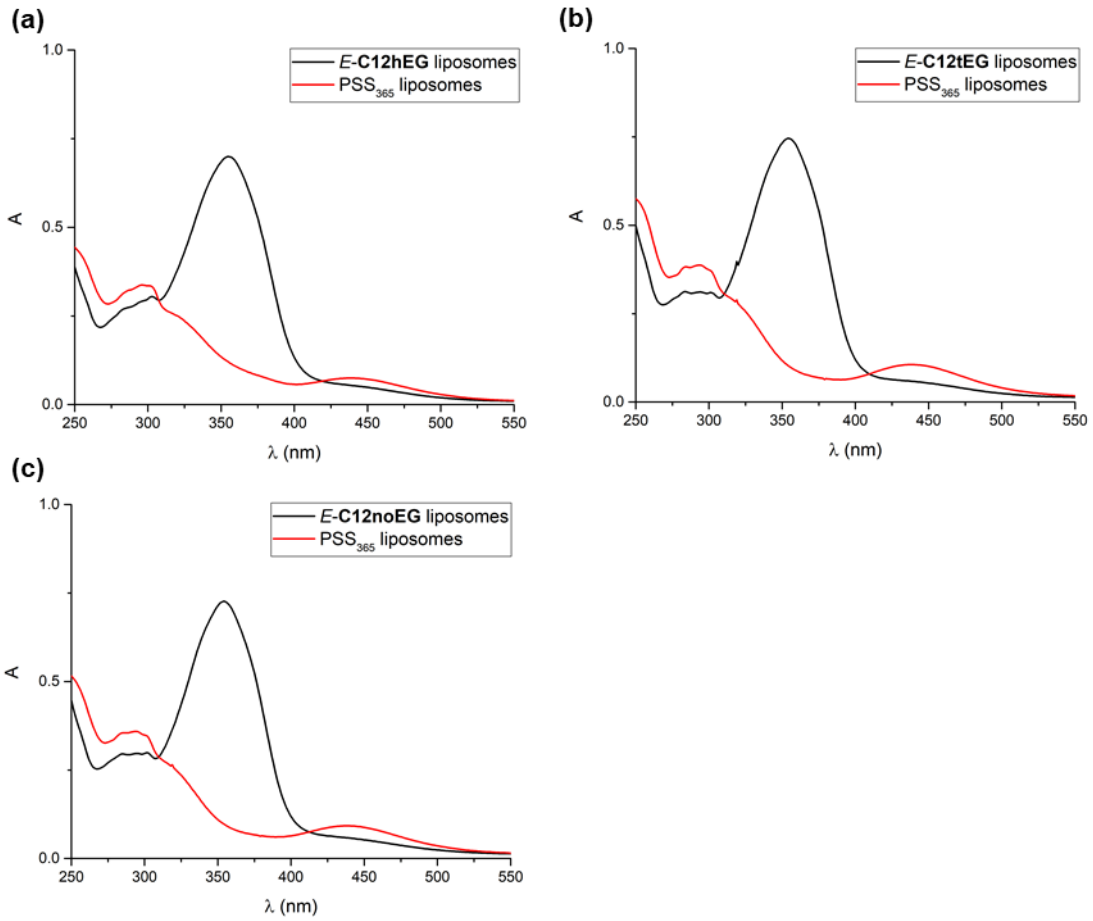

Figure 3.38. Absorption spectra of an aqueous suspension of liposomes functionalized with (a) *E*-**C12hEG**, (b) *E*-**C12tEG**, (c) *E*-**C12noEG** (black line) and absorption spectra at the photostationary state obtained upon irradiation at λ = 365 nm (red line); **guest** 9% mol/mol, [POPC] = 3.2×10^{-4} M, H_2O, 298 K.

The functionalized liposomes were monitored *via* UV-vis spectroscopy and DLS, making use of the same experimental procedure employed for **C10** and **C12** functionalized vesicles. The absorption spectrum of the *E*-**C12hEG** functionalized vesicles underwent considerable variations over time, with a pattern comparable to those displayed by *E*-**C10** and *E*-**C12** liposomes (**Figure 3.39**). The $\pi \rightarrow \pi^*$ transition band (λ_{max} = 355 nm), initially consistent with the one of the **C12hEG** compound in solution, decreases in intensity and exhibits a blue shift from 355 nm to 310 nm. DLS analysis performed on the freshly prepared sample showed a narrow population with an average diameter of 83 nm, which after 24 hours resulted polydisperse with the formation of several populations of larger diameter. Irradiation of the aggregated *E*-**C12hEG** functionalized liposomes with 365 nm light for 15 min induced the *E* to *Z* isomerization (**Figure 3.40**, red line). DLS analysis displayed the partial recovery of a monodisperse population (**Figure 3.41**), suggesting that the system preserved a photoinduced disaggregation reversibility like the **C12** functionalized liposomes.

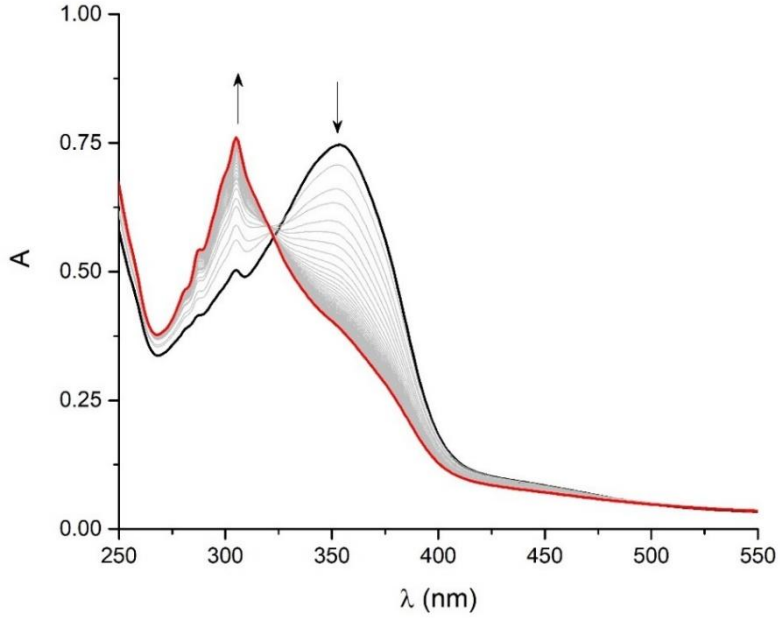

Figure 3.39. Changes in absorption of an aqueous suspension of liposomes functionalized with **C12hEG**, freshly extruded (black line) and after 24 h in the dark (red line); **C12hEG** 9% mol/mol, [POPC] = 3.2×10^{-4} M, H_2O, 298 K.

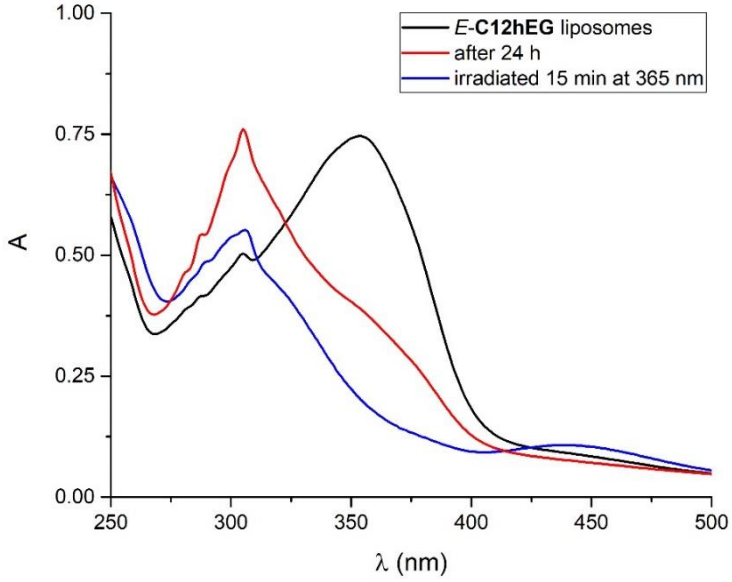

Figure 3.40. Absorption spectra of an aqueous suspension of liposomes functionalized with *E*-**C12hEG** when freshly extruded (black line), after 24 h in the dark (red line), and irradiated for 15 min at λ = 365 nm (blue line); **C12hEG** 9% mol/mol, [POPC] = 3.2×10^{-4} M, H_2O, 298 K.

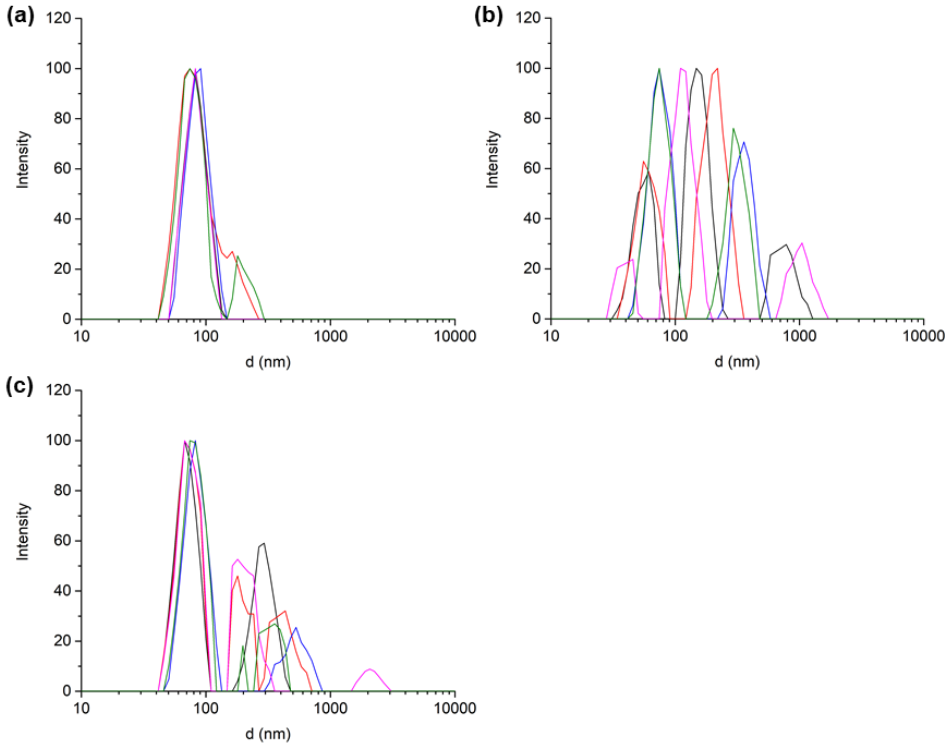

Figure 3.41. DLS graphs of an aqueous suspension of liposomes functionalized with *E*-**C12hEG** when (a) freshly extruded, (b) after 24 h in the dark and (c) irradiated 15 min at λ = 365 nm; **C12hEG** 9% mol/mol, [POPC] = 3.2×10^{-4} M, H_2O, 298 K. A single DLS analysis includes multiple individual scans, each reported in a different colour.

Vesicles functionalized with *E*-**C12tEG** exhibited similar spectral changes to those observed in **C12hEG** liposomes (**Figure 3.42**). The size and size distribution analysis showed a freshly extruded sample characterized by a monodisperse population with an average diameter of 85 nm, which as a consequence of the aggregation experiment, resulted polydisperse and comprised several populations of larger diameter (**Figure 3.44**).

Irradiation of the functionalized vesicles suspension with 365 nm light for 15 min led to the $E \rightarrow Z$ isomerization of *E*-**C12tEG** functionalized liposomes (**Figure 3.43**, blue line). However, this process did not affect the sample size and size distribution, suggesting that different kind of interactions had likely been established between *E*-**C12tEG** functionalized vesicles compared to the other systems investigated so far.

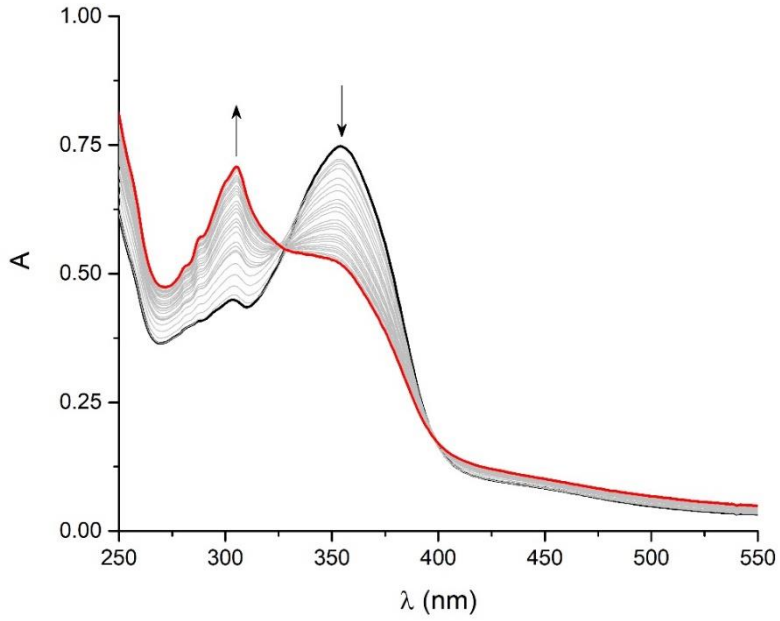

Figure 3.42. Change in absorbance of an aqueous suspension of liposomes functionalized with *E*-**C12tEG,** freshly extruded (black line) and after 24 h (red line); *E*-**C12tEG** 9% mol/mol, [POPC] = 3.2×10^{-4} M, H_2O, 298 K.

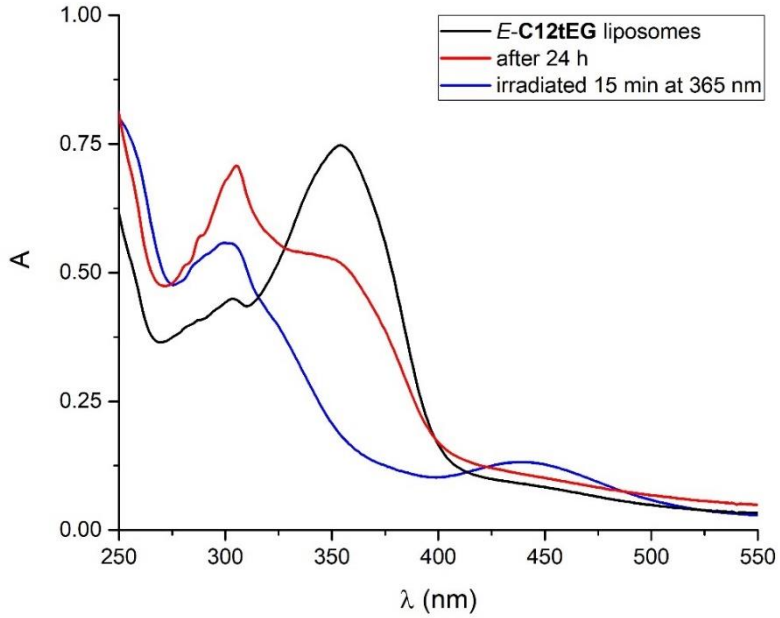

Figure 3.43. Absorption spectra of an aqueous suspension of liposomes functionalized with *E*-**C12tEG**, freshly extruded (black line), after 24 h (red line) and irradiated for 15 min at λ = 365 nm (blue line); *E*-**C12tEG** 9% mol/mol, [POPC] = 3.2×10^{-4} M, H_2O, 298 K.

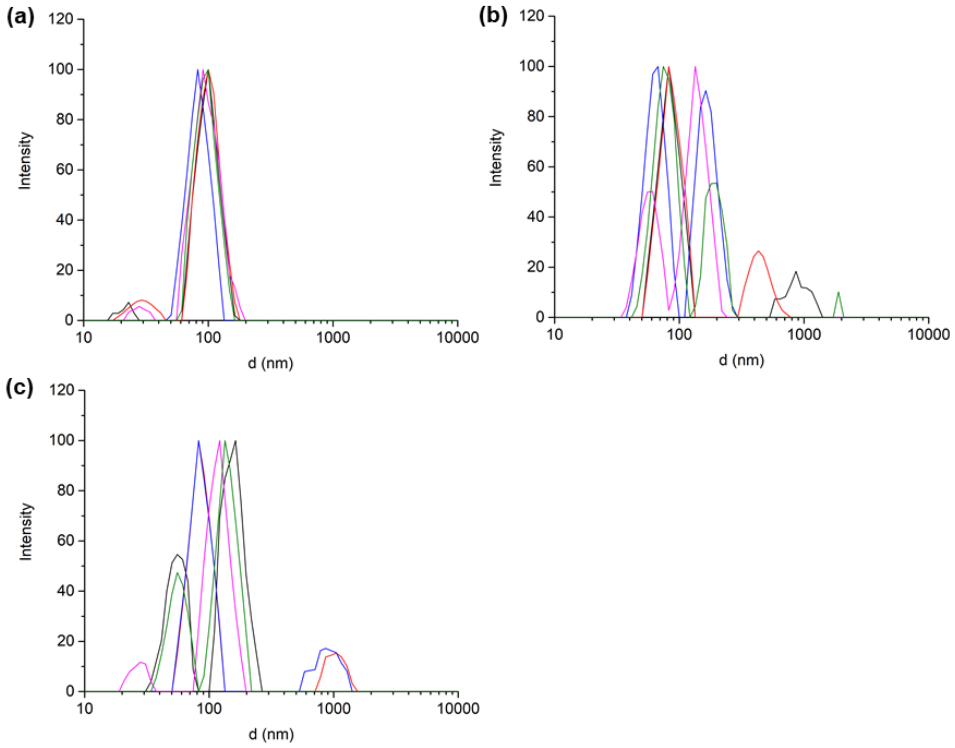

Figure 3.44. DLS graphs of an aqueous suspension of liposomes functionalized with *E*-**C12tEG** (a) freshly extruded, (b) after 24 h, and (c) after 15 min irradiation at λ = 365 nm; *E*-**C12tEG** 9% mol/mol, [POPC] = 3.2×10^{-4} M, H_2O, 298 K. A single DLS analysis includes multiple individual scans, each reported in a different colour.

In light of the encouraging difference in reactivity observed in the two models bearing a single ethylene glycol chain, the series was completed by monitoring the spectral variations over time in liposomes functionalized with *E*-**C12noEG**. Notably, very small variations were recorded that, moreover, differ from those showed by all the other functionalized liposomes (**Figure 3.45**). The absorption spectrum of *E*-**C12noEG** liposomes exhibits only a small increase over an extended monitoring period (70 h).

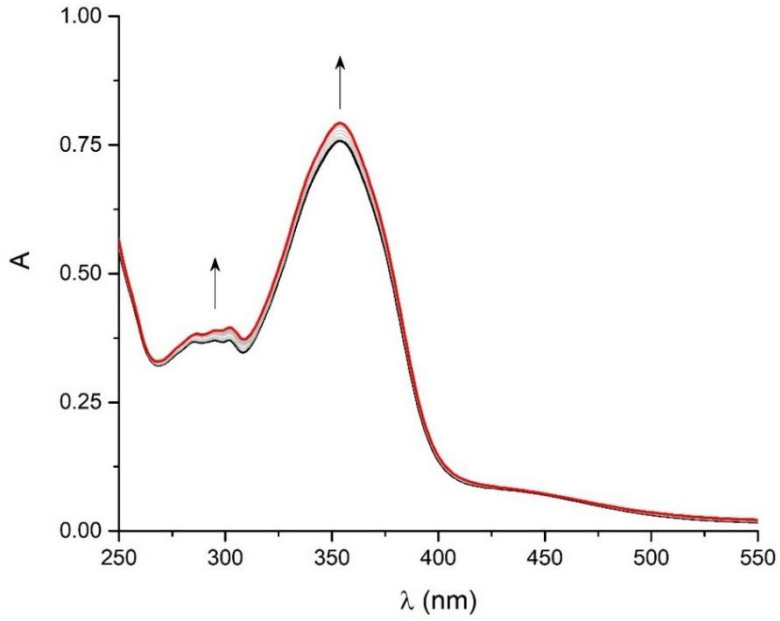

Figure 3.45. Changes in absorbance of an aqueous suspension of liposomes functionalized with *E*-**C12noEG**, freshly extruded (black line), and after 70 h (red line); *E*-**C12noEG** 9% mol/mol, [POPC] = 3.2×10^{-4} M, H_2O, 298 K.

The DLS analysis performed on the freshly extruded *E*-**C12noEG** liposomes showed a monodisperse population with an average diameter of 80 nm, which became polydisperse and composed of several populations of larger diameter after the experiment. Irradiation at 365 nm led to the $E \rightarrow Z$ isomerization of the axle, reaching the PSS in 15 min (**Figure 3.46**, blue line), however without afftecting the sample size and size distribution (**Figure 3.47**). The observed spectral variations suggest that the *E*-**C12noEG** liposomes take a different path compared to the vesicles functionalized with any of the previous axles.

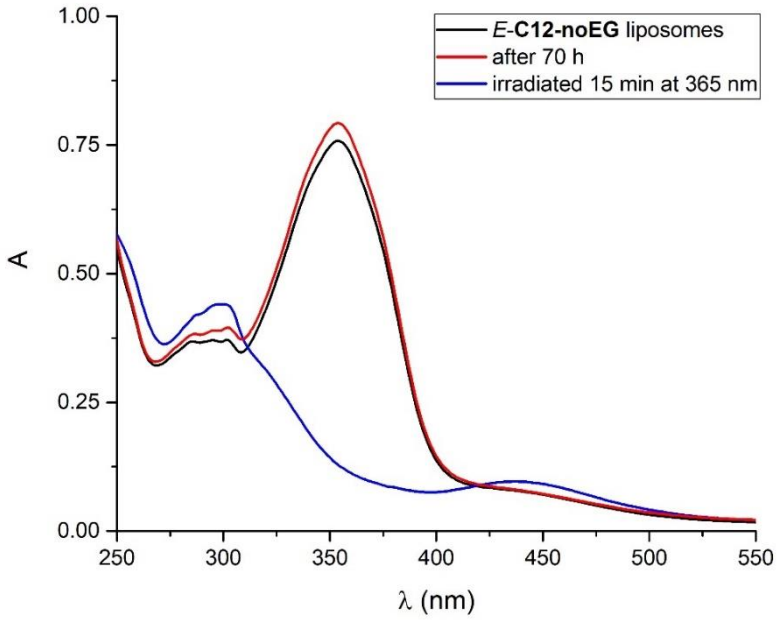

Figure 3.46. Absorption spectra of an aqueous suspension of liposomes functionalized with *E*-**C12noEG**, freshly extruded (black line), after 70 h (red line), and irradiated for 15 min at λ = 365 nm (blue line); *E*-**C12noEG** 9% mol/mol, [POPC] = 3.2×10^{-4} M, H_2O, 298 K.

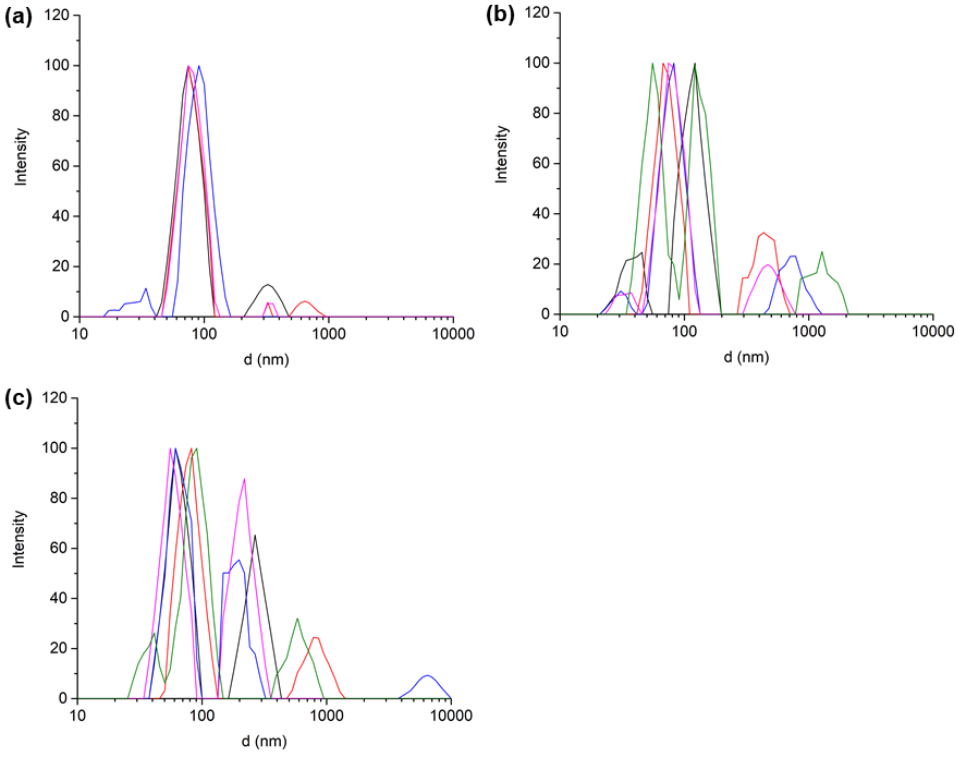

Figure 3.47. DLS graphs of an aqueous suspension of liposomes functionalized with *E*-**C12noEG**, (a) freshly extruded, (b) after 70 h, (c) irradiated 15 min at λ = 365 nm; *E*-**C12noEG** 9% mol/mol, [POPC] = 3.2×10^{-4} M, H_2O, 298 K. A single DLS analysis includes multiple individual scans, each reported in a different colour.

The difference between the aggregation behaviour of liposomes functionalized with **C12**, **C12-hEG**, **C12-tEG** and **C12-noEG** is clearly visible by comparing the time-dependent variations in absorbance at 300 nm recorded during the experiment performed on the four systems (**Figure 3.48**). The plot reported in **Figure 3.48** highlights an increase in the aggregation rate that depends on the number of ethylene glycol chains connected to the axles. Specifically, the parent molecule **C12** and the model compound **C12-hEG** containing a single ethylene glycol chain linked to the azobenzene moiety displayed higher aggregation rates.

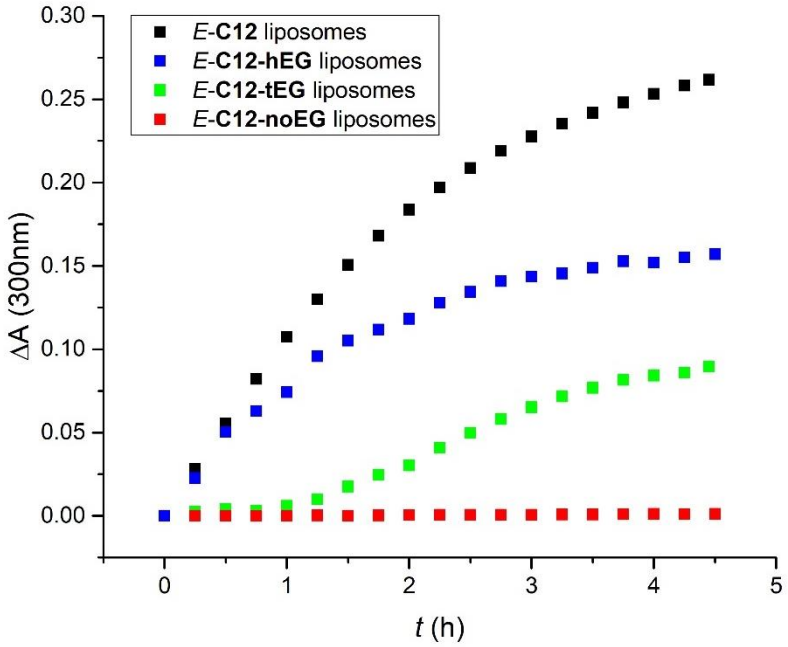

Figure 3.48. Normalized changes in absorbance of aqueous suspensions of liposomes functionalized with *E*-**C12** (black), *E*-**C12hEG** (blue), *E*-**C12tEG** (green), *E*-**C12noEG** (red); **guest** 9% mol/mol, [POPC] = 3.2×10^{-4} M, H_2O, 298 K.

Liposomes functionalized with the **C12hEG** axle - presenting the ethylene glycol chain attached to the azobenzene extremity - exhibited an aggregation trend in the UV-vis absorption spectra comparable to that of **C12** fuctionalized vesicles, also accompanied by an almost complete recover of a monodisperse population upon photoisomerization of the liposomes aggregates. Conversely, liposomes funtionalised with **C12tEG** - axle presenting the ethylene glycol chain attached at the end of the lipophilic spacer extremity - displayed changes in the absorption spectra similar to the previous model axle, but once the aggregation occurred they did not show disaggregation upon photoisomerization. This suggested a concomitant participation of another functional group to the aggregation

process. For this reason, it was hypothesised that the ethylene glycol chains might be involved in promoting vesicles encounter and therefore their aggregation. Moreover, in this molecular axle the ethylene glycol chain is not attached to the azobenzene functional group, potentially explaining why the aggregates are not affected by the *E* to *Z* isomerization, in contrast to **C10**, **C12** and **C12hEG** functionalized liposomes. On the contrary, the analyses performed on liposomes functionalized with **C12noEG** showed a different pattern in the change of the absorption spectrum over time, which was reflected in very slow and irreversible aggregation. In this context, it might be supposed that other functional groups of the axle affect liposome stability and lead to the slow formation of aggregates.

3.5 Computational investigation of the molecular axle C12

In order to better understand the role played by the axle components in the observed aggregation process, a detailed understanding of the arrangement of the axles in the bilayer is required. For this reason, preliminary studies on the positioning of the **C12** axle within the membrane were performed in collaboration with the Fois group at the University of Insubria by means of Metadynamics simulations (MTD). The simulations involved a squared portion of a POPC bilayer functionalized with 9% mol/mol of the **C12** molecular axle in an aqueous environment. The equilibrium simulation experiments pointed out that the *E*-**C12** guests are able to diffuse within the lattice once intercalated in the membrane, leading to the encounter between two of such molecules as displayed in **Figure 3.49a** and **3.50a**.

When the **C12** axles are in the *E* form (**Figure 3.49a**) one of the two molecules is folded around the other thus being more enclosed inside the membrane; this rearrangement causes the protrusion of the second axle from the membrane surface, of about 10-15 Å with respect to the phospholipid amine functionality (**Figure 3.49b**). In this context, the azobenzene and the head ethylene glycol chain are placed on the external surface of the bilayer. Conversely, when the **C12** axle is in the *Z* form, the azobenzene functionality exhibits its characteristic folded structure resulting in the positioning of such moiety together with the connected ethylene glycol chain, almost completely inside the membrane (**Figure 3.50a** and **Figure 3.50b**). Based on these initial data, it could be hypothesized that when the **C12** axle is in its *E* form, the interaction between the extravesicular moiety of an axle belonging to different liposomes could occur, giving rise to the observed azobenzene stacking and subsequent vesicle aggregation. However, upon isomerization of the azobenzene functionality to the *Z* isomer, such chromophore together with the connected ethylene glycol

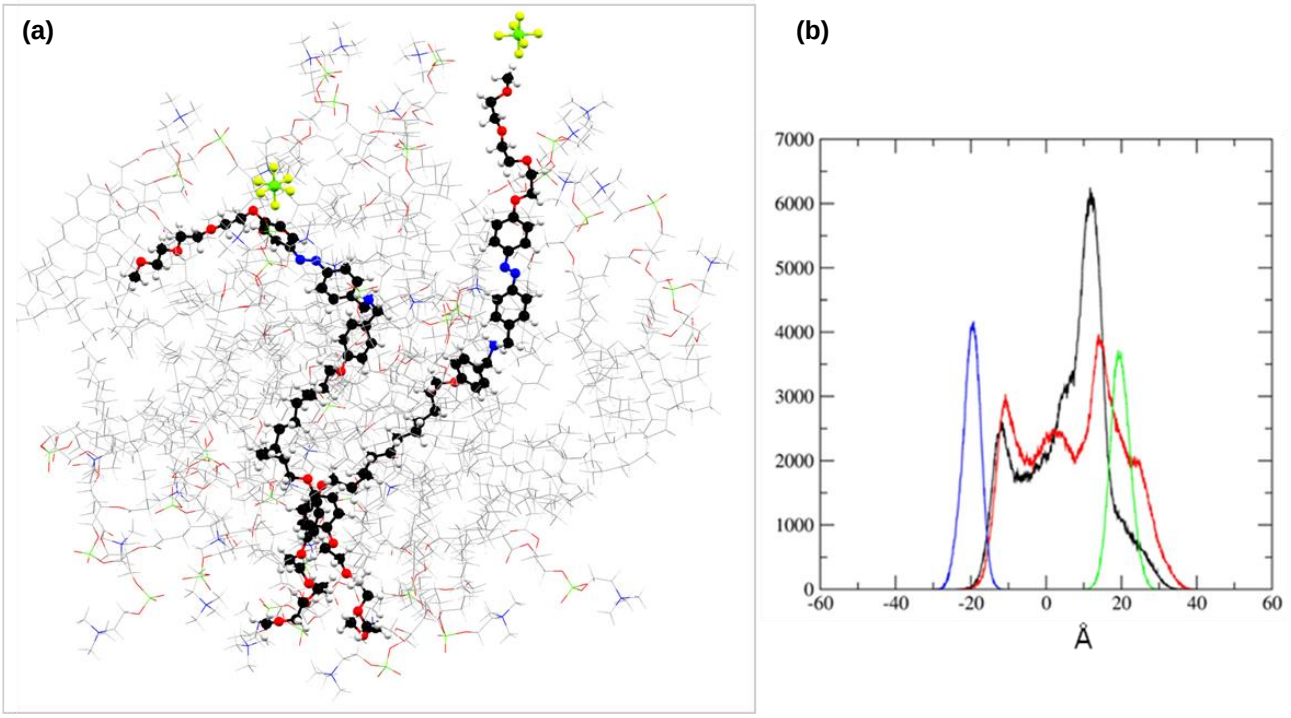

Figure 3.49. (a) Snapshot of the POPC bilayer functionalized with *E*-**C12** axles obtained from equilibrium MTD trajectory and (b) spatial distribution monitored over time of the *E*-**C12** axles (red and black curve) position relative to the inner and outer phospholipid phosphate groups (green and blue, respectively)

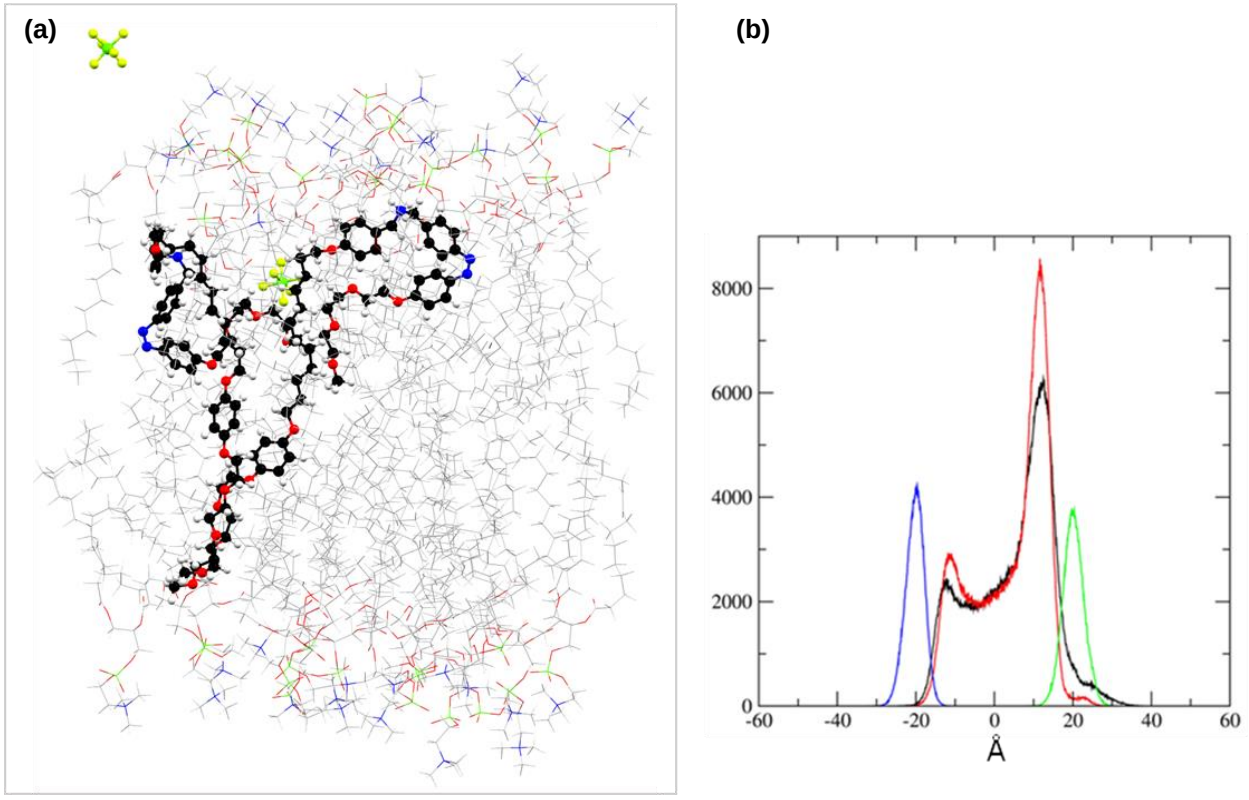

Figure 3.50. (a) Snapshot of the POPC bilayer functionalized with *Z*-**C12** axles obtained from equilibrium MTD trajectory and (b) spatial distribution monitored over time of the *Z*-**C12** axles (red and black curve) position relative to the inner and outer phospholipid phosphate groups (green and blue, respectively)

3.6 Conclusions and outlook

Two molecular axles, namely **C10** and **C12**, were designed and tailored to be inserted in a phospholipid bilayer membrane and comprising a photoactive azobenzene unit and an ammonium recognition site, with the aim to use them as components for molecular pumps. These molecules have been studied both in homogeneous solution and when intercalated in liposomes. The functionalized liposomes upon extrusion and suspension in water displayed a peculiar aptitude, undergoing aggregation when the molecular axles are in the *E* configuration. However, irradiation with light at 365 nm of the aggregated sample led to the $E \rightarrow Z$ isomerization of the axles that triggered liposome disaggregation. This trend resulted to be photoinduced, reversible and non-destructive.

To evaluate the role played by the structure of such molecular axles on the observed aggregation process, a family of model molecules were prepared. The three models **C12hEG**, **C12tEG** and **C12noEG** present the main structure of the **C12** axle and, once intercalated in the liposome membranes, underwent aggregation with rates that are dependent on the number and position of ethylene glycol chains. Importantly, when a single ethylene glycol chain was attached to azobenzene, the aggregation process occurred faster. Moreover, a reversible disaggregation behaviour upon $E \rightarrow Z$ isomerization was observed only when the ethylene glycol chain was attached to the azobenzene functionality. Preliminary computational studies were performed on a portion of a POPC bilayer functionalized with 9% mol/mol of the axle **C12**. Such studies confirmed that the azobenzene functional group can be located on the external surface of the vesicles when the axle is in the *E* form, but enclosed within the bilayer when in the *Z* form. These data support the hypothesis of an aggregation induced by the interactions of such moiety when the axle is in the *E* form, and their disaggregation upon photoisomerization to the *Z* form. However, further investigations need to be performed to clarify the exact role played by the axle length and the ethylene glycol chains in this aggregation phenomenon.

These results will be exploited for the development of systems designed to be intercalated in the liposomal membrane, with the aim to achieve the unidirectional active transport of a molecular substrate from the extravesicular environment to the vesicle core.

3.7 Experimental details

Matherials and methods

Solvents and reagents triethylene glycol monomethyl ether, tert-Butyl 4-formylphenylcarbamate, 4-hydroxybenzylamine, sodium borohydride, di-*tert*-butyl-dicarbonate, potassium carbonate, caesium carbonate, tosyl chloride, 4-methoxyphenol, phenol, sodium nitrite, hexafluorophosphoric acid, hydroquinone, 1,12-dibromododecane, methyl iodide, 16:0-18:1 PC 1-palmitoyl-2-oleoyl-*sn*-glycero-3-phosphocholine chloroform solution were all used as supplied by Fluorochem, Sigma-Aldrich or VWR without further purification.

Flash column chromatography was performed using Sigma Aldrich Silica 40 (230-400 mesh size or 40-63 μm) as the stationary phase. Gel permeation chromatography was performed using Biorad Biobeads SX-1 as the stationary phase. Thin layer chromatography was performed on TLC Silica gel 60 F254 coated aluminium plates from Merck.

- **NMR measurements**

^{1}H NMR spectra were recorded on an Agilent DD2 spectrometer operating at 500 MHz or a Varian Mercury spectrometer operating at 400 MHz; ^{13}C NMR spectra were recorded on an Agilent DD2 spectrometer operating at 126 MHz or a Varian Mercury spectrometer operating at 101 MHz; ^{19}F NMR spectra were recorded on an Agilent DD2 spectrometer operating at 470 MHz. Chemical shifts are quoted in ppm relative to tetramethylsilane ($SiMe_4$, $\delta = 0$ ppm), using the residual solvent peak as a reference standard; all coupling constants (*J*) are expressed in Hertz (Hz). Irradiation at λ = 365 nm was performed directly inside the NMR spectrometer on samples solutions between 5 and 10 mM, by using a Prizmatix UHP-T-365-SR LED Illuminator (1.5 W, λ_{max}= 369 nm, FWHM, 15.56 nm) equipped with and FCA-SMA adaptor for optical fiber. Quartz optical fiber (core 1000 μm) equipped with a SMA connector on one end was purchased from Thorlabs. The other end of the optical fiber was scraped to remove the protective coatings and submerged into the solution within the NMR tube. The photoisomerization processes were studied by recording sequential NMR spectra of the samples upon light irradiation in order to monitor changes in the concentrations of the isomers, through integration of peaks. The obtained experimental data was processed using MestReNova software and OriginPro 2019.

- **UV-vis measurements**

The absorption spectra in the 800-200 nm range were recorded using a PerkinElmer Lambda 750 double beam spectrophotometer. All the acquisitions were carried out at room-temperature on air-equilibrated solutions of the samples contained in spectrophotometric quartz cuvettes of 1 cm optical path length. The precision on the wavelength values was ± 1 nm. Molar absorption coefficient values were determined using the Lambert-Beer law and the experimental error associated with each value is estimated to be ± 10%.
Irradiation of samples was performed on 2.5 mL solution of sample in organic solvent (ca 1×10^{-5} M) or 2 mL of liposome suspension ([POPC] = 3.2×10^{-4} M) using a medium pressure Hg lamp (200 W) with constant stirring. The irradiation wavelength was selected using interference filters. All photoisomerizations were carried out by irradiating the samples for defined intervals of time and recording variations in the absorption spectra with the spectrophotometer until the photostationary state (PSS) was reached.

- **DLS measurements**

The liposomes were characterized on a Malvern Instruments DLS ZetaSizer Nano-ZS to estimate their size and zeta potential. For size measurements single-use PMMA cuvettes were used, containing 1 mL of diluted liposomal suspension

3.7.1 Preparation of vesicles

- **Preparation of pristine liposomes**

An appropriate amount of a POPC solution in $CHCl_3$ (6.5×10^{-6} mol) was evaporated under reduced pressure at 30°C to produce a thin film that was dried under vacuum for 1 h, then stored overnight at 4°C before rehydration. The lipid film was rehydrated with 1 mL of ultrapure water (or buffer solution). The resulting heterogeneous liposomal suspension was extruded 25 times through polycarbonate membranes (pore size 100 nm) mounted on an Avanti Polar Lipids (Alabaster, AL, USA) mini-extruder. The POPC concentration of liposomal solutions after rehydration were 6.5×10^{-3} M. Prior to being used, liposomal solution

was diluted with ultrapure water (or buffer solution) to achieve a final concentration of POPC equal to 3.25×10^{-4} M for DLS analysis.

- **Preparation of functionalized liposomes**

An appropriate amount of guest in CH_2Cl_2/MeOH (99:1 v/v) was added to a POPC solution in $CHCl_3$ (6.5×10^{-6} mol) to give a 10:100 guest/lipid ratio. The mixture was evaporated under reduced pressure at 30°C to produce a thin film that was dried under vacuum for 1 h, then stored overnight at 4°C before rehydration. The lipid film was rehydrated with 1 mL of ultrapure water (or buffer solution). The resulting heterogeneous liposomal suspension was extruded 25 times through polycarbonate membranes (pore size 100 nm) mounted on an Avanti Polar Lipids (Alabaster, AL, USA) mini-extruder. The POPC concentration of liposomal solutions after rehydration were 6.5×10^{-3} M. Prior to be used, liposomal solution was diluted with ultrapure water (or buffer solution) to achieve a final concentration of POPC equal to 3.25×10^{-4} M for aggregation experiment and DLS analysis.

3.7.2 Synthetic procedures

Triethylene glycol monomethyl ether tosyl ester, 1

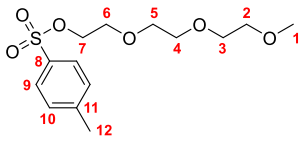

1

A chloroform solution (100 mL) of triethylene glycol monomethyl ether (34.4 mL, 220 mmol), tosyl chloride (46.1 g, 242 mmol), dimethylamino pyridine (125 mg, 1.0 mmol) and triethylamine (33.5 mL, 240 mmol) was stirred at 40 °C for 72 h. The resulting solution was cooled down to room temperature, washed with water (5×100 mL) and dried over anhydrous $MgSO_4$. Filtration and removal of the solvent under reduced pressure afforded the crude product which was purified by flash chromatography (chloroform:cyclohexane 50:50, R_f = 0.10) to obtain **1** as a pale yellow oil (28.6 g, 82%). ^{1}H NMR (500 MHz, chloroform-*d*) δ 7.76 - 7.66 (m, 2H, **9**), 7.33 - 7.23 (m, 2H, **10**), 4.09 - 4.04 (m, 2H, **7**), 3.62 - 3.57 (m, 2H, **6**), 3.54 - 3.47 (m, 6H, **3**+**4**+**5**), 3.46 - 3.43 (m, 2H, **2**), 3.28 (s, 3H, **1**), 2.36 (s, 3H, **12**). ^{13}C NMR (126 MHz, chloroform-*d*) δ 144.73, 132.75, 129.73, 127.79, 71.70, 70.51, 70.31 (×2), 69.18, 68.46, 58.81, 21.47.

4-(benzyloxy)phenol, 2

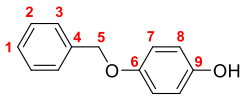

2

A solution of hydroquinone (6.05 g, 55.0 mmol), benzyl bromide (4.70 g, 27.5 mmol) and potassium carbonate (3.80 g, 27.5 mmol) in acetone (50 mL) was refluxed for 16 h. The solvent was removed under reduced pressure and the residue dissolved in ethyl acetate, washed with water (5×100 mL) and dried over anhydrous $MgSO_4$. Filtration and removal of the solvent under reduced pressure provided a crude solid which was purified by flash chromatography (chloroform, R_f = 0.3) to obtain the product **2** as a shiny off-white solid (2.94 g, 53%). ^{1}H NMR (500 MHz, methyl sulfoxide-d_6) δ 8.96 (s, 1H, OH), 7.43 - 7.40 (m, 2H, **3**), 7.39 - 7.34 (m, 2H, **2**), 7.33 - 7.28 (m, 1H, **1**), 6.85 - 6.80 (m, 2H, **8**), 6.71 - 6.65 (m, 2H, **7**), 4.98 (s, 2H, **5**). ^{13}C NMR (126 MHz, methyl sulfoxide-d_6) δ 151.39, 151.22, 137.59, 128.41, 127.72, 127.66, 115.79, 115.76, 69.75.

1-(benzyloxy)-4-(2-(2-(2-methoxyethoxy)ethoxy)ethoxy)benzene, 3

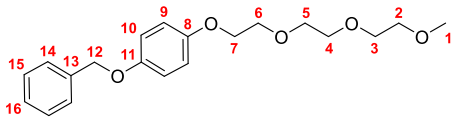

3

A solution of **1** (5.61 g, 17.6 mmol), **2** (2.94 g, 14.7 mmol) and caesium carbonate (7.2 g, 22.0 mmol) in dry acetonitrile (150 mL) was stirred at 80 °C for 18 h under a dinitrogen atmosphere. The solution was cooled down to room temperature and the solvent removed under reduced pressure to provide a crude mixture which was dissolved in dichloromethane (100 mL), washed with water (3×100 mL) and dried over anhydrous $MgSO_4$. The crude compound was purified by flash chromatography (hexane:ethyl acetate 80:20, R_f = 0.10) to provide the product **3** as a colourless oil (3.45 g, 68%). ^{1}H NMR (500 MHz, chloroform-*d*) δ 7.44 - 7.40 (m, 2H, **14**), 7.40 - 7.35 (m, 2H, **15**), 7.34 - 7.29 (m, 1H, **16**), 6.92 - 6.82 (m, 4H, **9**+**10**), 5.01 (s, 2H, **12**), 4.08 (dd, *J* = 5.7, 4.1 Hz, 2H, **7**), 3.83 (dd, *J* = 5.6, 4.1 Hz, 2H, **6**), 3.76 - 3.71 (m, 2H, **5**), 3.71 - 3.63 (m, 4H, **3**+**4**), 3.58 - 3.53 (m, 2H, **2**), 3.38 (s, 3H, **1**). ^{13}C NMR (126 MHz, chloroform-*d*) δ 153.26, 153.21, 137.39, 128.68, 128.01, 127.62, 115.88, 115.72, 72.06, 70.93, 70.79, 70.77, 70.70, 69.98, 68.16, 59.19.

4-(2-(2-(2-methoxyethoxy)ethoxy)ethoxy)phenol, 4

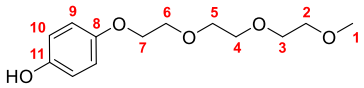

4

Neat sodium borohydride (477 mg, 12.60 mmol) was carefully added portionwise to a solution of **3** (1.46 g, 4.21 mmol) and $NiCl_2$•$6H_2O$ (1.50 g, 6.32 mmol) at 0 °C and the resulting dark solution warmed up to room temperature and stirred for 18 h. Removal of the solvent provided a dark crude residue which was suspended in ethyl acetate (100 mL) and washed with 0.1 M HCl (2×50 mL), $NaHCO_{3(aq)}$ (2×50 mL), and water (1×50 mL) and dried over anhydrous $MgSO_4$. Filtration and removal of the solvent provided the crude product which was purified by flash chromatography (hexane:ethyl acetate 50:50, R_f = 0.25) to obtain the product **4** as a colourless oil (788 mg, 73%). ^{1}H NMR (500 MHz, chloroform-*d*) δ 6.73 - 6.62 (m, 4H, **9**+**10**), 3.93 (dd, *J* = 5.8, 3.9 Hz, 2H, **7**), 3.77 - 3.70 (m, 2H, **6**), 3.69 - 3.57 (m, 6H, **3**+**4**+**5**), 3.53 - 3.48 (m, 2H, **2**), 3.30 (s, 3H, **1**). ^{13}C NMR (126 MHz, chloroform-*d*) δ 152.09, 150.37, 115.92, 115.51, 71.64, 70.46, 70.40, 70.23, 69.70, 67.79, 58.75.

***tert*-butyl (4-(((4-hydroxybenzyl)amino)methyl)phenyl)carbamate, 5**

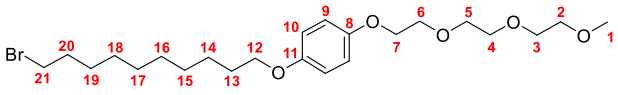

5

A solution of **4** (2.87 g, 11.2 mmol), 1,10-dibromodecane (16.8 g, 55.9 mmol), 18-crown-6 (148 mg, 0.56 mmol) and potassium carbonate (1.8 g, 13.4 mmol) in dry acetonitrile (150 mL) was stirred at 80 °C for 18 h under a dinitrogen atmosphere. The solution was cooled down to room temperature and the solvent removed under reduced pressure to provide a crude mixture which was dissolved in dichloromethane (100 mL), washed with water (3×100 mL) and dried over anhydrous $MgSO_4$. The crude compound was purified by flash chromatography (cyclohexane, R_f = 0.00 to remove excess 1,10-dibromodecane, then dichloromethane, R_f = 0.20, then dichloromethane:methanol 95:5, R_f = 0.60) to provide the product **5** as a colourless wax (4.92 g, 92%). ^{1}H NMR (500 MHz, chloroform-*d*)

δ 6.81 (q, *J* = 9.3 Hz, 4H, **9**+**10**), 4.06 (t, *J* = 4.9 Hz, 2H, **7**), 3.88 (t, *J* = 6.6 Hz, 2H, **12**), 3.81 (t, *J* = 4.9 Hz, 2H, **6**), 3.74 - 3.62 (m, 6H, **3**+**4**+**5**), 3.54 (m, 2H, **2**), 3.38 (m, 5H, **1**+**21**, 1.84 (p, *J* = 7.0 Hz, 2H, **13**), 1.73 (p, *J* = 6.8 Hz, 2H, **20**), 1.42 (d, *J* = 7.8 Hz, 4H, **19**+**14**), 1.29 (s, 8H, **15**+**16**+**17**+**18**). ^{13}C NMR (126 MHz, chloroform-*d*) δ 153.52, 152.91, 115.68, 115.40, 72.01, 70.86, 70.73, 70.63, 69.94, 68.62, 68.17, 59.09, 34.07, 32.88, 29.50, 29.43, 29.41, 29.40, 28.79, 28.22, 26.09.

tert-butyl (4-(((4-hydroxybenzyl)amino)methyl)phenyl)carbamate, 6

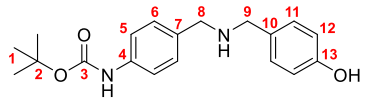

6

A solution of *tert*-butyl (4-formylphenyl)carbamate (5.6 g, 25.0 mmol) and 4-hydroxybenzylamine (5.5 g, 25.0 mmol) in absolute ethanol (200 mL) was concentrated at the rotary evaporator for three times, providing the intermediate imine as an orange solid. The latter was redissolved in methanol (100 mL) and sodium borohydride (1.9 g, 50 mmol) was carefully added portionwise, producing a visible effervescence. Once the effervescence stopped, the solution was left to react at room temperature for further 2 h, then the solvent removed under reduced pressure and the residue dissolved in ethyl acetate (100 mL) and washed with water (3×100 mL). The organic fraction was dried over anhydrous $MgSO_4$ and the solvent removed under reduced pressure to provide the product **6** as a colourless solid (10.4 g, 97%). The crude product was used without further purification. ^{1}H NMR (500 MHz, methanol-d_4) δ 7.41 (d, *J* = 8.3 Hz, 2H, **5**), 7.29 - 7.23 (m, 2H, **6**), 7.21 - 7.16 (m, 2H, **11**), 6.82 - 6.75 (m, 2H, **12**), 3.81 (s, 2H, **8**), 3.78 (s, 2H, **9**), 1.49 (s, 9H, **1**). ^{13}C NMR (126 MHz, methanol-d_4) δ 158.60, 155.12, 140.54, 131.64, 130.93, 130.76, 127.54, 119.80, 116.50, 80.90, 52.30, 52.16, 28.68.

tert-butyl (4-((_tert_-butoxycarbonyl)amino)benzyl)(4-hydroxybenzyl)carbamate, 7

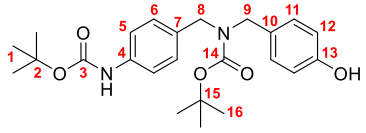

7

A THF solution (50 mL) of di-*tert*-butyl dicarbonate (5.9 g, 27.2 mmol) was added dropwise to a THF solution (150 mL) of **6** (8.9 g, 27.2 mmol) and the resulting mixture was stirred at room temperature for 16 h. The solvent was removed under reduced pressure to obtain a yellow solid which was purified by flash chromatography (dichloromethane:methanol 97:3, R_f = 0.50) to obtain the product **7** as a colourless solid (9.7 g, 98%). ^{1}H NMR (500 MHz, chloroform-*d*) δ 7.30 (s, 2H, **5**), 7.06 (m, 4H, **6**+**11**), 6.78 (m, 3H, **12**+NH), 4.42 - 4.11 (m, 4H, **8**+**9**), 1.51 (m, 18H, **1**+**16**). ^{13}C NMR (126 MHz, chloroform-*d*) δ 156.33, 155.77, 153.18, 146.88, 137.47, 132.60, 129.47, 128.84, 119.02, 115.61, 80.75, 80.53, 48.57, 48.13, 28.58, 28.43.

tert-butyl (4-((_tert_-butoxycarbonyl)amino)benzyl)(4-((8-(4-(2-(2-(2-methoxyethoxy)ethoxy)ethoxy) phenoxy)octyl)oxy)benzyl)carbamate, 8

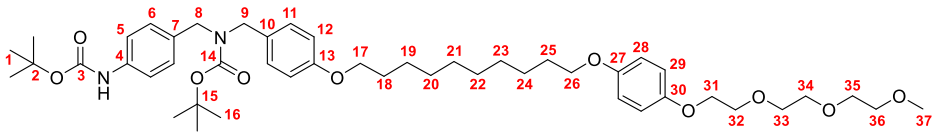

8

A solution of **7** (470 mg, 1.1 mmol), **5** (475 mg, 1.0 mmol), 18-crown-6 (148 mg, 0.56 mmol) and potassium carbonate (256 mg, 2.0 mmol) in dry acetonitrile (50 mL) was stirred at 80 °C for 18 h under a dinitrogen atmosphere. The solution was cooled down to room temperature and the solvent removed under reduced pressure to provide a crude mixture which was dissolved in dichloromethane (100 mL), washed with water (3×100 mL) and dried over anhydrous $MgSO_4$. The crude compound was purified by flash chromatography (ethyl acetate:hexane 40:60, R_f = 0.40) to provide the product **8** as a colourless wax (619 mg, 75%). ^{1}H NMR (500 MHz, chloroform-*d*) δ 7.31 (d, *J* = 8.1 Hz, 2H, **5**), 7.19 - 7.03 (m, 4H, **6**+**11**), 6.86 - 6.79 (m, 6H, **12**+**28**+**29**), 6.59 (s, 1H, NH), 4.37 - 4.15 (m, 4H, **8**+**9**), 4.07 (dd, *J* = 5.8, 4.1 Hz, 2H, **31**), 3.94 (t, *J* = 6.6 Hz, 2H, **17**), 3.89 (t, *J* = 6.6 Hz, 2H, **26**), 3.82 (dd, *J* = 5.7, 4.1 Hz, 2H, **32**), 3.74 - 3.63 (m, 6H, **33**+**34**+**35**), 3.57 - 3.52 (m, 2H, **36**), 3.37 (s, 3H, **37**), 1.80 - 1.71 (m, 4H, **18**+**25**), 1.50 (m, 22H, **1**+**16**+**19**+**24**), 1.34 (m, 8H, **20**+**21**+**22**+**23**). ^{13}C NMR (126 MHz, chloroform-*d*) δ 158.52, 156.05, 153.56, 152.94, 152.91, 137.57, 132.72, 129.88, 129.46, 128.26, 118.75, 115.72, 115.45, 114.58, 80.55, 80.01, 72.03, 70.89, 70.76, 70.66, 69.97, 68.69, 68.20, 68.11 (×2), 59.12, 48.48, 48.23, 29.59 (×2), 29.48 (×3), 29.39, 28.58, 28.45, 26.15 (×2).

4-(((4-((8-(4-(2-(2-(2-methoxyethoxy)ethoxy)ethoxy)phenoxy)octyl)oxy)benzyl)amino)methyl)aniline, 9

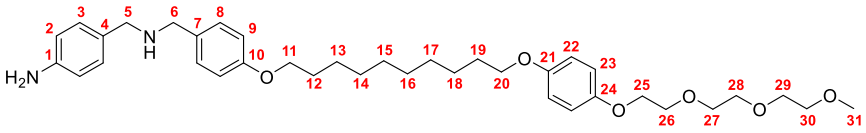

9

A solution of **8** (619 mg, 0.75 mmol) and HCl (37% in H_2O, 3.13 mL, 37.6 mmol) in methanol (50 mL) was stirred at 67 °C for 18 h. The resulting colourless precipitate was collected by filtration and washed with cold methanol, then suspended in water and reacted carefully with a saturated $NaHCO_{3(aq)}$ solution. The thus obtained suspension was extracted with dichloromethane (3×50 mL) and the combined organic phases washed with water (3×50 mL) and dried over anhydrous $MgSO_4$. Filtration and removal of the solvent under reduced pressure provided the product **9** as a colourless wax (439 mg, 94%). ^{1}H NMR (500 MHz, chloroform-*d*) δ 7.25 - 7.19 (m, 2H, **3**), 7.12 - 7.07 (m, 2H, **8**), 6.88 - 6.79 (m, 6H, **9**+**22**+**23**), 6.66 - 6.59 (m, 2H, **2**), 4.06 (dd, *J* = 5.8, 4.0 Hz, 2H, **25**), 3.93 (t, *J* = 6.6 Hz, 2H, **11**), 3.89 (t, *J* = 6.6 Hz, 2H, **20**), 3.82 (dd, *J* = 5.7, 4.1 Hz, 2H, **26**), 3.74 - 3.63 (m, 10H, **5**+**6**+**27**+**28**+**29**), 3.57 - 3.52 (m, 2H, **30**), 3.37 (s, 3H, **31**), 1.76 (m, 4H, **12**+**19**), 1.50 - 1.40 (m, 4H, **13**+**18**), 1.34 (d, *J* = 13.6 Hz, 8H, **14**+**15**+**16**+**17**). ^{13}C NMR (126 MHz, chloroform-*d*) δ 158.09, 153.42, 152.79, 145.41, 132.30, 130.10, 129.27, 129.24, 115.57, 115.30, 114.99, 114.32, 71.89, 70.74, 70.61, 70.51, 69.82, 68.52, 68.04, 67.94, 58.97, 52.58, 52.37, 29.46 (×2), 29.35 (×2), 29.34, 29.27, 26.01 (×2).

(*E*)-4-((4-(((4-((8-(4-(2-(2-(2-methoxyethoxy)ethoxy)ethoxy)phenoxy)octyl)oxy)benzyl)amino)methyl)phenyl)diazenyl)phenol, 10

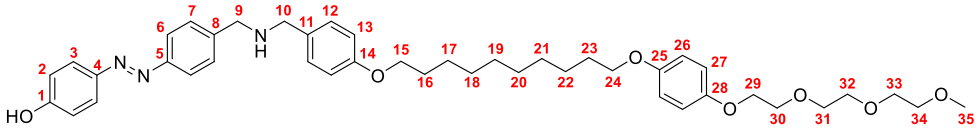

10

A solution of *tert*-butyl nitrite (754 µL, 6.34 mmol) in ethanol (5 mL) was added dropwise to a solution of **9** (439 mg, 0.70 mmol) and HPF_6 (60%$_{w/w}$ in H_2O, 175 µL, 1.1 mmol) in ethanol (50 mL) at 0 °C and the resulting mixture was left to warm up to room temperature and stirred for 2 h. The clear solution containing the diazonium salt was then added to a solution of phenol (398 mg, 4.23 mmol) and NaOH (2.0 M in H_2O, 3.5 mL, 7.0 mmol) in ethanol (15 mL) and the resulting red-orange solution was stirred at room temperature for 1 h. Removal of the solvent provided a deep orange residue which was dissolved in ethyl acetate (50 mL), washed with 1.0 M HCl (3×25 mL), $NaHCO_3$ (3×25 mL) and water (3×25 mL) and dried over anhydrous $MgSO_4$. Filtration and removal of the solvent under reduced pressure provided an orange crude product, which was purified by flash chromatography (ethyl acetate:hexane 50:50, R_f = 0.10, followed by ethyl acetate, R_f = 0.30) to provide the product **8** as an orange wax (325 mg, 63%). ^{1}H NMR (500 MHz, chloroform-*d*) δ 7.80 (m, 4H, **2**+**6**), 7.43 (d, *J* = 8.0 Hz, 2H, **7**), 7.25 (d, *J* = 8.2 Hz, 2H, **12**), 6.91 - 6.76 (m, 8H, **3**+**13**+**26**+**27**), 4.06 (t, *J* = 4.8 Hz, 2H, **29**), 3.93 (t, *J* = 6.5 Hz, 2H, **15**), 3.87 (d, *J* = 7.0 Hz, 4H, **9**+**24**), 3.84 - 3.78 (m, 4H, **10**+**30**), 3.76 - 3.63 (m, 6H, **31**+**32**+**33**), 3.56 (m, 2H, **34**), 3.38 (s, 3H, **35**), 1.76 (dp, *J* = 14.0, 6.8 Hz, 4H, **16**+**23**), 1.45 (m, 4H, **17**+**22**), 1.34 (m, 8H, **18**+**19**+**20**+**21**). ^{13}C NMR (126 MHz, chloroform-*d*) δ 160.15, 158.45, 153.42, 152.73, 152.04, 146.26, 141.35, 130.89, 124.90, 122.65, 116.10, 115.58, 115.34, 114.56, 71.84, 70.69, 70.57, 70.44, 69.83, 68.56, 67.99 (×2), 58.93, 52.45, 52.38, 29.68, 29.45 (×2), 29.35 (×2), 29.34, 29.24, 26.01 (×2).

***tert*-butyl (*E*)-(4-((4-hydroxyphenyl)diazenyl)benzyl)(4-((8-(4-(2-(2-(2-methoxyethoxy)ethoxy)ethoxy) phenoxy)octyl)oxy)benzyl)carbamate, 11**

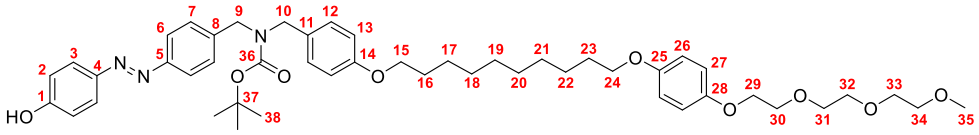

11

A THF solution (5 mL) of di-*tert*-butyl dicarbonate (98 mg, 0.45 mmol) was added dropwise to a THF solution (20 mL) of **10** (325 mg, 0.45 mmol) and the resulting mixture was stirred at room temperature for 16 h. The solvent was removed under reduced pressure to obtain the product **11** as an orange solid, which was which was used without further purifications (368 g, >99%). ^{1}H NMR (500 MHz, chloroform-*d*) δ 8.35 (s, 1H, OH), 7.84 (d, *J* = 8.1 Hz, 4H, **2**+**6**), 7.31 (m, 2H, **7**), 7.15 (m, 2H, **12**), 6.95 (d, *J* = 8.2 Hz, 2H, **3**), 6.86 (d, *J* = 8.1 Hz, 2H, **13**), 6.84 - 6.78 (m, 4H, **26**+**27**), 4.41 (m, 4H, **9**+**10**), 4.03 (t, *J* = 4.8 Hz, 2H, **29**), 3.92 (m, 2H, **15**), 3.86 (t, *J* = 6.5 Hz, 2H, **24**), 3.80 (t, *J* = 4.8 Hz, 2H, **30**), 3.73 - 3.62 (m, 6H, **31**+**32**+**33**), 3.58 - 3.51 (m, 2H, **34**), 3.36 (s, 3H, **35**), 1.75 (m, 4H, **16**+**23**), 1.53 (m, 9H, **38**), 1.44 (m, 4H, **17**+**22**), 1.34 (m, 8H, **18**+**19**+**20**+**21**). ^{13}C NMR (126 MHz, chloroform-*d*) δ 159.88, 158.43, 156.04, 153.32, 152.62, 151.94, 146.32, 140.21, 129.24 (m, ×2), 127.77 (m), 124.81, 122.60, 115.85, 115.47, 115.23, 114.49, 80.40, 71.72, 70.57, 70.51, 70.44, 70.30, 69.71, 68.41, 67.86 (×2), 58.78 (×2), 49.00, 48.59, 29.36 (×2), 29.25 (×2), 29.14 (×2), 28.36, 25.92 (×2).

tert-butyl (E)-(4-((8-(4-(2-(2-(2-methoxyethoxy)ethoxy)ethoxy)phenoxy)octyl)oxy)benzyl)(4-((4-(2-(2-(2-methoxyethoxy)ethoxy)ethoxy)phenyl)diazenyl)benzyl)carbamate, 12

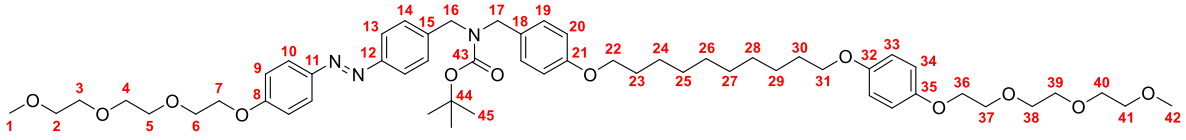

12

A solution of **11** (368 mg, 0.45 mmol), **1** (170 mg, 0.53 mmol), 18-crown-6 (74 mg, 0.28 mmol) and potassium carbonate (128 mg, 0.94 mmol) in dry acetonitrile (25 mL) was stirred at 80 °C for 18 h under a dinitrogen atmosphere. The solution was cooled down to room temperature and the solvent removed under reduced pressure to provide a crude mixture which was dissolved in dichloromethane (100 mL), washed with water (3×100 mL) and dried over anhydrous $MgSO_4$. Filtration and removal of the solvent under reduced pressure provided the crude product that was purified by flash chromatography (ethyl acetate:hexane 75:25, R_f = 0.35) to provide the product **12** as an orange wax (351 mg, 81%). ^{1}H NMR (500 MHz, methylene chloride-d_2) δ 7.95 - 7.90 (m, 2H, **13**), 7.87 - 7.82 (m, 2H, **9**), 7.34 (m, 2H, **14**), 7.21 - 7.09 (m, 2H, **19**), 7.09 - 7.03 (m, 2H, **10**), 6.88 - 6.79 (m, 6H, **20**+**33**+**34**), 4.51 - 4.28 (m, 4H, **16**+**17**), 4.24 - 4.18 (m, 2H, **7**), 4.07 - 4.02 (m, 2H, **36**), 3.95 (t, J = 6.6 Hz, 2H, **22**), 3.92 - 3.84 (m, 4H, **6**+**31**), 3.80 - 3.76 (m, 2H, **37**), 3.71 - 3.58 (m, 12H, **3**+**4**+**5**+**38**+**39**+**40**), 3.54 - 3.48 (m, 4H, **2**+**41**), 3.34 (d, J = 2.5 Hz, 6H, **1**+**42**), 1.76 (ddt, J = 14.6, 12.4, 6.2 Hz, 4H, **23**+**30**), 1.57 - 1.41 (m, 13H, **24**+**29**+**45**), 1.36 (d, J = 5.4 Hz, 8H, **25**+**26**+**27**+**28**). ^{13}C NMR (126 MHz, methylene chloride-d_2) δ 161.80, 158.96, 156.15, 153.94, 153.22, 152.33, 147.45, 141.54 (m), 130.25, 129.56 (m), 128.43 (m), 125.03, 123.01, 115.80, 115.67, 115.20, 114.82, 80.27, 72.32 (×2), 71.24, 71.13, 70.93 (×2), 70.86, 70.83, 70.19, 69.93, 68.95, 68.47 (×2), 68.29, 59.03 (×2), 49.34, 48.99, 29.92 (×2), 29.81 (×2), 29.79, 29.70, 28.57, 26.44, 26.43.

(_E_)-_N_-(4-((8-(4-(2-(2-(2-methoxyethoxy)ethoxy)ethoxy)phenoxy)octyl)oxy)benzyl)-1-(4-((4-(2-(2-(2-methoxyethoxy)ethoxy)ethoxy)phenyl)diazenyl)phenyl)methanaminium hexafluorophosphate, C10

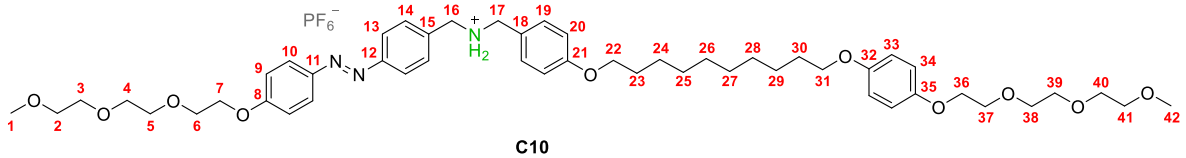

C10

An aqueous solution of hexafluorophosphoric acid (300 uL, 1.81 mmol) was added to a solution of **12** (351 mg, 0.36 mmol) in THF (10 mL) and the resulting mixture was stirred at room temperature for 18 h. The solvent was removed under reduced pressure and the dark residue dissolved in dichloromethane (100 mL) and washed with a saturated aqueous solution of KPF_6 containing a few drops of HPF_6 (3×20 mL). The organic fraction was dried over $MgSO_4$ and the solvent removed under reduced pressure to provide the crude product, which was purified by size exclusion chromatography (SX-1, dichloromethane) to obtain the product **C10** as an orange wax (367 mg, >99%). ^{1}H NMR (500 MHz, methylene chloride-d_2) δ 7.87 (dd, J = 8.4, 4.3 Hz, 6H, NH_2+**9**+**13**), 7.54 (d, J = 8.0 Hz, 2H, **14**), 7.36 (d, J = 8.2 Hz, 2H, **19**), 6.98 (d, J = 8.6 Hz, 2H, **10**), 6.93 (d, J = 8.2 Hz, 2H, **20**), 6.82 (d, J = 1.9 Hz, 4H, **33**+**34**), 4.24 (m, 4H, **7**+**36**), 4.15 (t, J = 4.5 Hz, 2H, **6**), 4.03 (t, J = 4.4 Hz, 2H, **37**), 3.95 (t, J = 6.6 Hz, 2H, **22**), 3.89 (t, J = 6.5 Hz, 2H, **31**), 3.83 (t, J = 4.5 Hz, 2H, **5**),

3.74 (t, *J* = 4.3 Hz, 2H, **38**), 3.64 (dd, *J* = 5.8, 3.2 Hz, 2H, **4**), 3.57 – 3.37 (m, 14H, **2**+**3**+**16**+**17**+**39**+**40**+**41**), 3.32 (d, *J* = 1.8 Hz, 6H, **1**+**42**), 1.75 (dp, *J* = 14.3, 6.8 Hz, 4H, **23**+**30**), 1.43 (d, *J* = 7.5 Hz, 4H, **24**+**29**), 1.34 (d, *J* = 12.9 Hz, 8H, **25**+**26**+**27**+**28**). ^{13}C NMR (126 MHz, methylene chloride-d_2) δ 161.92, 160.89, 154.35, 153.56, 152.70, 147.32, 132.64, 131.98, 131.01, 125.43, 123.49, 122.13, 115.94, 115.93, 115.39, 115.21, 72.17, 72.10, 71.36, 71.12, 70.83, 70.73, 70.61, 70.52, 70.50, 70.16, 68.91, 68.68, 68.61, 68.40, 59.25, 59.17, 52.31, 51.77, 29.74 (×2), 29.63, 29.59 (×2), 29.46, 26.32, 26.27. ^{19}F NMR (470 MHz, methylene chloride-d_2) δ –71.23 (d, *J* = 713.6 Hz, PF_6). HRMS-ESI (*m*/*z*): calcd for [$C_{50}H_{72}N_3O_{10}$], 874.5218; found 874.5218 [**M**]$^+$.

tert-butyl (4-((12-bromododecyl)oxy)benzyl)(4-((tert-butoxycarbonyl)amino)benzyl)carbamate, 13

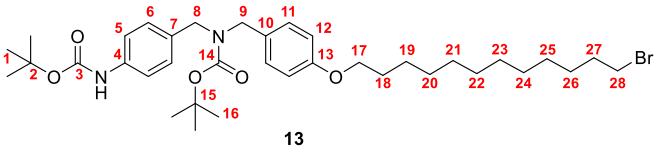

13

A solution of **7** (2.14 g, 5.00 mmol), 1,12-dibromododecane (8.20 g, 25.00 mmol), 18-crown-6 (528 mg, 2.50 mmol) and potassium carbonate (829 mg, 6.00 mmol) in dry acetonitrile (150 mL) was stirred at 80 °C for 18 h under a dinitrogen atmosphere. The solution was cooled down to room temperature and the solvent removed under reduced pressure to provide a crude mixture which was dissolved in dichloromethane (100 mL), washed with water (3×100 mL) and dried over anhydrous $MgSO_4$. Filtration and removal of the solvent under reduced pressure provided the crude product that was purified by flash chromatography (dichloromethane, R_f = 0.15) to provide the product **13** as an off-white wax (2.88 g, >99%). ^{1}H NMR (500 MHz, chloroform-*d*) δ 7.31 (d, *J* = 8.1 Hz, 2H, **5**), 7.12 (m, 4H, **6**+**11**), 6.87 - 6.82 (m, 2H, **12**), 6.48 (s, 1H, NH), 4.28 (m, 4H, **8**+**9**), 3.94 (t, *J* = 6.6 Hz, 2H, **17**), 3.41 (t, *J* = 6.9 Hz, 2H, **28**), 1.85 (p, *J* = 7.0 Hz, 2H, **27**), 1.77 (p, *J* = 6.8 Hz, 2H, **18**), 1.54 - 1.38 (m, 22H, **1**+**16**+**19**+**26**), 1.30 (d, *J* = 14.7 Hz, 12H, **20**+**21**+**22**+**23**+**24**+**25**). ^{13}C NMR (126 MHz, chloroform-*d*) δ 158.56, 156.09, 152.91, 137.54, 132.83, 129.93, 129.50 (m), 128.32 (m), 118.78, 114.62, 80.07, 68.18, 48.49, 48.06, 34.19, 32.98, 29.69, 29.67, 29.65, 29.56, 29.53, 29.44, 28.90, 28.62, 28.48, 28.31, 26.20.

tert-butyl (4-((tert-butoxycarbonyl)amino)benzyl)(4-((12-(4-(2-(2-(2-methoxyethoxy)ethoxy)ethoxy) phenoxy) dodecyl)oxy)benzyl)carbamate, 14

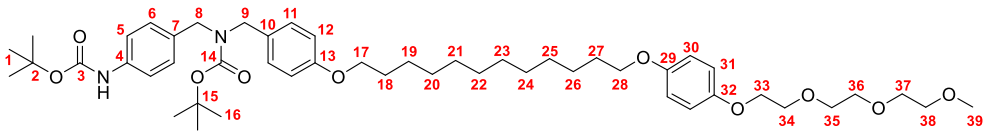

14

A solution of **13** (2.42 g, 4.19 mmol), **4** (1.41 g, 5.50 mmol), 18-crown-6 (605 mg, 2.29 mmol) and potassium carbonate (950 mg, 6.87 mmol) in dry acetonitrile (150 mL) was stirred at 80 °C for 18 h under a dinitrogen atmosphere. The solution was cooled down to room temperature and the solvent removed under reduced pressure to provide a crude mixture which was dissolved in dichloromethane (100 mL), washed with water (3×100 mL) and dried over anhydrous $MgSO_4$. Filtration and removal of the solvent under reduced pressure provided the crude product that was purified by flash chromatography (hexane:ethyl acetate 80:20 to elute the starting material at an R_f = 0.60, then hexane:ethyl acetate 60:40, to elute the product at an R_f = 0.45) to provide the product **14** as a pale yellow oil (2.87 g, 80%). ^{1}H NMR (500 MHz, chloroform-*d*) δ 7.31 (d, *J* = 8.1 Hz, 2H, **5**), 7.19 - 7.04

(m, 4H, **6**+**11**), 6.87 - 6.77 (m, 6H, **12**+**30**+**31**), 6.59 (s, 1H, NH), 4.28 (d, *J* = 42.0 Hz, 4H, **8**+**9**), 4.07 (dd, *J* = 5.7, 4.0 Hz, 2H, **33**), 3.94 (t, *J* = 6.6 Hz, 2H, **17**), 3.89 (t, *J* = 6.6 Hz, 2H, **28**), 3.82 (dd, *J* = 5.7, 4.1 Hz, 2H, **34**), 3.75 - 3.70 (m, 2H, **35**), 3.70 - 3.63 (m, 4H, **36**+**37**), 3.55 (dd, *J* = 5.8, 3.6 Hz, 2H, **38**), 3.37 (s, 3H, **39**), 1.75 (tq, *J* = 13.2, 6.8 Hz, 4H, **18**+**27**), 1.53 - 1.39 (m, 22H, **1**+**16**+**19**+**26**), 1.39 - 1.24 (m, 12H, **20**+**21**+**22**+**23**+**24**+**25**). ^{13}C NMR (126 MHz, chloroform-*d*) δ 158.52, 156.05, 153.57, 152.93, 152.91, 137.57, 132.72, 129.87, 129.46 (m), 128.27 (m), 118.75, 115.71, 115.45, 114.58 (×2), 80.02, 72.04, 70.89, 70.76, 70.66, 69.98, 68.71, 68.20, 68.13, 59.12, 48.48, 48.23, 29.67 (×4), 29.51 (×2), 29.49, 29.40, 28.59, 28.45, 26.16 (×2).

4-(((4-((12-(4-(2-(2-(2-methoxyethoxy)ethoxy)ethoxy)phenoxy)dodecyl)oxy)benzyl)amino)methyl) aniline, 15

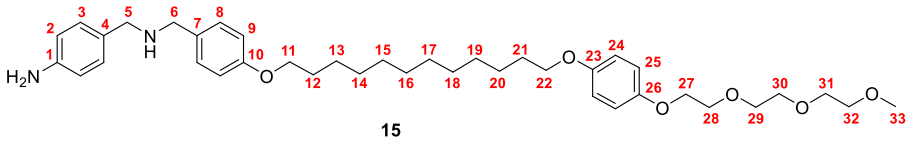

15

A solution of **14** (2.87 g, 3.37 mmol) and HCl (37% in H_2O, 8.90 mL, 108 mmol) in methanol (150 mL) was stirred at 67 °C for 18 h. The resulting colourless precipitate was collected by filtration and washed with cold methanol, then suspended in water and reacted carefully with a saturated $NaHCO_{3(aq)}$ solution. The thus obtained suspension was extracted with dichloromethane (3×50 mL) and the combined organic phases washed with water (3×50 mL) and dried over anhydrous $MgSO_4$. Filtration and removal of the solvent under reduced pressure provided the product **15** as a colourless solid (1.82 g, 83%). ^{1}H NMR (500 MHz, chloroform-*d*) δ 7.22 (d, *J* = 8.2 Hz, 2H, **3**), 7.11 (d, *J* = 8.0 Hz, 2H, **8**), 6.87 - 6.78 (m, 6H, **9**+**24**+**25**), 6.65 (d, *J* = 8.0 Hz, 2H, **2**), 4.07 (t, *J* = 4.9 Hz, 2H, **27**), 3.94 (t, *J* = 6.6 Hz, 2H, **11**), 3.89 (t, *J* = 6.6 Hz, 2H, **22**), 3.83 (t, *J* = 4.9 Hz, 2H, **28**), 3.75 - 3.64 (m, 10H, **5**+**6**+**29**+**30**+**31**), 3.55 (dd, *J* = 5.8, 3.7 Hz, 2H, **32**), 3.38 (s, 3H, **33**), 1.82 - 1.71 (m, 4H, **12**+**21**), 1.49 - 1.39 (m, 4H, **13**+**20**), 1.39 - 1.24 (m, 12H, **14**+**15**+**16**+**17**+**18**+**19**). ^{13}C NMR (126 MHz, chloroform-*d*) δ 158.23, 153.58, 152.93, 145.39, 132.51, 130.51, 129.38 (×2), 115.72, 115.45, 115.18, 114.46, 72.04, 70.89, 70.76, 70.66, 69.98, 68.71, 68.20, 68.12, 59.13, 52.74, 52.55, 29.66 (×2), 29.51 (×2), 29.49 (×2), 29.41 (×2), 26.16 (×2).

(*E*)-4-((4-(((4-((12-(4-(2-(2-(2-methoxyethoxy)ethoxy)ethoxy)phenoxy)dodecyl)oxy)benzyl)amino) methyl)phenyl)diazenyl)phenol, 16

16

A solution of *tert*-butyl nitrite (2.88 mL, 24.21 mmol) in ethanol (25 mL) was added dropwise to a solution of **15** (1.75 g, 2.69 mmol) and HPF_6 (60%$_{w/w}$ in H_2O, 667 µL, 4.03 mmol) in ethanol (100 mL) at 0 °C and the resulting mixture was left to warm up to room temperature and stirred for 2 h. The clear solution containing the diazonium salt was then added to a solution of phenol (1.52 g, 16.14 mmol) and NaOH (2.0 M in H_2O, 13.5 mL, 26.9 mmol) in ethanol (50 mL) and the resulting red-orange solution was stirred at room temperature for 1 h. Removal of the solvent provided a deep orange residue which was dissolved in ethyl acetate (100 mL), washed with 1.0 M HCl (3×50 mL), $NaHCO_3$ (3×50 mL) and water (3×50 mL) and dried over anhydrous $MgSO_4$. Filtration and removal of the solvent under reduced pressure provided an orange crude product, which was purified by flash

chromatography (ethyl acetate:cyclohexane 50:50, R_f = 0.10, followed by ethyl acetate, R_f = 0.30) to provide the product **16** as an orange wax (1.42 g, 70%). ^{1}H NMR (500 MHz, chloroform-*d*) δ 7.76 (t, *J* = 7.6 Hz, 4H, **2**+**6**), 7.42 (d, *J* = 8.0 Hz, 2H, **7**), 7.27 (d, *J* = 7.7 Hz, 2H, **12**), 6.93 - 6.70 (m, 8H, **3**+**13**+**28**+**29**), 4.06 (t, *J* = 4.9 Hz, 2H, **31**), 3.98 - 3.77 (m, 10H, **9**+**10**+**15**+**26**+**32**), 3.77 - 3.61 (m, 6H, **33**+**34**+**35**), 3.56 (t, *J* = 4.7 Hz, 2H, **36**), 3.38 (s, 3H, **37**), 1.75 (dt, *J* = 13.8, 6.8 Hz, 4H, **16**+**25**), 1.50 - 1.17 (m, 16H, **17**+**18**+**19**+**20**+**21**+**22**+**23**+**24**). ^{13}C NMR (126 MHz, chloroform-*d*) δ 159.99, 158.67, 153.51, 152.82, 152.20, 146.41, 140.74, 130.34, 129.86, 129.25, 124.97, 122.79, 116.16, 115.66, 115.41, 114.69, 71.96, 70.82, 70.70, 70.59, 69.95, 68.68, 68.11, 68.09, 59.09, 52.38, 29.64 (×4), 29.50, 29.46, 29.33, 26.13, 26.11.

tert-butyl (E)-(4-((4-hydroxyphenyl)diazenyl)benzyl)(4-((12-(4-(2-(2-(2-methoxyethoxy)ethoxy)ethoxy) phenoxy)dodecyl)oxy)benzyl)carbamate, 17

17

A THF solution (10 mL) of di-*tert*-butyl dicarbonate (410 mg, 1.88 mmol) was added dropwise to a THF solution (50 mL) of **16** (1.42 g, 1.88 mmol) and the resulting mixture was stirred at room temperature for 16 h. The solvent was removed under reduced pressure to obtain a crude orange solid, which was purified by flash chromatography (ethyl acetate:hexane 50:50, R_f = 0.30) to provide the product **17** as an orange solid (1.32 g, 82%). ^{1}H NMR (500 MHz, chloroform-*d*) δ 7.81 (d, *J* = 7.6 Hz, 4H, **2**+**6**), 7.29 (bs, 2H, **7**), 7.21 - 7.05 (m, 2H, **12**), 6.98 - 6.76 (m, 8H, **3**+**13**+**28**+**29**), 4.39 (dd, *J* = 42.9, 24.1 Hz, 4H, **9**+**10**), 4.06 (t, *J* = 4.9 Hz, 2H, **31**), 3.95 (t, *J* = 6.5 Hz, 2H, **15**), 3.88 (t, *J* = 6.6 Hz, 2H, **26**), 3.82 (t, *J* = 4.9 Hz, 2H, **32**), 3.73 (dd, *J* = 6.2, 3.7 Hz, 2H, **33**), 3.71 - 3.64 (m, 4H, **34**+**35**), 3.56 (dd, *J* = 5.6, 3.6 Hz, 2H, **36**), 3.38 (s, 3H, **37**), 1.76 (dp, *J* = 14.6, 6.9 Hz, 4H, **16**+**25**), 1.58 - 1.39 (m, 13H, **17**+**24**+**40**), 1.39 - 1.22 (m, 12H, **18**+**19**+**20**+**21**+**22**+**23**). ^{13}C NMR (126 MHz, chloroform-*d*) δ 159.24, 158.67, 156.26, 153.60, 152.92, 152.16, 146.95, 140.41, 129.58, 129.00 (m), 128.50 (m), 125.03, 122.84, 116.00, 115.75, 115.50, 114.72, 80.60, 72.04, 70.89, 70.77, 70.65, 70.02, 68.78, 68.21, 68.19, 59.14, 49.10, 48.91, 29.69 (×2), 29.67 (×2), 29.54, 29.52, 29.49, 29.38, 28.62, 26.19, 26.16.

tert-butyl (*E*)-(4-((12-(4-(2-(2-(2-methoxyethoxy)ethoxy)ethoxy)phenoxy)dodecyl)oxy)benzyl)(4-((4-(2-(2-(2-methoxyethoxy)ethoxy)ethoxy)phenyl)diazenyl)benzyl)carbamate, 18

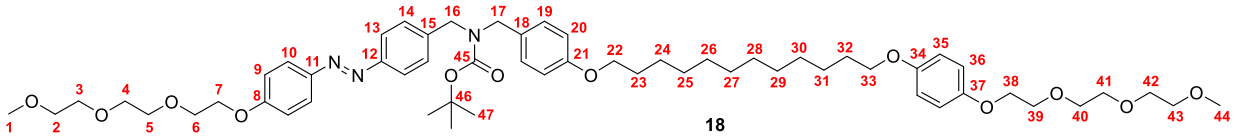

18

A solution of **17** (540 mg, 0.63 mmol), **1** (241 mg, 0.76 mmol), 18-crown-6 (83 mg, 0.30 mmol) and potassium carbonate (131 mg, 0.95 mmol) in dry acetonitrile (50 mL) was stirred at 80 °C for 18 h under a dinitrogen atmosphere. The solution was cooled down to room temperature and the solvent removed under reduced pressure to provide a crude mixture which was dissolved in dichloromethane (50 mL), washed with water (3×50 mL) and dried over anhydrous $MgSO_4$. Filtration and removal of the solvent under reduced pressure provided the crude product that was purified by flash chromatography (ethyl acetate:hexane 75:25, R_f = 0.35) and size-exclusion chromatography (Biobeads SX-1, dichloromethane) to provide the product **18** as an orange wax (501 mg, 80%). ^{1}H NMR (500 MHz, chloroform-*d*) δ 7.90 (d, *J* = 8.6 Hz, 2H, **13**), 7.83 (d, *J* = 8.0 Hz, 2H, **9**), 7.31 (d, *J*

= 22.3 Hz, 2H, **14**), 7.13 (d, *J* = 22.3 Hz, 2H, **19**), 7.03 (d, *J* = 8.6 Hz, 2H, **10**), 6.91 - 6.74 (m, 6H, **20**+**35**+**36**), 4.37 (dd, *J* = 50.0, 30.7 Hz, 4H, **16**+**17**), 4.21 (t, *J* = 4.8 Hz, 2H, **7**), 4.07 (t, *J* = 4.9 Hz, 2H, **38**), 3.94 (t, *J* = 6.5 Hz, 2H, **22**), 3.92 - 3.86 (m, 4H, **6**+**33**), 3.82 (t, *J* = 4.9 Hz, 2H, **39**), 3.78 - 3.60 (m, 12H, **3**+**4**+**5**+**40**+**41**+**42**), 3.55 (m, 4H, **2**+**43**), 3.37 (d, *J* = 3.2 Hz, 6H, **1**+**44**), 1.76 (dp, *J* = 14.3, 6.8 Hz, 4H, **23**+**32**), 1.58 - 1.39 (m, 13H, **24**+**31**+**47**), 1.39 + 1.24 (m, 12H, **25**+**26**+**27**+**28**+**29**+**30**). ^{13}C NMR (126 MHz, chloroform-*d*) ^{13}C NMR (126 MHz, cdcl$_3$) δ 161.38, 158.62, 156.05, 153.57, 152.93, 152.11, 147.20, 140.91, 129.70, 129.54, 128.70, 124.77 (×2), 122.82, 115.72, 115.44, 114.96, 114.64, 114.60, 114.45, 80.25, 72.04 (×2), 71.00, 70.89, 70.78, 70.76, 70.69, 70.66, 69.97, 69.74, 68.71, 68.20, 68.15, 67.84, 59.14, 59.13, 48.90, 48.57, 29.67 (×2), 29.51 (×2), 29.49 (×2), 29.39 (×2), 28.57, 26.16 (×2).

(*E*)-*N*-(4-((12-(4-(2-(2-(2-methoxyethoxy)ethoxy)ethoxy)phenoxy)dodecyl)oxy)benzyl)-1-(4-((4-(2-(2-(2-methoxyethoxy)ethoxy)ethoxy)phenyl)diazenyl)phenyl)methanaminium hexafluorophosphate, C12

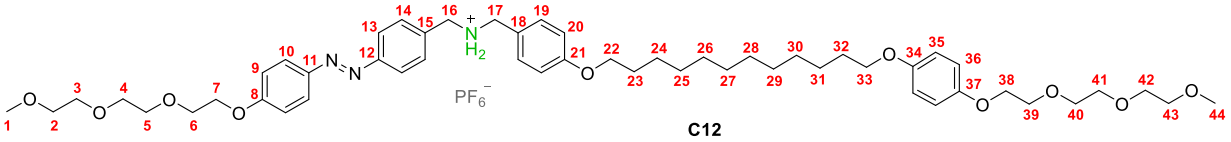

An aqueous solution of hexafluorophosphoric acid (230 µL, 1.39 mmol) was added to a solution of **18** (277 mg, 0.28 mmol) in THF (10 mL) and the resulting mixture was stirred at room temperature for 18 h. The solvent was removed under reduced pressure and the dark residue dissolved in dichloromethane (25 mL) and washed with a saturated aqueous solution of KPF_6 containing a few drops of HPF_6 (3×25 mL). The organic fraction was dried over $MgSO_4$ and the solvent removed under reduced pressure to provide the crude product, which was purified by size exclusion chromatography (SX-1, dichloromethane) to obtain the product **C12** as an orange wax (288 mg, 99%). ^{1}H NMR (500 MHz, methylene chloride-*d*$_2$:methanol-*d*$_4$ 99:1) δ 8.03 (s, 2H, NH_2), 7.91 - 7.84 (m, 4H, **9**+**13**), 7.54 (d, *J* = 8.0 Hz, 2H, **14**), 7.34 (d, *J* = 8.2 Hz, 2H, **19**), 7.04 - 6.96 (m, 2H, **10**), 6.93 (d, *J* = 8.4 Hz, 2H, **20**), 6.85 - 6.75 (m, 4H, **35**+**36**), 4.27 - 4.12 (m, 6H, **7**+**16**+**17**), 4.02 (dd, *J* = 5.5, 3.5 Hz, 2H, **38**), 3.95 (t, *J* = 6.6 Hz, 2H, **22**), 3.89 (t, *J* = 6.5 Hz, 2H, **33**), 3.84 (dd, *J* = 5.5, 3.4 Hz, 2H, **6**), 3.77 - 3.72 (m, 2H, **39**), 3.66 (dd, *J* = 5.8, 3.2 Hz, 2H, **5**), 3.60 – 3.43 (m, 14H, **2**+**3**+**4**+**40**+**41**+**42**+**43**), 3.32 (d, *J* = 4.0 Hz, 6H, **1**+**44**), 1.74 (tt, *J* = 14.3, 6.8 Hz, 4H, **23**+**32**), 1.43 (qd, *J* = 9.0, 7.6, 2.9 Hz, 4H, **24**+**31**), 1.38 - 1.23 (m, 12H, **25**+**26**+**27**+**28**+**29**+**30**). ^{13}C NMR (126 MHz, methylene chloride-*d*$_2$:methanol-*d*$_4$ 99:1) δ 162.02, 160.91, 154.30, 153.64, 152.77, 147.32, 132.44, 131.96, 131.03, 125.42, 123.56, 121.90, 115.93, 115.89, 115.48, 115.23, 72.20, 72.13, 71.31, 71.10, 70.85, 70.77, 70.66, 70.56, 70.46, 70.08, 68.95, 68.63 (×2), 68.37, 59.20, 59.12, 51.83, 51.28, 29.81, 29.80, 29.74 (×2), 29.64, 29.61, 29.58, 29.48, 26.31, 26.27. ^{19}F NMR (470 MHz, chloroform-*d*) δ –71.61 (d, *J* = 712.5 Hz, PF_6). HRMS-ESI (*m*/*z*): calcd for [$C_{52}H_{76}N_3O_{10}$], 902.5530; found 902.5531 [**M**]$^+$.

***tert*-butyl (4-((tert-butoxycarbonyl)amino)benzyl)(4-((12-(4-methoxyphenoxy)dodecyl)oxy)benzyl) carbamate, 19**

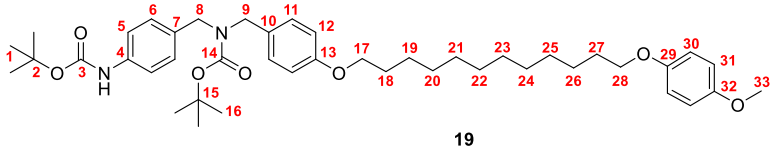

A solution of **13** (2.14 g, 3.70 mmol), 4-methoxyphenol (598 mg, 4.81 mmol), 18-crown-6 (587 mg, 2.20 mmol) and potassium carbonate (819 mg, 5.90 mmol) in dry acetonitrile (100 mL) was stirred

at 80 °C for 18 h under a dinitrogen atmosphere. The solution was cooled down to room temperature and the solvent removed under reduced pressure to provide a crude mixture which was dissolved in dichloromethane (100 mL), washed with water (3×100 mL) and dried over anhydrous $MgSO_4$. Filtration and removal of the solvent under reduced pressure provided the crude product that was purified by flash chromatography (hexane:ethyl acetate 80:20, R_f = 0.80) to provide the product **19** as a pale yellow oil (1.89 g, 71%). ^{1}H NMR (500 MHz, chloroform-*d*) δ 7.34 (d, *J* = 8.0 Hz, 2H, **5**), 7.14 (m, 4H, **6**+**11**), 6.88 - 6.80 (m, 6H, **12**+**30**+**31**), 6.78 (s, 1H, NH), 4.44 - 4.16 (m, 4H, **8**+**9**), 3.95 (t, *J* = 6.6 Hz, 2H, **17**), 3.91 (t, *J* = 6.6 Hz, 2H, **28**), 3.76 (s, 3H, **33**), 1.77 (ddd, *J* = 14.7, 12.1, 7.1 Hz, 4H, **18**+**27**), 1.60 - 1.41 (m, 22H, **1**+**16**+**19**+**26**), 1.41 - 1.23 (m, 12H, **20**+**21**+**22**+**23**+**24**+**25**). ^{13}C NMR (126 MHz, chloroform-*d*) δ 158.47, 155.99, 153.69, 153.34, 152.92, 137.62, 132.57, 129.81, 129.40 (m), 128.17 (m), 118.72, 115.46, 114.65, 114.53, 80.39, 79.94, 68.67, 68.05, 55.72, 48.43, 48.20, 29.61 (×2), 29.45 (×2), 29.43 (×2), 29.34 (×2), 28.52, 28.39, 26.10 (×2).

4-(((4-((12-(4-methoxyphenoxy)dodecyl)oxy)benzyl)amino)methyl)aniline, 20

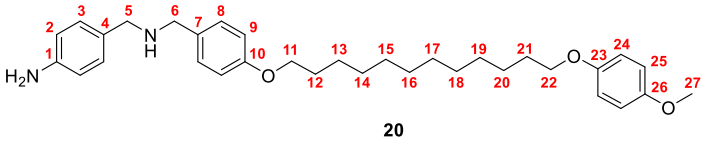

20

A solution of **19** (1.62 g, 2.60 mmol) and HCl (37% in H_2O, 7.0 mL, 83 mmol) in methanol (100 mL) was stirred at 67 °C for 18 h. The resulting colourless precipitate was collected by filtration and washed with cold methanol, then suspended in water and reacted carefully with a saturated $NaHCO_{3(aq)}$ solution. The thus obtained suspension was extracted with dichloromethane (3×50 mL) and the combined organic phases washed with water (3×50 mL) and dried over anhydrous $MgSO_4$. Filtration and removal of the solvent under reduced pressure provided a crude solid, which was purified by flash chromatography (methylene chloride:methanol 95:5, R_f = 0.20) to provide the product **20** as a colourless solid (938 mg, 70%). ^{1}H NMR (400 MHz, methylene chloride-*d_2*:methanol-*d_4* 99:1) δ 7.22 (d, *J* = 8.4 Hz, 2H, **3**), 7.09 (d, *J* = 8.3 Hz, 2H, **8**), 6.85 (d, *J* = 8.3 Hz, 2H, **9**), 6.81 (s, 4H, **24**+**25**), 6.66 (d, *J* = 8.4 Hz, 2H, **2**), 3.93 (t, *J* = 6.6 Hz, 2H, **11**), 3.88 (t, *J* = 6.6 Hz, 2H, **22**), 3.73 (s, 4H, **27**), 3.71 (s, 2H, **5**), 3.66 (s, 2H, **6**) 1.74 (dt, *J* = 10.3, 7.3 Hz, 4H, **12**+**21**), 1.52 - 1.22 (m, 16H, **13**+**14**+**15**+**16**+**17**+**18**+**19**+**20**). ^{13}C NMR (126 MHz, methylene chloride-*d_2*:methanol-*d_4* 99:1) δ 159.41, 154.07, 153.71, 146.99, 130.62, 130.52, 128.30, 125.86, 115.70, 115.38, 114.94, 114.90, 69.06, 68.50, 55.98, 51.46, 51.16, 29.94 (×2), 29.78 (×2), 29.75 (×2), 29.62 (×2), 26.39, 26.37.

(*E*)-4-((4-(((4-((12-(4-methoxyphenoxy)dodecyl)oxy)benzyl)amino)methyl)phenyl)diazenyl)phenol, 21

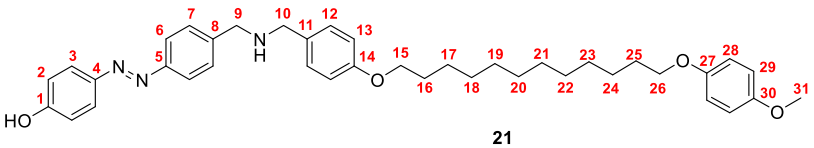

21

A solution of *tert*-butyl nitrite (1.05 mL, 8.80 mmol) in ethanol (25 mL) was added dropwise to a solution of **20** (507 mg, 0.97 mmol) and HPF_6 (60%$_{w/w}$ in H_2O, 283 µL, 1.96 mmol) in ethanol (100 mL) at 0 °C and the resulting mixture was left to warm up to room temperature and stirred for 2 h. The clear solution containing the diazonium salt was then added to a solution of phenol (552 mg, 5.87 mmol) and NaOH (2.0 M in H_2O, 3.90 mL, 7.82 mmol) in ethanol (50 mL) and the resulting red-orange solution was stirred at room temperature for 1 h. Removal of the solvent provided a deep orange residue which was dissolved in ethyl acetate (100 mL), washed with 1.0 M HCl (3×50 mL), $NaHCO_3$ (3×50 mL) and water (3×50 mL) and dried over anhydrous $MgSO_4$. Filtration and removal

of the solvent under reduced pressure provided an orange crude product, which was purified by flash chromatography (ethyl acetate:cyclohexane 50:50, R_f = 0.20, followed by ethyl acetate, R_f = 0.30) to provide the product **21** as an orange wax (467 mg, 77%). ^{1}H NMR (500 MHz, methylene sulfoxide-d_6:methanol-d_4 85:15, 323 K) δ 7.80 - 7.72 (m, 4H, **2**+**6**), 7.47 (d, *J* = 8.1 Hz, 2H, **7**), 7.22 (d, *J* = 8.3 Hz, 2H, **12**), 6.96 - 6.90 (m, 2H, **3**), 6.85 - 6.75 (m, 6H, **13**+**28**+**29**), 3.89 (t, *J* = 6.5 Hz, 2H, **15**), 3.84 (t, *J* = 6.5 Hz, 2H, **26**), 3.73 (s, 2H, **9**), 3.66 (s, 3H, **31**), 3.63 (s, 2H, **10**), 1.65 (m, 4H, **16**+**25**), 1.36 (m, 4H, **17**+**24**), 1.25 (d, *J* = 7.8 Hz, 12H, **18**+**19**+**20**+**21**+**22**+**23**). ^{13}C NMR (126 MHz, methylene sulfoxide-d_6:methanol-d_4 85:15, 323 K) δ 160.98, 157.96, 153.67, 153.15, 151.47, 145.77, 143.66, 132.55, 129.34, 128.88, 124.81, 122.16, 116.01, 115.58, 114.80, 114.38, 68.29, 67.74, 55.42, 51.97, 51.93, 29.22 (×2), 29.19 (×2), 29.09, 29.02 (×3), 25.76 (×2).

tert-butyl (*E*)-(4-((4-hydroxyphenyl)diazenyl)benzyl)(4-((12-(4-methoxyphenoxy)dodecyl)oxy)benzyl) carbamate, 22

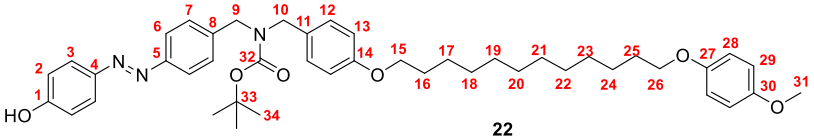

22

A THF solution (5 mL) of di-*tert*-butyl dicarbonate (86 mg, 0.39 mmol) was added dropwise to a THF solution (25 mL) of **21** (223 mg, 0.36 mmol) and the resulting mixture was stirred at room temperature for 16 h. The solvent was removed under reduced pressure to obtain a crude orange solid, which was purified by flash chromatography (hexane:ethyl acetate 70:30, R_f = 0.35) to provide the product **22** as an orange solid (242 mg, 94%). ^{1}H NMR (500 MHz, methylene chloride-d_2:methanol-d_4 99:1) δ 7.89 - 7.77 (m, 4H, **2**+**6**), 7.32 (d, *J* = 7.9 Hz, 2H, **7**), 7.14 (d, *J* = 8.0 Hz, 2H, **12**), 6.94 (dd, *J* = 7.5, 3.2 Hz, 2H, **3**), 6.87 - 6.82 (m, 2H, **13**), 6.81 (s, 4H, **28**+**29**), 4.50 - 4.25 (m, 4H, **9**+**10**), 3.94 (t, *J* = 6.6 Hz, 2H, **15**), 3.89 (t, *J* = 6.6 Hz, 2H, **26**), 3.74 (s, 3H, **31**), 1.80 - 1.69 (m, 4H, **16**+**25**), 1.55 - 1.39 (m, 13H, **17**+**24**+**34**), 1.32 (m, 12H, **18**+**19**+**20**+**21**+**22**+**23**). ^{13}C NMR (126 MHz, methylene chloride-d_2:methanol-d_4 99:1) δ 158.96 (×2), 156.33 (m), 154.10, 153.74, 152.37, 148.30, 142.77 (m), 130.19, 129.58 (m), 128.45 (m), 125.24, 122.92, 116.09, 115.72, 114.92, 114.84, 80.48, 69.07, 68.51, 56.01, 38.05, 37.67, 29.99 (×4), 29.81 (×2), 29.80, 29.69, 28.55, 26.43 (×2).

tert-butyl (*E*)-(4-((12-(4-methoxyphenoxy)dodecyl)oxy)benzyl)(4-((4-methoxyphenyl)diazenyl)benzyl) carbamate, 23

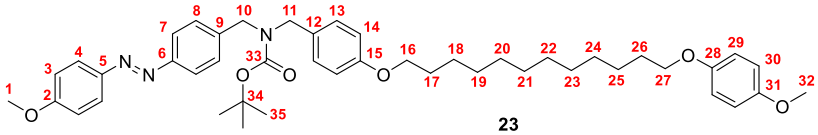

23

A solution of **22** (242 mg, 0.33 mmol), methyl iodide (62 µL, 0.67 mmol), 18-crown-6 (53 mg, 0.20 mmol) and potassium carbonate (51 mg, 0.37 mmol) in dry acetonitrile (50 mL) was stirred at 80 °C for 18 h under a dinitrogen atmosphere. The solution was cooled down to room temperature and the solvent removed under reduced pressure to provide a crude mixture which was dissolved in dichloromethane (25 mL), washed with water (3×50 mL) and dried over anhydrous $MgSO_4$. Filtration and removal of the solvent under reduced pressure provided the crude product that was purified by flash chromatography (hexane:ethyl acetate 80:20, R_f = 0.45) to provide the product **23** as an orange wax (170 mg, 70%). ^{1}H NMR (500 MHz, methylene chloride-d_2:methanol-d_4 99:1) δ 7.93 - 7.88 (m, 2H, **7**), 7.84 - 7.80 (m, 2H, **3**), 7.32 (s, 2H, **8**), 7.14 (s, 2H, **13**), 7.06 - 7.00 (m, 2H, **4**), 6.87 - 6.82 (m, 2H, **14**), 6.81 (s, 4H, **29**+**30**), 4.53 - 4.23 (m, 4H, **10**+**11**), 3.94 (t, *J* = 6.6 Hz, 2H, **16**), 3.88 (s, 5H, **1**+**27**), 3.73 (s, 3H, **32**), 1.79 - 1.68 (m, 4H, **17**+**26**), 1.55 - 1.39 (m, 13H, **18**+**25**+**35**), 1.39 - 1.24 (m,

12H, **19**+**20**+**21**+**22**+**23**+**24**). ^{13}C NMR (126 MHz, methylene chloride-d_2:methanol-d_4 99:1) δ 162.63, 158.95, 156.47, 154.08, 153.72, 152.34, 147.34, 141.41 (m), 130.07, 129.57 (m), 128.77 (m), 125.01, 122.98, 115.73, 114.92, 114.86, 114.64, 80.67, 69.09, 68.52, 55.98, 55.97, 29.96 (×2), 29.79 (×2), 29.76, 29.66, 28.50 (×2), 26.40 (×2).

(*E*)-*N*-(4-((12-(4-methoxyphenoxy)dodecyl)oxy)benzyl)-1-(4-((4-methoxyphenyl)diazenyl)phenyl) methanaminium hexafluorophosphate, C12noEG

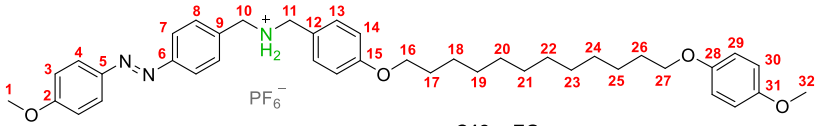

C12noEG

An aqueous solution of hexafluorophosphoric acid (170 uL, 1.00 mmol) was added to a solution of **23** (170 mg, 0.23 mmol) in THF (10 mL) and the resulting mixture was stirred at room temperature for 18 h. The solvent was removed under reduced pressure and the dark residue dissolved in dichloromethane (25 mL) and washed with a saturated aqueous solution of KPF_6 containing a few drops of HPF_6 (3×25 mL). The organic fraction was dried over $MgSO_4$ and the solvent removed under reduced pressure to provide the crude product, which was purified by size exclusion chromatography (SX-1, dichloromethane) to obtain the product **C12noEG** as an orange wax (175 mg, 97%). ^{1}H NMR (500 MHz, methylene chloride-d_2:methanol-d_4 99:1) δ 7.95 - 7.87 (m, 4H, **3**+**7**), 7.57 - 7.51 (m, 2H, **8**), 7.36 - 7.30 (m, 2H, **13**), 7.06 - 7.00 (m, 2H, **4**), 6.97 - 6.91 (m, 2H, **14**), 6.80 (s, 4H, **29**+**30**), 4.11 (s, 2H, **10**), 4.06 (s, 2H, **11**), 3.94 (t, *J* = 6.6 Hz, 2H, **16**), 3.90 - 3.86 (m, 5H, **27**+**1**), 3.73 (s, 3H, **32**), 1.80 - 1.67 (m, 4H, **17**+**26**), 1.42 (m, 4H, **18**+**25**), 1.38 - 1.23 (m, 12H, **19**+**20**+**21**+**22**+**23**+**24**). ^{13}C NMR (126 MHz, methylene chloride-d_2:methanol-d_4 99:1) δ 163.08, 160.74, 154.07, 153.70, 153.68, 147.20, 132.61, 131.78, 131.11, 125.32, 123.56, 122.05, 115.70, 115.51, 114.90, 114.71, 69.06, 68.62, 56.02, 55.98, 50.44, 49.99, 29.94 (×2), 29.78 (×2), 29.75 (×2), 29.54 (×2), 26.39, 26.34. ^{19}F NMR (470 MHz, methylene chloride-d_2:methanol-d_4 99:1) δ –71.51 (d, *J* = 710.4 Hz, PF_6). HRMS-ESI (*m*/*z*): calcd for [$C_{40}H_{52}N_3O_4$], 638.3958; found 638.3958 [**M**]$^+$.

***tert*-butyl (*E*)-(4-((4-(2-(2-(2-methoxyethoxy)ethoxy)ethoxy)phenyl)diazenyl)benzyl)(4-((12-(4-methoxyphenoxy)dodecyl)oxy)benzyl)carbamate, 24**

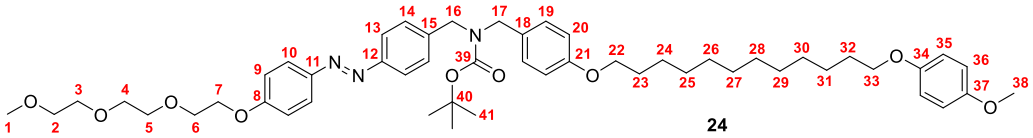

24

A solution of **22** (994 mg, 1.37 mmol), **1** (524 mg, 1.65 mmol), 18-crown-6 (181 mg, 0.69 mmol) and potassium carbonate (284 mg, 2.06 mmol) in dry acetonitrile (25 mL) was stirred at 80 °C for 18 h under a dinitrogen atmosphere. The solution was cooled down to room temperature and the solvent removed under reduced pressure to provide a crude mixture which was dissolved in Dichloromethane (100 mL), washed with water (3×100 mL) and dried over anhydrous $MgSO_4$. Filtration and removal of the solvent under reduced pressure provided the crude product that was purified by flash chromatography (ethyl acetate:hexane 50:50, R_f = 0.40) to provide the product **24** as an orange oil (977 mg, 82%). ^{1}H NMR (500 MHz, chloroform-*d*:methanol-d_4 90:10) δ 7.84 (d, *J* = 8.9 Hz, 2H, **13**), 7.77 (d, *J* = 8.3 Hz, 2H, **9**), 7.25 (dd, *J* = 27.6, 7.5 Hz, 2H, **14**), 7.13 - 7.01 (m, 2H, **19**), 7.00 - 6.94 (m, 2H, **10**), 6.82 - 6.72 (m, 6H, **20**+**35**+**36**), 4.31 (dd, *J* = 46.6, 30.2 Hz, 4H, **16**+**17**), 4.15 (dd, *J* = 5.7, 3.9 Hz, 2H, **7**), 3.88 (t, *J* = 6.6 Hz, 2H, **22**), 3.85 - 3.80 (m, 4H, **6**+**33**), 3.71 - 3.66 (m, 5H, **5**+**38**), 3.65 - 3.57 (m, 4H, **3**+**4**), 3.51 - 3.47 (m, 2H, **2**), 3.31 (s, 3H, **1**), 1.75 - 1.64 (m, 4H, **23**+**32**), 1.50 - 1.32 (m, 13H, **24**+**31**+**41**), 1.32 - 1.18 (m, 12H, **25**+**26**+**27**+**28**+**29**+**30**). ^{13}C NMR (126

MHz, chloroform-*d*:methanol-d_4 90:10) δ 161.25, 158.44, 156.11, 153.55, 153.19, 151.91, 146.96, 140.67 (m), 129.32, 128.78 (m), 128.45 (m), 124.63, 122.67, 115.39, 114.79, 114.55, 114.52, 80.42, 71.79, 70.74, 70.52, 70.41, 69.54, 68.65, 68.03, 67.62, 58.88, 55.65, 48.89, 48.41, 29.49 (×4), 29.33 (×2), 29.29, 29.19, 28.32, 25.96 (×2).

(*E*)-N-(4-((4-(2-(2-(2-methoxyethoxy)ethoxy)ethoxy)phenyl)diazenyl)benzyl)-1-(4-((12-(4-methoxyphenoxy)dodecyl)oxy)phenyl)methanaminium hexafluorophosphate, C12hEG

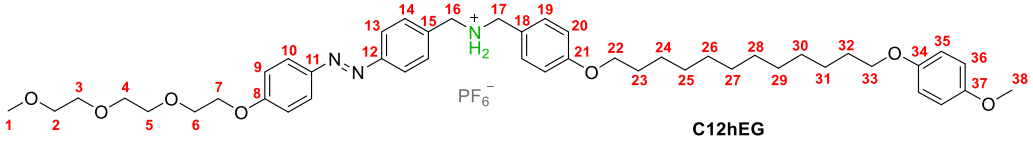

C12hEG

An aqueous solution of hexafluorophosphoric acid (4.63 mL, 28.00 mmol) was added to a solution of **24** (974 mg, 1.11 mmol) in THF (30 mL) and the resulting mixture was stirred at room temperature for 18 h. The solvent was removed under reduced pressure and the dark residue dissolved in dichloromethane (100 mL) and washed with a saturated aqueous solution of KPF_6 containing a few drops of HPF_6 (3×50 mL). The organic fraction was dried over $MgSO_4$ and the solvent removed under reduced pressure to provide the crude product, which was purified by size exclusion chromatography (SX-1, dichloromethane) to obtain the product **C12hEG** as an orange solid (890 mg, 96%). ^{1}H NMR (500 MHz, methylene chloride-d_2:methanol-d_4 90:10) δ 7.95 - 7.86 (m, 4H, **9**+**13**), 7.57 - 7.51 (m, 2H, **14**), 7.36 - 7.31 (m, 2H, **19**), 7.07 - 7.02 (m, 2H, **10**), 6.95 (d, *J* = 8.7 Hz, 2H, **20**), 6.80 (s, 4H, **35**+**36**), 4.22 - 4.16 (m, 4H, **7**+**16**), 4.12 (s, 2H, **17**), 3.96 (t, *J* = 6.6 Hz, 2H, **22**), 3.90 - 3.83 (m, 4H, **6**+**33**), 3.72 (s, 3H, **38**), 3.70 - 3.66 (m, 2H, **5**), 3.64 - 3.56 (m, 4H, **3**+**4**), 3.53 - 3.48 (m, 2H, **2**), 3.32 (s, 3H, **1**), 1.74 (m, 4H, **23**+**32**), 1.42 (m, 4H, **24**+**31**), 1.38 - 1.24 (m, 12H, **25**+**26**+**27**+**28**+**29**+**30**). ^{13}C NMR (126 MHz, methylene chloride-d_2:methanol-d_4 90:10) δ 161.31, 160.92, 154.03, 153.67, 153.31, 147.25, 132.32, 131.98, 130.81, 125.41, 123.59, 122.05, 115.62, 115.42, 114.93, 114.85, 72.02, 71.64, 70.78, 70.51, 70.34, 68.94, 68.62, 68.46, 59.38, 55.95, 51.99, 51.53, 29.95 (×4), 29.78 (×2), 29.76, 29.54, 26.40, 26.39, 26.35, 26.33. ^{19}F NMR (470 MHz, methylene chloride-d_2:methanol-d_4 90:10) δ –71.93 (d, *J* = 712.2 Hz, 6F, PF_6). HRMS-ESI (*m*/*z*): calcd for $[C_{46}H_{64}N_3O_7]$, 770.4744; found 770.4744 [**M**]$^+$.

***tert*-butyl (*E*)-(4-((12-(4-(2-(2-(2-methoxyethoxy)ethoxy)ethoxy)phenoxy)dodecyl)oxy)benzyl)(4-((4-methoxyphenyl)diazenyl)benzyl)carbamate, 25**

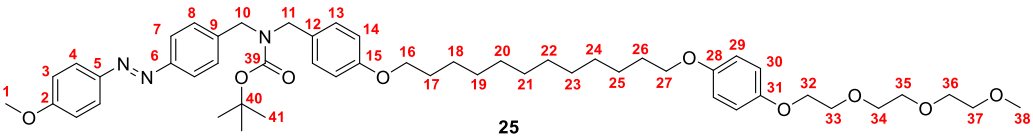

25

A solution of **17** (300 mg, 0.35 mmol), Methyl iodide (65 µL, 1.05 mmol), 18-crown-6 (46 mg, 0.17 mmol) and potassium carbonate (67 mg, 0.53 mmol) in dry acetonitrile (50 mL) was stirred at 80 °C for 18 h under a dinitrogen atmosphere. The solution was cooled down to room temperature and the solvent removed under reduced pressure to provide a crude mixture which was dissolved in dichloromethane (25 mL), washed with water (3×50 mL) and dried over anhydrous $MgSO_4$. Filtration and removal of the solvent under reduced pressure provided the crude product that was purified by flash chromatography (hexane:ethyl acetate 60:40, R_f = 0.25) to provide the product **25** as an orange wax (272 mg, 89%). ^{1}H NMR (500 MHz, chloroform-*d*) δ 7.96 - 7.87 (m, 2H, **7**), 7.83 (tt, *J* = 6.2, 2.0 Hz, 2H, **3**), 7.30 (d, *J* = 21.5 Hz, 2H, **8**), 7.12 (d, *J* = 23.6 Hz, 2H, **13**), 7.04 - 6.96 (m, 2H, **4**), 6.82

(ddt, *J* = 16.1, 9.2, 4.5 Hz, 6H, **14**+**29**+**30**), 4.36 (dd, *J* = 47.8, 30.8 Hz, 4H, **10**+**11**), 4.06 (dq, *J* = 5.2, 2.8 Hz, 2H, **32**), 3.93 (td, *J* = 6.6, 2.4 Hz, 2H, **16**), 3.87 (dt, *J* = 6.8, 3.9 Hz, 5H, **1**+**27**), 3.83 - 3.79 (m, 2H, **33**), 3.71 (tt, *J* = 4.1, 2.2 Hz, 2H, **34**), 3.69 - 3.61 (m, 4H, **35**+**36**), 3.54 (tt, *J* = 4.4, 2.3 Hz, 2H, **37**), 3.36 (t, *J* = 2.4 Hz, 3H, **38**), 1.75 (dtd, *J* = 14.9, 7.7, 2.6 Hz, 4H, **17**+**26**), 1.46 (dd, *J* = 30.9, 10.5 Hz, 13H, **18**+**25**+**41**), 1.37 - 1.22 (m, 12H, **19**+**20**+**21**+**22**+**23**+**24**). ^{13}C NMR (126 MHz, chloroform-*d*) δ 162.19, 158.60, 156.14, 153.55, 152.91, 152.04, 147.06, 140.87, 129.63, 129.50, 128.68, 124.84, 122.81, 115.72, 115.46, 114.65, 114.33, 80.39, 72.00, 70.85, 70.71, 70.61, 69.96, 68.75, 68.18, 59.09, 55.69, 49.48, 48.92, 29.66 (×4), 29.50 (×2), 29.47, 29.37, 28.53 (×2), 26.14 (×2).

(*E*)-*N*-(4-((12-(4-(2-(2-(2-methoxyethoxy)ethoxy)ethoxy)phenoxy)dodecyl)oxy)benzyl)-1-(4-((4-methoxyphenyl)diazenyl)phenyl)methanaminium hexafluorophosphate, C12tEG

An aqueous solution of hexafluorophosphoric acid (260 uL, 1.56 mmol) was added to a solution of **25** (272 mg, 0.31 mmol) in THF (10 mL) and the resulting mixture was stirred at room temperature for 18 h. The solvent was removed under reduced pressure and the dark residue dissolved in dichloromethane (25 mL) and washed with a saturated aqueous solution of KPF_6 containing a few drops of HPF_6 (3×25 mL). The organic fraction was dried over $MgSO_4$ and the solvent removed under reduced pressure to provide the crude product, which was purified by size exclusion chromatography (SX-1, dichloromethane) to obtain the product **C12tEG** as an orange wax (244 mg, 86%). ^{1}H NMR (500 MHz, chloroform-*d*:methanol-d_4 99:1) δ 7.91 - 7.82 (m, 4H, **3**+**7**), 7.52 (d, *J* = 8.0 Hz, 2H, **8**), 7.30 (d, *J* = 8.2 Hz, 2H, **13**), 7.01 - 6.96 (m, 2H, **4**), 6.88 (d, *J* = 8.3 Hz, 2H, **14**), 6.83 - 6.75 (m, 4H, **29**+**30**), 4.06 - 3.99 (m, 4H, **10**+**32**), 3.96 (s, 2H, **11**), 3.92 - 3.84 (m, 7H, **1**+**16**+**27**), 3.80 (dd, *J* = 5.7, 4.0 Hz, 2H, **33**), 3.72 - 3.67 (m, 2H, **34**), 3.67 - 3.60 (m, 4H, **35**+**36**), 3.54 - 3.50 (m, 2H, **37**), 3.35 (s, 3H, **38**), 1.77 - 1.67 (m, 4H, **17**+**26**), 1.40 (m, 4H, **18**+**25**), 1.36 - 1.21 (m, 12H, **19**+**20**+**21**+**22**+**23**+**24**). ^{13}C NMR (126 MHz, chloroform-*d*:methanol-d_4 99:1) δ 162.59, 160.27, 153.55, 153.31, 152.90, 146.94, 132.10, 131.56, 130.85, 125.12, 123.34, 121.58, 115.72, 115.48, 115.25, 114.39, 71.97, 70.83, 70.69, 70.57, 69.95, 68.77, 68.24, 68.18, 59.07, 55.70, 29.64 (×6), 29.48, 29.47, 29.45, 29.25, 26.12, 26.08. ^{19}F NMR (470 MHz, chloroform-*d*:methanol-d_4 99:1) δ –71.70 (d, *J* = 726.8 Hz, PF_6). HRMS-ESI (*m*/*z*): calcd for [$C_{46}H_{64}N_3O_7$], 770.4744; found 770.4744 [**M**]$^+$.

NMR data

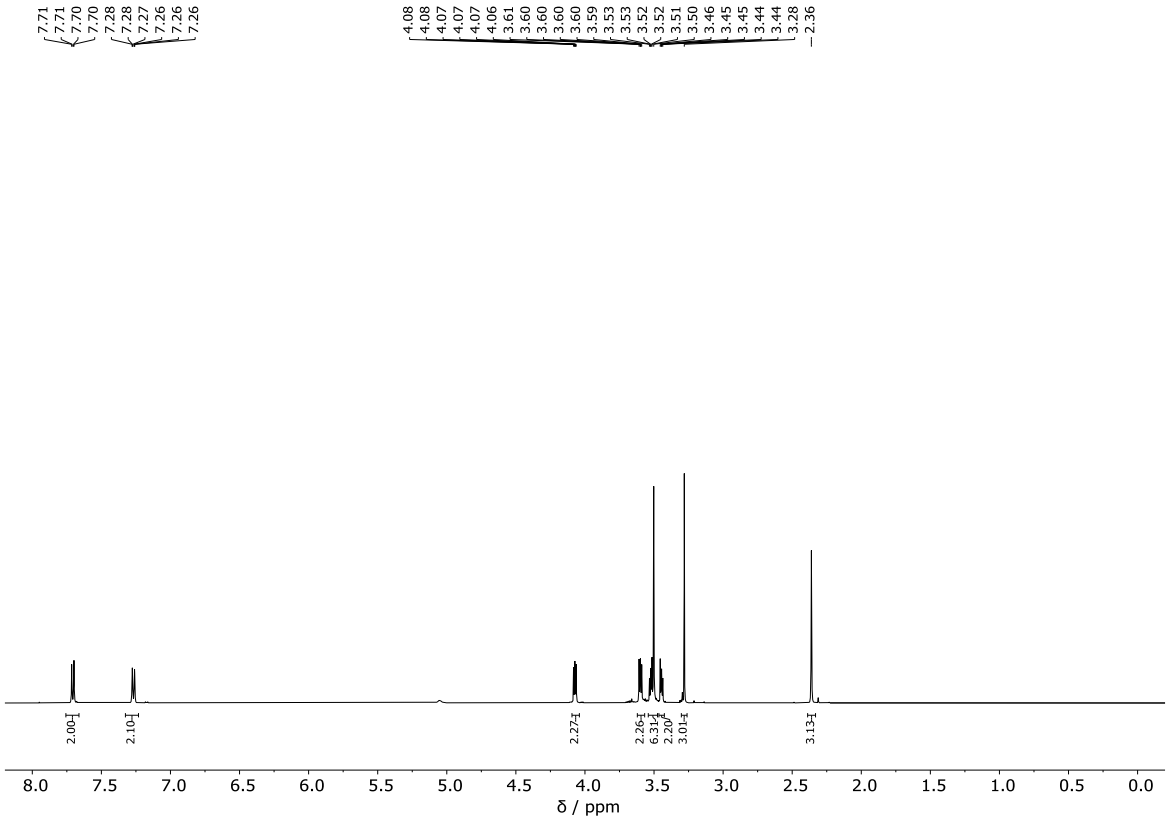

Figure S1. ^{1}H NMR spectrum of **1** (Chloroform-*d*, 298 K, 500 MHz).

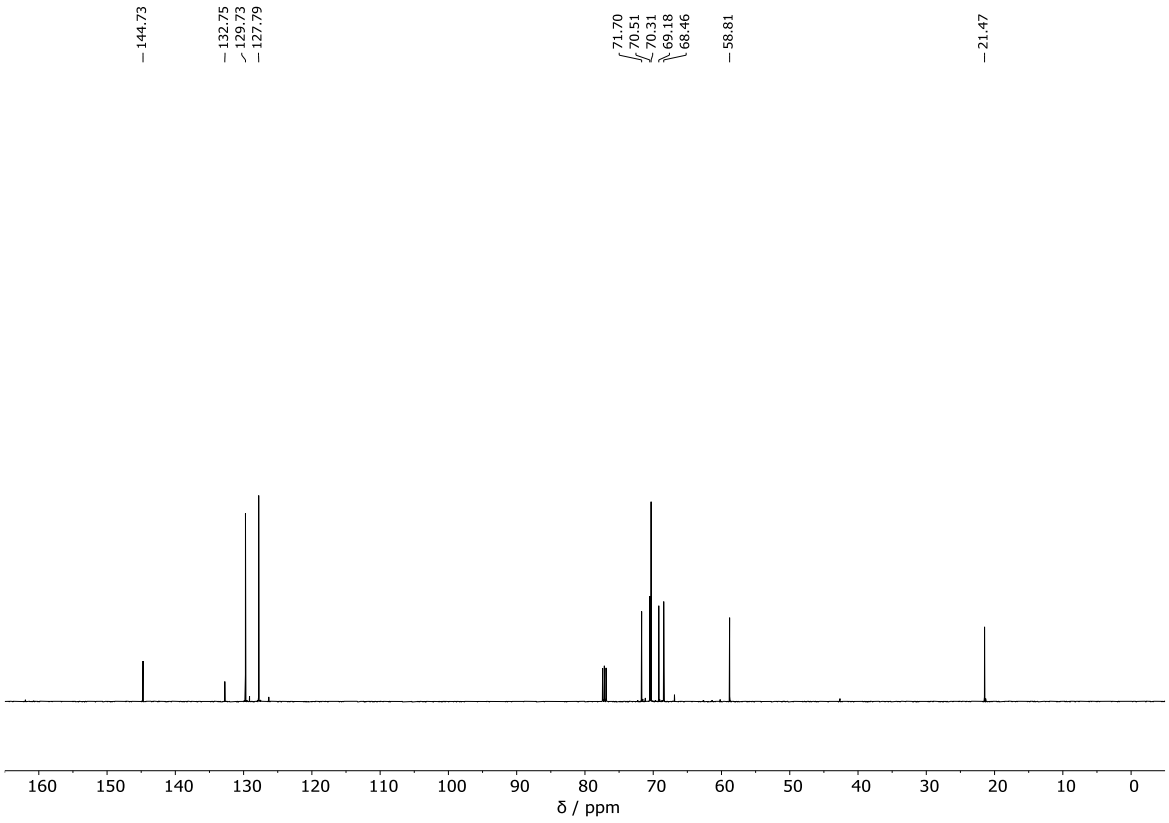

Figure S2. ^{13}C NMR spectrum of **1** (Chloroform-*d*, 298 K, 101 MHz).

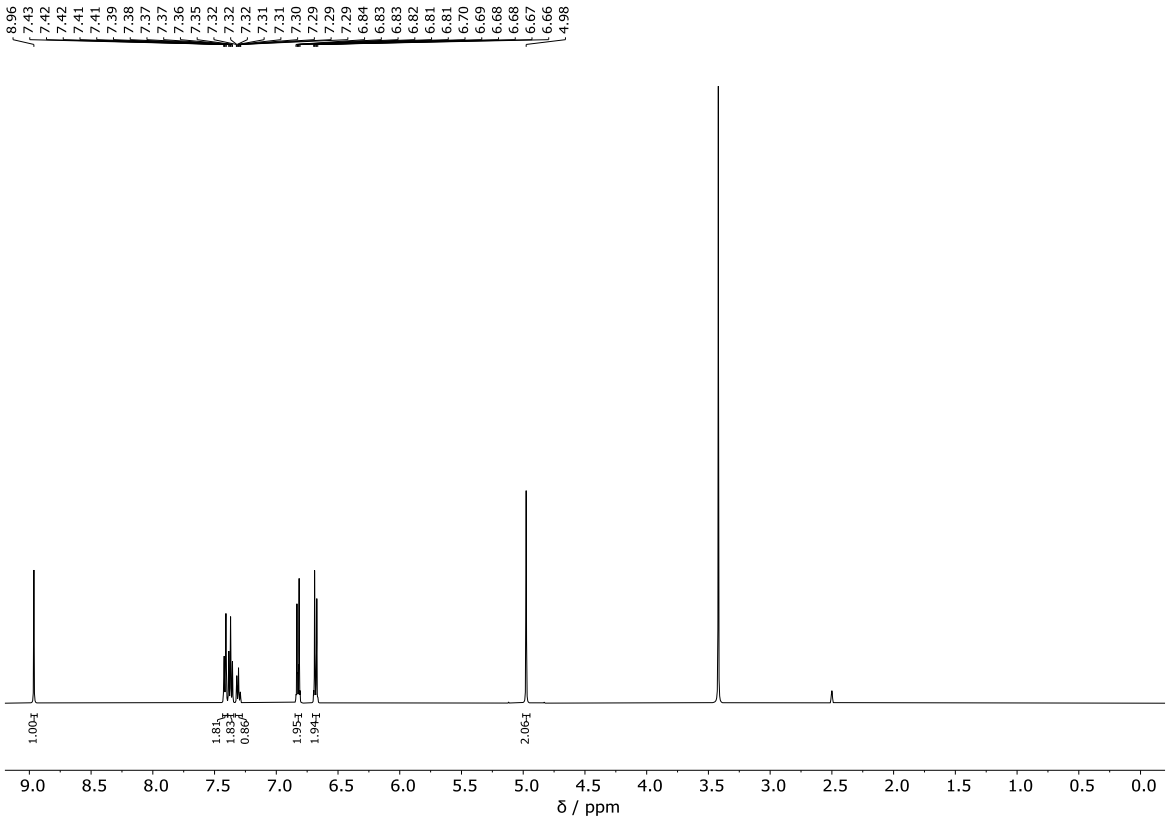

Figure S3. ^{1}H NMR spectrum of **2** (Methyl Sulfoxide-d_6, 298 K, 500 MHz).

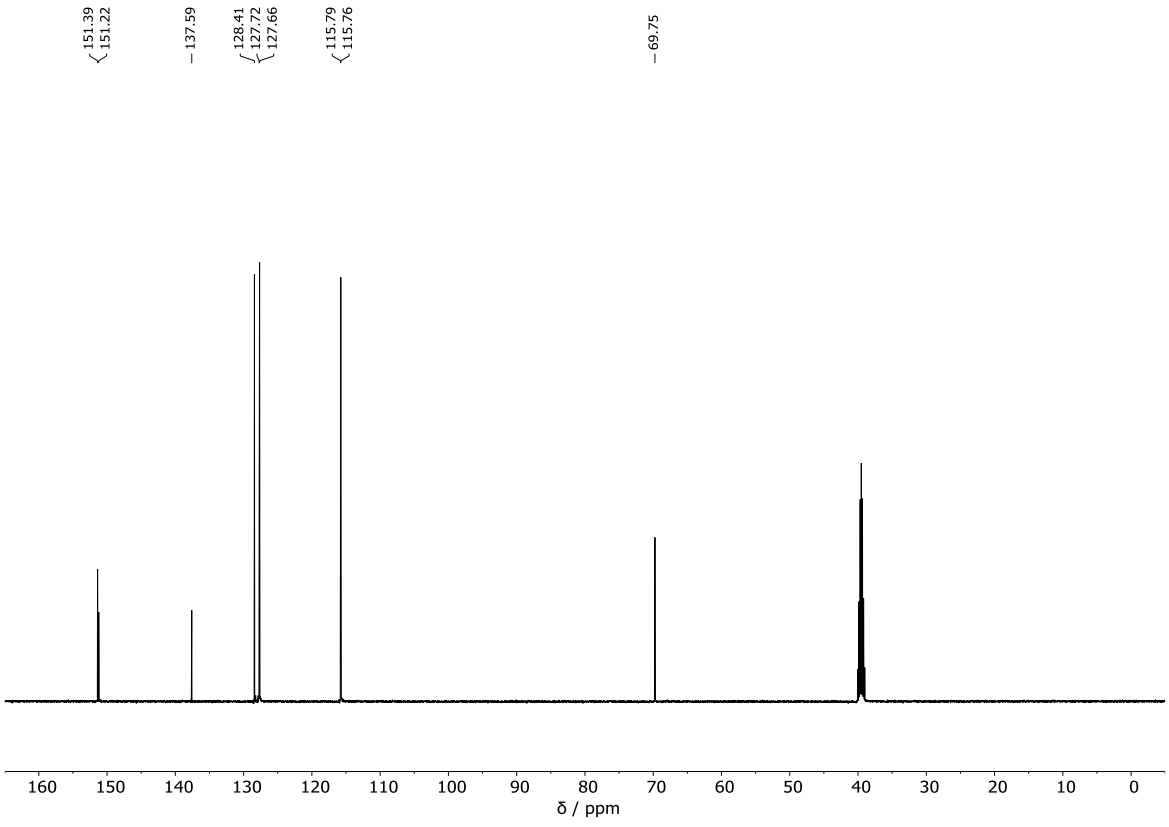

Figure S4. ^{13}C NMR spectrum of **2** (Methyl Sulfoxide-d_6, 298 K, 126 MHz).

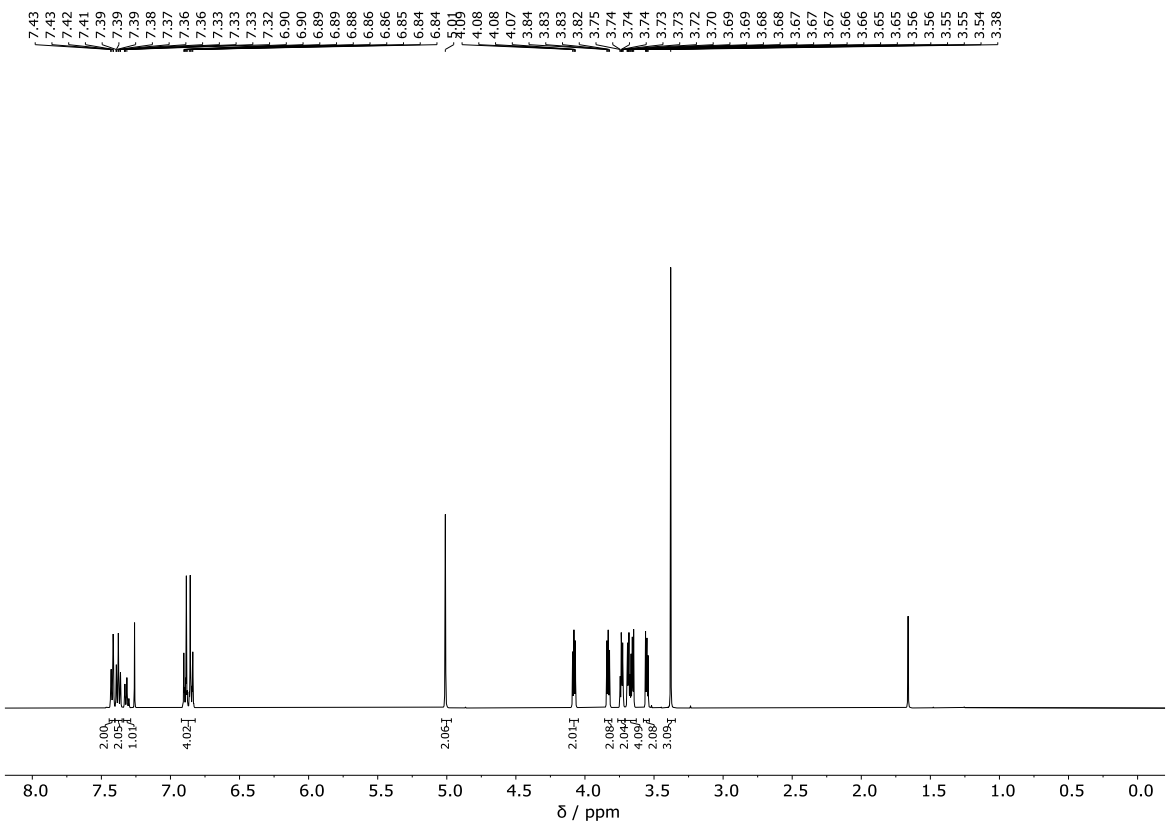

Figure S5. ^{1}H NMR spectrum of **3** (Chloroform-*d*, 298 K, 500 MHz).

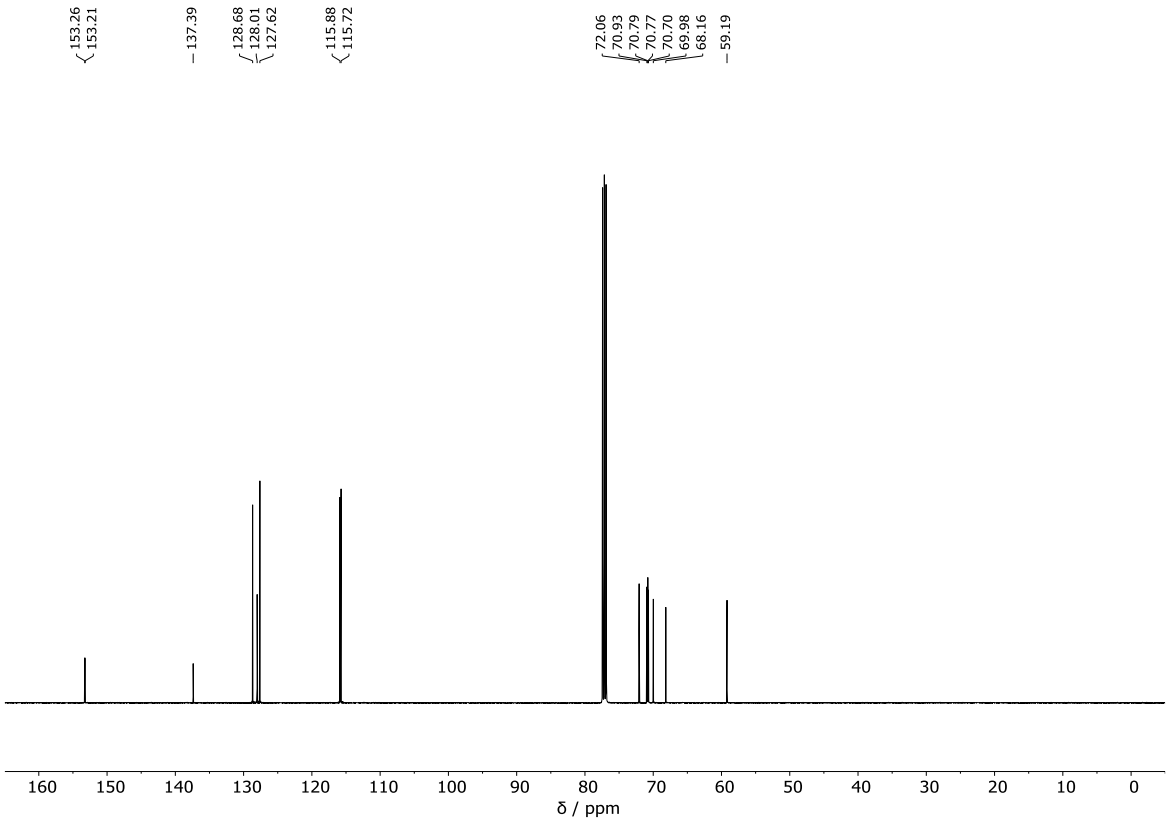

Figure S6. ^{13}C NMR spectrum of **3** (Chloroform-*d*, 298 K, 126 MHz).

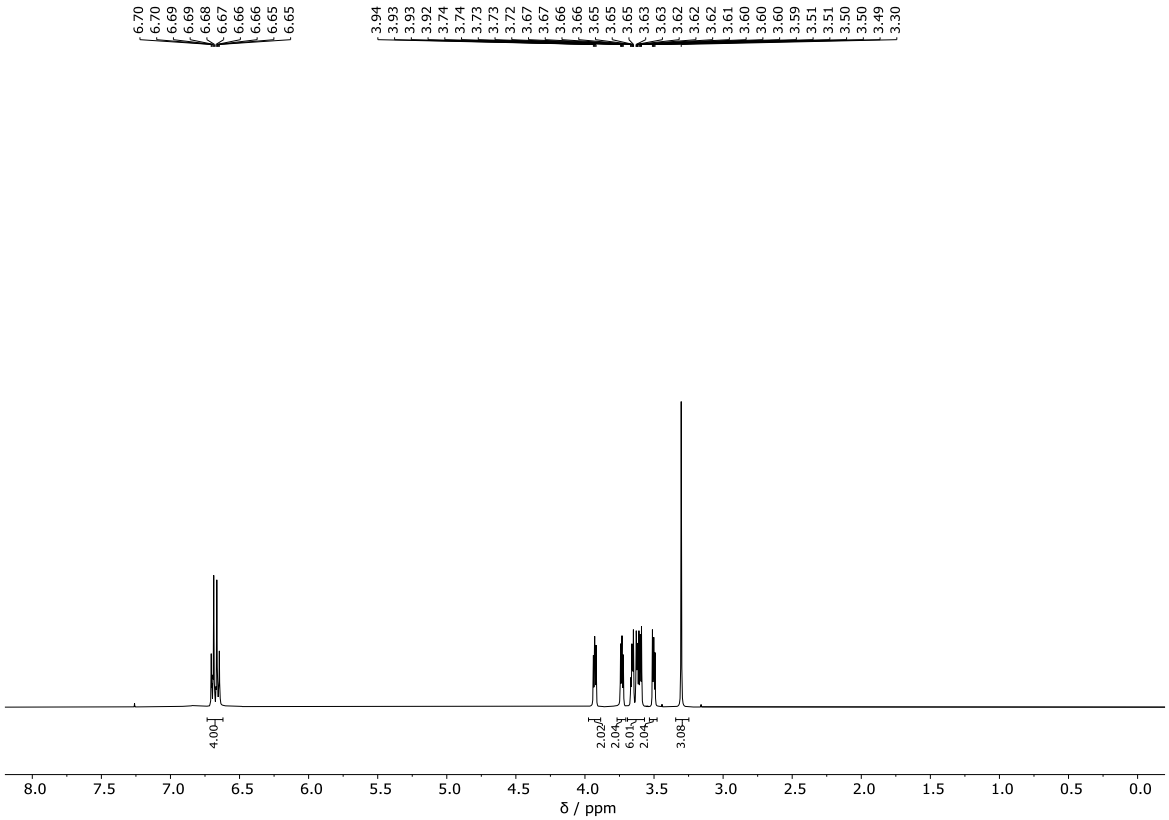

Figure S7. ^{1}H NMR spectrum of **4** (Chloroform-*d*, 298 K, 500 MHz).

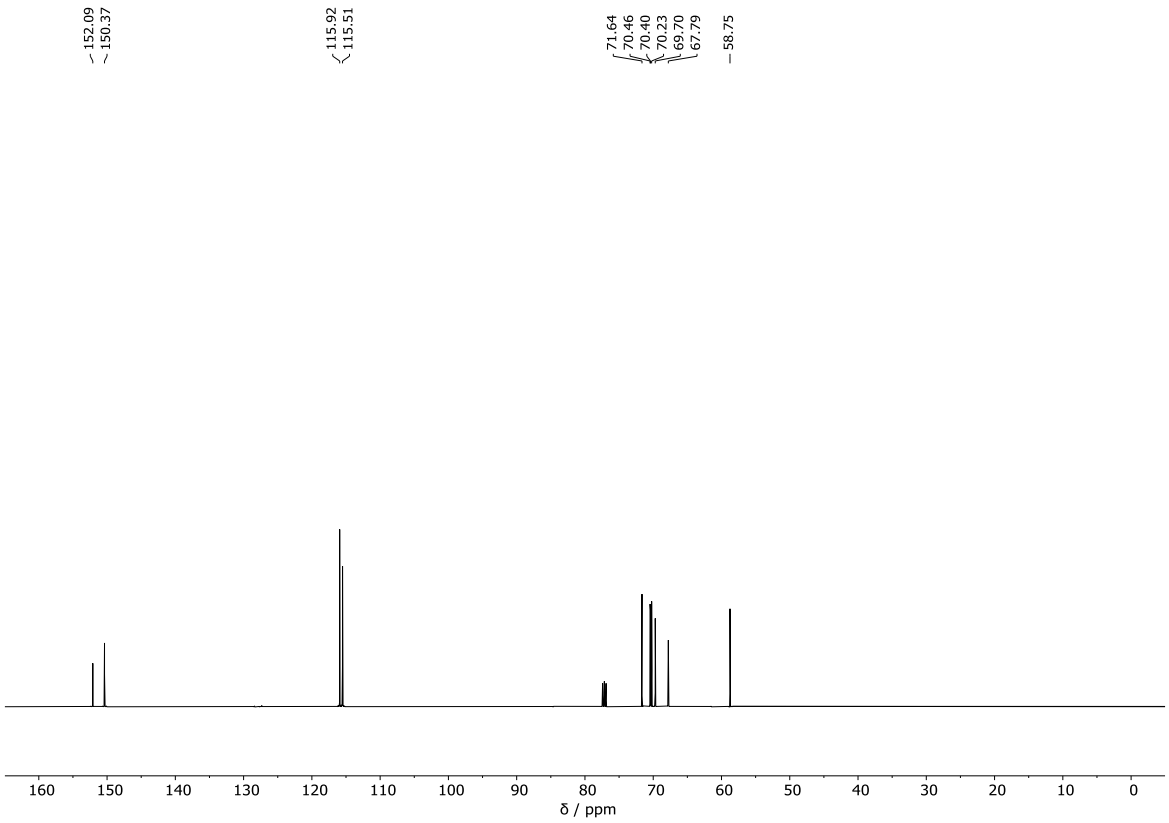

Figure S8. ^{13}C NMR spectrum of **4** (Chloroform-*d*, 298 K, 126 MHz).

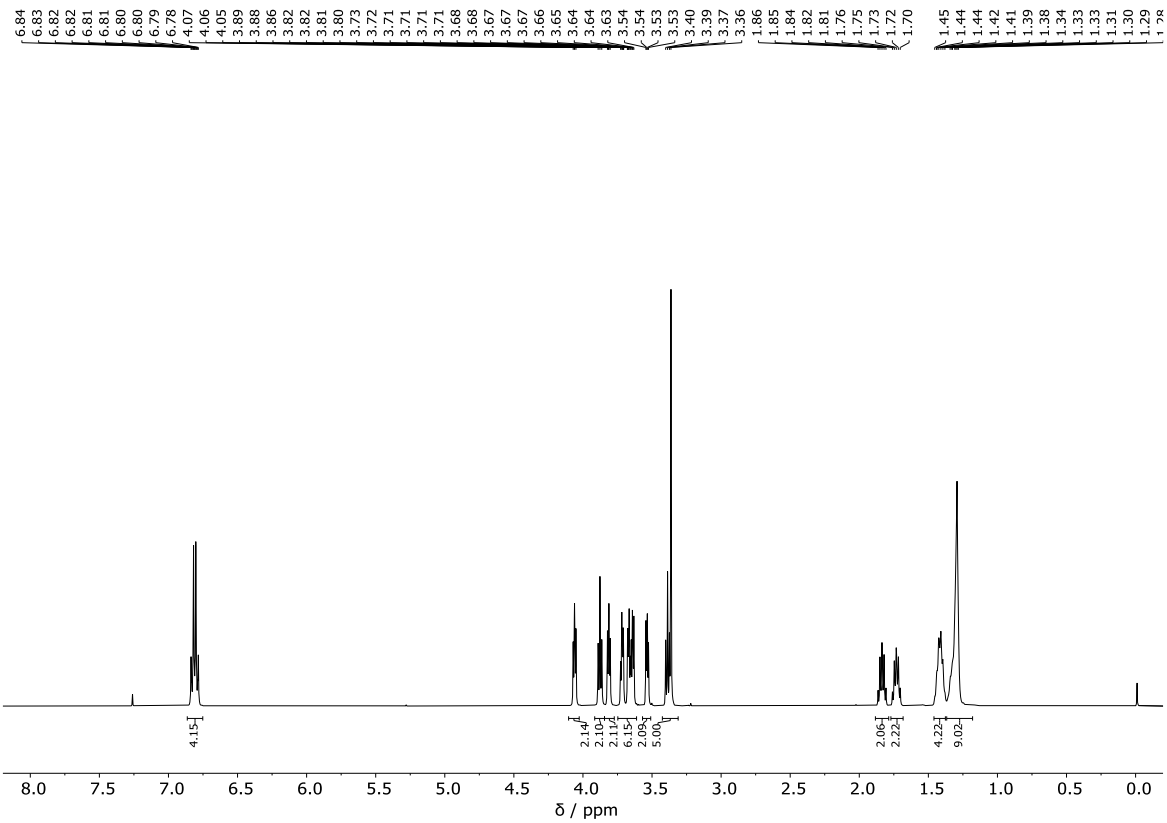

Figure S9. ^{1}H NMR spectrum of **5** (Chloroform-*d*, 298 K, 500 MHz).

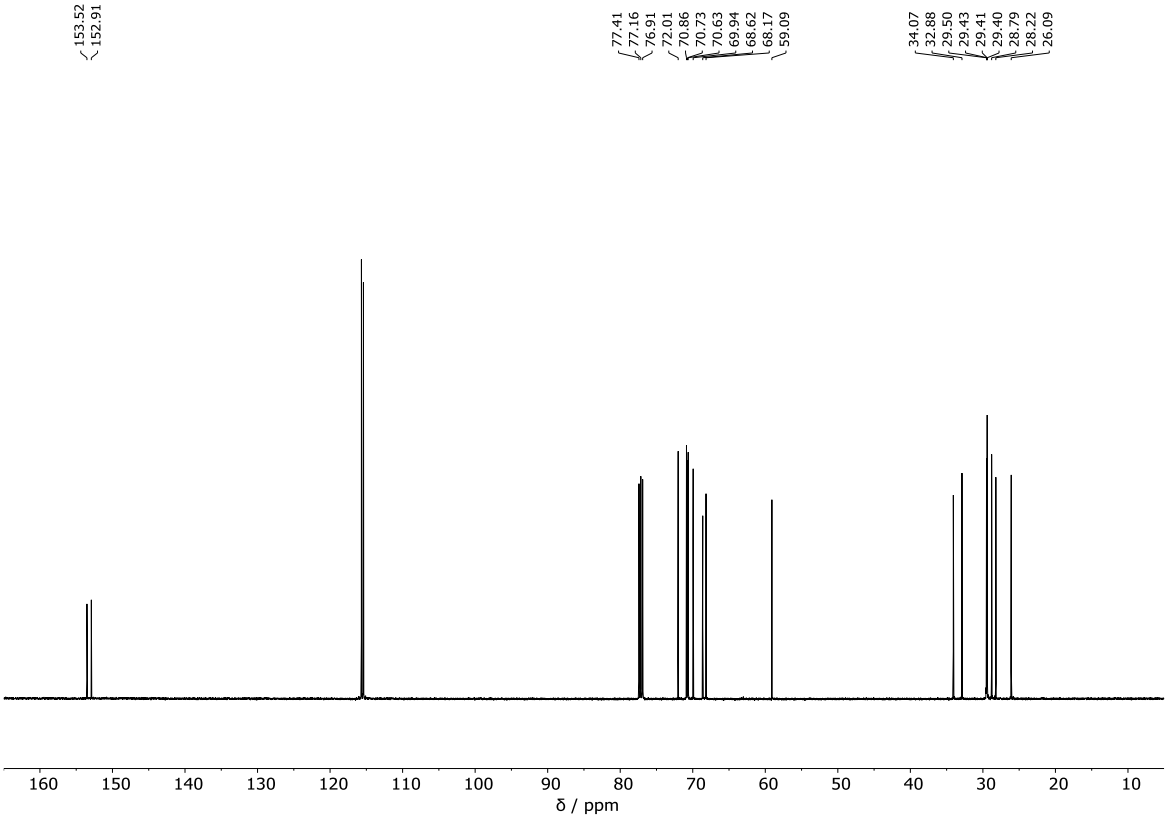

Figure S10. ^{13}C NMR spectrum of **5** (Chloroform-*d*, 298 K, 126 MHz).

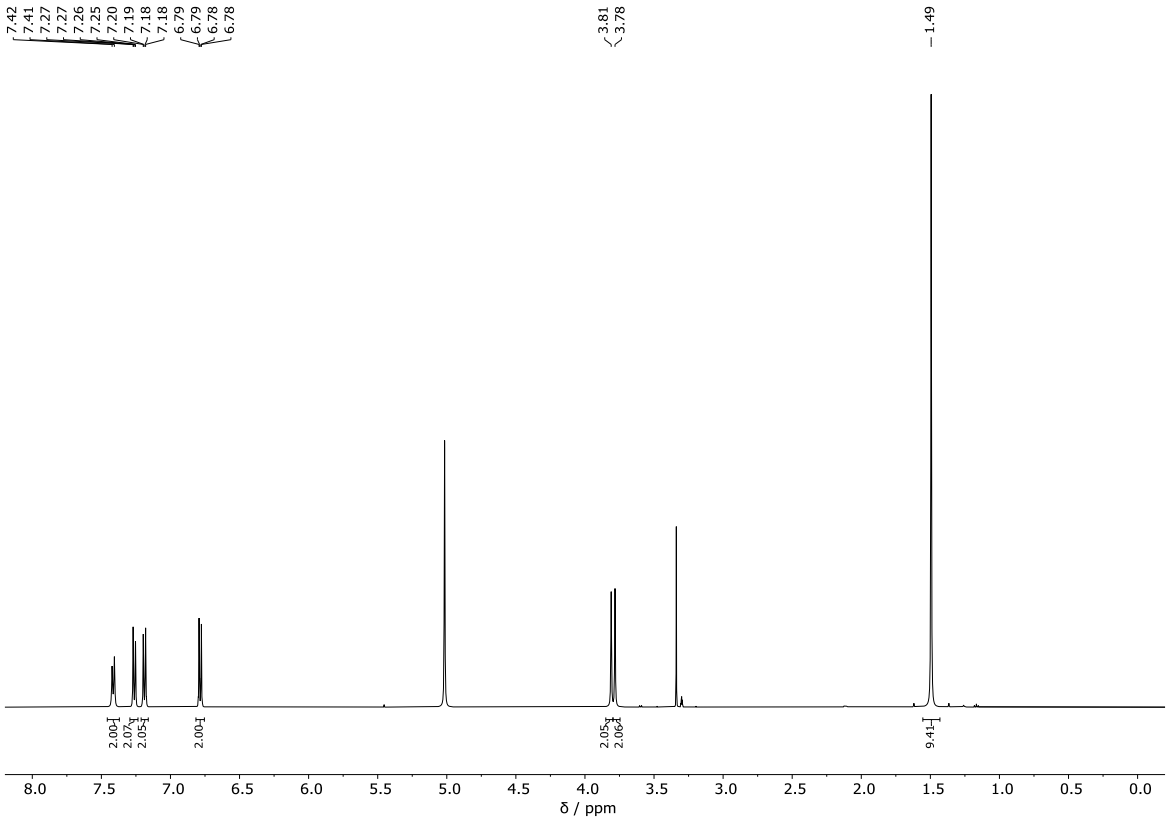

Figure S11. ^{1}H NMR spectrum of **6** (Methanol-d_4, 298 K, 500 MHz).

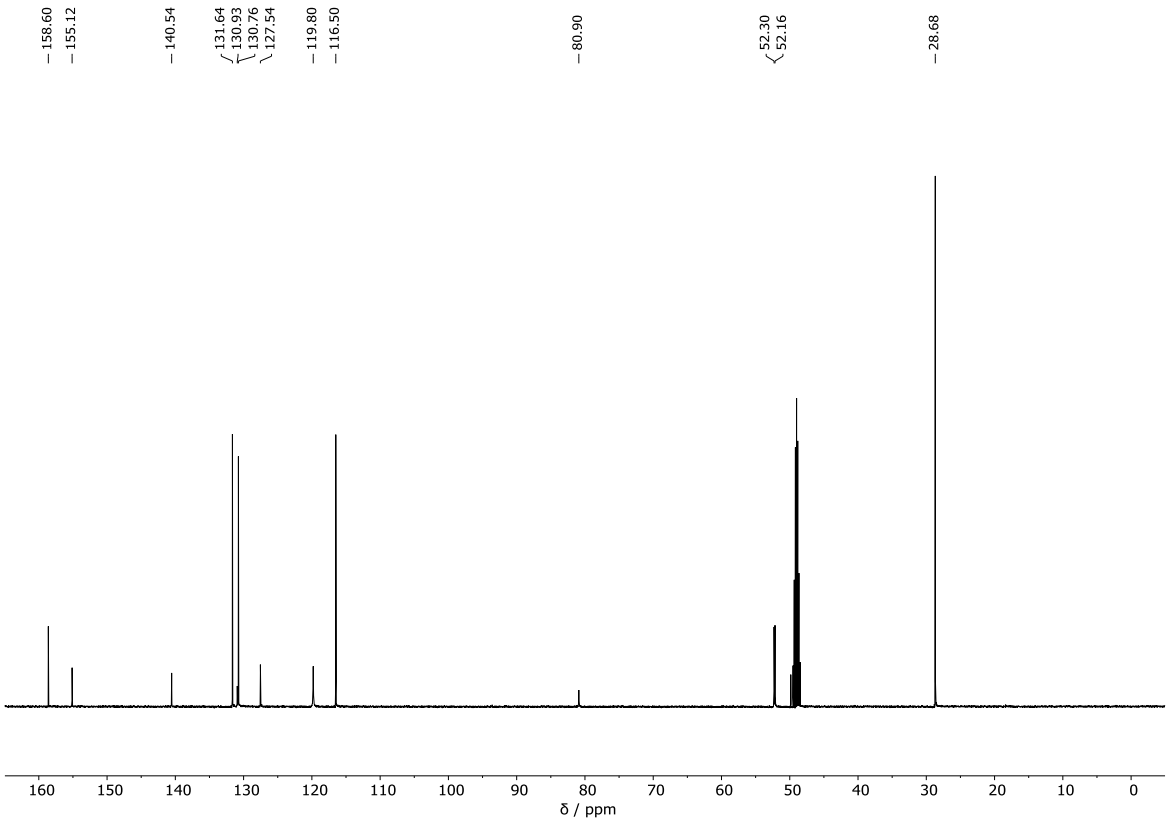

Figure S12. ^{13}C NMR spectrum of **6** (Methanol-d_4, 298 K, 126 MHz).

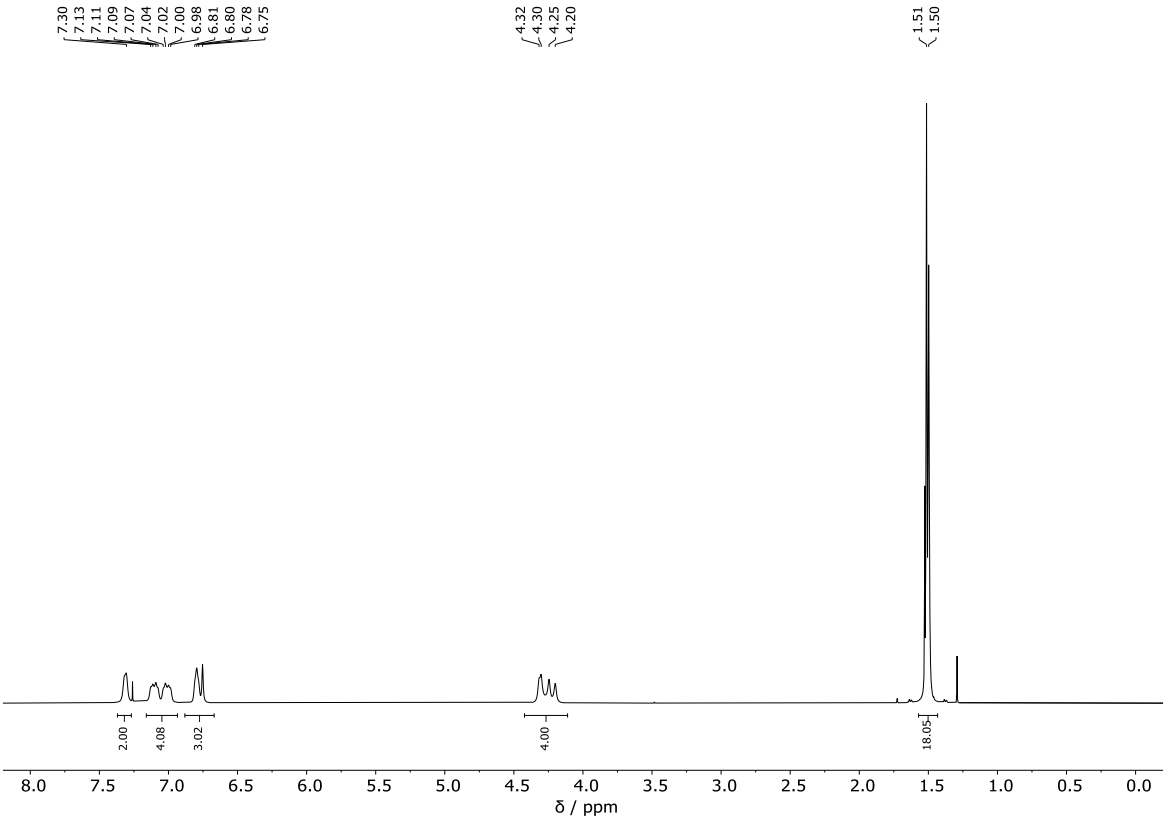

Figure S13. ^{1}H NMR spectrum of **7** (Acetonitrile-d_3, 298 K, 500 MHz).

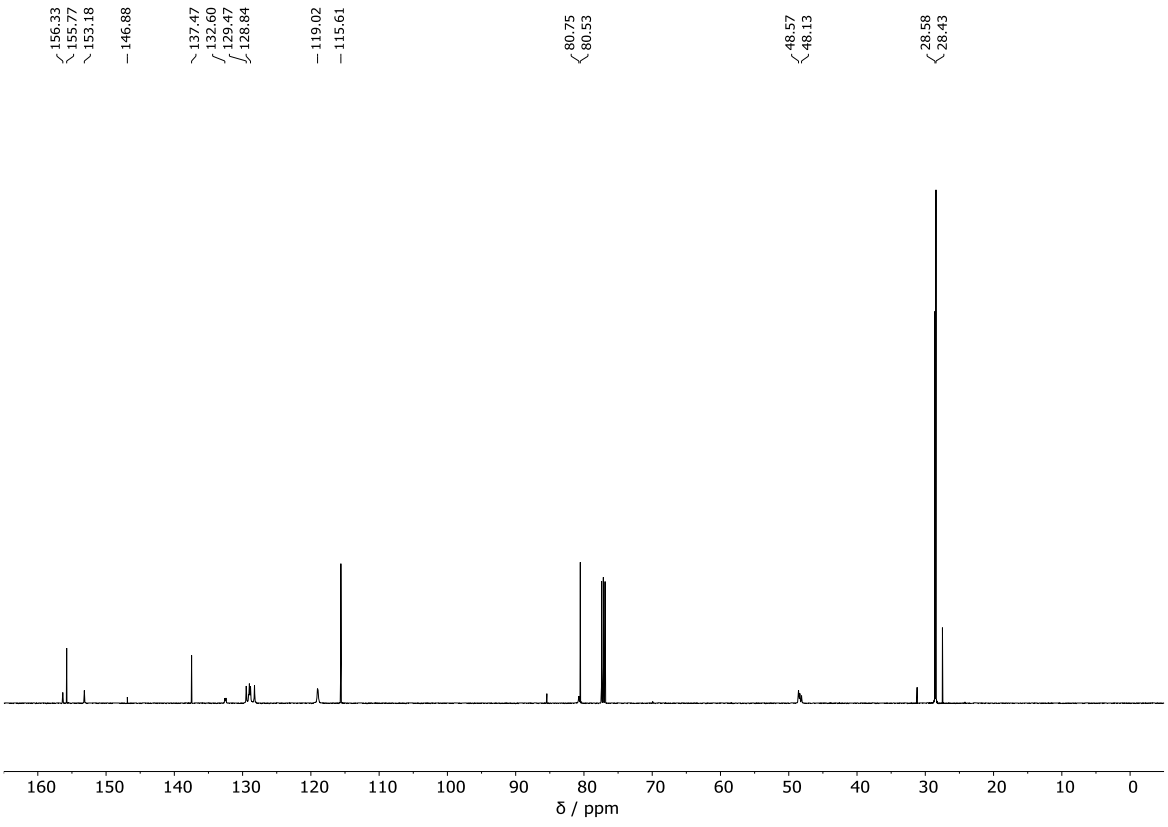

Figure S14. ^{13}C NMR spectrum of **7**(Acetonitrile-d_3, 298 K, 126 MHz).

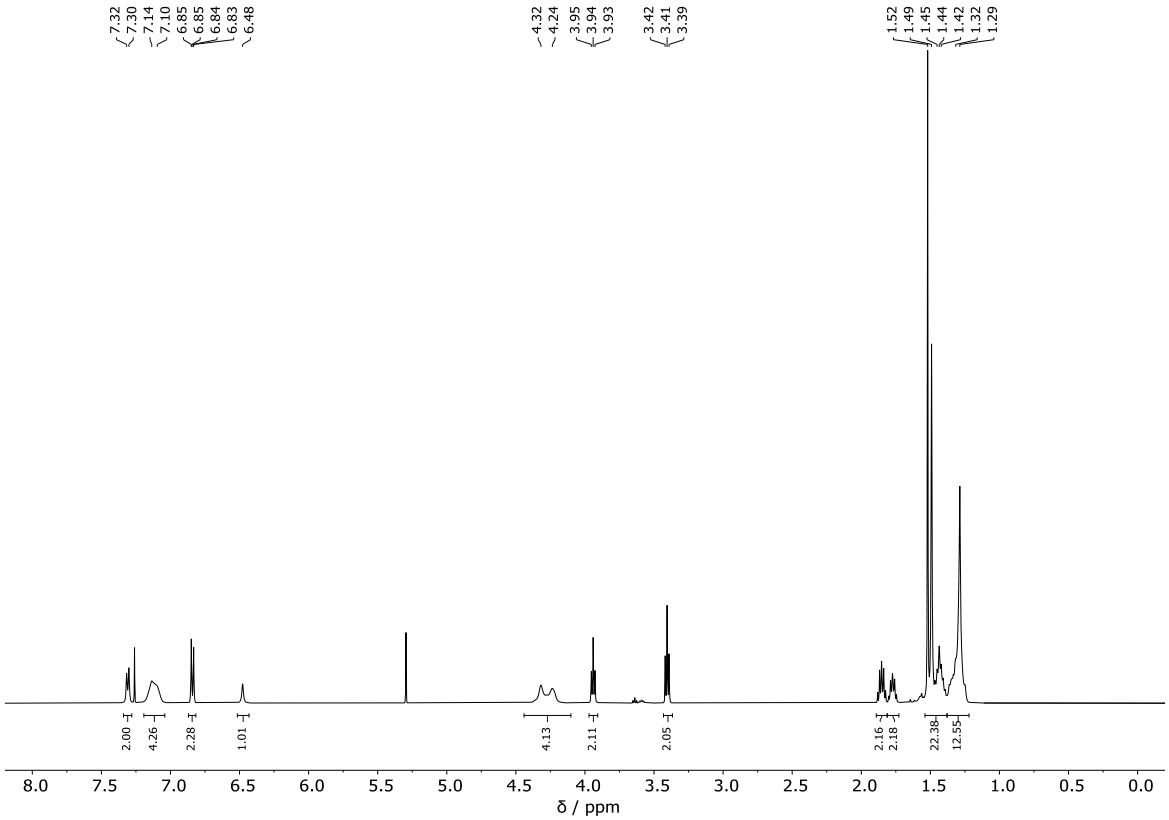

Figure S15. ^{1}H NMR spectrum of **8** (Chloroform-*d*, 298 K, 500 MHz).

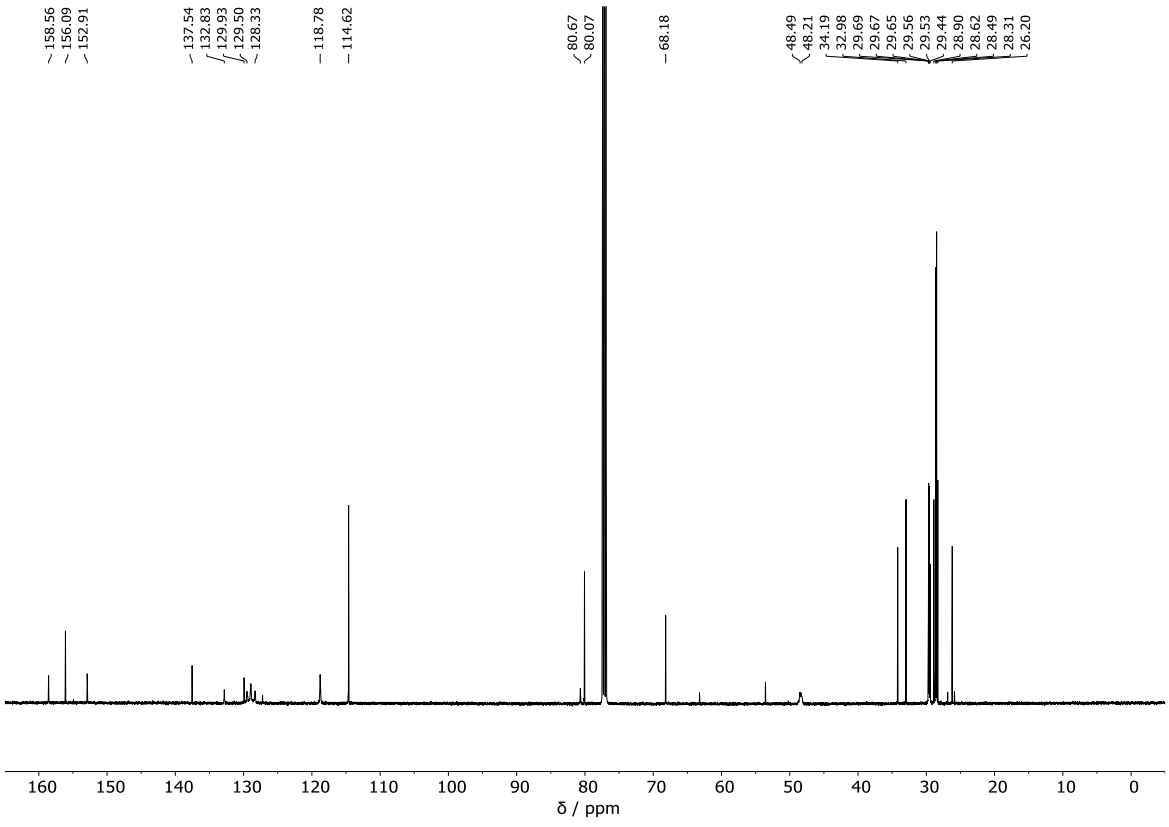

Figure S16. ^{13}C NMR spectrum of **8** (Chloroform-*d*, 298 K, 126 MHz).

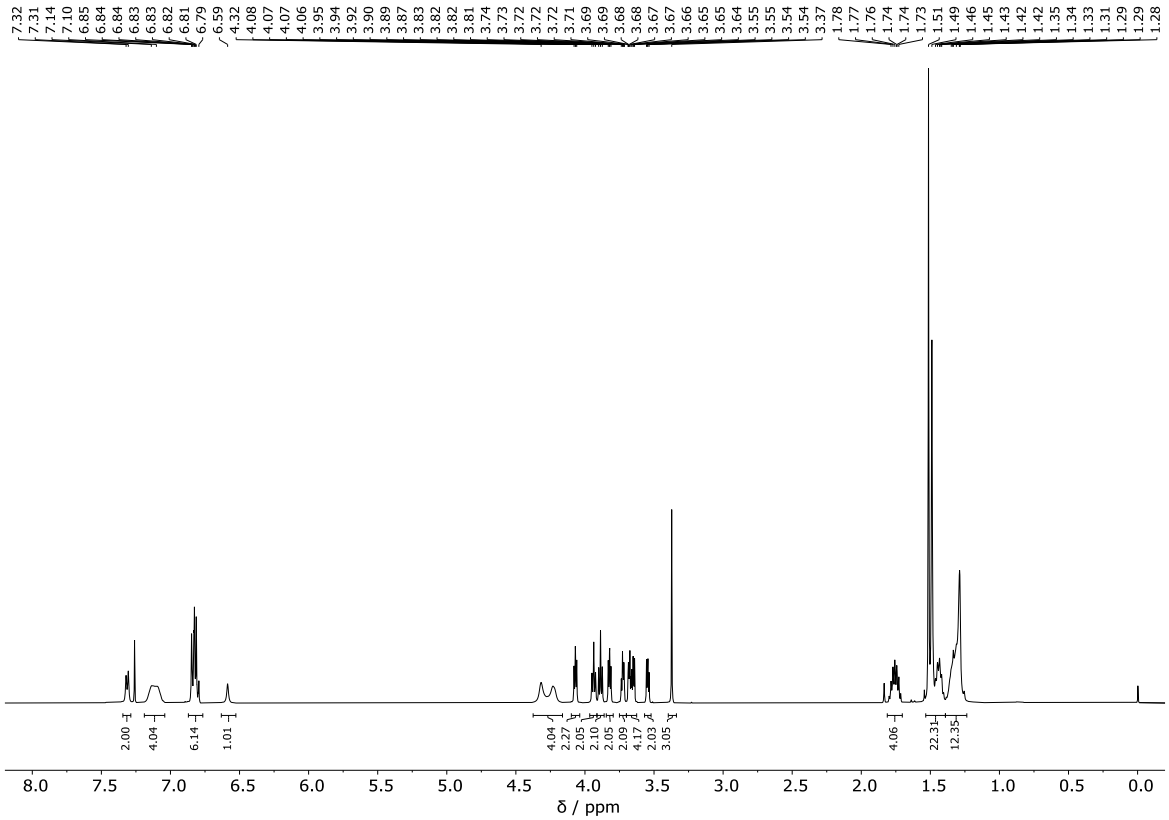

Figure S17. ^{1}H NMR spectrum of **9** (Chloroform-*d*, 298 K, 500 MHz).

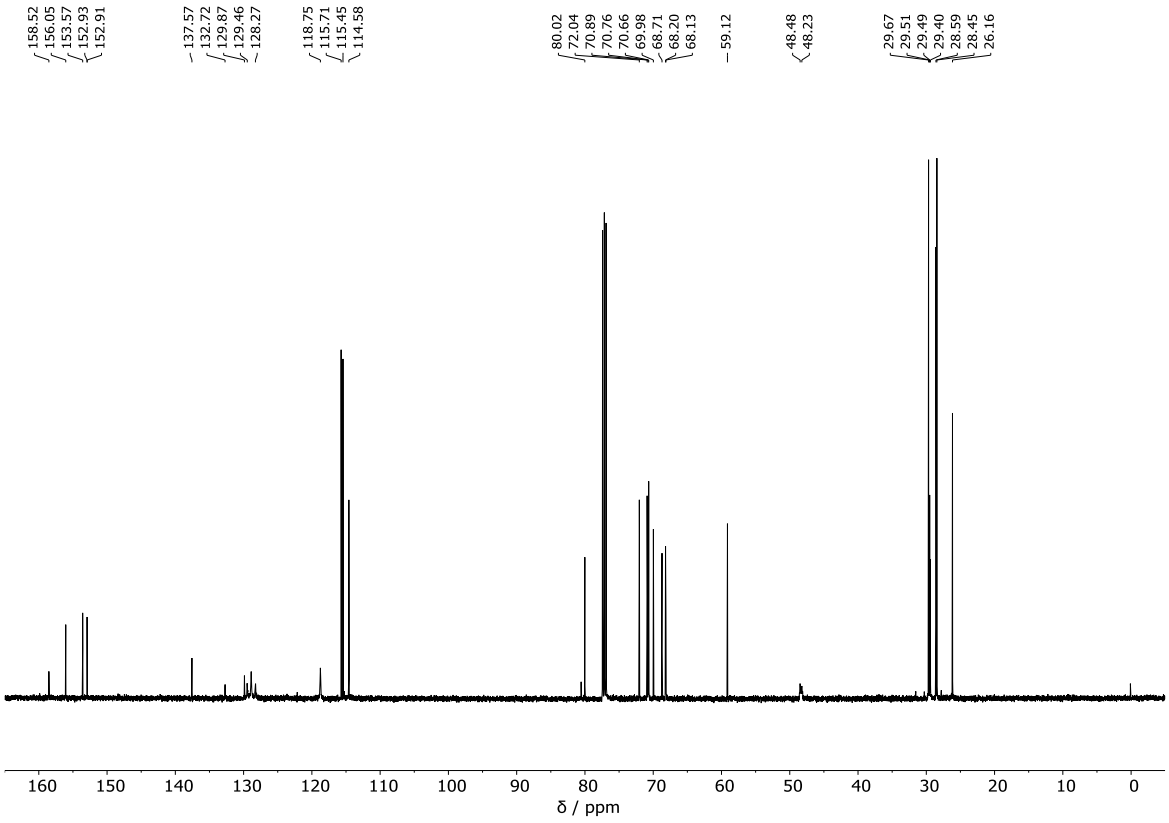

Figure S18. ^{13}C NMR spectrum of **9** (Chloroform-*d*, 298 K, 126 MHz).

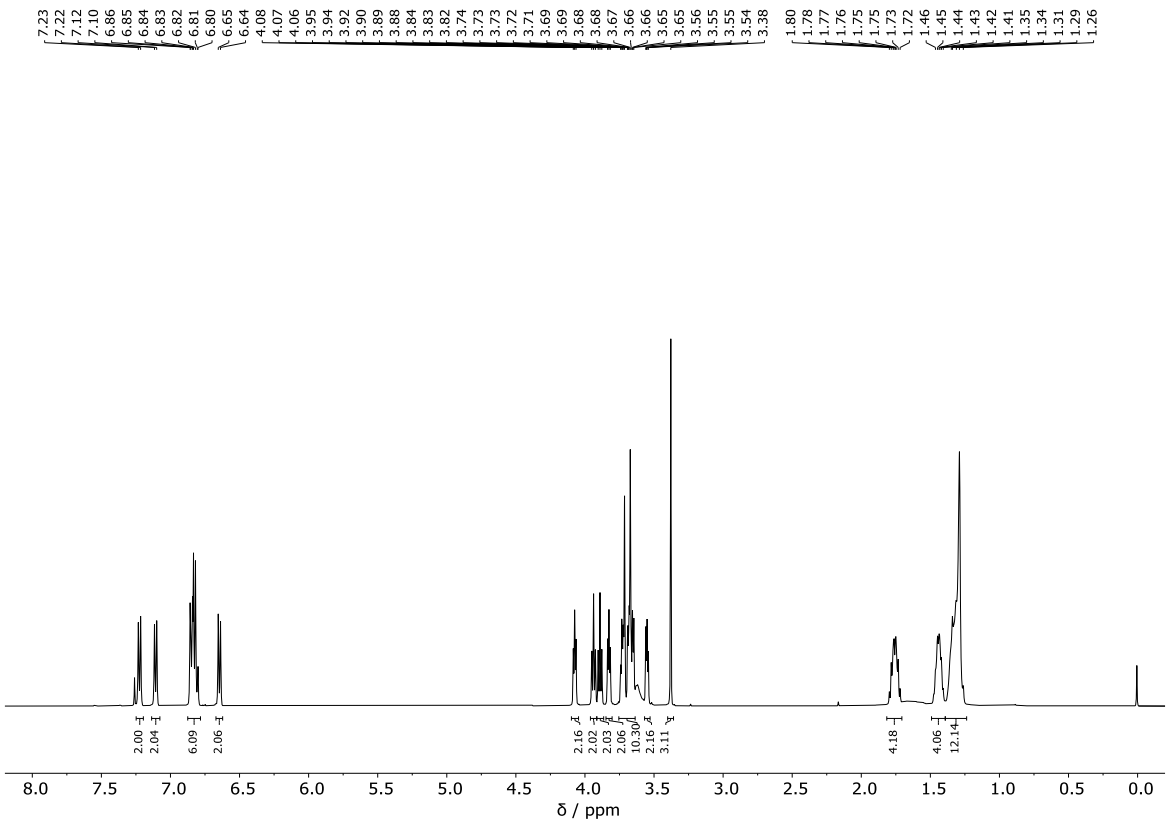

Figure S19. ^{1}H NMR spectrum of **10** (Chloroform-*d*, 298 K, 500 MHz).

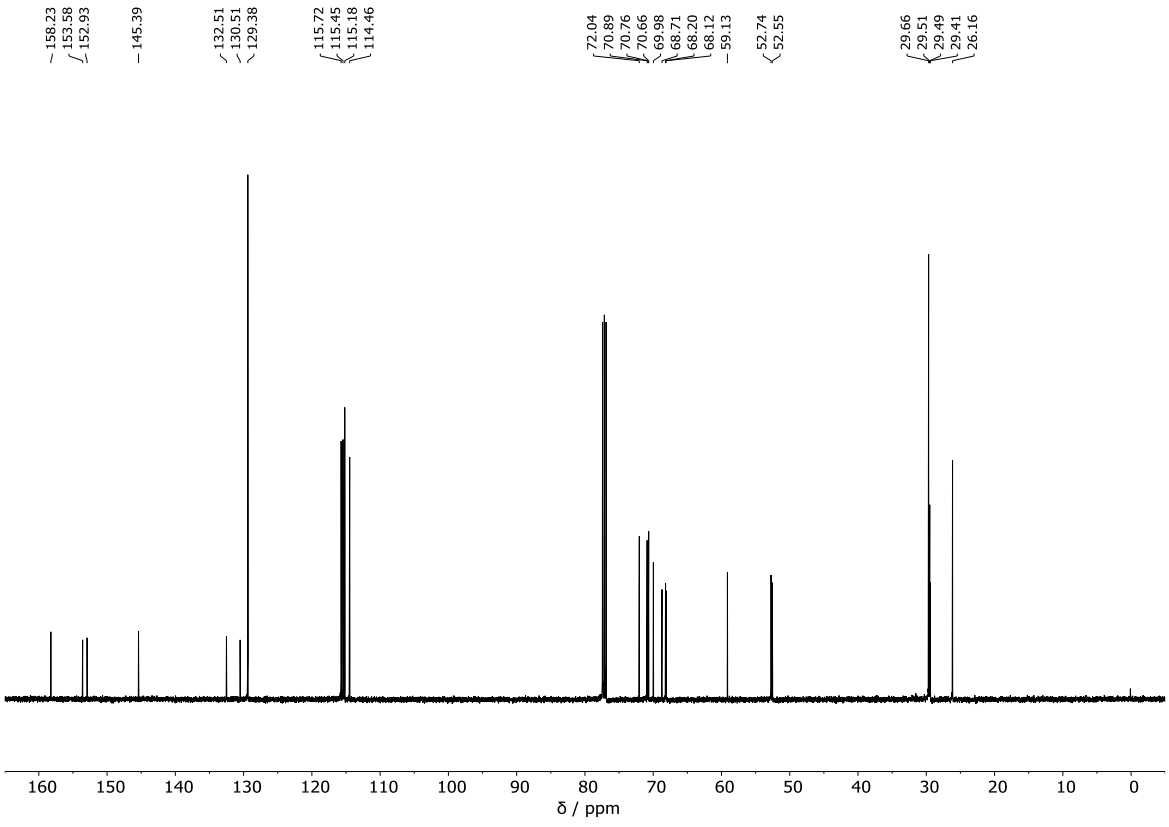

Figure S20. ^{13}C NMR spectrum of **10** (Chloroform-*d*, 298 K, 126 MHz).

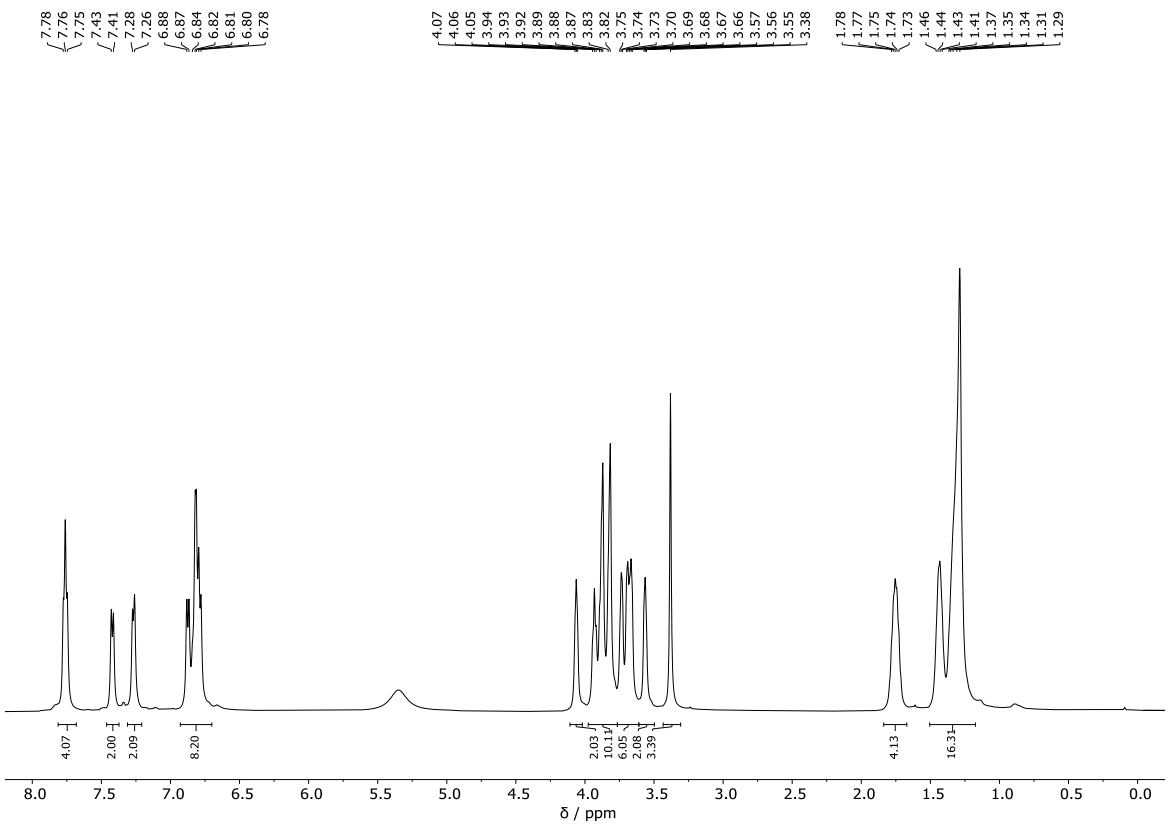

Figure S21. ^{1}H NMR spectrum of **11** (Chloroform-*d*, 298 K, 500 MHz).

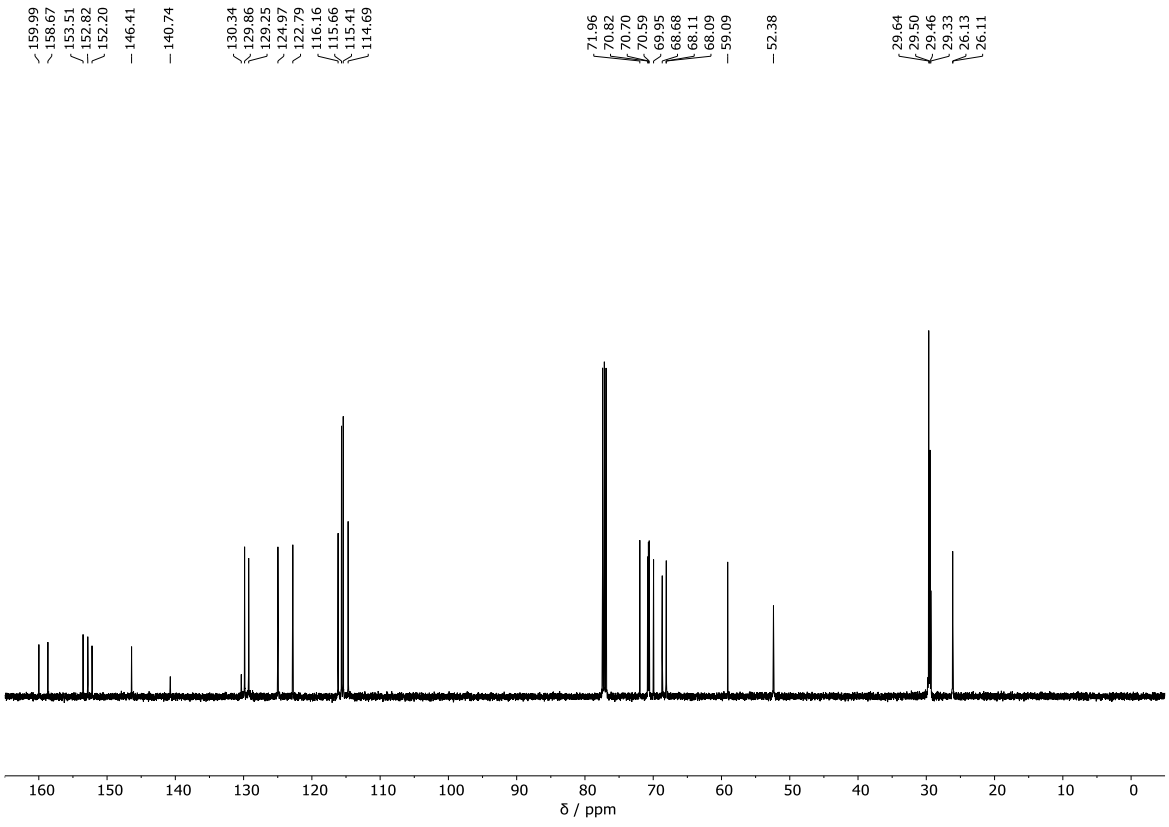

Figure S22. ^{13}C NMR spectrum of **11** (Chloroform-*d*, 298 K, 126 MHz).

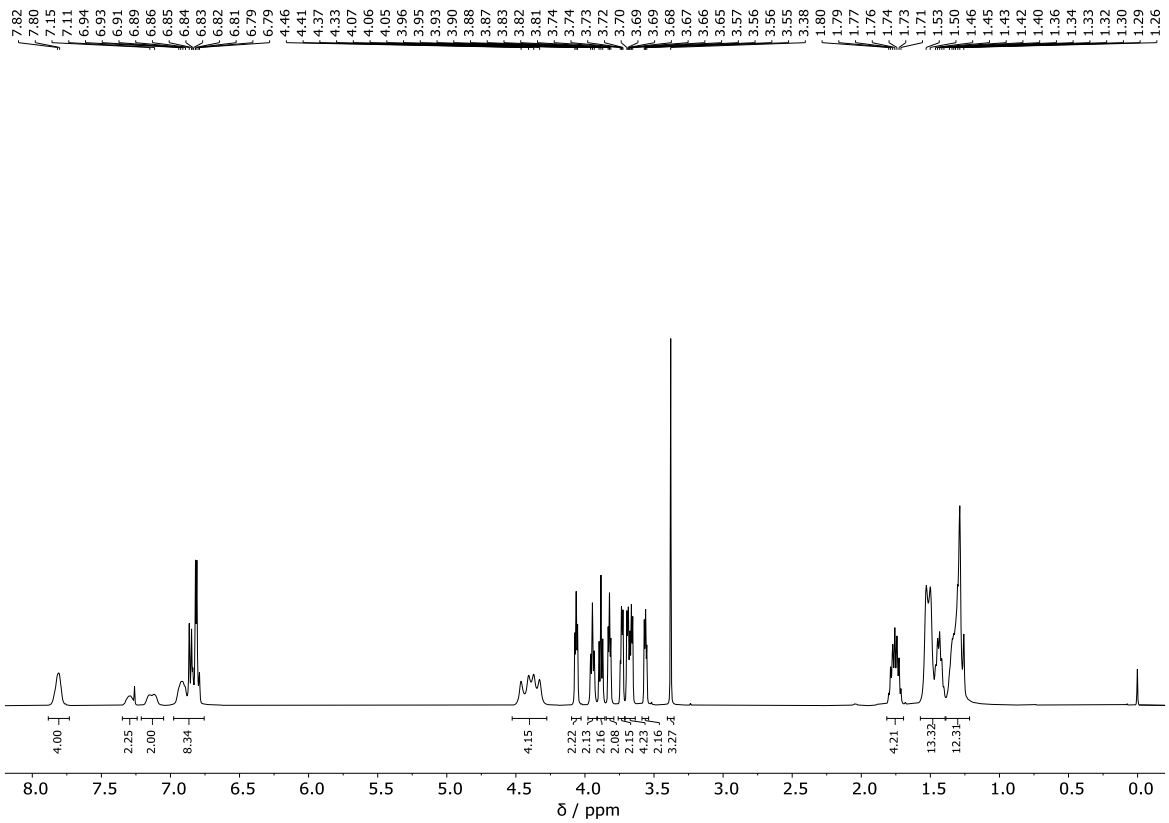

Figure S23. ^{1}H NMR spectrum of **12** (Chloroform-*d*, 298 K, 500 MHz).

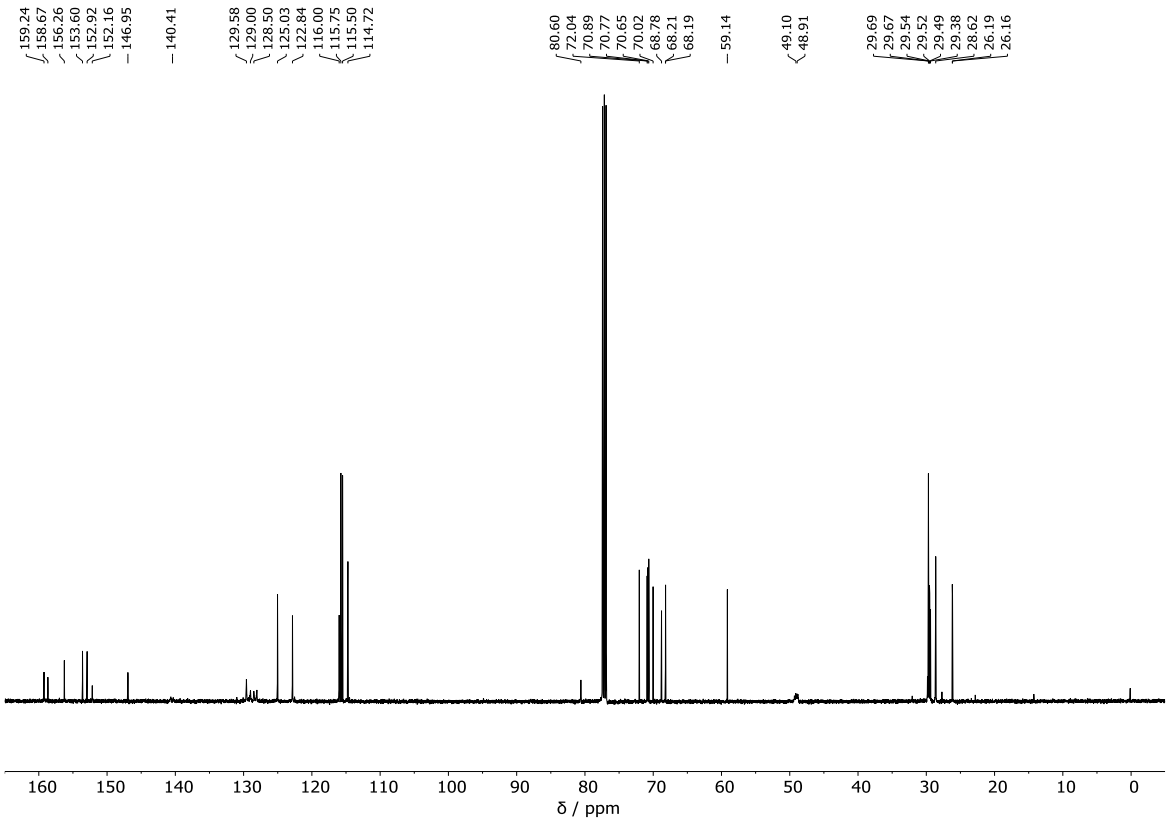

Figure S24. ^{13}C NMR spectrum of **12** (Chloroform-*d*, 298 K, 126 MHz).

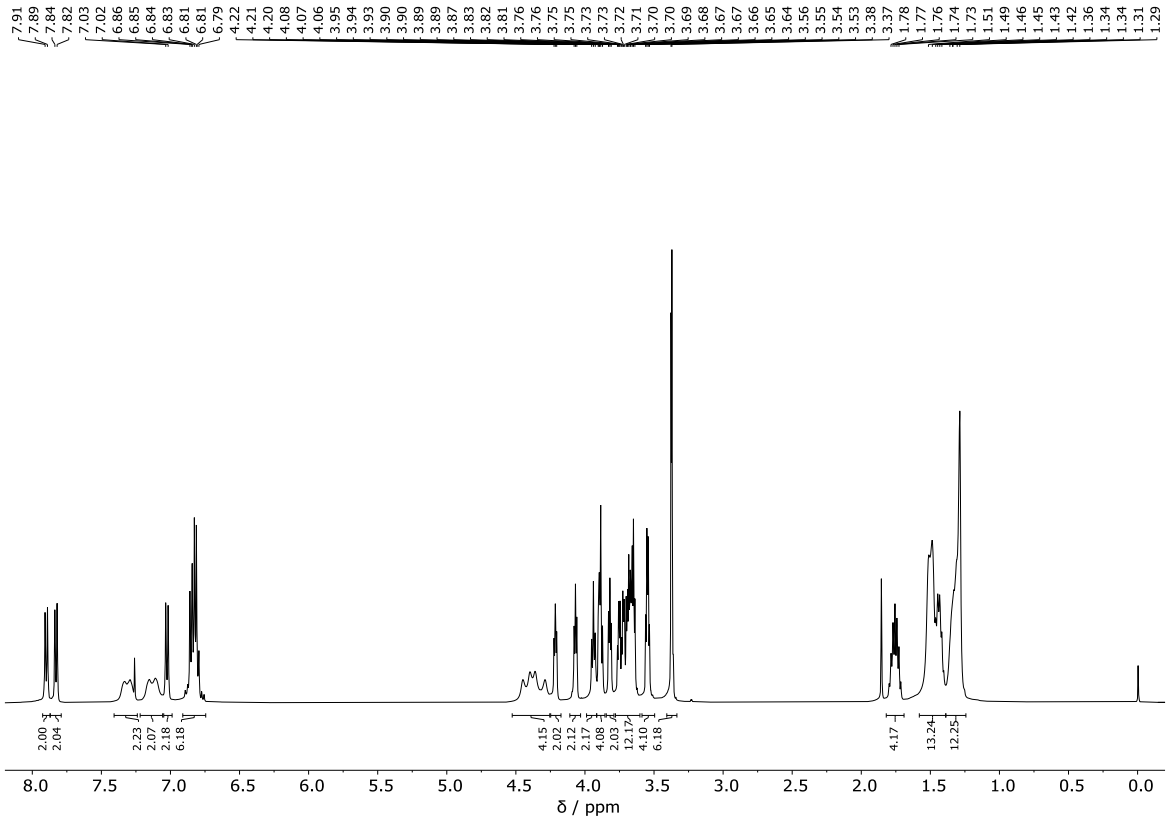

Figure S25. ^{1}H NMR spectrum of **13** (Chloroform-*d*, 298 K, 500 MHz).

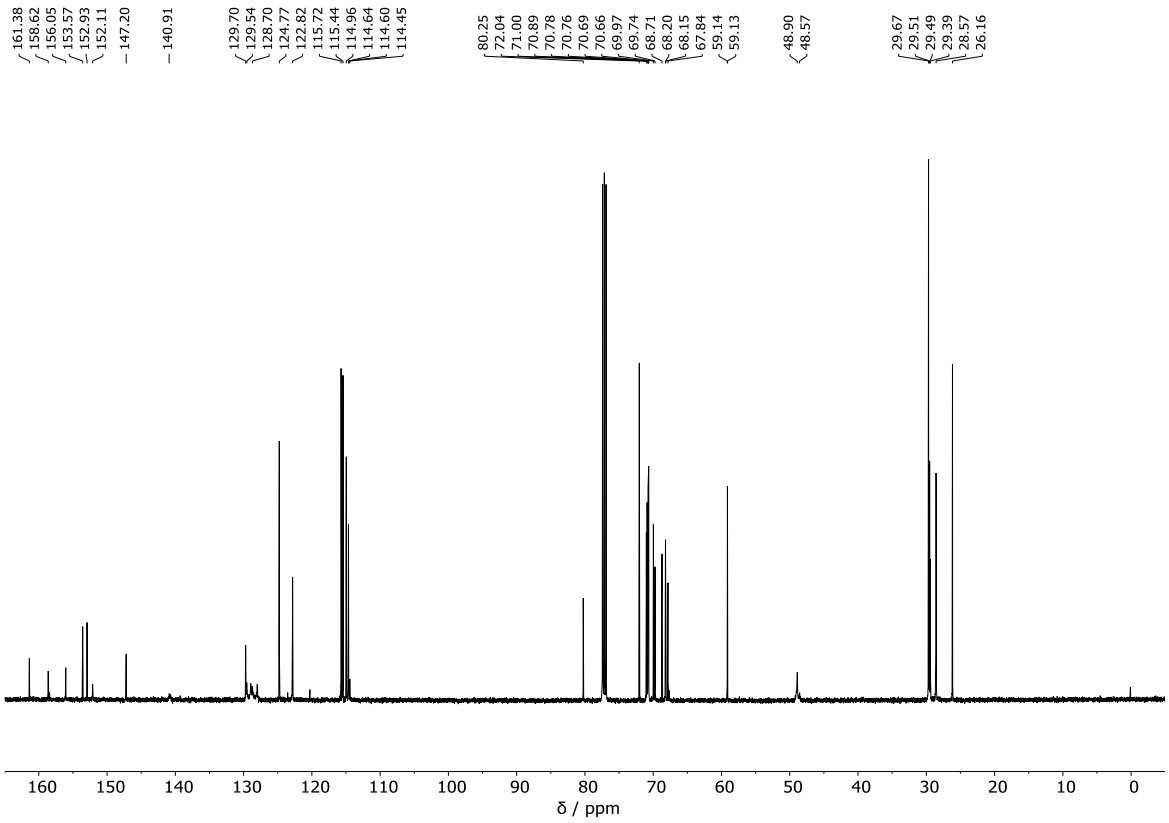

Figure S26. ^{13}C NMR spectrum of **13** (Chloroform-*d*, 298 K, 126 MHz).

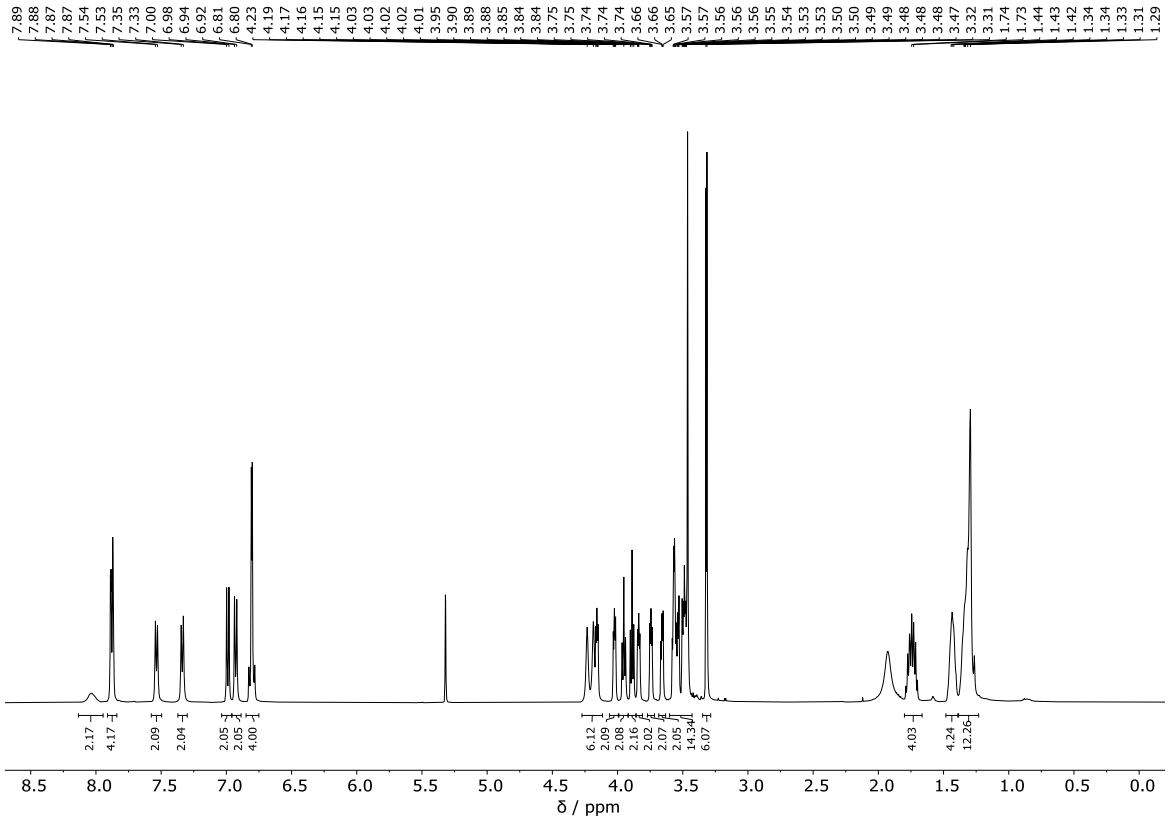

Figure S27. ^{1}H NMR spectrum of *E*-**C12** (Methylene Chloride-d_2:Methanol-d_4 99:1, 298 K, 500 MHz).

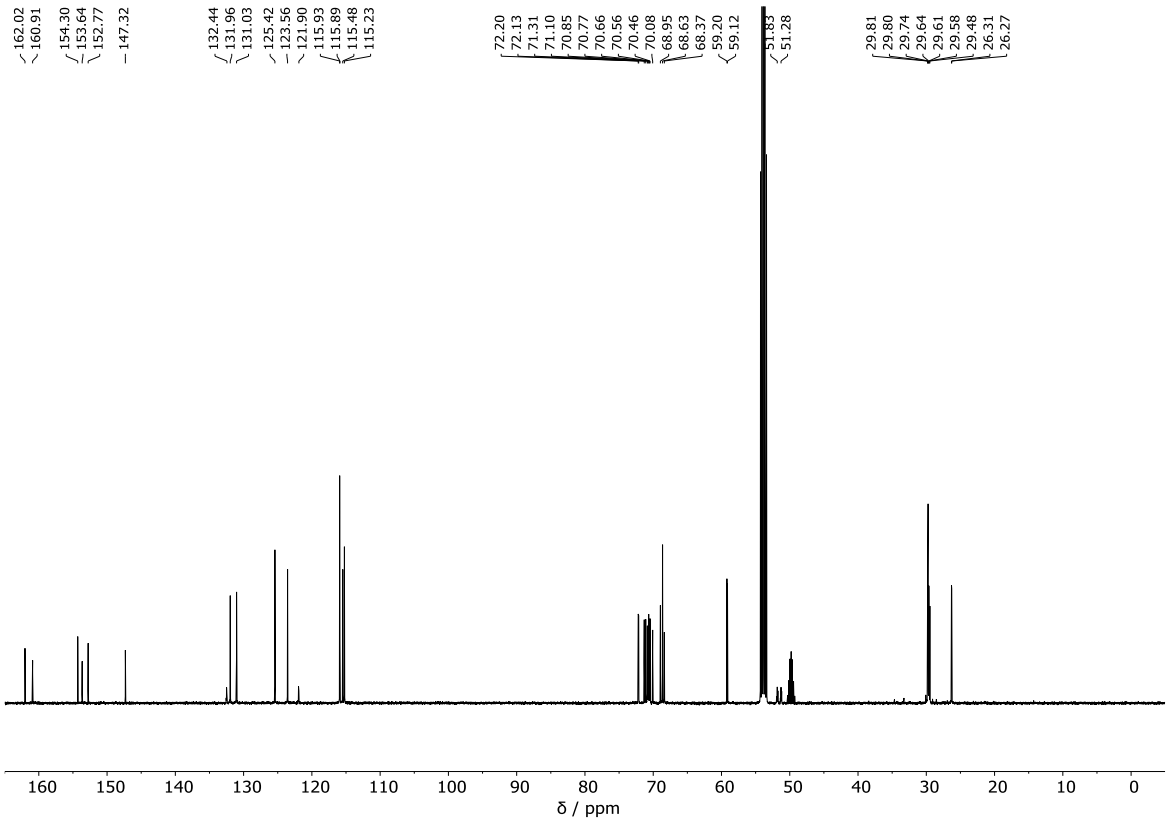

Figure S28. ^{13}C NMR spectrum of *E*-**C12** (Methylene Chloride-d_2:Methanol-d_4 99:1, 298 K, 126 MHz).

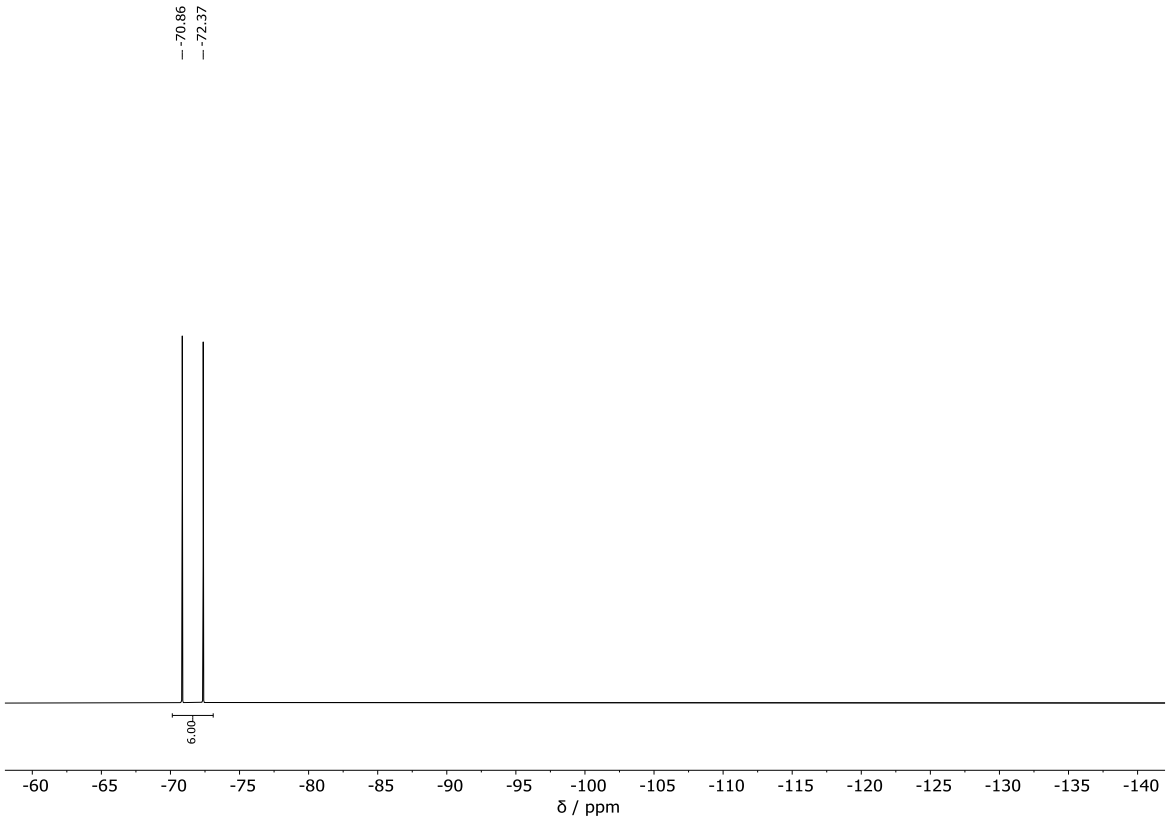

Figure S29. ^{19}F NMR spectrum of *E*-**C12** (Methylene Chloride-d_2:Methanol-d_4 99:1, 298 K, 470 MHz).

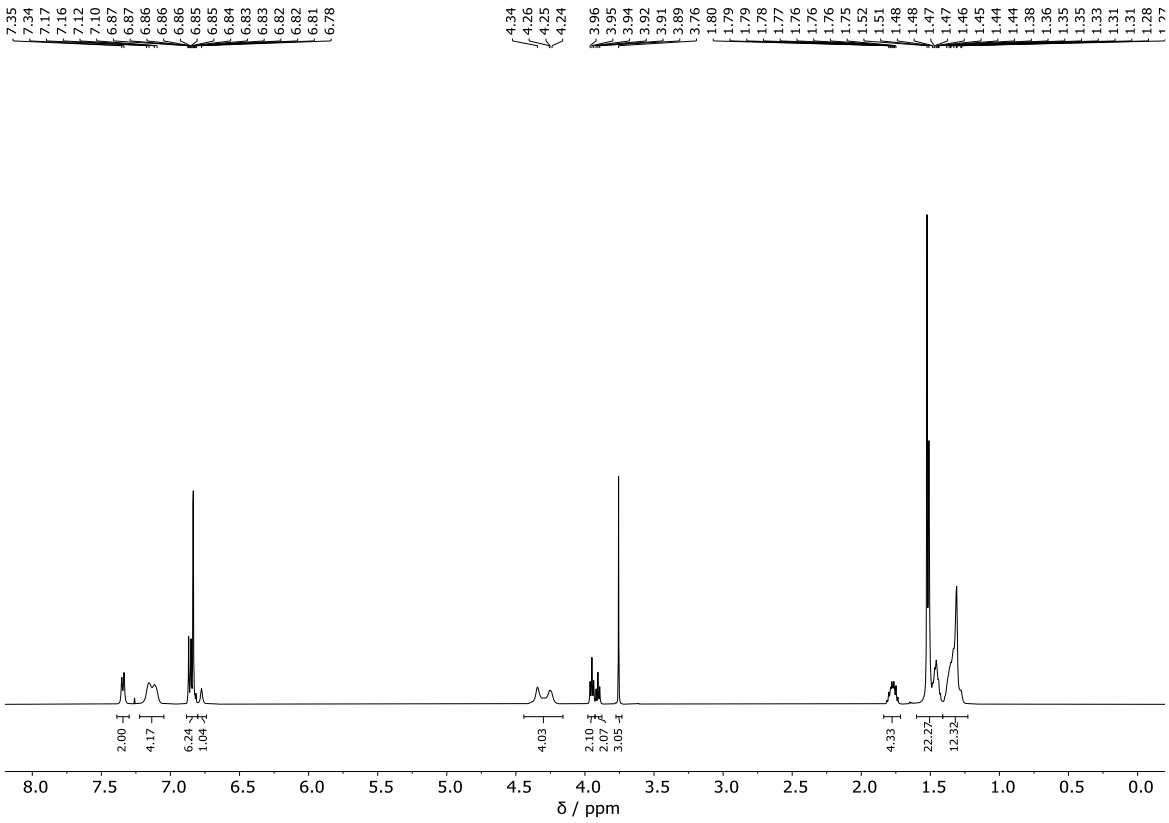

Figure S30. ^{1}H NMR spectrum of **14** (Chloroform-*d*, 298 K, 500 MHz).

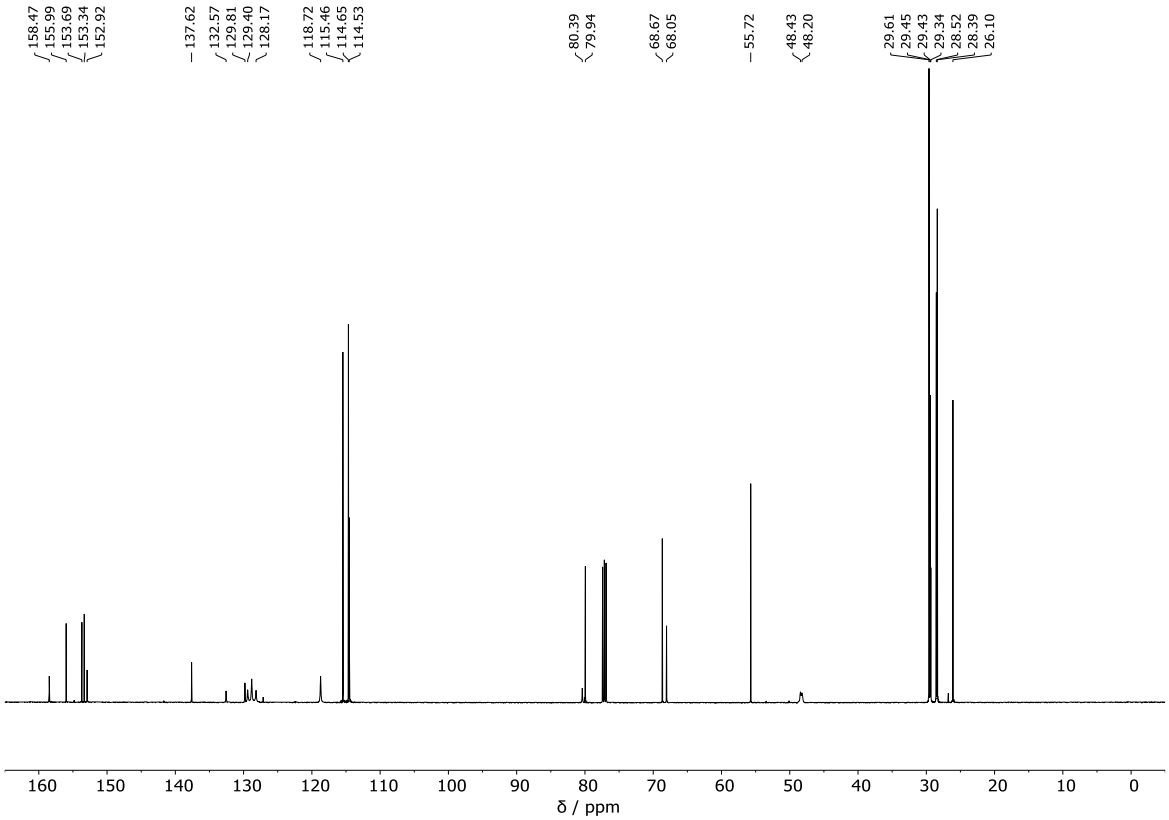

Figure S31. ^{13}C NMR spectrum of **14** (Chloroform-*d*, 298 K, 126 MHz).

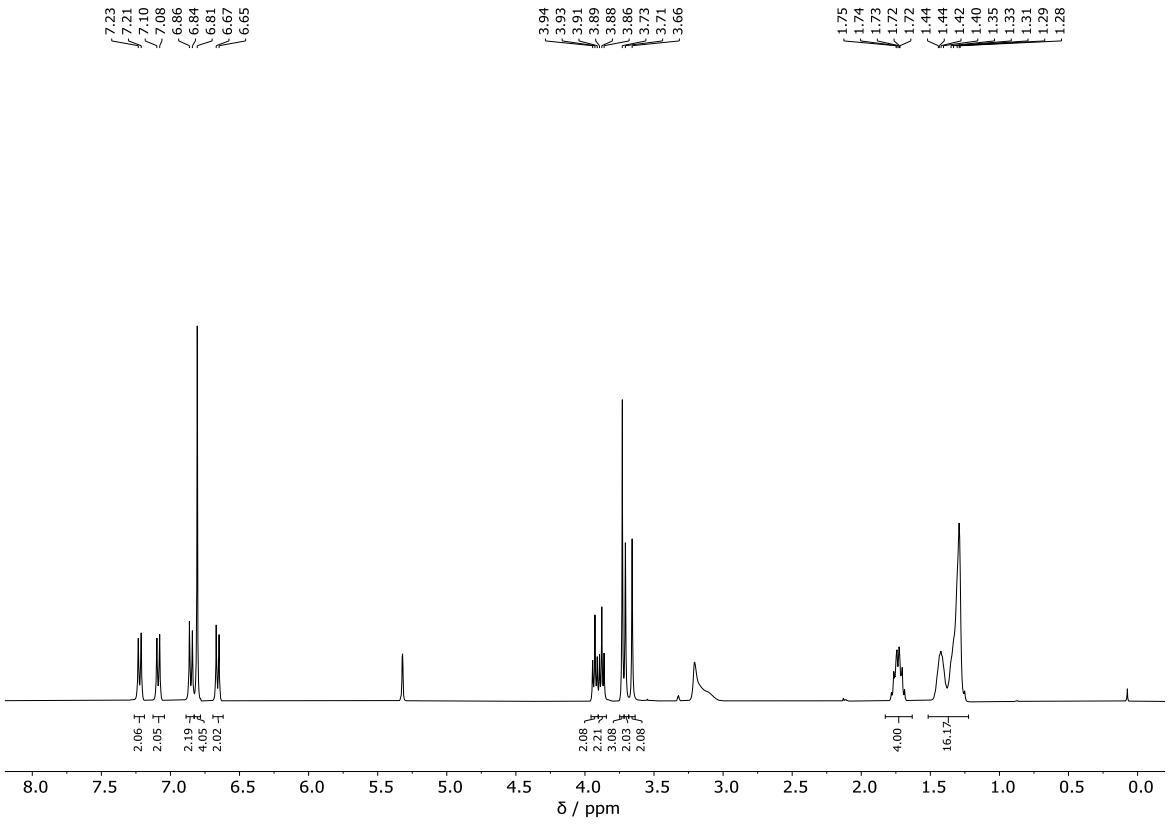

Figure S32. ^{1}H NMR spectrum of **15** (Methylene Chloride-d_2:Methanol-d_4 99:1, 298 K, 400 MHz).

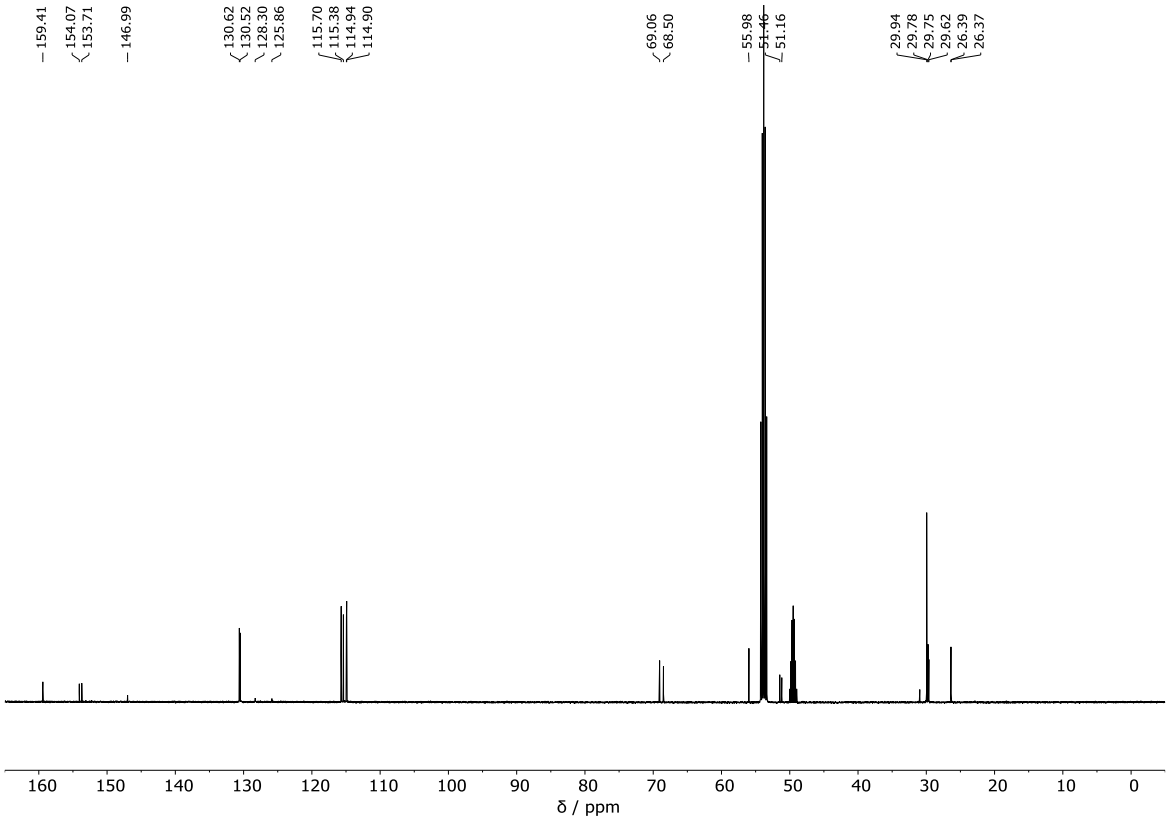

Figure S33. ^{13}C NMR spectrum of **15** (Methylene Chloride-d_2:Methanol-d_4 99:1, 298 K, 126 MHz).

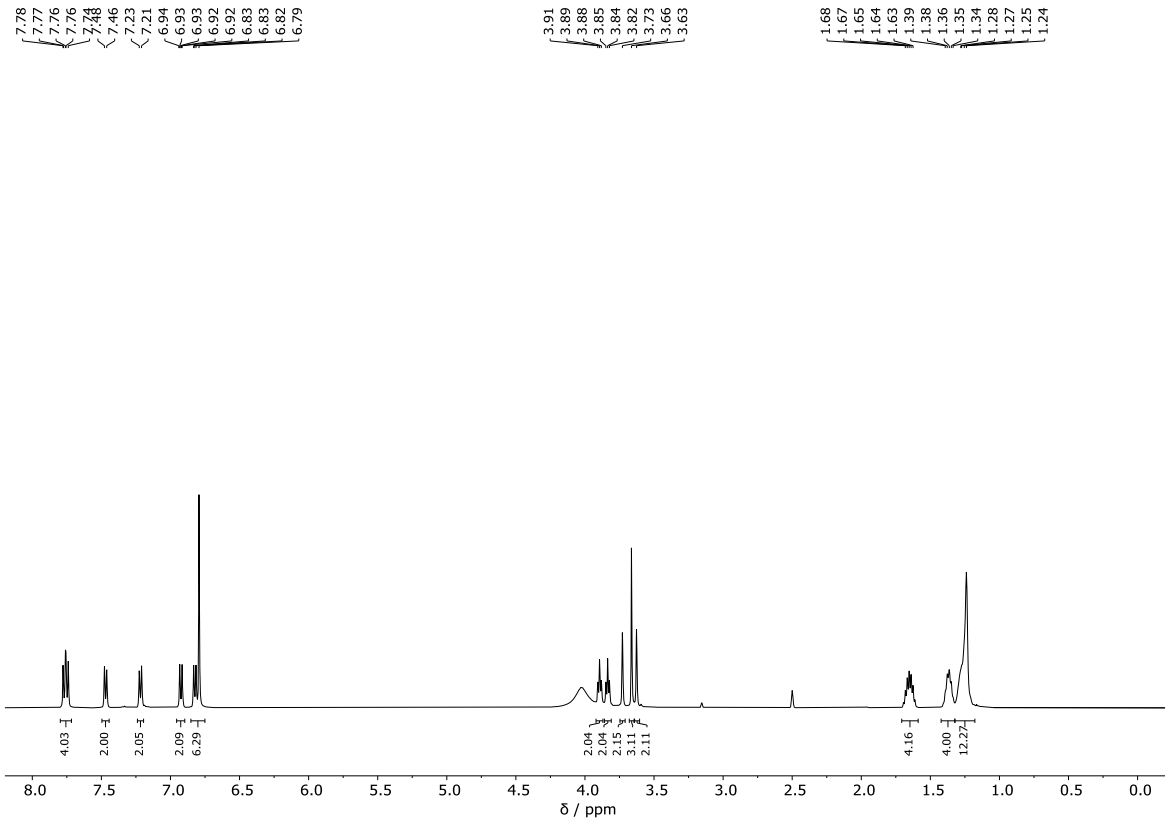

Figure S34. ^{1}H NMR spectrum of **16** (Methylene Sulfoxide-d_6:Methanol-d_4 85:15, 323 K, 500 MHz).

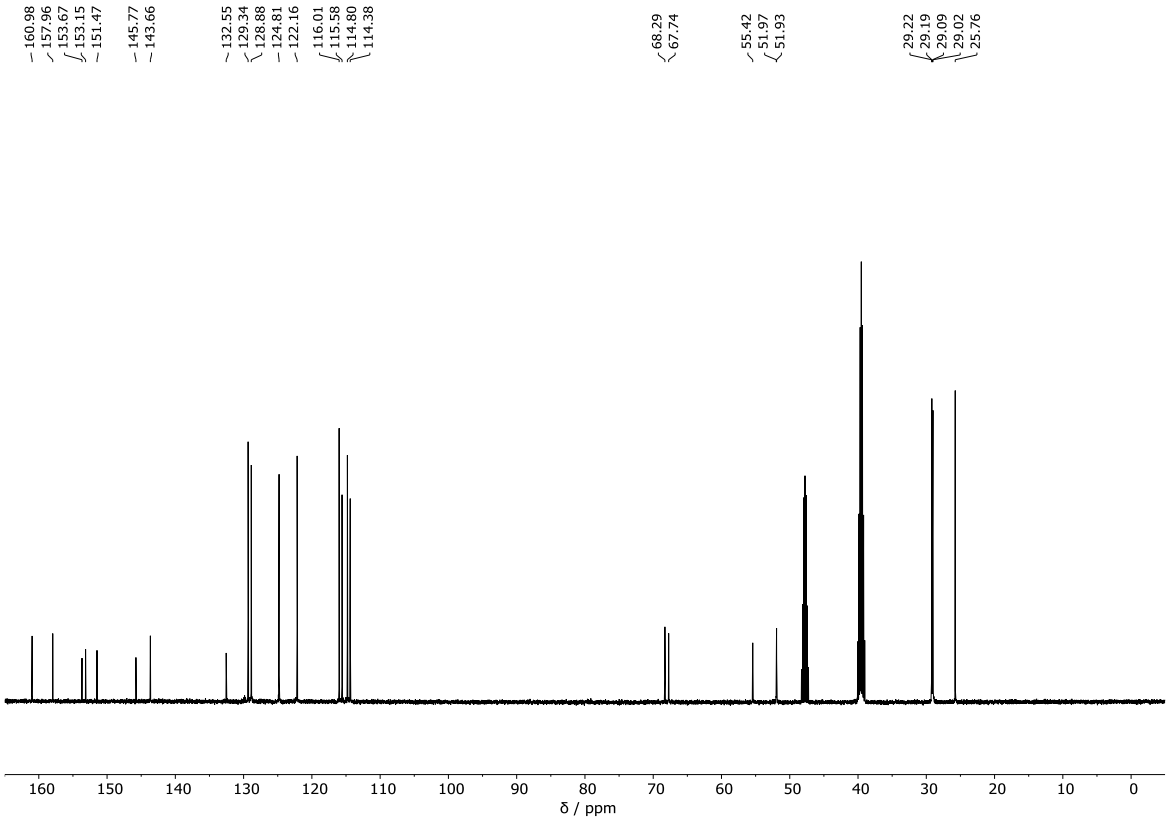

Figure S35. ^{13}C NMR spectrum of **16** (Methylene Sulfoxide-d_6:Methanol-d_4 85:15, 323 K, 126 MHz).

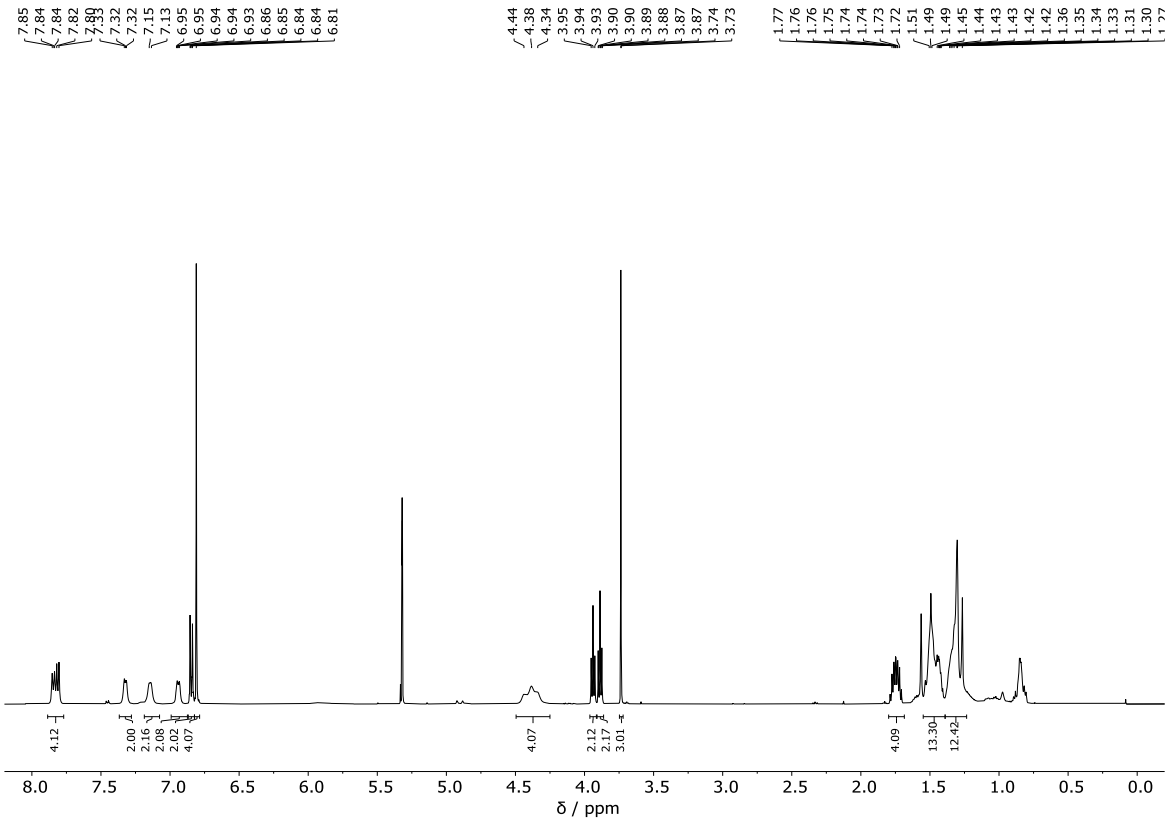

Figure S36. ^{1}H NMR spectrum of **17** (Methylene Chloride-d_2, 298 K, 500 MHz).

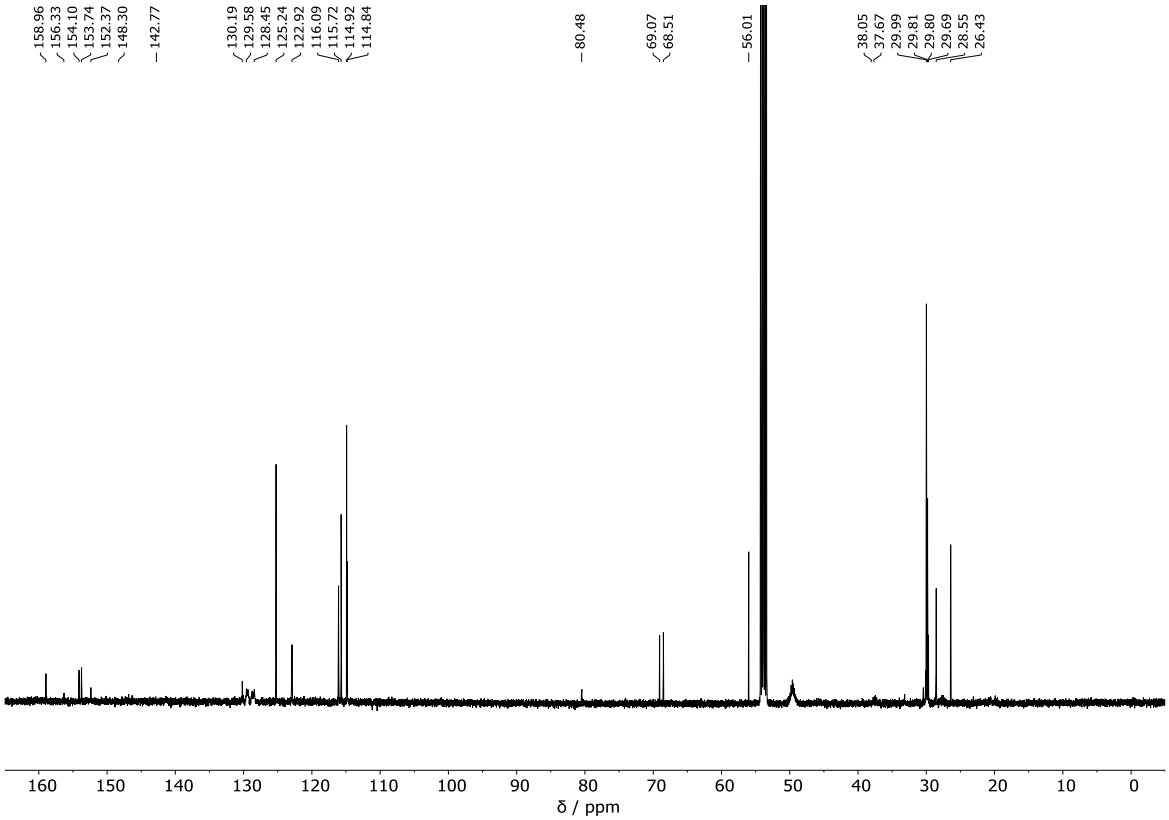

Figure S37. ^{13}C NMR spectrum of **17** (Methylene Chloride-d_2:Methanol-d_4 99:1, 298 K, 126 MHz).

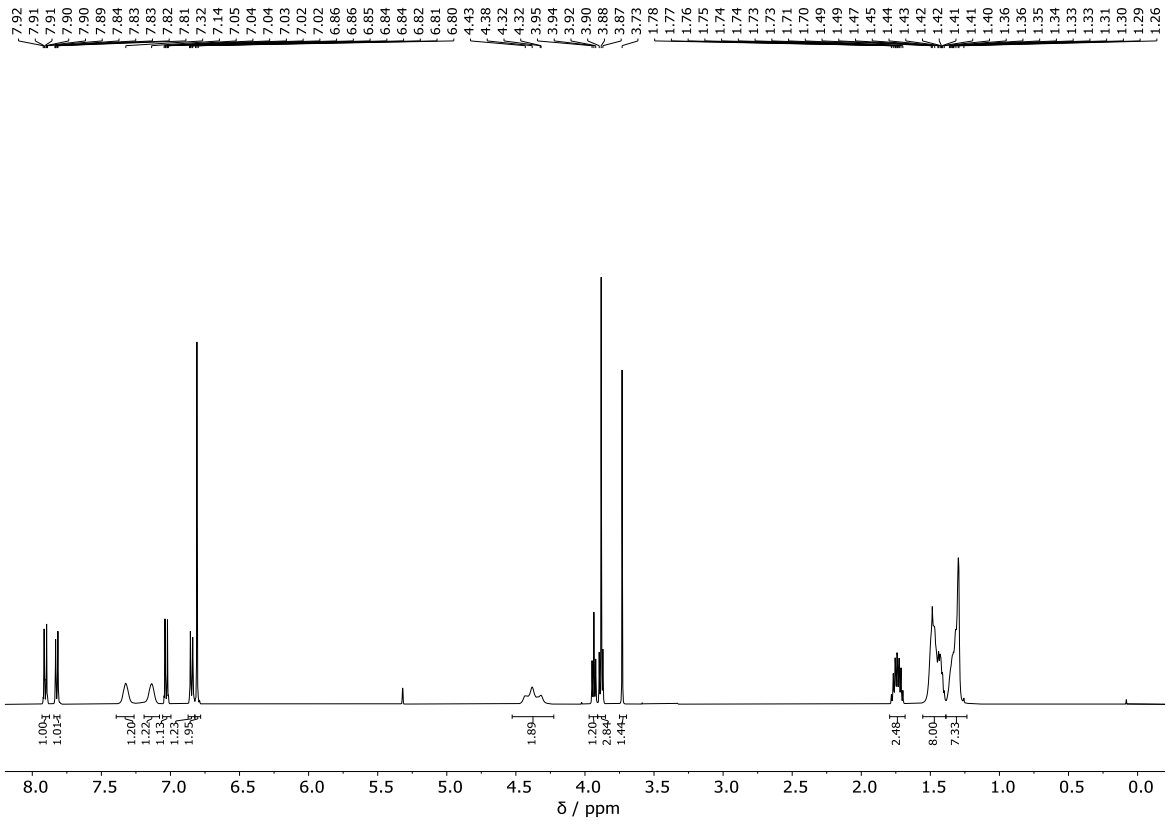

Figure S38. ^{1}H NMR spectrum of **18** (Methylene Chloride-d_2:Methanol-d_4 99:1, 298 K, 500 MHz).

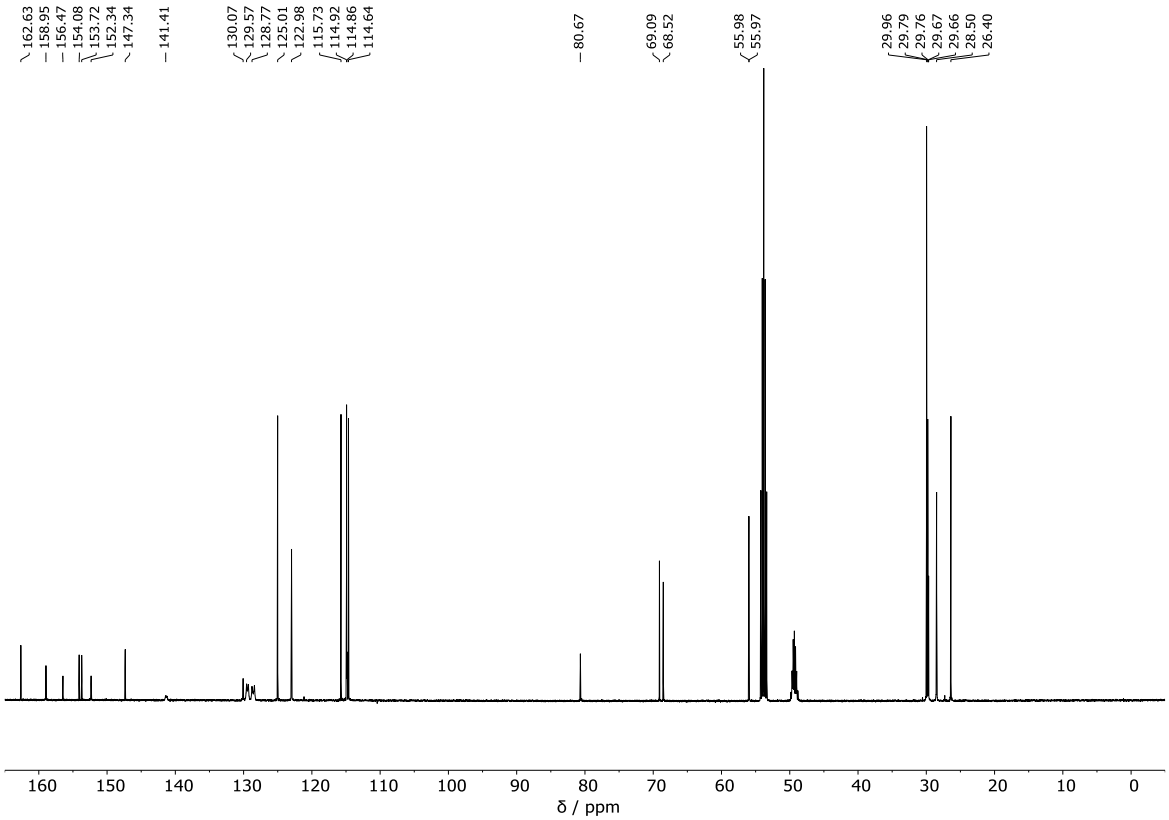

Figure S39. ^{13}C NMR spectrum of **18** (Methylene Chloride-d_2:Methanol-d_4 99:1, 298 K, 126 MHz).

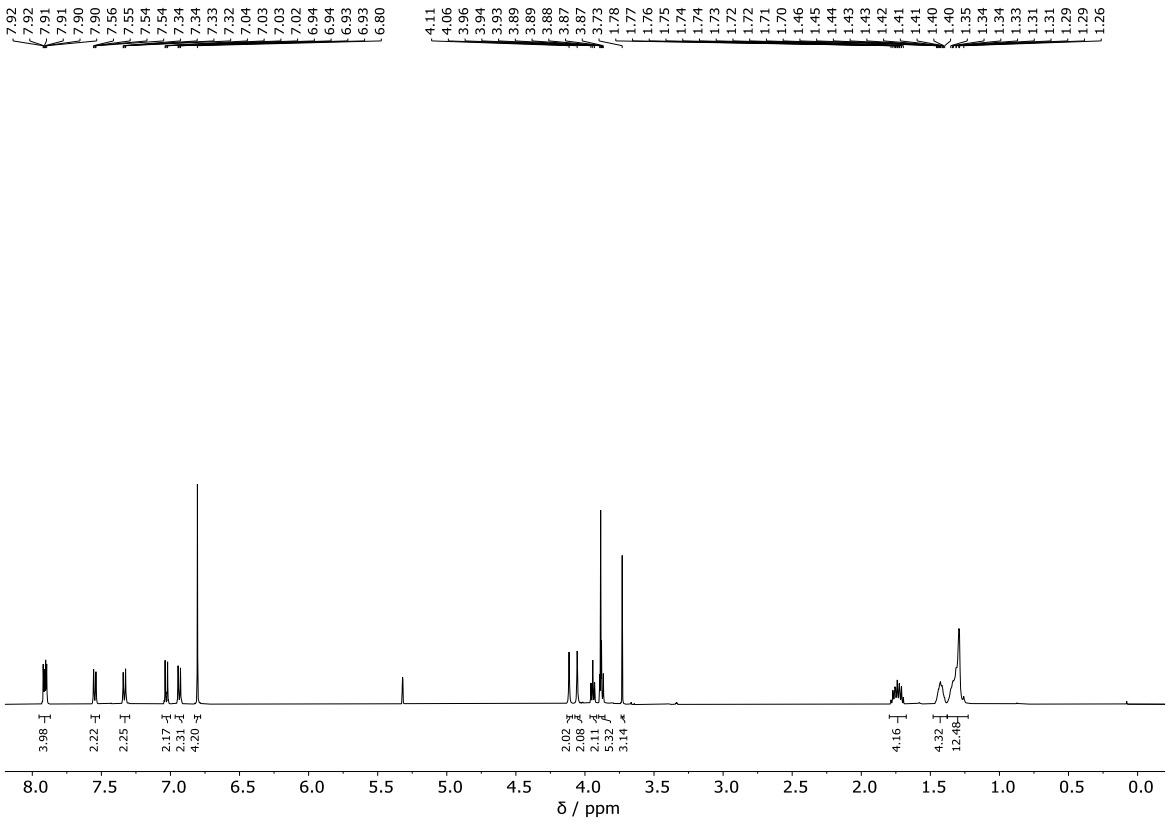

Figure S40. ^{1}H NMR spectrum of ***E*-C12noEG** (Methylene Chloride-d_2:Methanol-d_4 99:1, 298 K, 500 MHz).

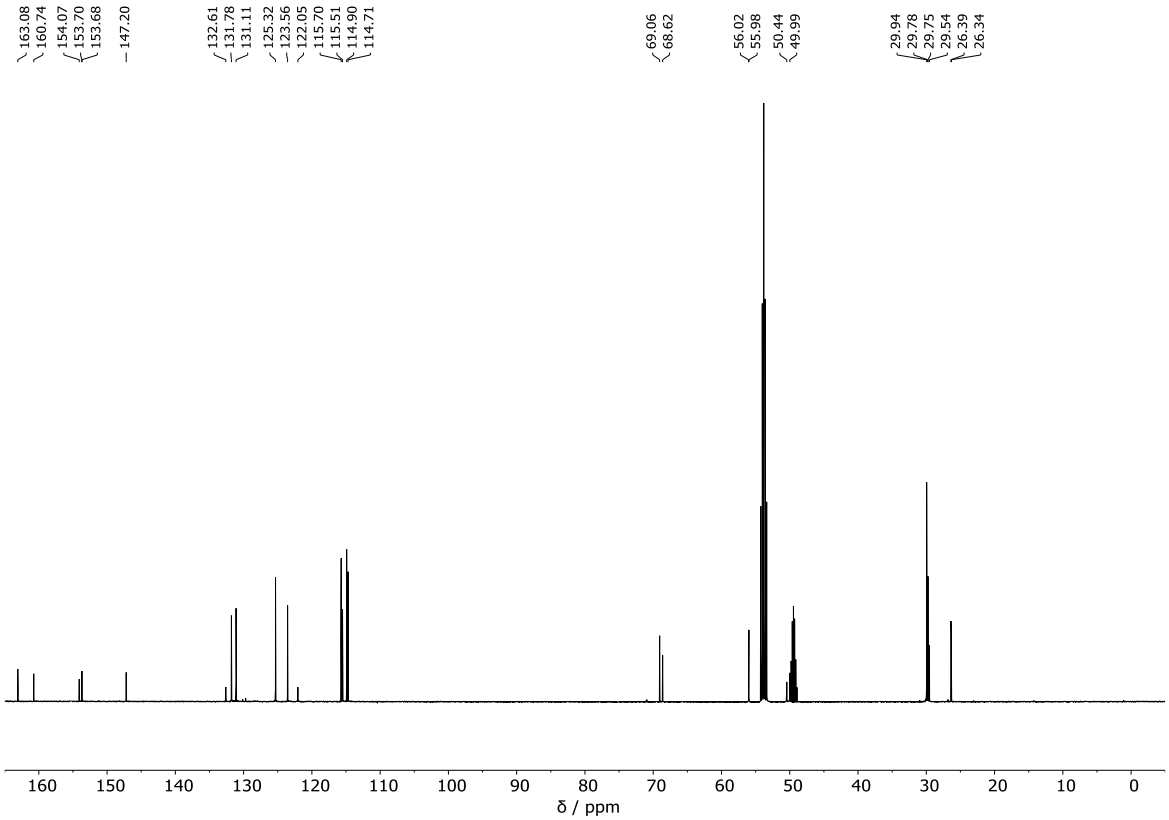

Figure S41. ^{13}C NMR spectrum of ***E*-C12noEG** (Methylene Chloride-d_2:Methanol-d_4 99:1, 298 K, 126 MHz).

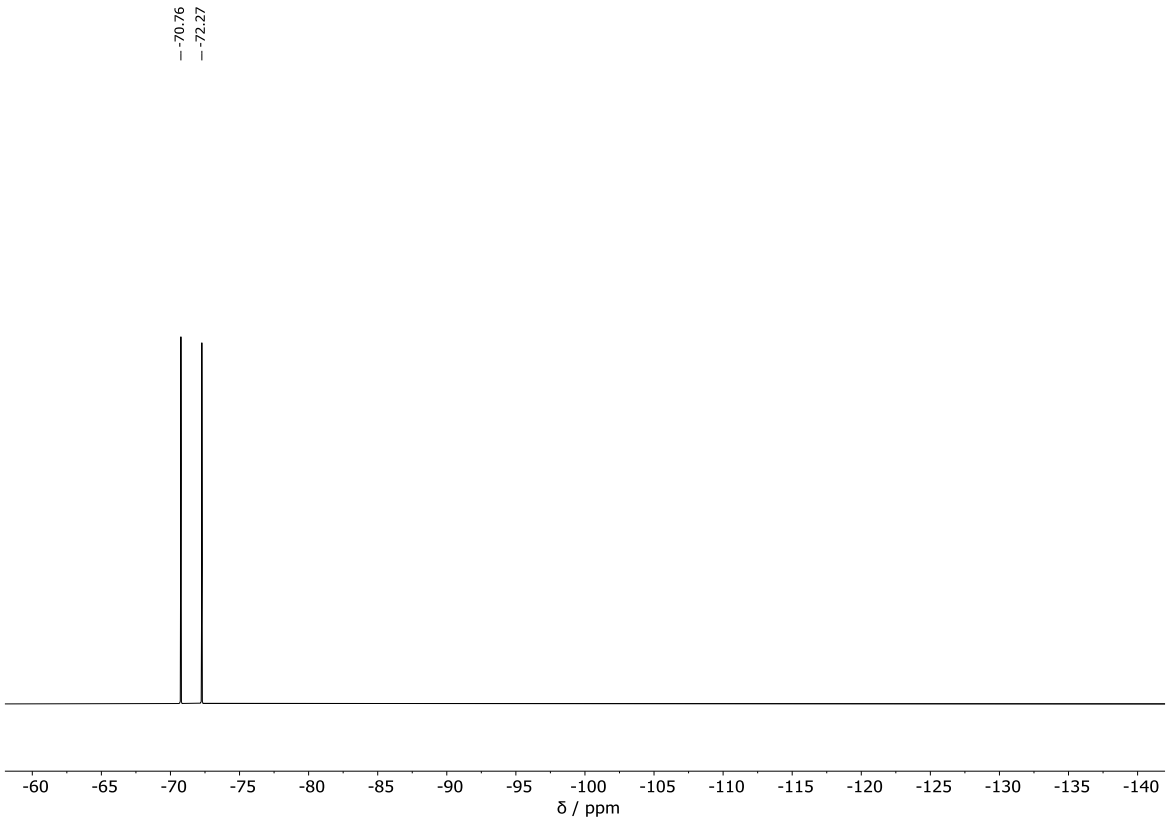

Figure S42. ^{19}F NMR spectrum of ***E*-C12noEG** (Methylene Chloride-d_2:Methanol-d_4 99:1, 298 K, 470 MHz).

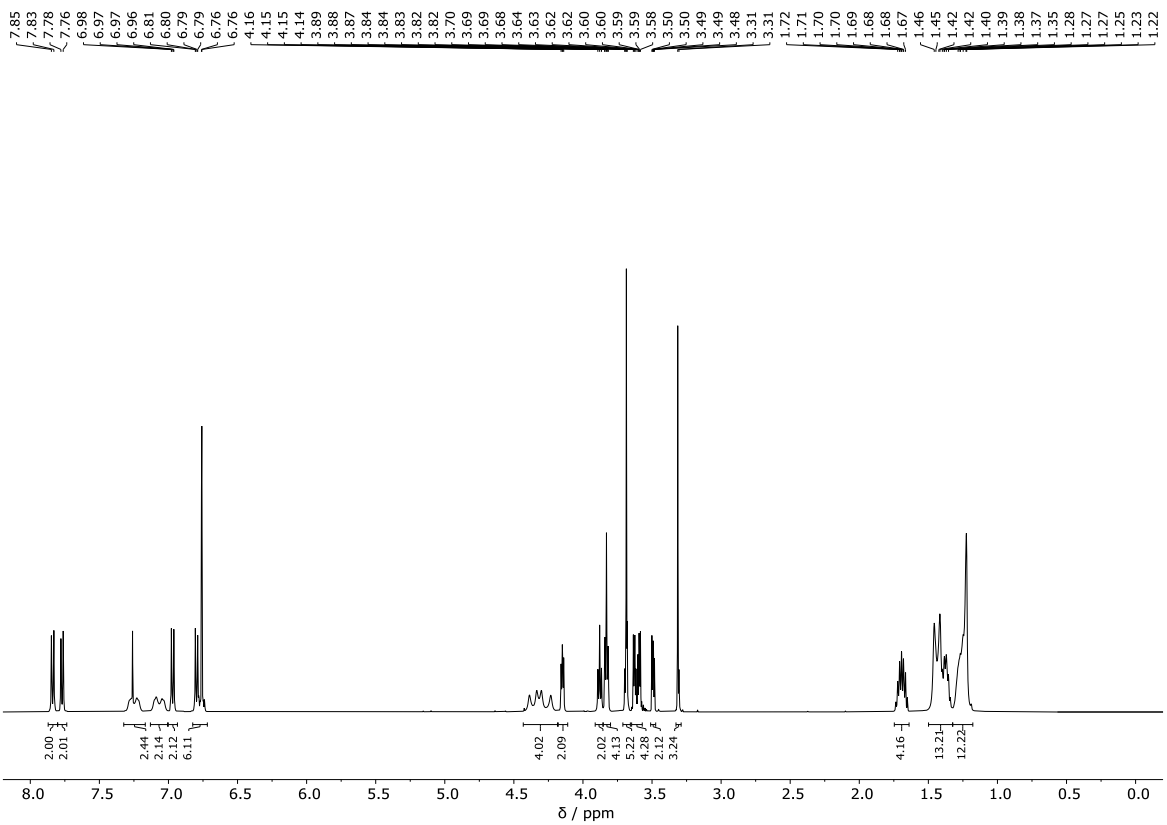

Figure S43. ^{1}H NMR spectrum of **19** (Chloroform-*d*:Methanol-d_4 90:10, 298 K, 500 MHz).

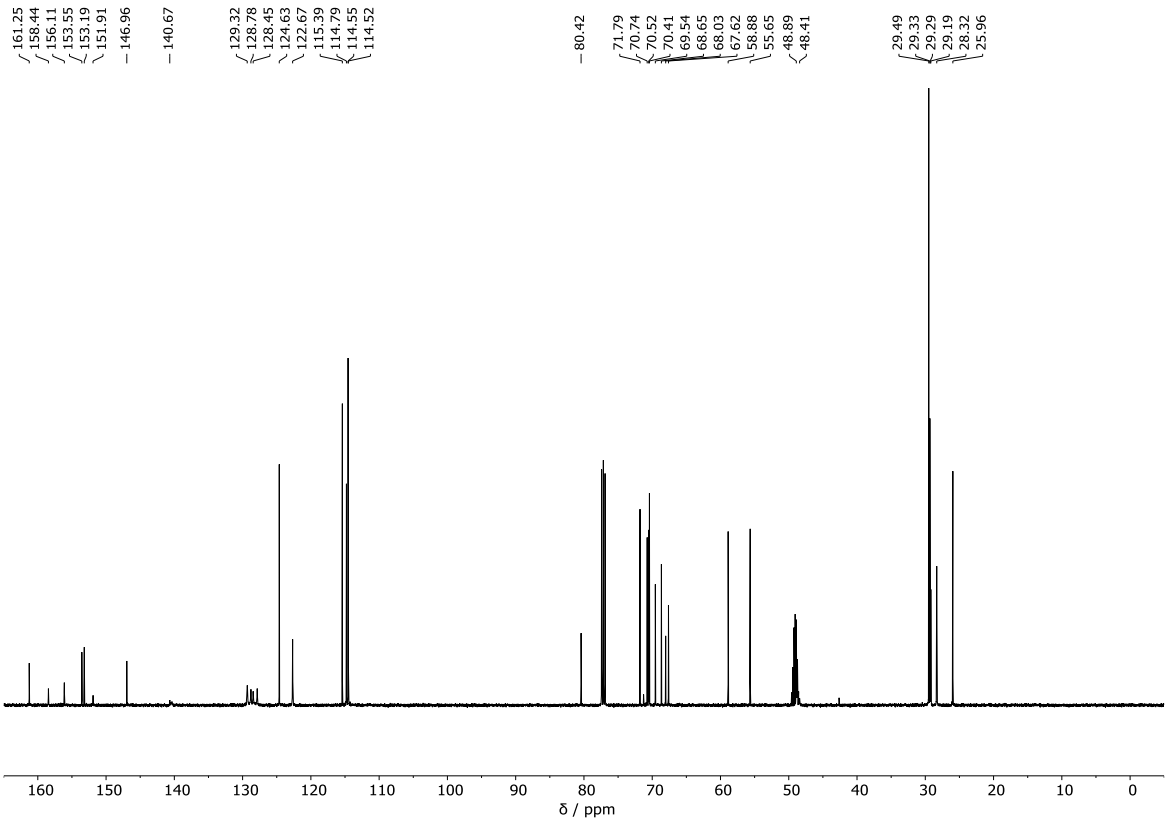

Figure S44. ^{13}C NMR spectrum of **19** (Chloroform-*d*:Methanol-d_4 90:10, 298 K, 126 MHz).

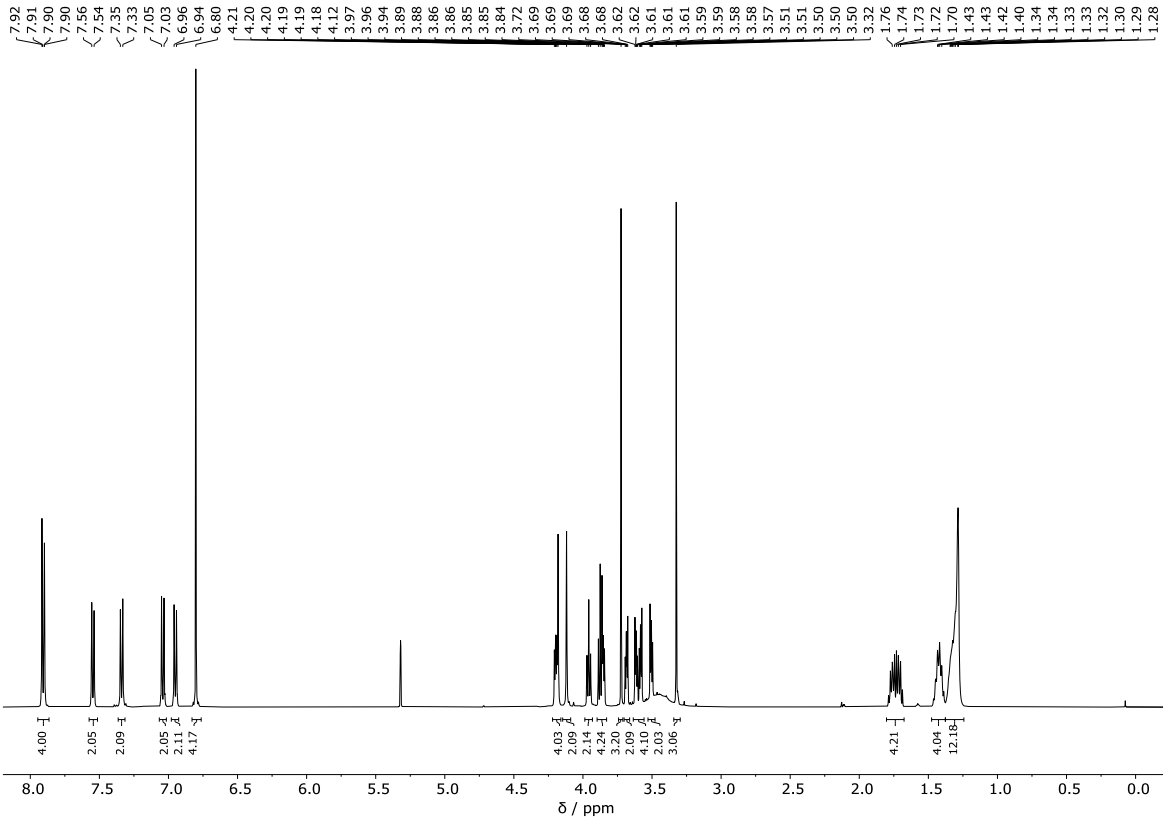

Figure S45. ^{1}H NMR spectrum of *E*-**C12hEG** (Methylene Chloride-d_2:Methanol-d_4 90:10, 298 K, 500 MHz).

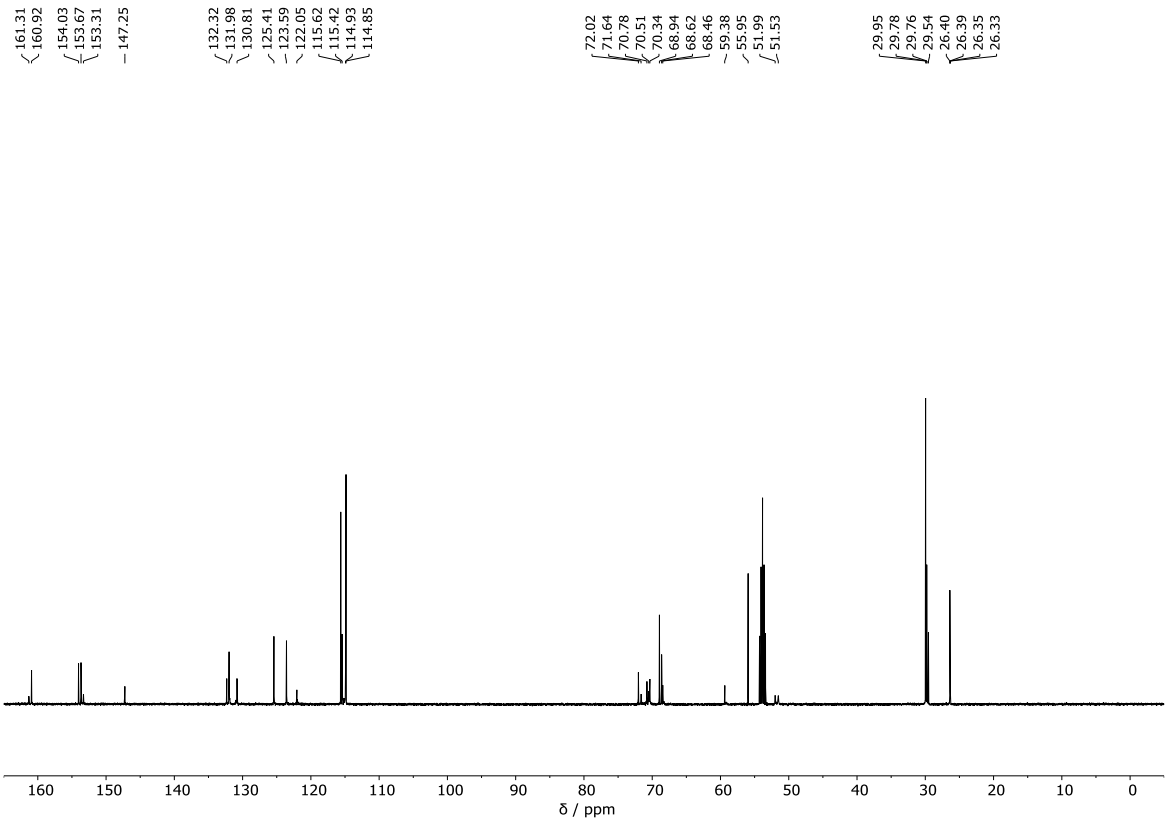

Figure S46. ^{13}C NMR spectrum of *E*-**C12hEG** (Methylene Chloride-d_2:Methanol-d_4 90:10, 298 K, 126 MHz).

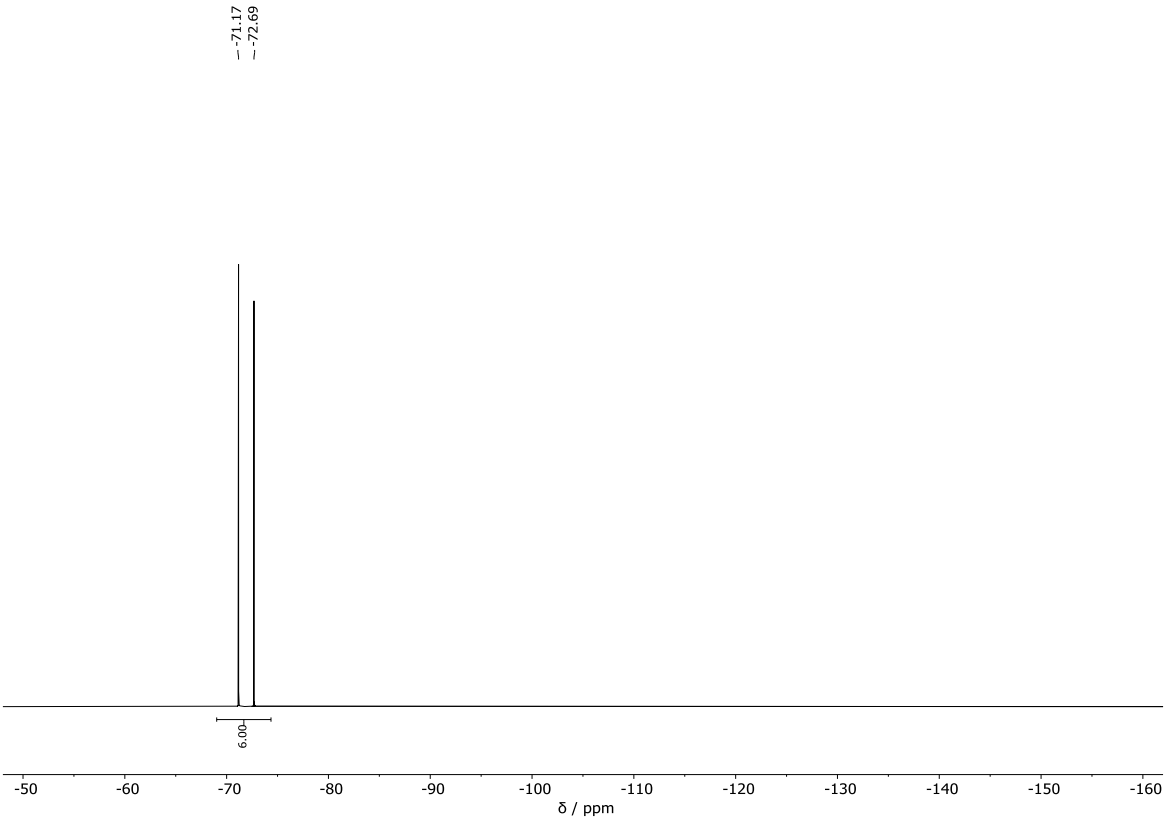

Figure S47. ^{19}F NMR spectrum of ***E*-C12hEG** (Methylene Chloride-d_2:Methanol-d_4 90:10, 298 K, 470 MHz).

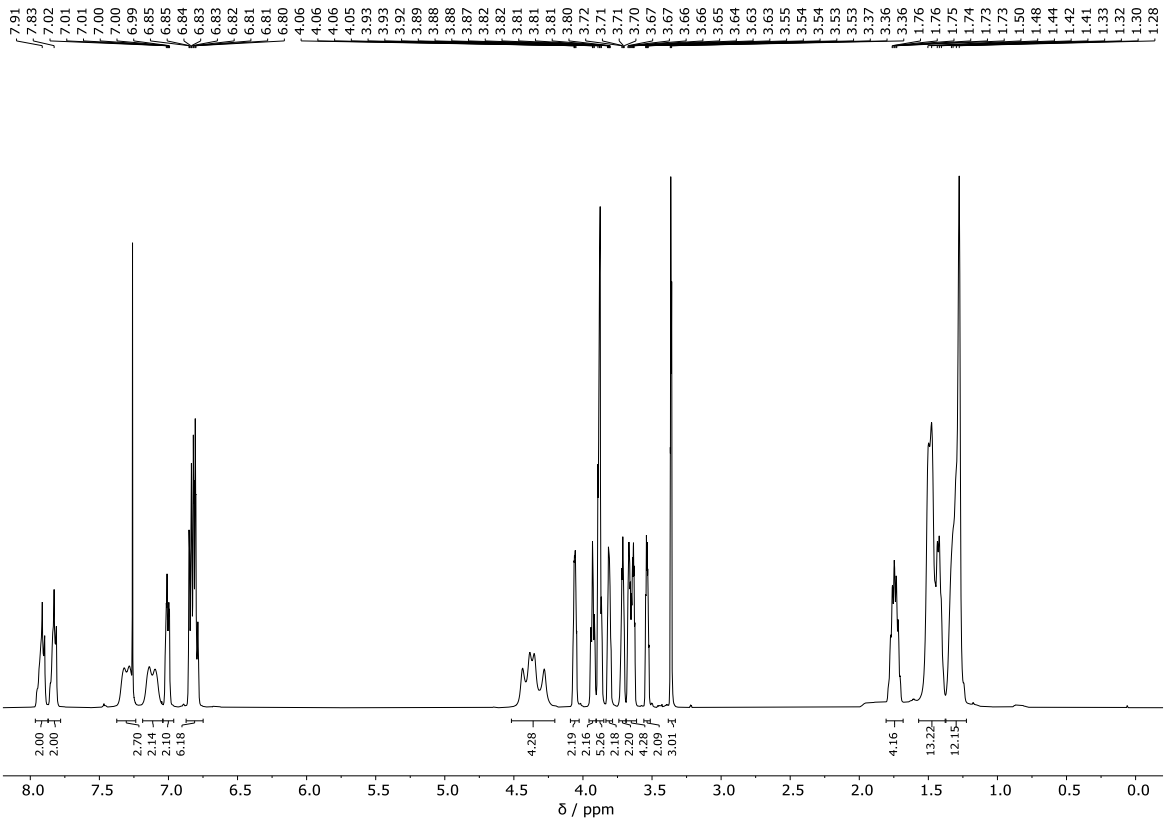

Figure S48. ^{1}H NMR spectrum of **20** (Chloroform-*d*, 298 K, 500 MHz).

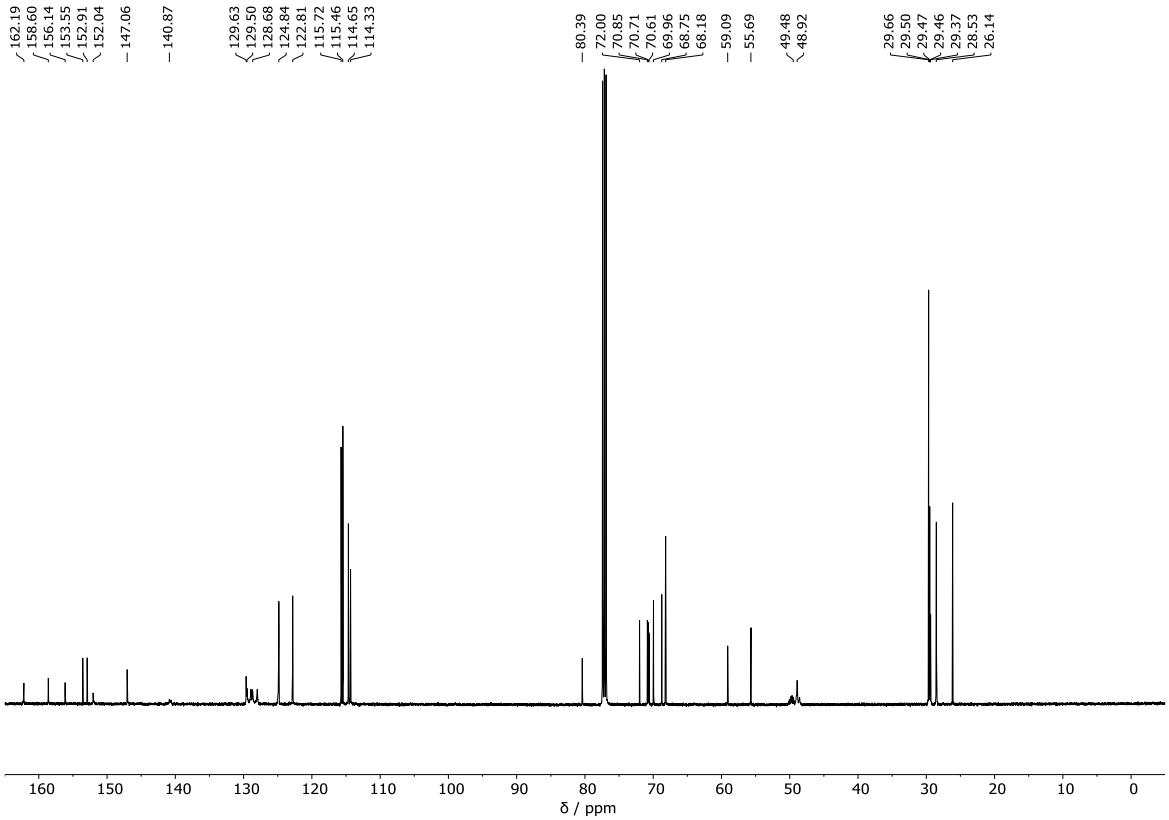

Figure S49. ^{13}C NMR spectrum of **20** (Chloroform-*d*, 298 K, 126 MHz).

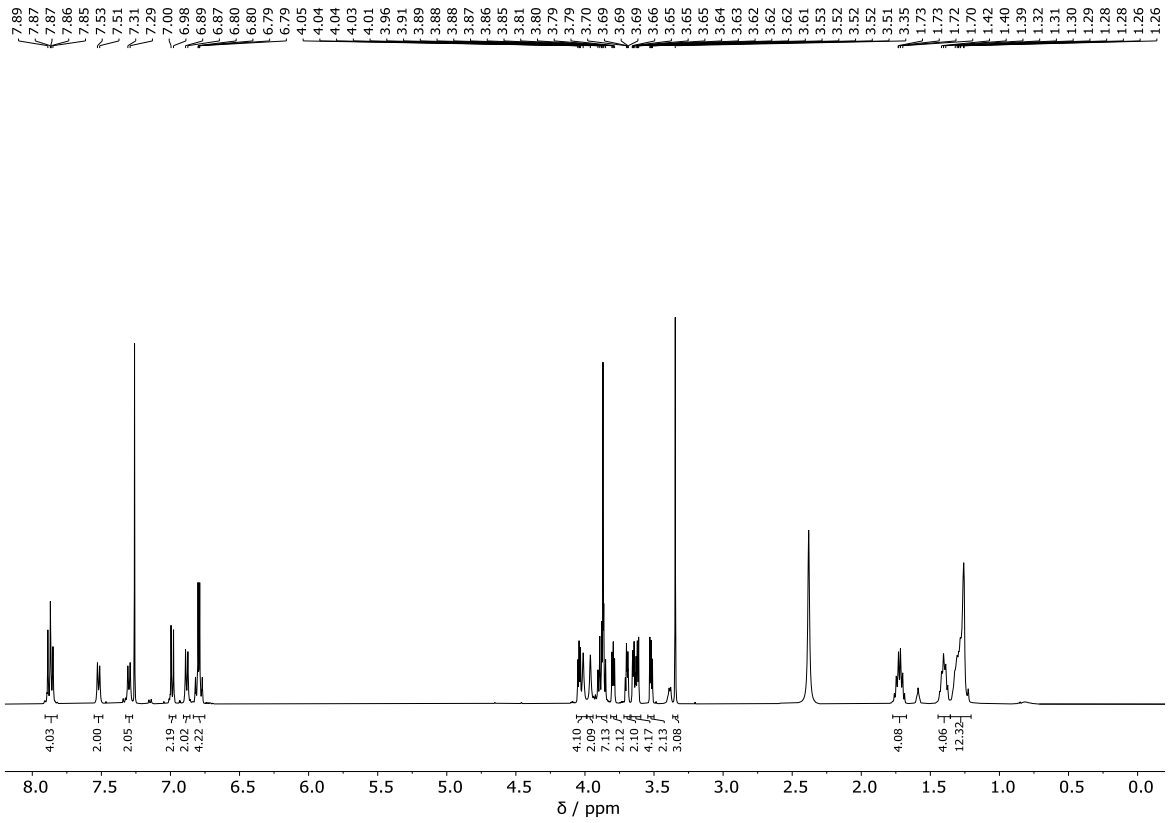

Figure S50. ^{1}H NMR spectrum of ***E*-C12tEG** (Chloroform-*d*:Methanol-d_4 99:1, 298 K, 500 MHz).

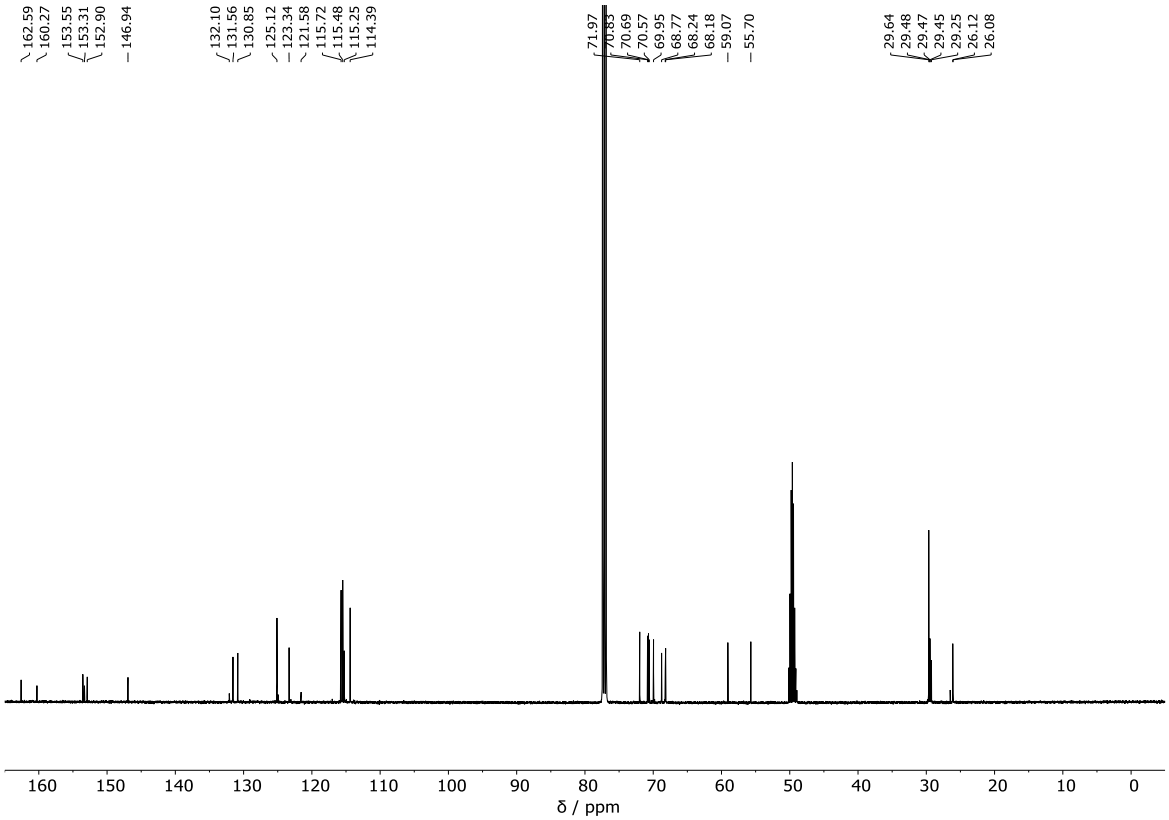

Figure S51. ^{13}C NMR spectrum of *E*-**C12tEG** (Chloroform-*d*:Methanol-d_4 99:1, 298 K, 126 MHz).

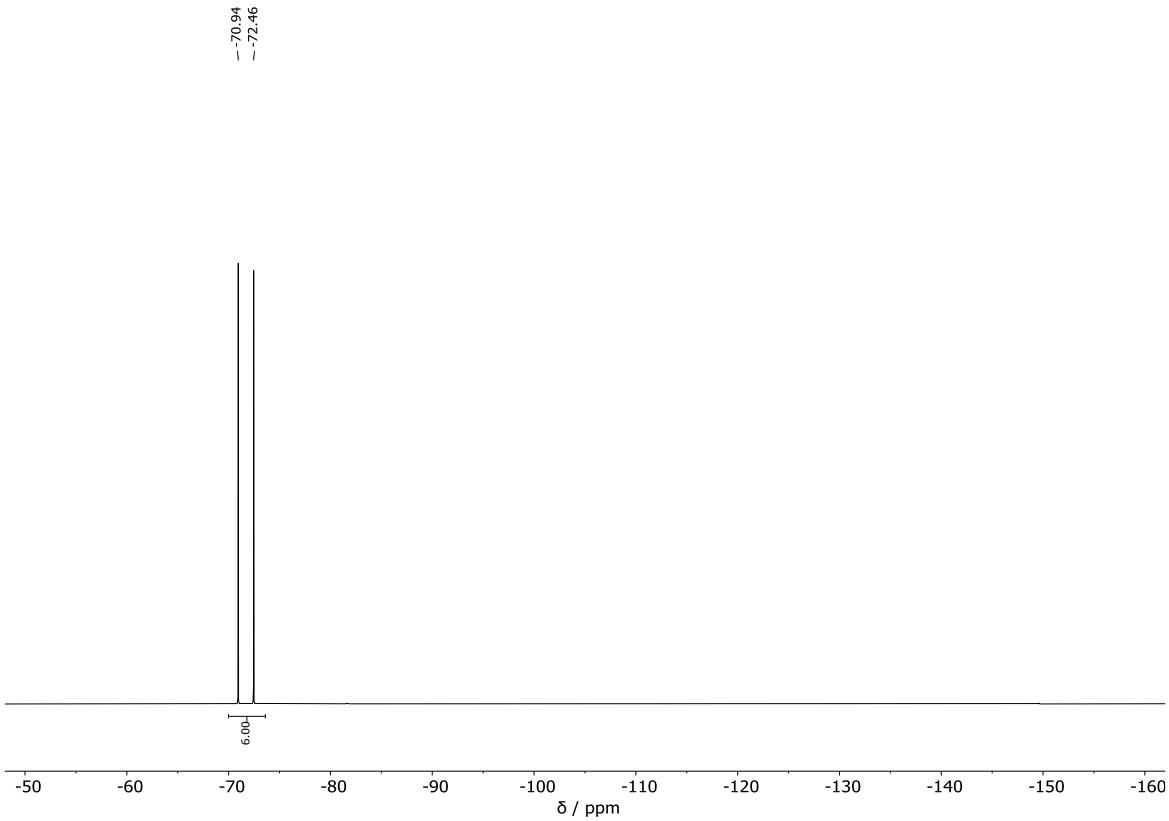

Figure S52. ^{19}F NMR spectrum of *E*-**C12tEG** (Chloroform-*d*:Methanol-d_4 99:1, 298 K, 470 MHz).

[1] Stillwell, W., An Introduction to Biological Membranes: From Bilayers to Rafts, Elsevier, Amsterdam, **2013**

[2] Credi, A., *Angew. Chem. Int. Ed*., **2019**, 58, 13, 4108.

[3] Wang, W.; Li, R.; Gokel, G. W., *Chem. Eur. J.,* **2009**, 15, 10543.

[4] Bo, Q.; Zhao, Y., *Langmuir*, **2007**, 23, 5746.

4. Chemically induced mismatch of rings and stations in [3]rotaxanes

4.1 Introduction

Rotaxanes are one of the archetypal structures of Mechanically Interlocked Molecules; they consist of a linear molecule threaded through a macrocycle and interlocked by bulky endgroups. Thanks to the dynamic nature of the mechanical bond, rotaxanes have been attracting a great deal of attention in the last two decades for their potential applications in artificial molecular machines, catalysis, sensing and smart materials.[1,2,3,4,5,6,7,8,9] In rotaxane systems, tailored functions can be attained by taking advantage of the precise relative arrangement of the ring and axle components, which can be engineered through chemical design and controlled by external stimuli. The careful disposition of the molecular subunits is typically facilitated by introducing specific recognition sites (*stations*) on the axle component in order to establish non-covalent interactions with the macrocycle(s). A considerable number of rotaxanes have been synthesized making use of a template-directed methodology, exploiting the axle recognition site to template the formation of the MIM;[10,11,12] nonetheless, strategies that do not require permanent recognition motifs on the components to be interlocked have also been developed.[13] In a rotaxane, the balance between the number of stations with respect to that of the rings is a primary design element that leads to very different properties. Many examples are reported of rotaxanes presenting an equal number of stations and rings – meaning that every macrocycle encircles a station – or with a higher number of stations compared to that of rings, that is the case of molecular shuttles, in which the translational movement of the ring between the stations is achieved randomly or by applying a chemical or physical stimulus.[11,12,14,15,16,17,18,19,20,21] However, the remaining combination, in which the number of rings is higher with respect to that of stations, has been much less investigated. This situation is particularly interesting because the relative arrangement of the components is dominated only by weak intermolecular interactions, giving rise to peculiar structural and/or dynamic effects.[22,23,24,25,26] Such a 'frustrated' system could embed novel co-conformational phenomena ranging from the exclusive competition of the rings for the station in a highly dynamic fashion to an

arrangement in which the two rings come together toward the recognition site[27] without necessarily interacting with each other.[28,29,30]

This chapter regards the synthesis and study of the [3]rotaxane **Rot**H_2^{3+}, which consists of two dibenzo-24-crown-8 (DB24C8) rings interlocked with an axle containing two lateral dibenzylammonium and one central triazolium stations (**Scheme 4.2**). The ammonium stations can be deactivated by deprotonation,[14,31] affording rotaxanes **Rot**H^{2+} and **Rot**$^+$ (**Scheme 4.3**) in which the number of stations is respectively equal or lower than the number of rings.

4.2 Synthesis of **Rot**H_2^{3+}

The synthesis of **Rot**H_2^{3+} exploited a convergent approach. Reaction of 3,5-di-*tert*-butylbenzyl bromide with sodium azide led to the formation of the azide derivative **1** in quantitative yield, that upon reduction provided the benzylamine **2**. The reductive amination between **2** and 4-hydroxybenzaldehyde and subsequent protection with di-*tert*-butyl dicarbonate led to the formation of intermediate **4** in an overall 71% yield. Carbamate **4** is the common building block for the synthesis of the two moieties composing the molecular axle of the rotaxane. Reaction of **4** with propargyl bromide, followed by deprotection and protonation provided the alkyne-containing salt **6** in an overall 70% yield. Alternatively, reaction of **4** with 1,2-dibromoethane, followed by substitution with sodium azide and final deprotection-protonation led to the formation of the second axle fragment **9**, comprising an ammonium recognition site and the azide functional group (**Scheme 4.1**). A copper(I)-catalyzed azide-alkyne cycloaddition reaction (AAC) between **6** and **9** in the presence of DB24C8 provided the dicationic [3]rotaxane compound **10** • 2(HPF_6) in 78% yield. Finally, reaction of **10** • 2(HPF_6) with iodomethane followed by anion exchange led to the desired tricationic rotaxane **Rot**H_2^{3+} in 91% yield (**Scheme 4.2**).

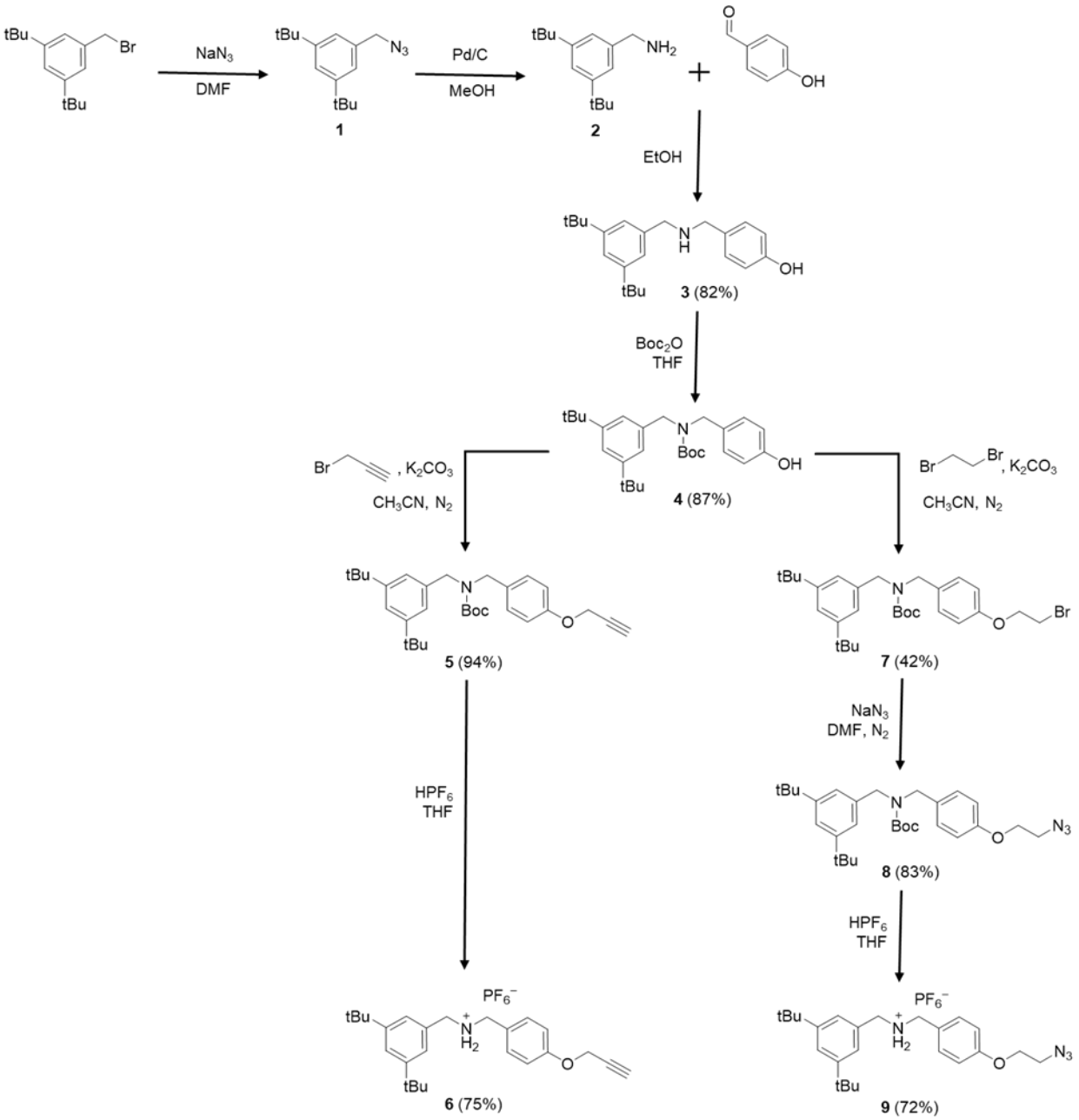

Scheme 4.1. Synthesis of intermediates **6** and **9**.

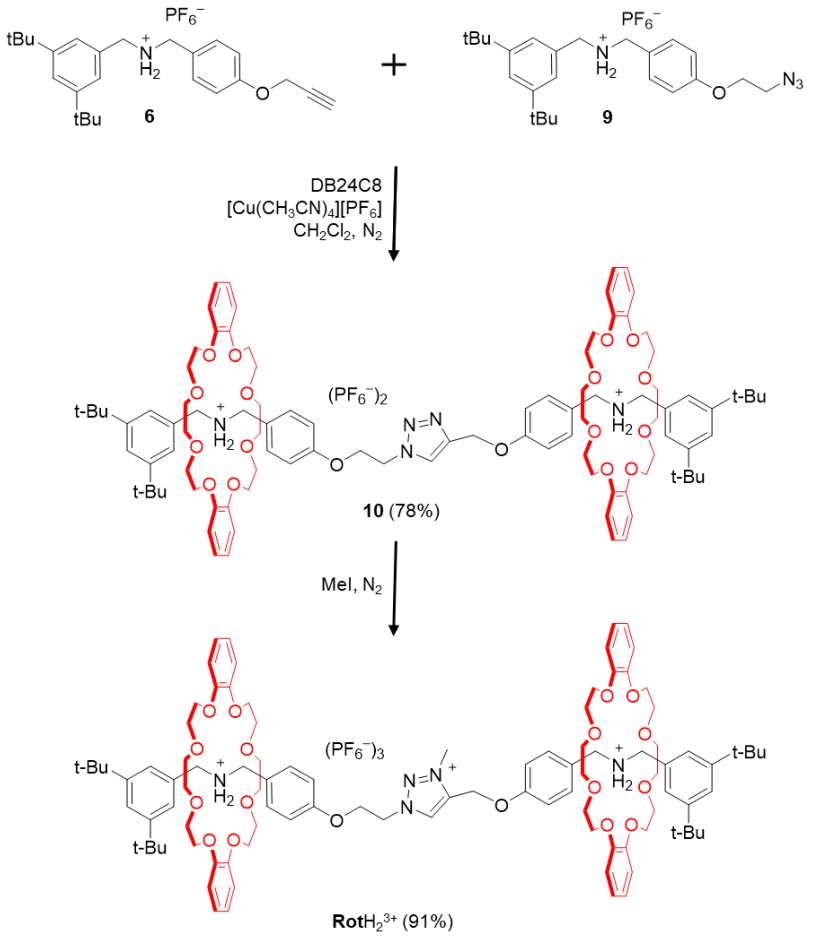

Scheme 4.2. Synthesis of **Rot**H_2^{3+}.

The trication **Rot**H_2^{3+} was fully characterized by ^1H and ^{13}C NMR spectroscopy and mass spectrometry. The ^1H NMR spectrum of **Rot**H_2^{3+} is reported in **Figure 4.1**.

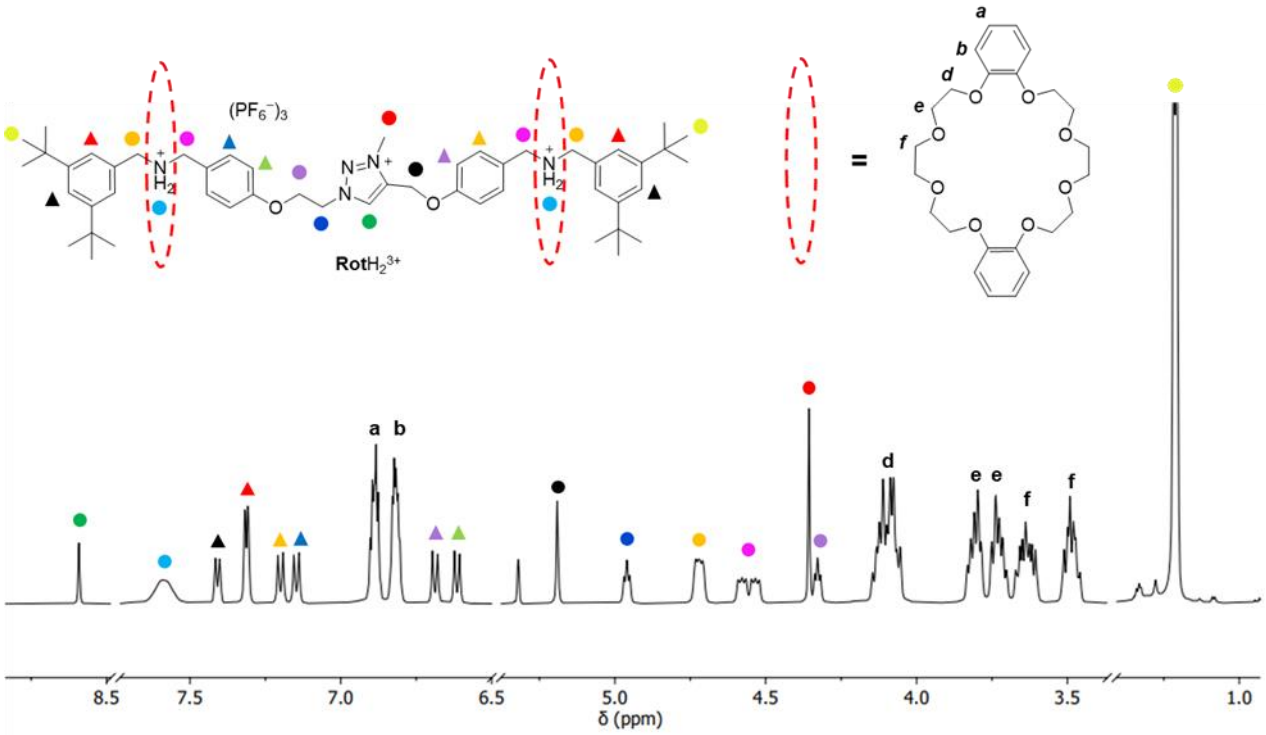

Figure 4.1. ^1H NMR spectrum of **Rot**H_2^{3+}, 500 MHz, methylene chloride-d_2, 298 K.

In the spectrum, a number of relevant resonances can be identified, including the sharp singlet at 8.6 ppm related to the triazolium C-H (green dot) and the broad signal at 7.6 ppm associated to the acidic protons of the two ammonium stations (light blue dot), which form hydrogen bond with the crown ether rings.[31] The same interaction causes a characteristic multiplicity in the resonances related to the benzylic protons (orange and pink dots), which display multiplets arising at 4.71 ppm and 4.65 ppm. The uneven methylene and ethylene bridges connecting the central triazolium cation to the peripheral dibenzylammonium portions are assigned to the sharp singlet at 5.20 ppm (black dot) and the two triplets at 4.96 ppm and 4.36 ppm (blue and purple dots), respectively. Finally, the methyl group of the triazolium station appears as a a sharp singlet at 4.36 ppm (red dot).

4.3 Base induced switching studies

The tricationic **Rot**H_2^{3+} comprises one permanent triazolium and two switchable ammonium stations, where the latter can be deactivated by reaction of the rotaxane with a suitable base (**Scheme 4.3**). The behaviour of **Rot**H_2^{3+} as a consequence of deprotonation was monitored by ^{1}H NMR throughout the sequential addition of the polymer-supported phosphazene base **B1** (**Figure 4.2**). The progressive reaction between **Rot**H_2^{3+} and **B1** gives rise to the formation of two new products as indicated by the appearance of two independent sets of resonances each containing a new triazolium related signal. Focusing on such resonances, a considerable downfield shift is observed upon deprotonation – 9.35 and 9.21 ppm compared to 8.60 ppm in **Rot**H_2^{3+} – attributed to the complexation of the triazolium station by a crown ether ring, as a result of the deactivation of one of the ammonium stations. Upon addition of 1 equiv. of **B1** (**Figure 4.2**, red spectrum) the triazolium resonances of **Rot**H_2^{3+} disappear completely and only the two new signals persist (green dots), suggesting the complete mono-deprotonation of **Rot**H_2^{3+}, and consequently the formation of the two dicationic isomers **Rot**H^{2+}-I and **Rot**H^{2+}-II.

To confirm the stoichiometric monodeprotonation of **Rot**H_2^{3+}, a control experiment was performed by reacting the rotaxane with 1 equivalent of the homogeneous phosphazene base P1-*tert*-butyl (**B2**) under the same reaction conditions employed with **B1**. Such experiment provided a ^{1}H NMR spectrum identical to that recorded during the heterogeneous deprotonation, confirming the stoichiometric addition of the polymer-supported phosphazene base (**Figure 4.3**).

The formation of the two isomers **Rot**H^{2+}-I and **Rot**H^{2+}-II derives from the quasi-symmetry of the axle that confers a non-equivalent nature to the two ammonium stations of **Rot**H_2^{3+}.

The identity of the two dicationic rotaxanes was assigned in accordance with their relative stability obtained by means of DFT studies (**Section 4.6**).

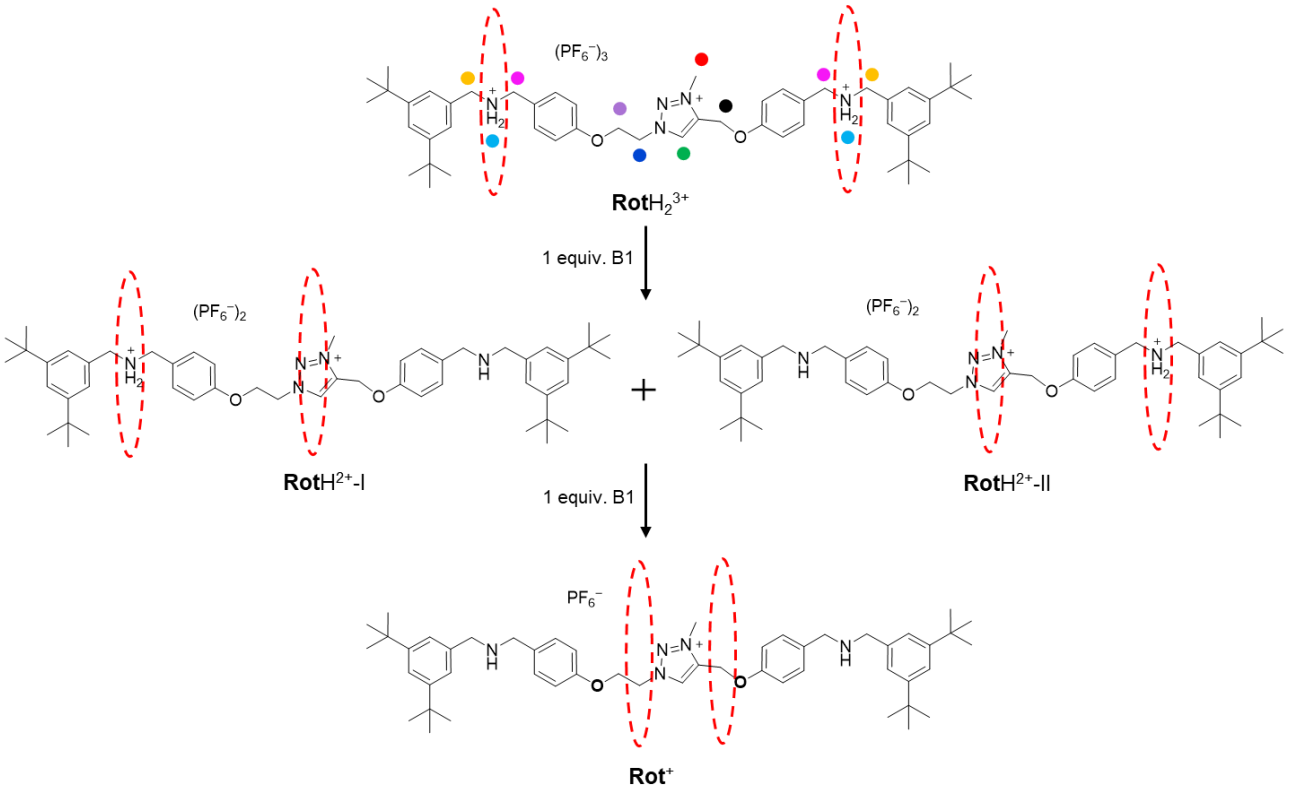

Scheme 4.3. Reactivity of **Rot**H_2^{3+} towards deprotonation.

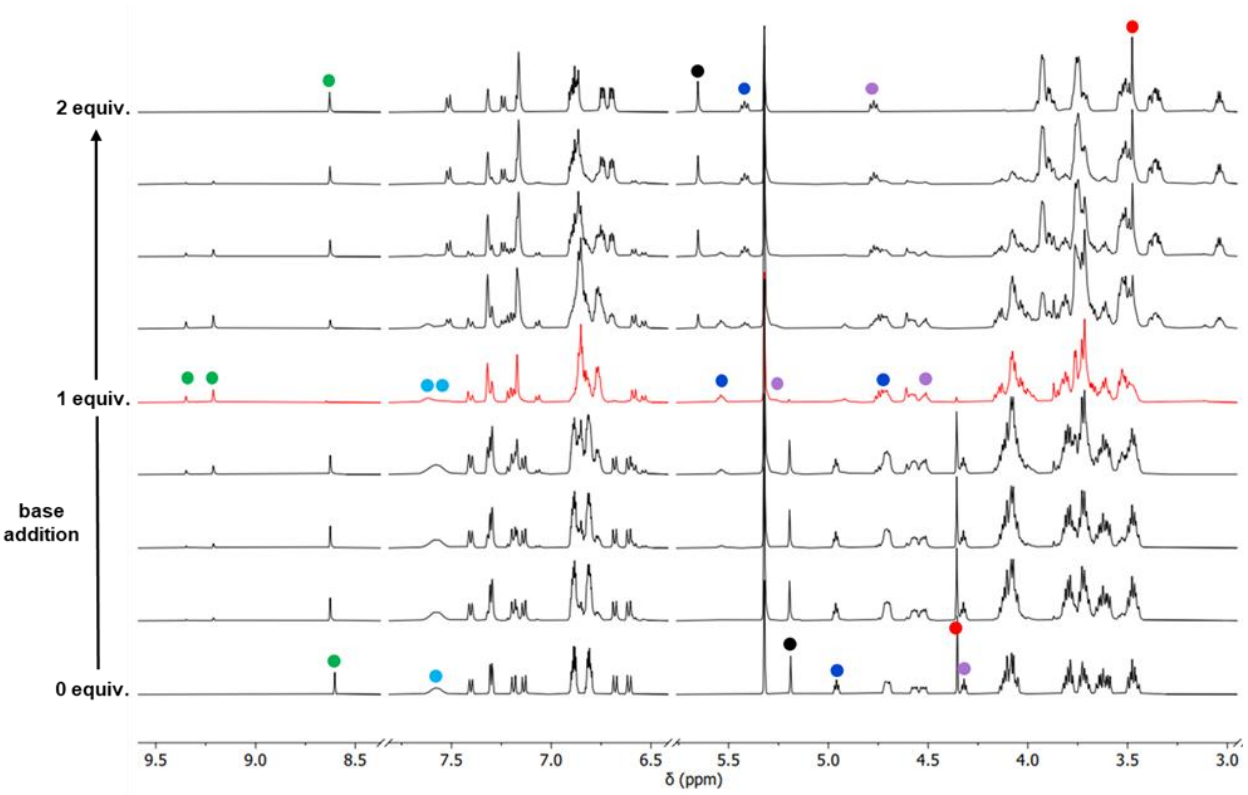

Figure 4.2. Deprotonation of **Rot**H_2^{3+} by addition of **B1**, the red line indicates the spectrum obtained after addition of 1 equivalent of **B1**; 500 MHz, Methylene Chloride-d_2, 298 K.

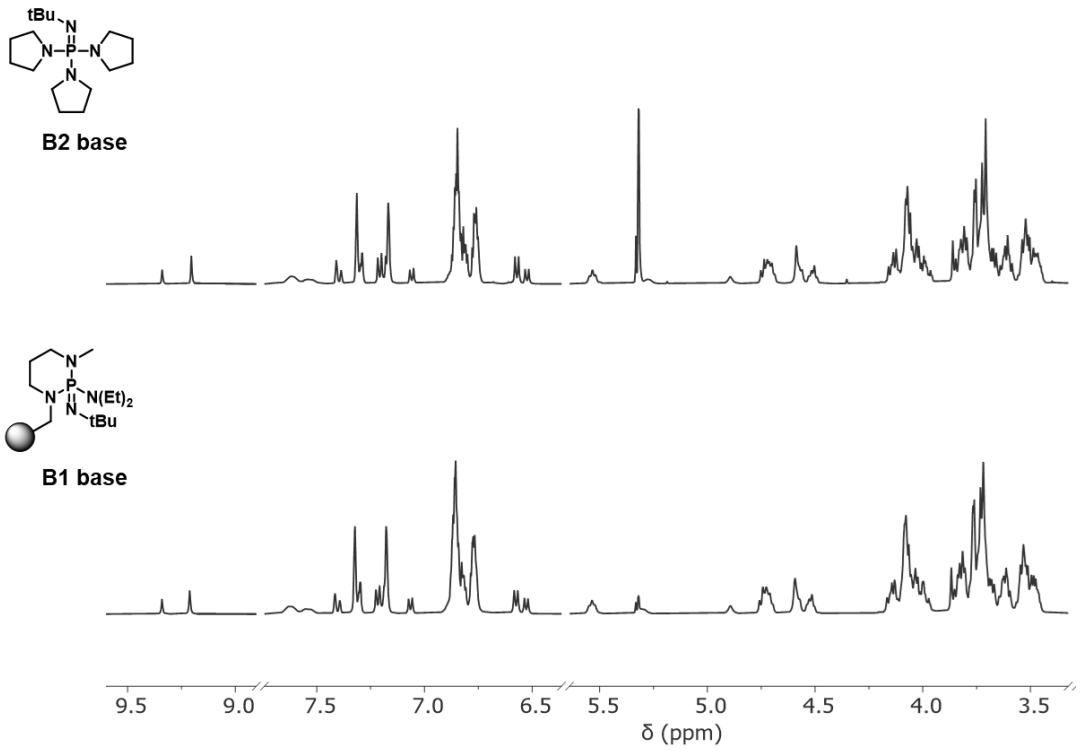

Figure 4.3. Comparison of the ^{1}H NMR spectra of **Rot**H_2^{3+} upon addition of 1 equivalent of the heterogeneous base **B1** (bottom) or 1 equivalent of the homogeneous base **B2** (top); 500 MHz, methylene chloride-d_2, 298 K.

An important information is given by the ratio between dications **Rot**H^{2+}-I and **Rot**H^{2+}-II, present in a 30:70 ratio that does not change over the whole deprotonation reaction. On one hand, this information suggest that the two species are in thermodynamic equilibrium and possess different stabilities; on the other hand, they exhibit distinct resonances in the ^{1}H NMR spectrum, indicating that the exchange between the two isomers is slow on the NMR time scale. To further investigate this aspect, an exchange spectroscopy (EXSY) experiment was carried out on the mixture containing **Rot**H^{2+}-I and **Rot**H^{2+}-II. In the bidimensional ^{1}H/^{1}H spectrum, exchange peaks between the two isomers were detected, thus confirming the presence of an exchange pathway between the isomers (**Figure 4.4**).

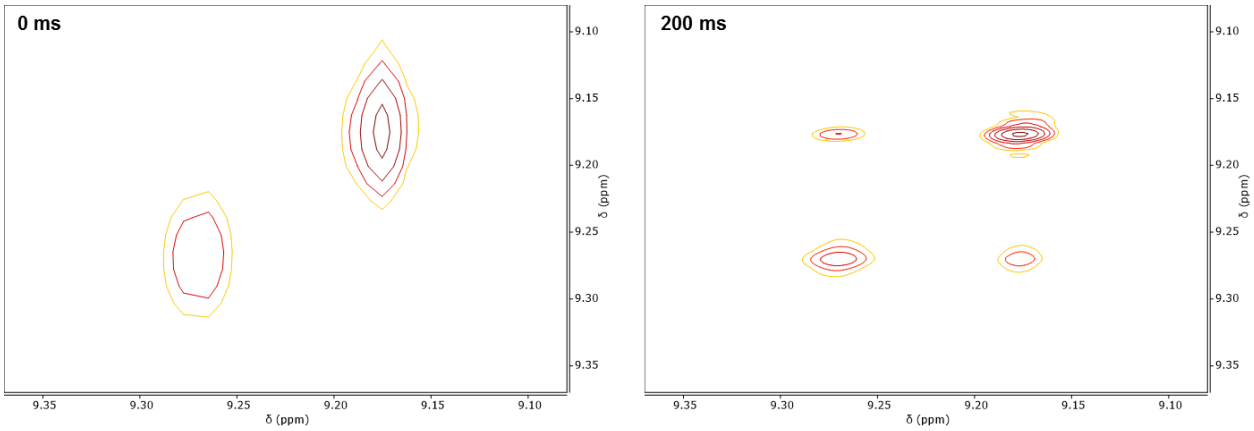

Figure 4.4. Portion of the ^{1}H-^{1}H EXSY spectrum of the mixture of **Rot**H_2^+-I and **Rot**H_2^+-II displaying the triazolium proton (green dot, **Figure 4.2**) at mixing time t_{mix} = 0 ms (left) and t_{mix} = 200 ms (right); 500 MHz, Acetonitrile-d_3, 298 K.

Reaction of **Rot**H^{2+}-I and **Rot**H^{2+}-II with a second equivalent of **B1** led to the deprotonation of the remaining ammonium station and to the convergent formation of the monocation **Rot**$^+$ as the only product.

The deprotonation of **Rot**H_2^{3+} into **Rot**$^+$ causes significant shifts in the NMR resonances, as it can be observed in **Figure 4.2**. More specifically, the signals related to the nuclei placed around the triazolium core, such as those of the methylene and ethylene bridges, deshield (black or blue/purple dots, respectively); conversely, the triazolium methyl group (red dot) shields, while the triazolium aromatic proton remains almost unaltered (green dot). Altogether, such variations suggest that upon formation of the monocationic rotaxane **Rot**$^+$ both rings moved toward the triazolium station, but neither of them is encircling it.[32,33,34]

The presence of the macrocycles in the surroundings of the triazolium core would indeed imply them being away from the amine sites. As a consequence, the latter would be now available for functionalization. To further validate such hypothesis, **Rot**$^+$ was reacted with di-*tert*-butyl dicarbonate, providing the bis-carbamate **Rot**Boc_2^+. Upon careful analysis of the ^{1}H NMR spectrum of the reaction mixture, it can clearly be noticed that most of the resonances remained unchanged compared to those observed in **Rot**$^+$. The only signals that underwent variations are those related to the nuclei directly influenced by the new carbamate groups that exhibit shifted and broadened peaks, confirming the formation of the desired product **Rot**Boc_2^+.

The strong similarity between the ^{1}H NMR spectra of **Rot**Boc$_2^+$ and **Rot**$^+$ confirmed the effective displacement of the crowns from the amine sites and thus their effective translation toward the triazolium core.

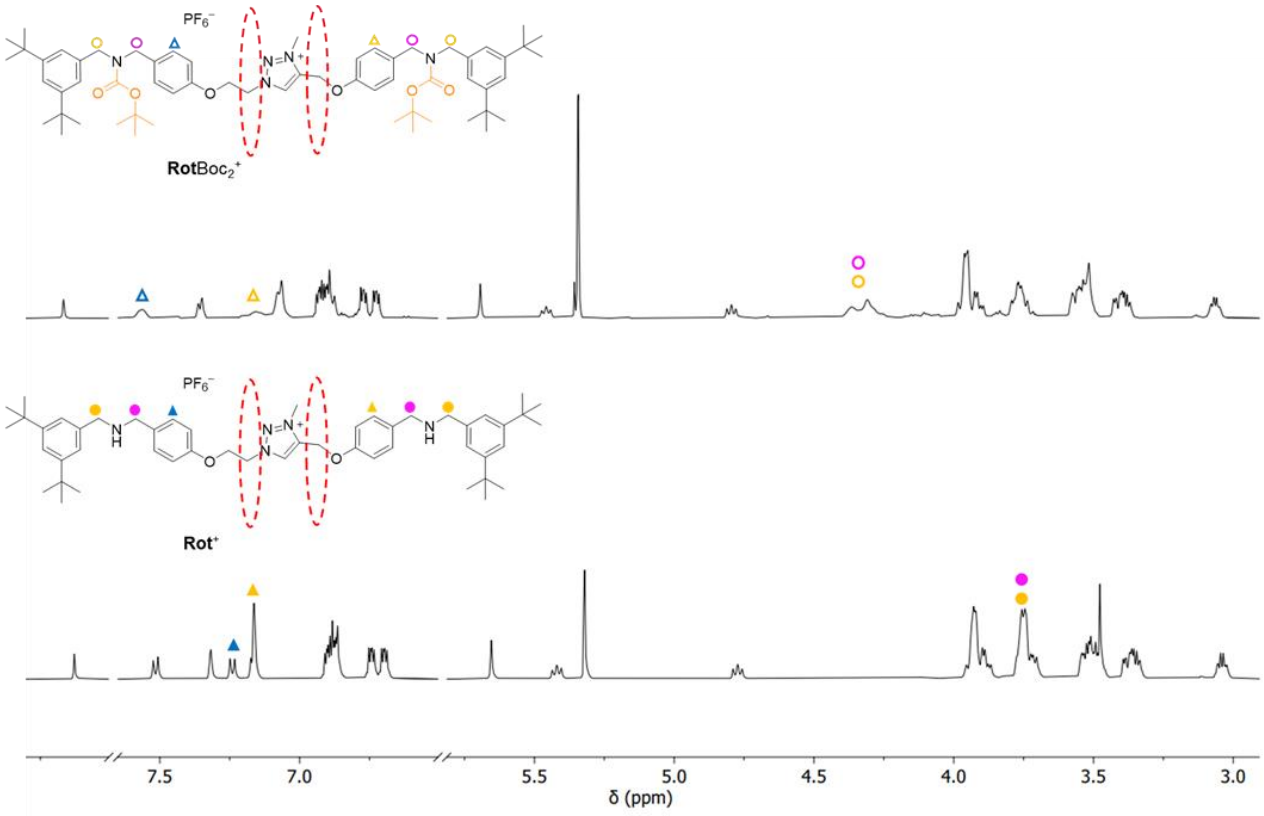

Figure 4.5. Comparison between the ^{1}H NMR spectrum of **Rot**$^+$ (bottom) and **Rot**Boc$_2^+$ (top); 500 MHz, Methylene Chloride-d_2, 298 K.

4.3.1 Synthesis and study of the free thread molecule

To evaluate the effect of the mechanical bond on the properties of the system presented, the individual axle unit **12**, lacking the interlocked macrocycles, was synthesized and studied. The synthesis started from intermediates **6** and **9**, which were linked together through a copper-catalysed click reaction, providing the dicationic compound **11** in 84% yield. Subsequently, reaction of **11** with iodomethane, followed by deprotection and protonation, provided the tricationic thread **12** in 41% yield (**Scheme 4.4**). Compound **12** was fully characterized by ^{1}H, ^{13}C NMR and mass spectrometry.

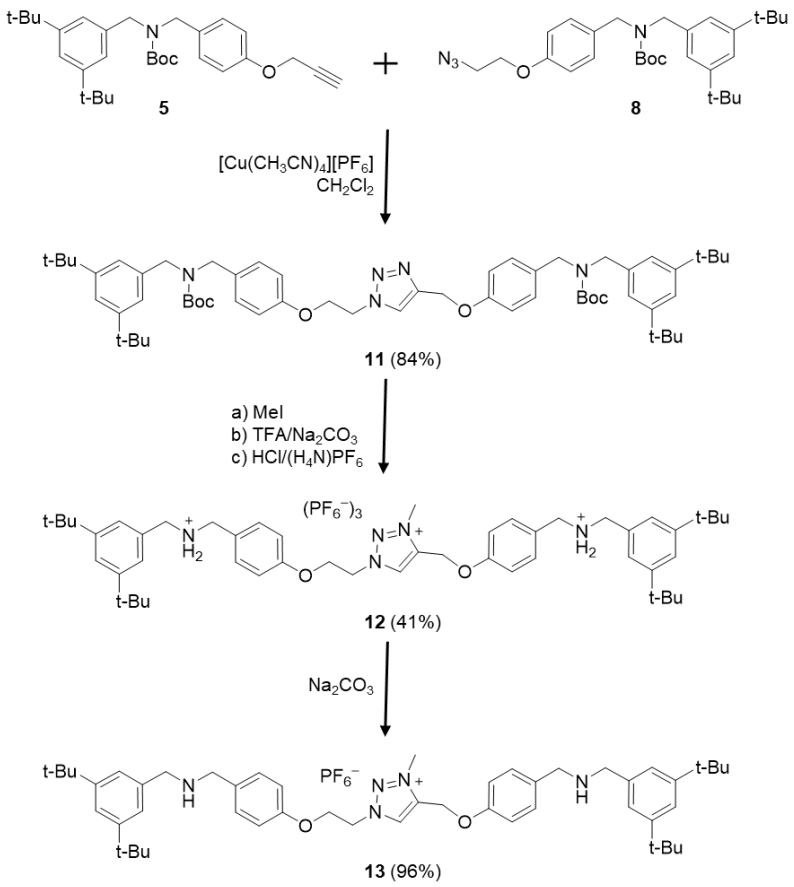

Scheme 4.4. Synthesis of the tricationic axle **12** and monocation **13**.

The behaviour of the free tricationic axle compound **12** with respect to deprotonation was investigated by means of ^{1}H NMR. Reaction of the tricationic thread with the homogeneous base **B2**, displayed significative variations in chemical shift only for the resonances related to the benzylic protons (**Figure 4.6**, orange and pink dots). Moreover, in contrast to the slow exchange between rotaxanes **Rot**H^{2+}-I and **Rot**H^{2+}-II, mono-deprotonation of the tricationic axle led to the formation of two dicationic species in fast exchange. As a consequence of the fast exchange, the two species cannot be individually detected and only one set of resonances is present in the spectrum (**Figure 4.6**, red spectrum).

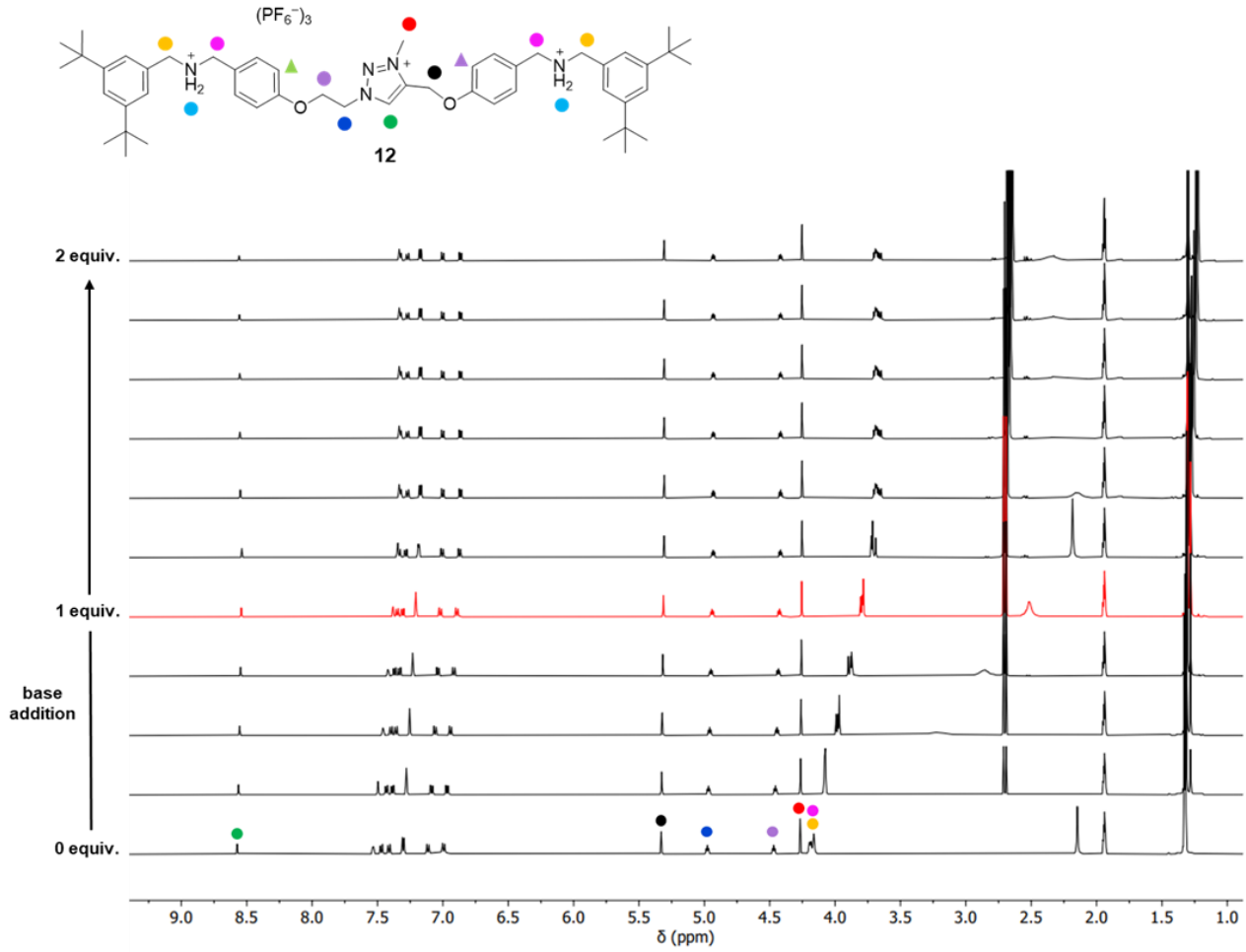

Figure 4.6 Deprotonation of **12** with the homogeneous base **B2**, the red line indicates the spectrum obtained after addition of 1 equivalent of **B2**; 500 MHz, Acetonitrile-d_3, 298 K.

4.4 Variable-temperature NMR studies

The monocation **Rot**$^+$ is a [3]rotaxane in which two rings share a single triazolium station. It can be thus envisaged that the ion-dipole interaction holding both rings close to the station would be weaker compared to that with a single macrocycle, therefore conferring high dynamicity to the system. To further evaluate this aspect, **Rot**$^+$ was investigated by means of variable-temperature NMR analysis. Comparing the ^{1}H NMR spectra recorded at 10 K intervals in the temperature range spanning from 233 K to 343 K it is possible to identify important variations in chemical shifts for specific resonances (**Figure 4.7**). As temperature rises, the resonance relative to the *ortho*-aryl protons on the methylene bridge side (purple triangle) undergoes shielding whereas those related to the protons on the ethylene bridge side (green triangle, purple dot) deshield. Combined together, these trends suggest the

simultaneous translation of both rings toward the ethylene bridge. Additionally, only minor changes affected the chemical shift of the ethylene bridge protons (blue dot) and the methylene bridge protons (black dot), indicating that these nuclei experienced a similar local magnetic environment at different temperatures. Differently from the unidirectional variations observed above, a peculiar trend is displayed by the triazolium aryl proton resonance (green dot). Upon increasing the temperature, this characteristic singlet undergoes an initial shielding, shifting from 9.04 ppm at 233 K to 8.73 ppm at 313 K; however, upon an additional increase in temperature, an opposite variation is observed, with a low-field shift up to 8.76 ppm at 343 K. Such an unusual behaviour likely arises from a multimodal dynamic system that involves multiple co-conformations whose population distribution is temperature dependent.

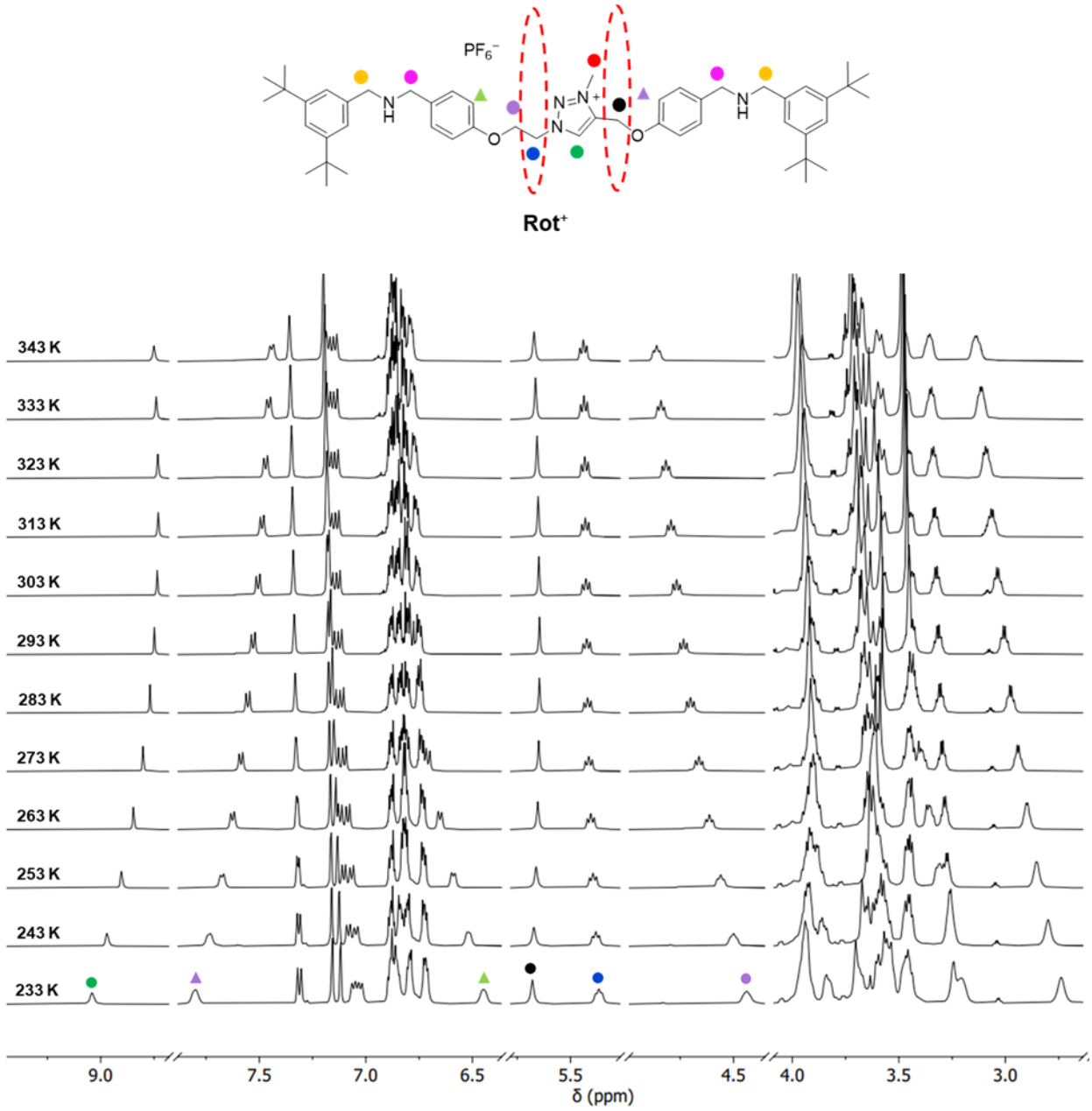

Figure 4.7. Portion of the variable-temperature ^{1}H NMR spectra of **Rot**$^{+}$ between 233 K and 243 K; 500 MHz, Acetonitrile-d_3.

The multiple co-conformations inferring the bidirectional temperature-dependent variations arise from the presence of the mechanical bond. To validate such interpretation, a control experiment was performed on the free monocationic axle compound **13**. Variable-temperature ^{1}H NMR analysis on **13** exhibited just unidirectional chemical shift variations

(**Figure 4.8**), thus confirming that the peculiar temperature-dependent behaviour observed for **Rot**$^{+}$ is linked to the displacement of the rings along the axle.

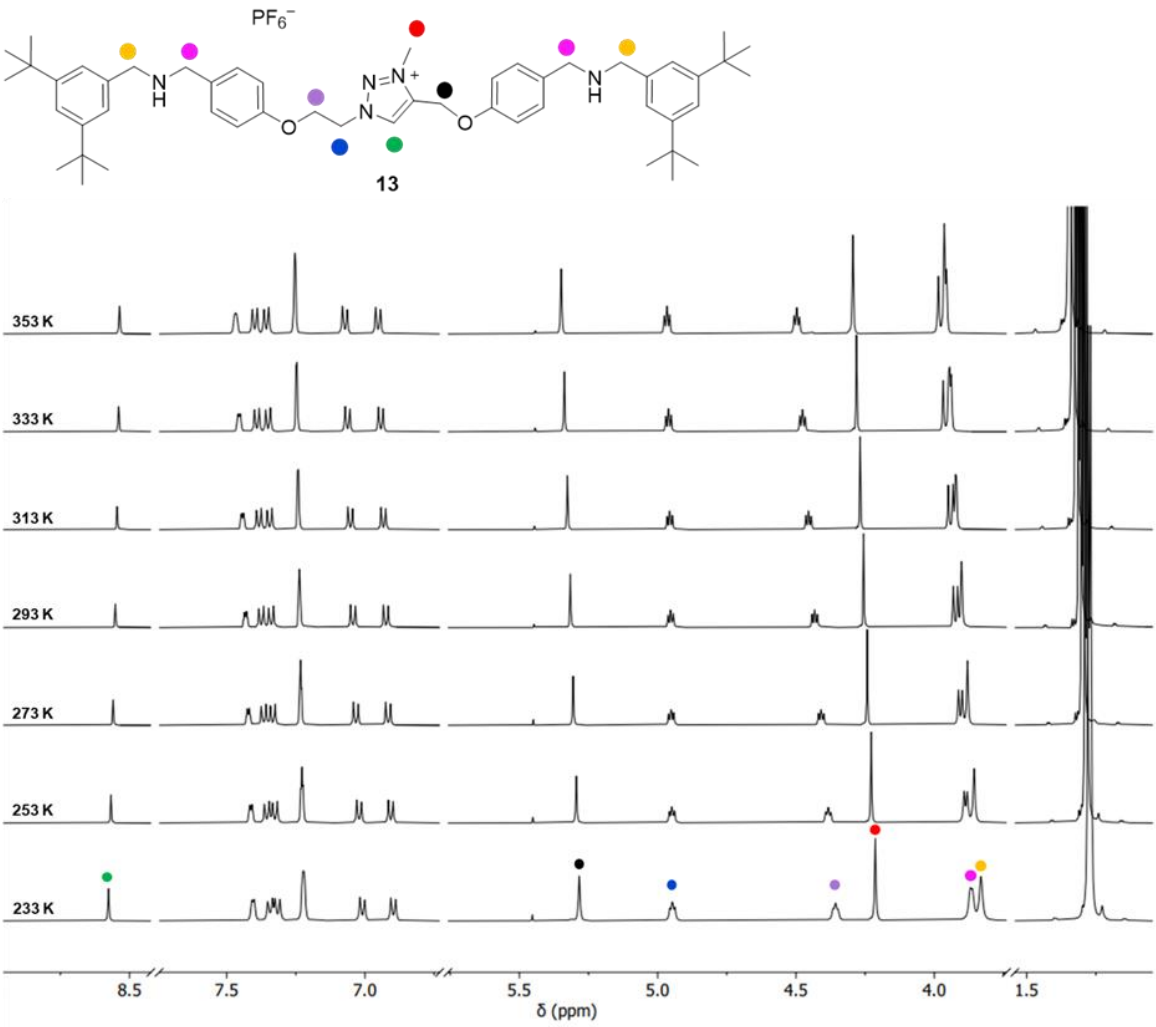

Figure 4.8. Variable-temperature ^{1}H NMR spectra of **13**between 233 K and 243 K; 500 MHz, Acetonitrile-d_3.

4.5 Thermodynamic analysis of deprotonation

The complexation of the ammonium stations by the crown ethers has a considerable impact on the thermodynamic properties of the ammonium functionality.[35,36,37] For this reason, the different relative positions of the crown ether rings in **Rot**H_2^{3+}, **Rot**H^{2+} and **Rot**$^{+}$ are expected to confer individual thermodynamic features to each of the ammonium functional groups. In order to investigate the effect of this peculiar situation, the rotaxanes were studied by combined NMR and UV-vis spectroscopies.

4.5.1 UV-vis spectroscopic titration

Spectrophotometric titration of **Rot**H_2^{3+} with the base **B2** (**Figure 4.9**) was performed to evaluate the influence of the presence of the rings on the acidity of the ammonium cations. Fitting of the data recorded during the titration provided the two observed pK_a values relative to the first (pK'$_{obs}$) and second (pK''$_{obs}$) deprotonation of the ammonium stations.

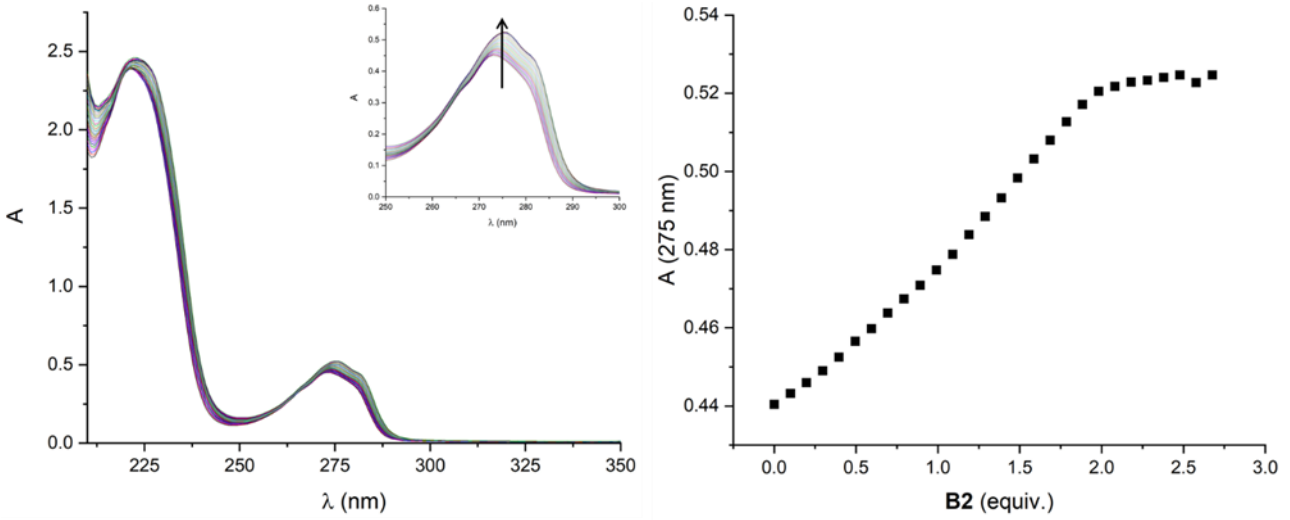

Figure 4.9. Spectrophotometric titration of **Rot**H_2^{3+} with **B2**; [**Rot**H_2^{3+}] = 3.96×10^{-5} M, Acetonitrile, 298 K.

A reference titration was also performed on the tricationic free thread **12** with triethylamine (**Figure 4.10**), providing the two dissociation constants pK_1' = 16.9 and pK_2' = 17.5 upon first and second deprotonation, respectively.

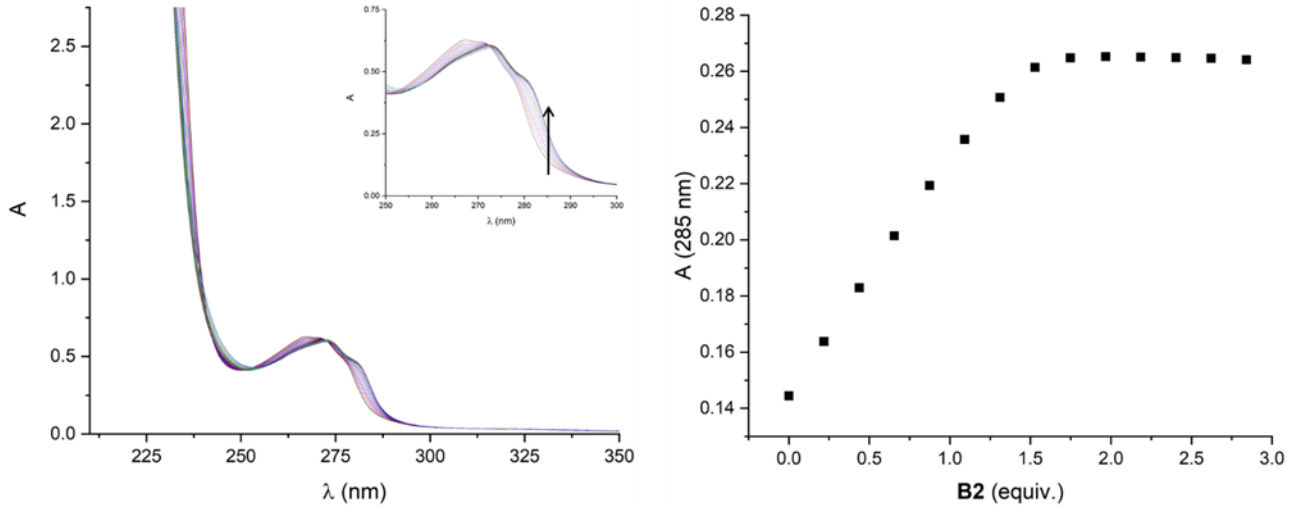

Figure 4.10. Spectrophotometric titration of **12** with **triethylamine**; [**12**] = 3.13×10^{-5} M, Acetonitrile, 298 K.

4.5.2 Acid-base network

The system composed of **Rot**H_2^{3+} in all its protonation states can be depicted with the four rotaxanes connected through a network of acid-base equilibria as represented in **Figure 4.11**. Such equilibria are characterized by the dissociation constants K_1-K_4, while the exchange between **Rot**H^{2+}-I and **Rot**H^{2+}-II is regulated by the equilibrium constant K_{ex}.

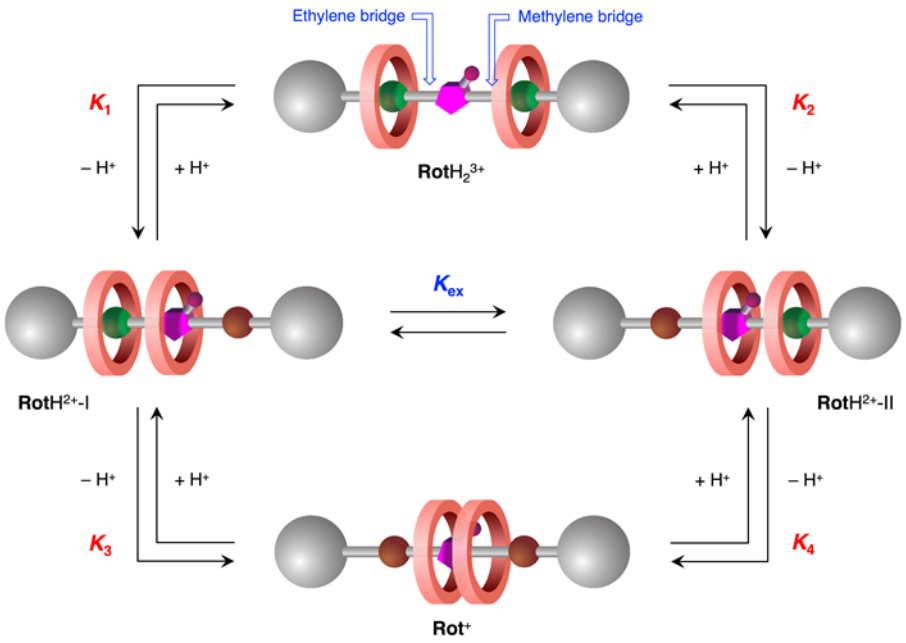

Figure 4.11. Schematic representation of the equilibria involved in the interconversion between **Rot**H_2^{3+}, **Rot**H^{2+} (I and II), and **Rot**$^+$. Color codes: ammonium cation (green sphere), amine functional group (brown sphere), triazolium cation (magenta pentagon).

The constants K_1-K_4 were determined by solving the equations reported in **Scheme 4.12**, that describe the reaction network at the equilibrium, using the acidity constant obtained in the spectrophotometric titration of **Rot**H_2^{3+}. As an initial approximation, we reasonably assumed that **Rot**H^{2+}-I and **Rot**H^{2+}-II had the same molar absorption coefficient at the observation wavelength, because the two forms differ only for the position of the encircled ammonium unit with respect to the triazolium. Additionally, K_{ex} was determined by NMR spectroscopy. The squared reaction network was initially divided in two halves, each of which corresponds to a single deprotonation step. Subsequently, the equations for the mono-deprotonation of **Rot**H_2^{3+} to give **Rot**H^{2+}-I and **Rot**H^{2+}-II were solved to determine the values pK_1 = 23.5 and pK_2 = 23.2; an analogous reasoning was applied to solve the bottom half network and determine pK_3 = 24.2 and pK_4 = 24.5.

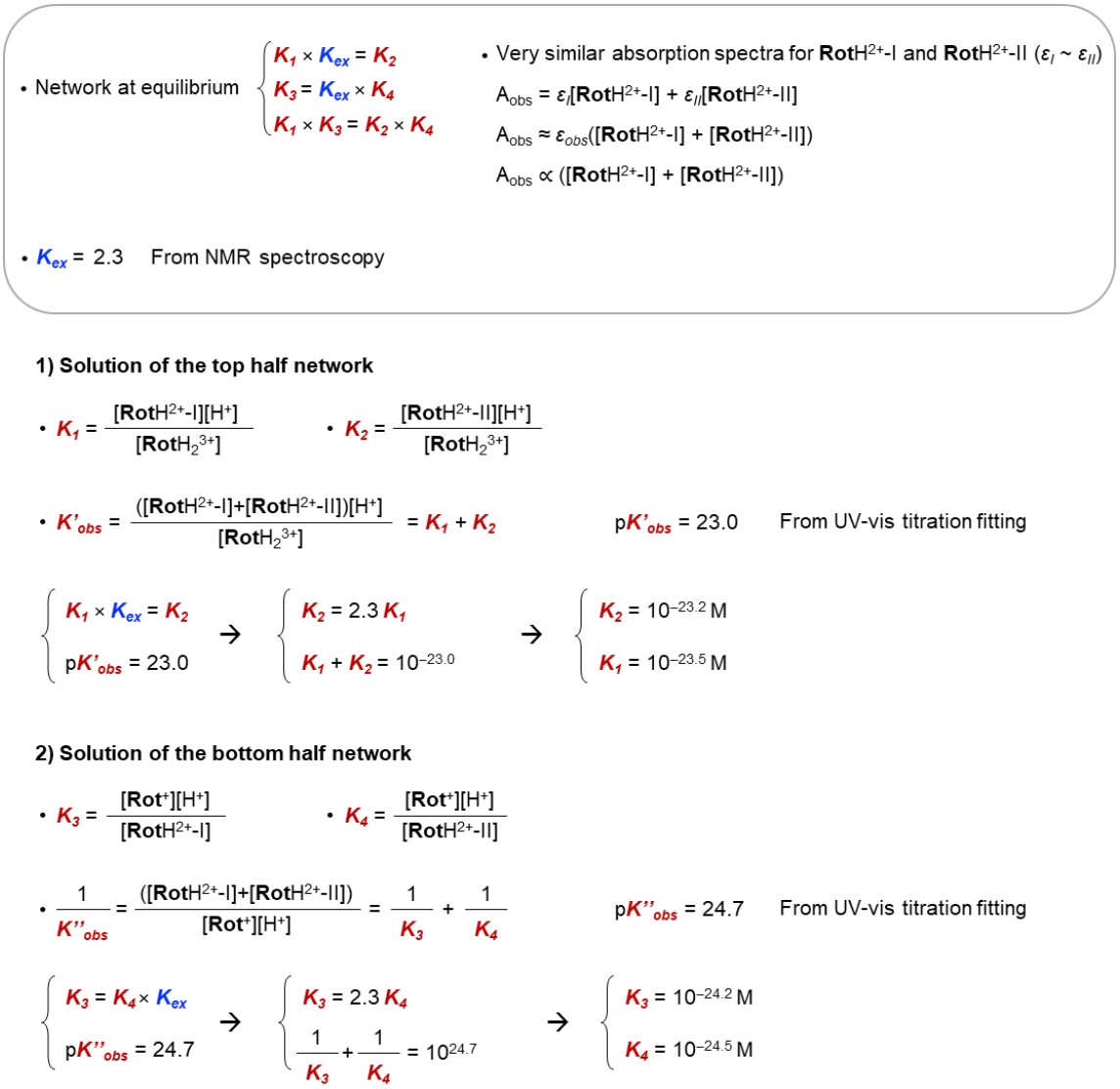

Scheme 4.12. Determination of the dissociation constants of **Rot**H_2^{3+}, **Rot**H^{2+}-I and **Rot**H^{2+}-II.

The dications **Rot**H^{2+}-I and **Rot**H^{2+}-II are in slow equilibrium on the ^{1}H NMR timescale and possible causes of the slow proton exchange could be (i) the removal of a proton from the complexed ammonium station that is kinetically hindered and/or (ii) the proton exchange between forms I and II that could involve the displacement of two rings. It is important to point out that the supramolecular coordination of the rings in the rotaxane resulted to be necessary to express the difference between the acidity constant of the two ammonium stations. Indeed, even if such units are not chemically identical because of the different length in the alkyl bridges (ethylene or methylene) and the oriented triazolium cation, the

deprotonation of one ammonium station of the free axle compound **12** provided two species that resulted to be in fast exchange and for this reason could not be individually detected.
Moreover, in **Rot**H_2^{3+} the two ammonium units not only become much harder to deprotonate because of the rings encircling them, but also exhibit clearly different pK_a values. Specifically, the ammonium on the ethylene bridge side is about two times easier to deprotonate than that on the other side, while the deprotonation of the tricationic free thread **12** to the relative monocation provided two similar and lower pK_a suggesting that such molecular axle can be considered as a simple diprotic acid.
Another important information arises from the network, by comparing the acidity of the complexed ammonium station when the triazolium cation is free or complexed by the ring, as it can be done by comparing K_1 ($10^{-23.5}$ M) and K_4 ($10^{-24.5}$ M). In this context, the local chemical environment of the ammonium site on the methylene bridge side of **Rot**H_2^{3+} and **Rot**H^{2+}-II is the same, and because of this it can be hypothesized that in **Rot**H^{2+}-II the steric interaction between the ring on the triazolium and that on the ammonium disfavors the shuttling of the latter, thus making the station less acidic ($K_4 < K_1$). An analogous consideration can be done concerning the acidity of the ammonium station on the ethylene bridge side by comparing this time, the values of K_2 ($10^{-23.2}$ M) and K_3 ($10^{-24.2}$ M) where $K_3 < K_2$.
From this comparison a ΔpK_a = 1.0 unit is observed between the two ammonium sites in the rotaxane, while the free axle **12** differ of a ΔpK_a = 0.6 units, highlighting once more the influence of the mobile macrocycles on the acid-base equilibrium network.

4.6 Molecular modelling

In order to get an insight on the structure-property relationship of the presented [3]rotaxanes: **Rot**H_2^{3+}, **Rot**H^{2+}-I, **Rot**H^{2+}-II and **Rot**$^+$, a computational investigation was carried out in collaboration with the Fois group at the University of Insubria. The optimized geometry of **Rot**H_2^{3+}, **Rot**H^{2+}-I and **Rot**H^{2+}-II, that present a number of stations higher or equal to the number of rings, was simulated via DFT. On the other hand for **Rot**$^+$, in which the number of rings is higher compared to the number of stations, a finite temperature DFT-Metadynamics approach was employed.
The optimized geometry of **Rot**H_2^{3+} shows each of the two crowns located on one ammonium station (**Figure 4.12**). Such system resulted to be stabilized by the electrostatic

interactions between the crowns oxygen atoms and the ammonium moieties, and by π-π interactions established between the phenyl groups of both rings and the aryl stoppers of the axle. This feature is clearly evidenced by the face-to-face arrangement of the aromatic units of the rings with the close aryl groups of the axle. The distances between the ammonium hydrogen atoms and the oxygen atoms of the rings are 1.857 Å for the ring positioned on the ethylene bridge side, and 1.882 Å for the ring on the methylene bridge side, highlighting the formation of strong hydrogen bonds.

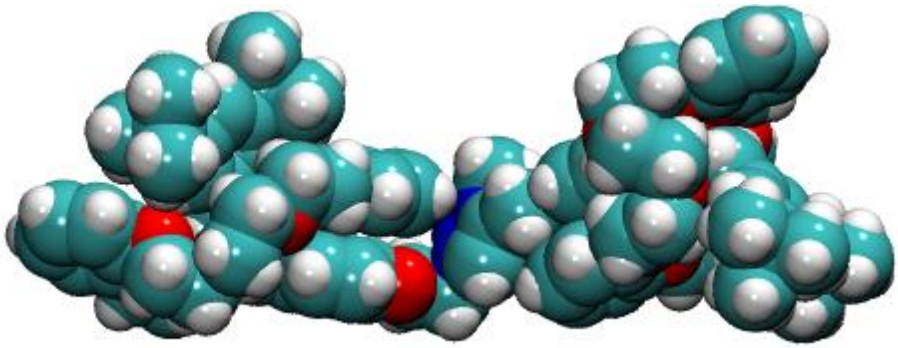

Figure 4.12. Optimized geometry of **Rot**H_2^{3+}. Color codes: C = cyan spheres; N = blue spheres; O = red spheres; H = white spheres. The rotaxane is oriented with the ethylene bridge side placed on the left end of the figure.

The optimized geometries of **Rot**H^{2+}-I and **Rot**H^{2+}-II are reported in **Figure 4.13** and **Figure 4.14**, respectively. The structures of these dicationic species are markedly different with respect to **Rot**H_2^{3+} but also significantly different between each other.

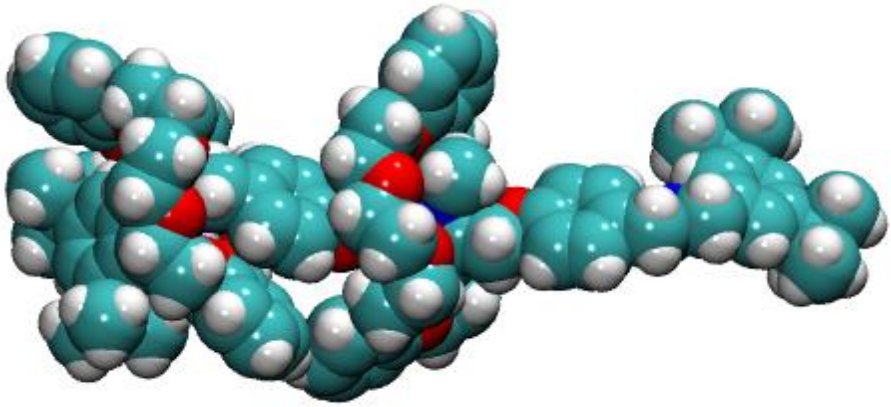

Figure 4.13. Optimized geometry of **Rot**H^{2+}-I. Color codes as in **Figure 4.12.**

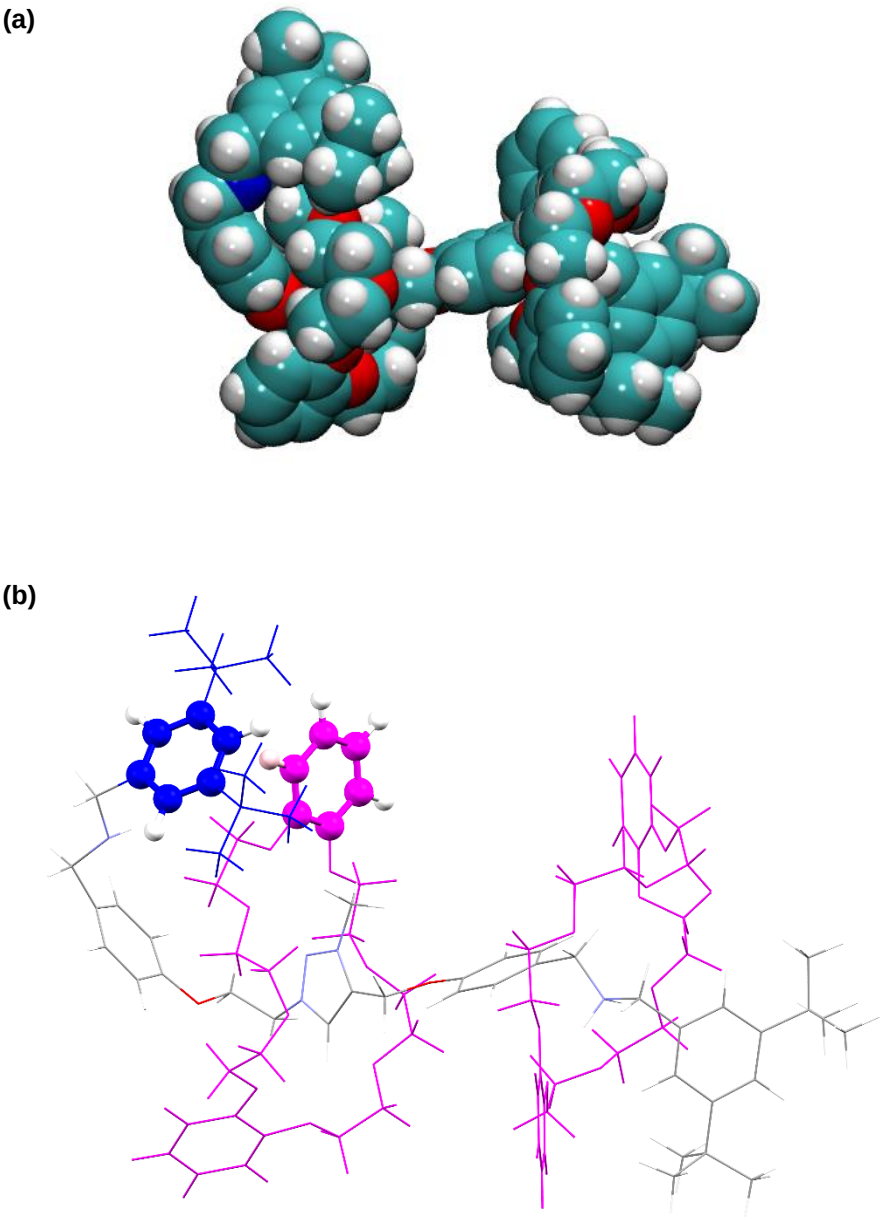

Figure 4.14. a) Optimized geometry of **Rot**H^{2+}-II; color codes as in **Figure 4.12.** b) Highlight of the edge-to-face π-π interaction between the crown ether ring (magenta) and the axle.

Specifically, **Rot**H^{2+}-I, that was formed upon deprotonation of the ammonium station on the methylene bridge side of **Rot**H_2^{3+}, exhibited the translation of the ring along the axle up to the triazolium station where it formed a new hydrogen bond with the triazolium proton (H_{Tz}-O_{ring} = 2.118 Å), while the ring on the ethylene side remains bound to its ammonium station (H_{Am}-O_{ring} = 1.894 Å). In this context, the methylene side of the axle did not exhibit substantial rearrangement remaining approximately in a linear conformation.

Conversely, **Rot**H^{2+}-II, formed upon the deprotonation of the **Rot**H_2^{3+} ammonium station on the ethylene bridge side, exhibited a migration of the ring to the triazolium station where a new hydrogen bond is formed with the triazolium proton (distance H_{Tz}-O_{ring} = 2.050 Å), while the ring on the methylene side remains bound to its ammonium station (distance H_{Am}-O_{ring} = 1.894 Å). Interestingly, this translational movement was accompanied by a noticeable rearrangement of the ethylene side of the axle, suggesting a greater conformational flexibility with respect to the methylene side of the axle.

The energy difference between the optimized geometries of **Rot**H^{2+}-I and **Rot**H^{2+}-II amounted to 1.4 kcal mol^{-1} in favour of the **Rot**H^{2+}-II structure. The slightly greater stability of the latter may be ascribed to the edge-to-face π-π interaction of the ring on the methylene side of the axle, evidenced in **Figure 4.14b**, as well as to the stronger hydrogen-bond interactions between the rings and the axle components.

Further important information arises from the simulation of ^{1}H NMR spectra of **Rot**H^{2+}-I, **Rot**H^{2+}-II and **Rot**H_2^{3+} (**Figure 4.15**). By comparison of the calculated spectra belonging to **Rot**H_2^{3+} with those of the dications **Rot**H^{2+}-I, **Rot**H^{2+}-II, it can be seen that the calculations reproduce the chemical shift trend of the triazolium proton well (i, **Figure 4.15**) through the first deprotonation step, thus confirming that the presence of one ring on the triazolium station induces a significant change of chemical shift of such proton.

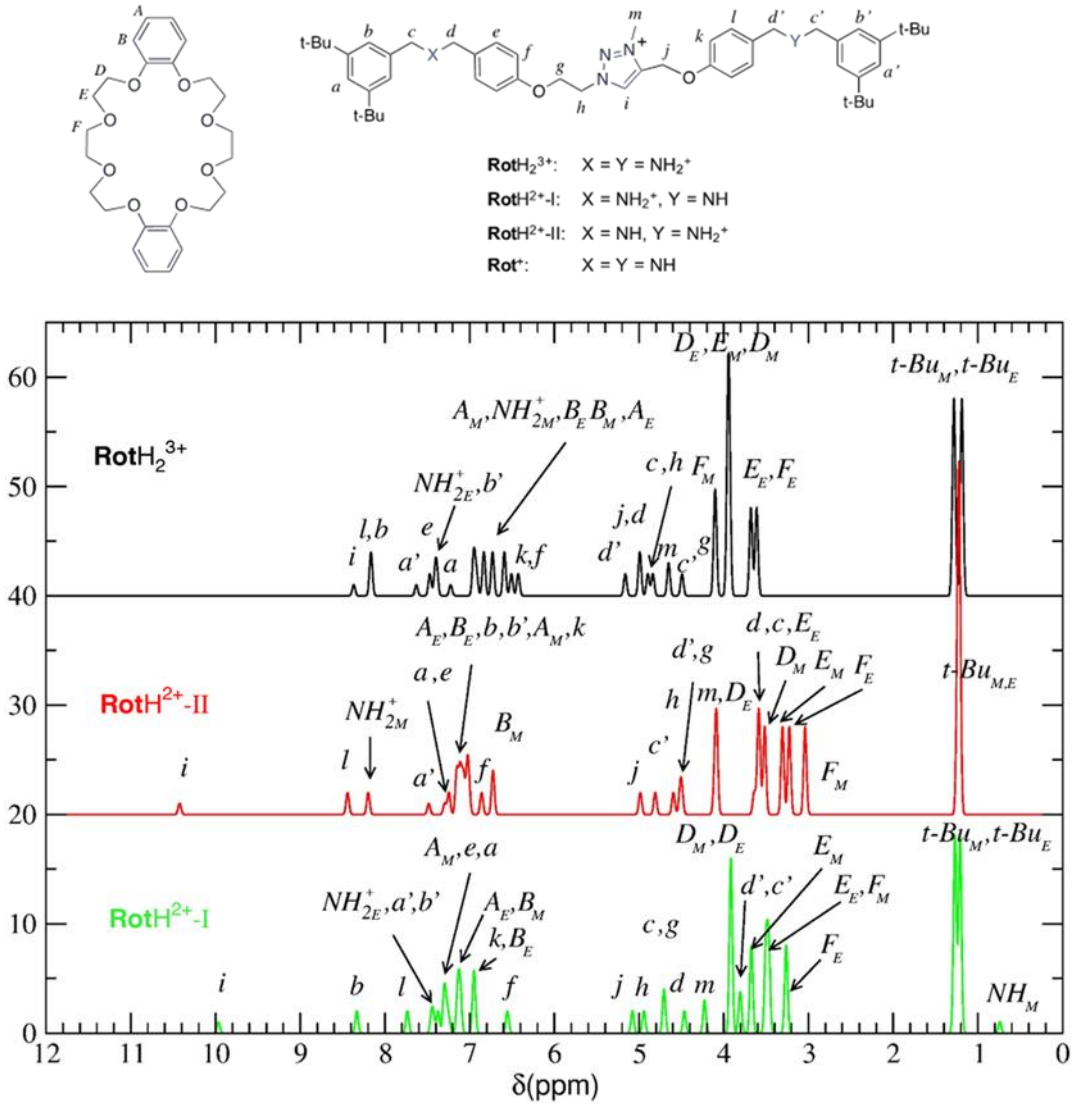

Figure 4.15. Simulated ^{1}H-NMR spectra of the optimized geometry of **Rot**H_2^{3+} (top panel, black line); **Rot**H^{2+}-II (middle panel, red line); **Rot**H^{2+}-I (bottom panel, green line). Labels are as shown in the structures reported below. Lower-case and upper-case letters refer respectively to protons of the axle and of the two rings. The subscripts *M*, *E*, refer to protons on the methylene (*M*) or ethylene (*E*) side of the axle, respectively.

Concerning **Rot**$^{+}$, a more complex behaviour was expected because of the presence of two rings in competition for the sole triazolium station. The free energy profile for the shuttling of the two macrocycles with respect to the central triazolium site has been calculated and is reported in **Figure 4.16**. As a consequence of the large dimensions of the system, the free energy profile has been calculated in vacuum, therefore the predicted barriers are higher compared to the real ones. However previous studies performed on rotaxanes indicated that, although the inclusion of solvent molecules decreases the barriers by about 15 kcal mol^{-1}, the transition state structures do not change appreciably with respect to vacuum

calculations.[38] Therefore, while the barriers are quantitatively overestimated, the free energy path provides a qualitatively correct picture of the shuttling process. The profile displays three free energy wells with comparable depth characterized by a very different mutual arrangement of the molecular components.

The structures representative of the three minima, namely **A**, **B** and **C**, are shown in **Figure 4.17**. In structure **A**, one macrocycle is located close to the triazolium station and the other one is on the ethylene bridge side; in structure **B**, both macrocycles are close to the central triazolium station; in structure **C**, one ring is close to the triazolium station and the other is on the methylene bridge side. The profile reported in **Figure 4.16** highlights a significantly lower barrier for the **B** → **C** path with respect to the **B** → **A** one. Importantly, such multi-well free energy profile can explain the unusual temperature-dependent behaviour observed analysing **Rot**$^+$ by means of VT-NMR.

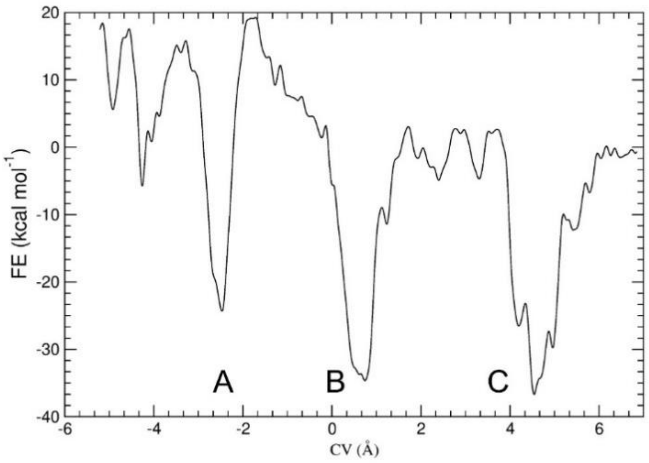

Figure 4.16. Free energy profile (kcal mol^{-1}) for the shuttling of the two macrocycles along the axle in **Rot**$^+$. The Collective Variable (Å) represents the displacement of the ethereal oxygen atoms of the two rings with respect to the triazolium nitrogen atoms. The three different co-conformations of **Rot**$^+$ characterized by deep free energy minima are labelled **A**, **B** and **C**.

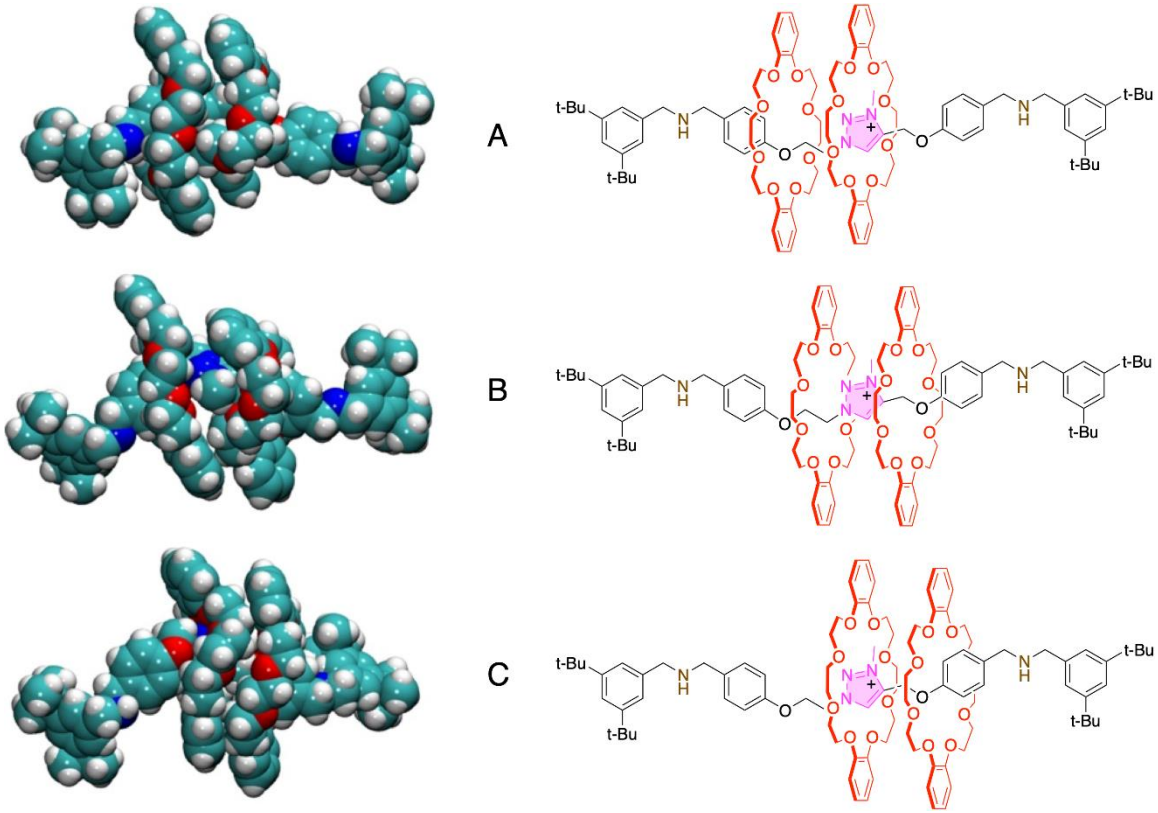

Figure 4.17. Graphical representations of the three co-conformations extracted from the combined Metadynamics-DFT simulation of **Rot**$^{+}$ at room temperature. The reported co-conformations are representative of the three free energy minima labelled **A**, **B**, **C**. Color code: C cyan, N blue, O red, H white.

At low temperatures the most stable structure **C** is predominant, while at intermediate temperatures both **C** and **B** are present in comparable concentrations. On the other hand, structure **A** required higher temperatures to increase his population, since such co-conformation is less stable than **B** and **C**. In order to verify this hypothesis, individual ^{1}H NMR spectra of **A**, **B** and **C** were calculated (**Figure 4.18**). In the simulated spectra, the triazolium proton (i, **Figure 4.18**), undergoes an initial deshielding, followed by shielding during the transition **C** → **B** → **A**, which is in agreement with the experimental VT-NMR data (**Figure 4.7**). When a ring encircles the triazolium station the triazolium proton appeared deshielded, while when the ring is far from the triazolium proton the chemical shift decreases, likewise to what already observed with **Rot**H^{2+}-I, **Rot**H^{2+}-II and **Rot**H$_2^{3+}$ respectively.

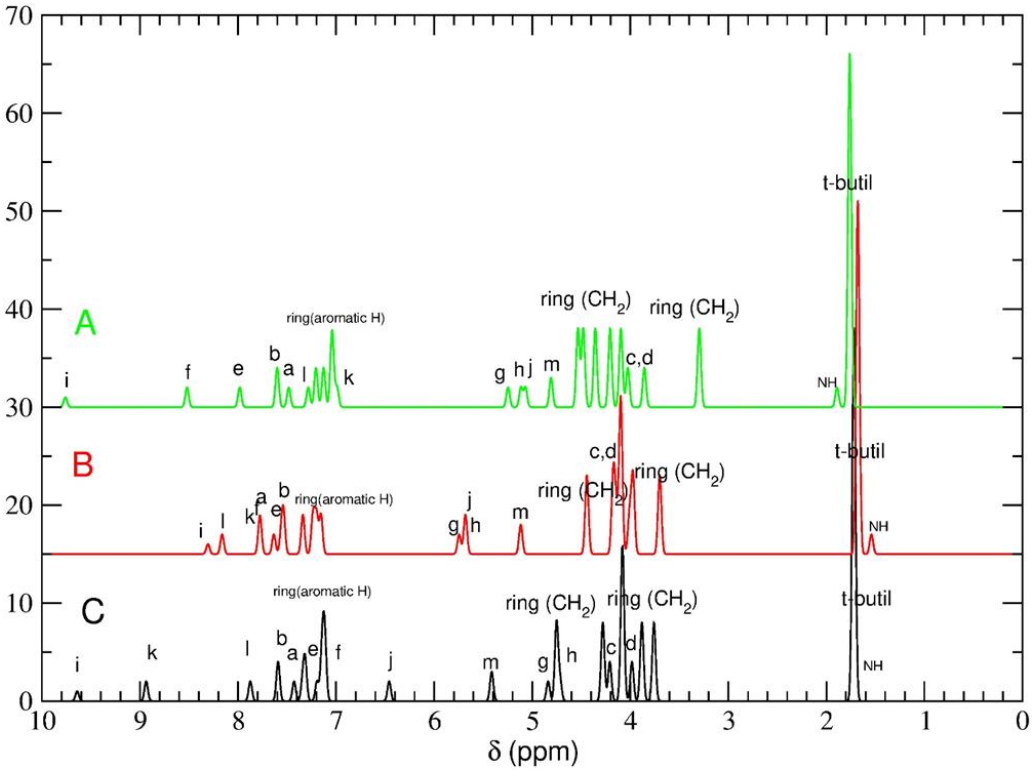

Figure 4.18. Simulated ^{1}H-NMR spectra for the free energy minima **A** (green line), **B** (red line), **C** (black line).

For this reason, in both **A** and **C**, where the macrocycle is positioned very close to the triazolium station, the triazolium proton is deshielded. Conversely, in structure **B**, in which both macrocycles are relatively distant from the triazolium station, the calculated signal for the triazolium proton is located at a lower chemical shift.

Besides the thermodynamic properties of the three co-conformers, additional information is provided by the energy profile describing the interconversion between them. The energy barrier for the **B** → **A** conversion is higher than that of the **B** → **C** one, suggesting that a directionally controlled shuttling motion could be in principle achieved in triazolium-based rotaxanes, exploiting the intrinsic asymmetry of the triazolium group and coupling it to additional ratcheting mechanisms. The triazolium can indeed be approximated to a flat rigid section bearing an off-axis methyl, and in this context the transit of the ring occurs according to two non-equivalent paths (**Figure 4.19**).

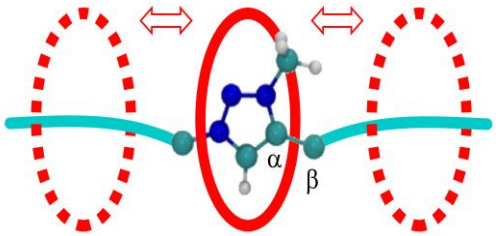

Figure 4.19. Ball-and-stick representation of a triazolium unit encircled by a macrocycle (red oval). Color code: C, cyan; N, blue; H, white. The red hollow arrows represent two non-equivalent shuttling directions for the macrocycle.

In particular, in the **B** → **A** path, the macrocycle should first impact the bulkier methyl group, causing a rotation of the triazolium along the C_α-C_β single bond (right-hand side in **Figure 4.19**). As a result, the transit of the macrocycle is obstructed until the triazolium rotation occurs and therefore requires a greater free energy cost (**Figure 4.20.a**). On the other hand, in the **B** → **C** path, the macrocycle should first pass over the flat rigid part of the triazolium, hindering in this way the triazolium rotation (left-hand side in **Figures 4.19**). Consequently, the passage is easier and the **B** → **C** transit can be completed at a lower free energy cost than the **B** → **A** path (**Figure 4.20.b**).

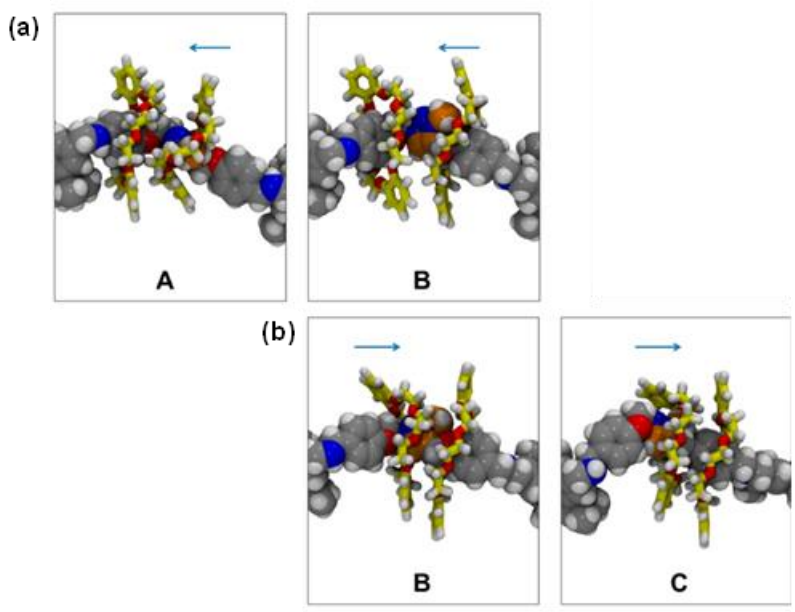

Figure 4.20. Snapshots taken from the DFT-Metadynamics simulation of **Rot**$^+$, (a) right-to-left transit of a DB24C8 macrocycle over the triazolium station, describing the **B** → **A** path, (b) left-to-right transit of a DB24C8 macrocycle over the triazolium station, describing the **B** → **C** path. Color code: H, white; N, blue; O, red. C atoms belonging to the axle in grey, C atoms belonging to the DB24C8 ring in yellow, C atoms of the triazolium group in orange.

4.7 Conclusions

A [3]rotaxane that comprises two acid-base-switchable ammonium stations and a permanent triazolium station has been designed and investigated. The system thus conceived gives access to a family of rotaxanes, namely **Rot**H_2^{3+}, **Rot**H^{2+} and **Rot**$^+$, that contain a number of recognition sites respectively larger, equal or lower than the number of interlocked macrocyclic rings.

Detailed spectroscopic studies and DFT-Metadynamics calculations showed that these molecules exhibit markedly different structural and dynamic properties. In **Rot**H_2^{3+}, the two crown ethers encircle the ammonium stations, making them harder to deprotonate by a base in solution if compared to the deprotonation of the tricationic free thread compound **12**; moreover, the ammonium sites exhibit different pK_a values because of the inherent asymmetry of the axle. The dicationic species **Rot**H^{2+} can exist in two non-equivalent isomeric forms that differ for the position of the ammonium site (and of its surrounding macrocycle) with respect to the central triazolium. While upon mono-deprotonation of the free axle **12** these two isomers are in fast equilibrium and could not be individually observed, in the rotaxane the proton exchange between the isomers becomes slow due to the presence of the rings. For this reason, the two forms of **Rot**H^{2+} could be studied, and the peculiar effect of the moving rings on the acidity of the ammonium sites has been thoroughly characterized.

The fully deprotonated species **Rot**$^+$, that presents the sole triazolium station and two rings, is a rare arrangement, despite the large number of studies on rotaxanes available in the literature. Such species analyzed by means of NMR spectroscopy confirmed the expected high dynamicity and frustration of the system. Computational modelling has been employed to identify the stable co-conformations available to the rotaxane and to simulate the related NMR spectra. This approach enabled us to interpret the non-trivial spectroscopic results and understand the dynamic properties of **Rot**$^+$. The stable co-conformations of this rotaxane present one macrocycle encircling the triazolium station and the other ring located in the vicinity. However, a deep energy minimum in which the two crown ethers are very close together and share the recognition site was also identified. Another significant information arises from the different barriers observed for the transit of a macrocycle over the triazolium unit, depending on the approaching direction along the axle (**B** $\rightarrow$ **A** or **B** $\rightarrow$ **C**). Such barriers resulted different because of the presence of the asymmetrically positioned methyl substituent on the triazolium station.

This study shows that interesting and unusual thermodynamic and kinetic phenomena can emerge by interlocking multiple macrocyclic rings with a molecular axle and inducing a mismatch between rings and stations. Moreover, the investigated systems are constituted by simple molecular components with a well-established chemistry. Research in this direction is important to foster the use of MIMs with designed physico-chemical and mechanical properties as components of functional nanostructured devices and materials.

4.8 Experimental details

Solvents and reagents [3,5-di-*tert*-butyl-benzyl bromide, sodium azide, 4-hydroxybenzaldehyde, sodium borohydride, di-*tert*-butyl-dicarbonate, 1,2-dibromoethane, propargyl bromide, hexafluorophosphoric acid, dibenzo-24-crown-8, methyl iodide, ammonium hexafluorophosphate, polystyrene-supported BEMP, P1-*t*-Bu] and triethylamine were all used as supplied by Fluorochem, Sigma-Aldrich or VWR without further purification.

^{1}H NMR spectra were recorded on an Agilent DD2 spectrometer operating at 500 MHz or a Varian Mercury spectrometer operating at 400 MHz; ^{13}C NMR spectra were recorded on an Agilent DD2 spectrometer operating at 126 MHz or a Varian Mercury spectrometer operating at 101 MHz. Chemical shifts are quoted in ppm relative to tetramethylsilane ($SiMe_4$, $\delta = 0$ ppm), using the residual solvent peak as a reference standard; all coupling constants (*J*) are expressed in Hertz (Hz). Exchange rate constant quantification was carried out using the MestreLab EXSYCalc software.

Flash column chromatography was performed using Sigma Aldrich Silica 40 (230-400 mesh size or 40-63 μm) as the stationary phase. Size exclusion chromatography was performed using Biorad Biobeads SX-3 as the stationary phase. Thin layer chromatography was performed on TLC Silica gel 60 F254 coated aluminium plates from Merck. Hydrogenation reactions were carried out in a H-Cube flow reactor equipped with a 10 % Pd/C catalyst at a H_2 pressure of 10 bar and a flow rate of 1 mL min^{-1} using methanol as the solvent.

UV acidity determination experiments

The absorption spectra in the 800-200 nm range were recorded using a PerkinElmer Lambda 750 double beam spectrophotometer. All the acquisitions were carried out at room-temperature on air-equilibrated solutions of the samples contained in spectrophotometric quartz cuvettes of 1 cm optical path length. The precision on the wavelength values was ± 1 nm. The titration experiments were performed in acetonitrile using triethylamine (pK_a = 18.8) or phosphazene **B2** (P1-*t*-Bu, pK_a = 26.9) bases. The pK_a values for the ammonium stations were calculated based on the titration curve fitting,

carried out on the HyperSpec suite. The error on the pK_a values is estimated to be ±0.1 units, calculated as the average mean square root in the pK_a values of the ammonium stations investigated.

NMR acidity measurements

Deprotonation experiments were carried out in acetonitrile using phosphazene compounds as heterogeneous **B1** (polystyrene-supported BEMP) and homogeneous **B2** (P1-*t*-Bu, pK_a = 26.9) bases.

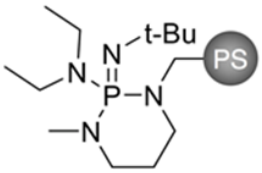

B1

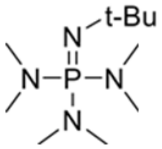

B2

Computational Details

Computational investigation performed in collaboration with the Fois group at the University of Insubria.

Quantum chemical calculations

A model structure of the complex **Rot**H_2^{3+}, consisting of two identical dibenzo-24-crown-8 (DB24C8) rings interlocked with an axle containing two lateral dibenzylammonium (Am) and one central triazolium (Tz) stations, was optimized by adopting the D95(d,p)[39] basis set and the range-separated hybrid functional ωB97XD[40] as density functional approximation to DFT.

From this optimized structure, two different starting geometries for the **Rot**H^{2+} model were created by removing one proton from one of the two lateral dibenzylammonium stations. These computational models correspond to the two isomers **Rot**H^{2+}-I and **Rot**H^{2+}-II, formed upon mono-deprotonation of the parent compound **Rot**H_2^{3+}. In particular, the starting structures for **Rot**H^{2+}-I and

RotH^{2+}-II were obtained by deprotonating the Am on the methyl group side, and the Am on the ethyl group side, respectively. These two geometries were optimized at the same level of theory as **Rot**H_2^{3+} - namely, ωB97XD/D95(d,p).

The calculations of the NMR spectra of the above-mentioned optimized structures of **Rot**H_2^{3+} **Rot**H^{2+}-I and **Rot**H^{2+}-II, were performed by using as basis set a QZP (quadruple-ζ with polarization) for all the protons[41] and cc-pCVDZ (double-ζ with polarization and tight-core) for the heavy atoms[42] (O, C, N) and adopting a DFT approximation optimized for proton NMR chemical shifts[43]. The chemical shifts of all the protons were calculated by taking as a reference the chemical shift of the protons of tetrametilsilane (TMS). The chemical shifts of the protons reported in this work were calculated from the average over equivalent protons.

The above calculations were performed with the Gaussian 09 code[44] using an implicit solvent model for CH_2Cl_2 or CH_3CN.[45]

Ab initio molecular dynamics and Metadynamics calculations

The finite-temperature behavior of **Rot**$^+$ was modelled via *ab initio* molecular dynamics[46], combined with statistical sampling according to the *ab initio* metadynamics[47,48] scheme.

A Generalized Gradient Approximation to density functional theory (DFT) was used to describe electron-electron interactions – in particular, the PBE functional in combination with empirical dispersion corrections (*i.e.* PBE-D2).[49,50] Ion cores-electron interactions were treated with ultra-soft pseudopotentials.[51] Plane-waves (PW) were used as basis set. The cutoffs for the PW expansion of the wavefunctions and density were 25 Ry and 200 Ry, respectively. Calculations were performed using periodic boundary conditions, which were applied to a simulation cell of size 70×30×30 Å. Such a size is sufficiently large to allow for a Γ-point-only sampling, and to minimize interactions of the rotaxane with periodic images.

Each simulation system was constituted by the neutral ring DB24C8 and by the positively charged axle. In all cases, the simulation cell contained a total of 255 atoms.

A guess configuration was obtained by removing one proton from both the two lateral dibenzylammonium stations of the parent compound. A*b initio* molecular dynamics (AIMD) equilibration (elapsed time: 10 ps) was performed at 300 K (27 °C). This temperature was chosen in order to favour a faster equilibration of the system. Additionally, it corresponds roughly to the central part of the temperature conditions at which the variable temperature NMR experiments were conducted (T = from –40 to 70 °C).

The simulations were carried out in the canonical NVT ensemble and with Nose-Hoover chain thermostats for the ionic degrees of freedom.[52,53] The AIMD equations[46,54] were integrated with a time

step of 5 atomic units (a.u.), *i.e*. 0.121 fs. The (fictitious) mass of the wavefunction's coefficients was 500 a.u.

The shuttling process was explored by performing two *ab initio* metadynamics (MTD). In the first run, we selected as collective variable (CV), the displacement of the 8 oxygen atoms of the DB24C8 macrocycle on the side of the ethylene bridge, with respect to the nitrogen atoms of the Tz station (see path B→ C in Figure 10, main text). In the second run, we adopted as CV the displacement of the 8 oxygen atoms of the ring on the methylene bridge side with respect to the Tz nitrogen atoms (see path B→A in Figure 10, main text). For the evolution of the CV, we employed the Lagrange-Langevin dynamics with friction of 0.001 a.u. The selected target temperature was 300 K as in the equilibration runs. The metadynamics parameters adopted for the gaussian hills in the production simulations were the following in all the runs: perpendicular width = 0.02 a.u., height = 0.002 a.u. The sampling was accomplished in ~3000 metadynamics steps.

Due to the size of the simulation cell, all the PW simulations were performed in the gas phase.

All PW calculations were carried out with the CPMD (Car-Parrinello-Molecular-Dynamics) computer program[55] running on the Shaheen II supercomputer at Kaust.

4.8.1 Synthetic procedures

3,5-di-*tert*-butylbenzyl azide, 1

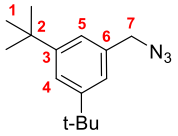

A solution of 3,5-di-*tert*-butylbenzyl bromide (10.34 g, 36.50 mmol) and sodium azide (2.37 g, 36.50 mmol) in dimethylformamide (200 mL) was heated to 70 °C for 2 h. Cooling to room temperature and removal of the solvent under reduced pressure provided a crude solid which was suspended in diethyl ether (100 mL), washed with water (3×100 mL) and dried over anhydrous $MgSO_4$. Filtration and removal of the solvent under reduced pressure provided the azide **1** as a pale yellow oil (8.96 g, quantitative), which was used without further purification. ^{1}H NMR (500 MHz, chloroform-*d*) δ 7.47 (t, *J* = 1.9 Hz, 1H, **4**), 7.20 (d, *J* = 1.9 Hz, 2H, **5**), 4.39 (s, 2H, **7**), 1.40 (s, 18H, **1**). ^{13}C NMR (126 MHz, chloroform-*d*) δ 151.51, 134.68, 122.51, 122.42, 55.62, 34.96, 31.55.

3,5-di-*tert*-butylbenzyl amine, 2

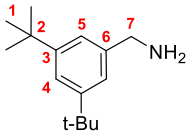

A solution of the azide **1** (8.96 g, 36.50 mmol) in methanol (730 mL) was reduced using a flow hydrogenation reactor equipped with a 10 % Pd/C catalyst and in situ generated H_2 (10 bar) at a flow rate of 1 mL min^{-1}. Removal of the solvent under reduced pressure provided the product **2** as a colourless oil (8.01 g, quantitative), which was used without further purification. ^{1}H NMR (500 MHz, chloroform-*d*) δ 7.34 (t, *J* = 1.9 Hz, 1H, **4**), 7.17 (d, *J* = 1.9 Hz, 2H, **5**), 3.88 (s, 2H, **7**), 1.35 (s, 18H, **1**). ^{13}C NMR (126 MHz, chloroform-*d*) δ 150.99, 142.53, 121.29, 120.90, 47.18, 34.86, 31.51.

4-(((3,5-di-*tert*-butylbenzyl)amino)methyl)phenol, 3

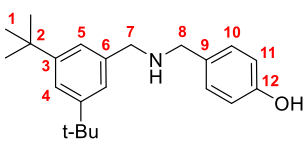

An ethanol solution (200 mL) of **2** (3.11 g, 14.16 mmol) and 4-hydroxybenzaldehyde (1.73 g, 14.16 mmol) was dried azeotropically at the rotary evaporator. The procedure was repeated three times, affording the imine intermediate, which was re-dissolved in ethanol (200 mL) and reduced by portionwise addition of $NaBH_4$ (1.18 g, 17.00 mmol) providing a vigorous effervescence and a final light-yellow solution. Once the effervescence terminated, the solution was heated to reflux for 30

min, then cooled down to room temperature and the solvent removed under reduced pressure. The crude product was dissolved in ethyl acetate (150 mL), washed with water (3×150 mL) and dried over $MgSO_4$. Filtration and removal of the solvent under reduced pressure provided an off-white solid which was purified by recrystallisation from cyclohexane to obtain the product **3** as a colourless solid (3.79 g, 82%). ^{1}H NMR (400 MHz, chloroform-*d*) δ 7.34 (t, *J* = 1.8 Hz, 1H, **4**), 7.18 (d, *J* = 1.8 Hz, 2H, **5**), 7.13 - 7.07 (m, 2H, **10**), 6.63 - 6.57 (m, 2H, **11**), 3.85 (s, 2H, **8**), 3.76 (s, 2H, **7**), 1.31 (s, 18H, **1**). ^{13}C NMR (101 MHz, chloroform-*d*) δ 156.24, 151.13, 138.15, 130.04, 129.94, 122.79, 121.44, 115.99, 53.86, 52.83, 34.94, 31.59.

***tert*-butyl 3,5-di-*tert*-butylbenzyl(4-hydroxybenzyl)carbamate, 4**

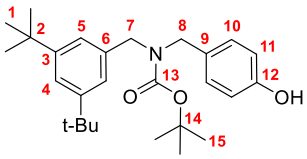

A tetrahydrofuran solution (100 mL) of di-*tert*-butyl dicarbonate (2.65 mL, 11.52 mmol) was added dropwise to a tetrahydrofuran solution (500 mL) of **3** (3.75 g, 11.52 mmol). The resulting mixture was stirred at room temperature for 16 h. Upon reaction completion, the solvent was removed under reduced pressure and the residue dissolved in ethyl acetate (150 mL), washed with water (3×150 mL) and dried over $MgSO_4$. Filtration and removal of the solvent under reduced pressure provided a yellow solid which was purified by flash chromatography (hexane:ethyl acetate 70:30, R_f = 0.65) to obtain the product **4** as a colourless solid (4.275 g, 87%). ^{1}H NMR (400 MHz, chloroform-*d*) δ 7.33 (t, *J* = 1.7 Hz, 1H, **4**), 7.05 (m, 4H, **5**+**10**), 6.79 (m, 2H, **11**), 6.29 (s, 1H, O*H*), 4.34 (dd, *J* = 20.9, 18.6 Hz, 4H, **7**+**8**), 1.53 (s, 9H, **15**), 1.32 (s, 18H, **1**). ^{13}C NMR (101 MHz, chloroform-*d*) δ 155.62, 150.91, 137.10, 136.70, 129.41, 129.10, 128.91, 122.29, 121.91, 121.18, 115.51, 80.34, 49.91, 49.41, 48.90, 48.68, 34.79, 31.50, 28.56.

***tert*-butyl 3,5-di-*tert*-butylbenzyl(4-(prop-2-yn-1-yloxy)benzyl)carbamate, 5**

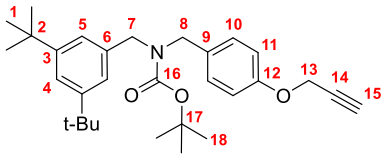

A dry acetonitrile (250 mL) suspension containing compound **4** (1.20 g, 2.82 mmol), propargyl bromide (911 µL, 8.46 mmol) and K_2CO_3 (780 mg, 5.64 mmol) was stirred at 50 °C for 96 h under a dinitrogen atmosphere. The mixture was then cooled down to room temperature and the solvent removed under reduced pressure. The residue was dissolved in dichloromethane (100 mL), washed with water (3×100 mL) and dried over $MgSO_4$. Filtration and removal of the solvent under reduced pressure provided an orange oil which was purified by flash chromatography (hexane:ethyl acetate

85:15, R_f = 0.37) to obtain the product **5** as a brown/orange oil (1.23 g, 94%). ^{1}H NMR (400 MHz, chloroform-*d*) δ 7.32 (t, *J* = 1.8 Hz, 1H, **4**), 7.22 - 6.98 (m, 4H, **5**+**10**), 6.93 (d, *J* = 8.6 Hz, 2H, **11**), 4.69 (d, *J* = 2.4 Hz, 2H, **13**), 4.47 - 4.17 (m, 4H, **7**+**8**), 2.52 (t, *J* = 2.4 Hz, 1H, **15**), 1.51 (s, 9H, **18**), 1.31 (s, 18H, **1**). ^{13}C NMR (101 MHz, chloroform-*d*) δ 156.91, 156.10, 150.97, 137.39, 137.12, 131.38, 129.51, 128.95, 122.41, 122.01, 121.23, 114.99, 79.93, 78.75, 75.62, 55.97, 50.04, 49.55, 48.90, 48.63, 34.90, 31.61, 28.63.

N-(3,5-di-*tert*-butylbenzyl)-1-(4-(prop-2-yn-1-yloxy)phenyl)methanaminium hexafluorophosphate, 6

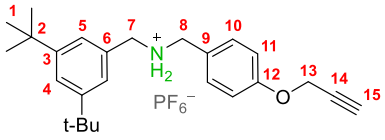

A tetrahydrofuran solution (1 mL) of HPF_6 (1.3 mL of a 55% aqueous solution, 9.00 mmol) was added to a tetrahydrofuran solution (10 mL) of compound **5** (1.40 g, 3.02 mmol) and the resulting mixture stirred at room temperature for 4 h. The solvent was removed under reduced pressure, water (50 mL) was then added and the mixture was extracted with dichloromethane (3×50 mL) and the combined organic phases washed with water (3×50 mL). The solvent was removed under reduced pressure providing a light brown crude product that was purified by recrystallisation from cyclohexane, obtaining the product **6** as a colourless solid (1.15 g, 75%). ^{1}H NMR (500 MHz, chloroform-*d*) δ 7.47 (s, 1H, **4**), 7.30 - 7.25 (m, 2H, **10**), 7.17 (d, *J* = 1.8 Hz, 2H, **5**), 6.98 (d, *J* = 8.5 Hz, 2H, **11**), 4.63 (d, *J* = 2.1 Hz, 2H, **13**), 4.11 (d, *J* = 21.6 Hz, 4H, **7**+**8**), 2.51 (m, 1H, **15**), 1.31 (s, 18H, **1**). ^{13}C NMR (126 MHz, Chloroform-*d*) δ 158.88, 152.67, 131.59, 128.40, 124.25, 124.04, 122.12, 115.91, 78.07, 76.14, 55.91, 51.77, 50.52, 35.10, 31.39. ^{19}F NMR (470 MHz, chloroform-*d*) δ –0.47 (d, *J* = 715.4 Hz, 6F).

tert-butyl 4-(2-bromoethoxy)benzyl(3,5-di-*tert*-butylbenzyl)carbamate, 7

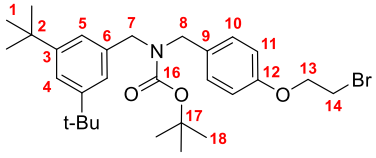

Compound **4** (1.57 g, 3.68 mmol), 1,2-dibromoethane (5 mL, 58 mmol), KI (30 mg, 0.18 mmol) and K_2CO_3 (1.27 g, 9.20 mmol) were suspended in dry acetonitrile (10 mL) under a dinitrogen atmosphere and stirred at 70 °C for 5 days. The mixture was then cooled down to room temperature and ethyl acetate (20 mL) was added. The organic phase was washed with water (3×50 mL), dried over $MgSO_4$. Filtration and removal of the solvent under reduced pressure provided a pale yellow solid which was purified by flash chromatography (hexane:ethyl acetate 90:10) to obtain the product

7 as a colourless solid (820 mg, 42%). ^{1}H NMR (400 MHz, chloroform-*d*) δ 7.32 (s, 1H, **4**), 7.24 - 6.96 (m, 4H, **5**+**10**), 6.86 (d, *J* = 8.4 Hz, 2H, **11**), 4.44 - 4.23 (m, 6H, **7**+**8**+**14**), 3.64 (t, *J* = 6.3 Hz, 2H, **13**), 1.51 (s, 9H, **17**), 1.31 (s, 18H, **1**). ^{13}C NMR (126 MHz, chloroform-d) δ 157.28, 155.98, 150.84, 137.25, 131.13, 129.51, 128.91, 122.26, 121.87, 121.10, 114.75, 79.82, 67.94, 49.89, 49.42, 48.47, 34.77, 31.47, 29.10, 28.50.

tert-butyl 4-(2-azidoethoxy)benzyl(3,5-di-_tert_-butylbenzyl)carbamate, 8

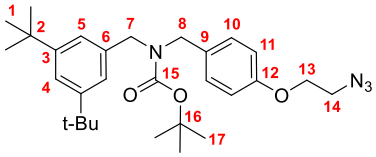

Compound **7** (1.28 g, 2.40 mmol) and sodium azide (200 mg, 3.10 mmol) were suspended in dry dimethylformamide (20 mL) under a dinitrogen atmosphere and stirred at 70 °C for 3 h. The mixture was then cooled down to room temperature and water (20 mL) was added, followed by extraction with diethyl ether (3×30 mL). The combined organic phases were washed with water (3×30 mL) and dried over $MgSO_4$. Filtration and removal of the solvent under reduced pressure provided the product **8** as a colourless solid (980 mg, 83%). ^{1}H NMR (500 MHz, chloroform-*d*) δ 7.33 (s, 1H, **4**), 7.25 - 6.97 (m, 4H, **5**+**10**), 6.88 (d, *J* = 8.4 Hz, 2H, **11**), 4.46 - 4.24 (m, 4H, **7**+**8**), 4.16 (t, *J* = 5.0 Hz, 2H, **14**), 3.61 (t, *J* = 4.9 Hz, 2H, **13**), 1.52 (s, 9H, **17**), 1.32 (s, 18H, **1**). ^{13}C NMR (126 MHz, chloroform-*d*) δ 157.58, 156.13, 150.99, 137.40, 131.18, 129.62, 128.99, 122.43, 122.06, 121.26, 114.72, 79.97, 67.17, 50.34, 50.02, 49.56, 48.92, 48.62, 34.92, 31.62, 28.65.

_N_-(4-(2-azidoethoxy)benzyl)-1-(3,5-di-_tert_-butylphenyl)methanaminium hexafluorophosphate, 9

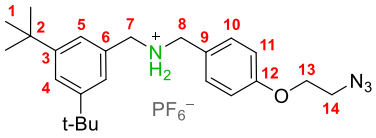

A tetrahydrofuran solution (1 mL) of HPF_6 (1.3 mL of a 55% aqueous solution, 9.00 mmol) was added to a tetrahydrofuran solution (10 mL) of compound **8** (930 mg, 1.90 mmol) and the resulting mixture stirred at room temperature for 4 h. Water (50 mL) was then added and the mixture was extracted with dichloromethane (3×50 mL) and the combined organic phases washed with water (3×50 mL). The solvent was removed under reduced pressure providing a light brown crude product that was purified by recrystallisation from cyclohexane, obtaining the product **9** as a colourless solid (741 mg, 72%). ^{1}H NMR (500 MHz, chloroform-*d*) δ 7.47 (s, 1H, **4**), 7.30 - 7.25 (m, 2H, **10**), 7.18 (m, 2H, **5**), 6.92 (d, *J* = 8.5 Hz, 2H, **11**), 4.18 - 4.06 (m, 6H, **7**+**8**+**14**), 3.57 (t, *J* = 4.8 Hz, 2H, **13**), 1.31 (s, 18H, **1**). ^{13}C NMR (126 MHz, Chloroform-*d*) δ 159.62, 152.72, 131.69, 128.36, 124.29, 124.00, 121.86,

115.58, 67.10, 51.83, 50.63, 50.18, 35.10, 31.38. ^{19}F NMR (470 MHz, chloroform-*d*) δ –70.47 (d, *J* = 715.4 Hz, 6F).

Triazole-linked [3]rotaxane, 10

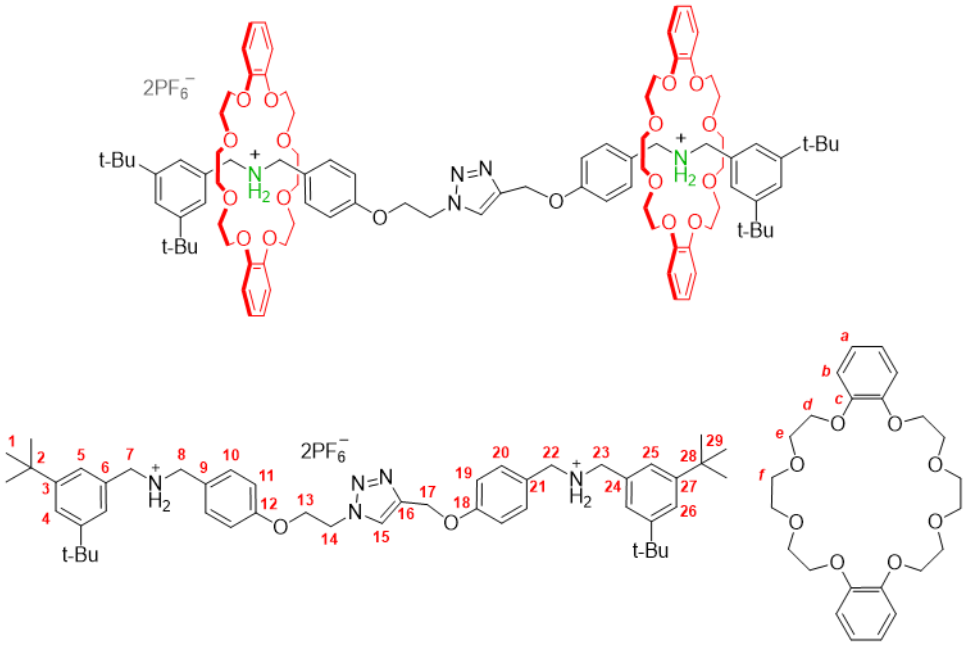

Compound **6** (150 mg, 0.28 mmol), compound **9** (143 mg, 0.28 mmol) and DB24C8 (630 mg, 1.40 mmol) were dissolved in dry dichloromethane (20 mL) and stirred for 10 min at room temperature under a dinitrogen atmosphere. The catalyst $[Cu(MeCN)_4][PF_6]$ (59 mg, 0.61 mmol) was then added and the resulting mixture stirred at room temperature for 48 h. The mixture was then diluted with dichloromethane (50 mL) and washed with sodium ethylenediaminotetraacetate (0.1 M in H_2O, 3×25 mL), water (3×25 mL) and dried over $MgSO_4$. Filtration and removal of the solvent under reduced pressure provided a pale-yellow solid which was purified by Size-Exclusion Chromatography (dichloromethane) to obtain the product **10** as a colourless solid (425 mg, 78%). ^{1}H NMR (500 MHz, methylene chloride-d_2) δ 7.94 (s, 1H, **15**), 7.53 (s, 4H, NH_2), 7.42 - 7.37 (m, 2H, **4**+**26**), 7.29 (m, 4H, **5**+**25**), 7.12 (d, *J* = 8.7 Hz, 2H, **20**), 7.11 (d, *J* = 8.7 Hz, 2H, **10**), 6.92 - 6.80 (m, 8H, ***a***), 6.84 - 6.75 (m, 8H, ***b***), 6.67 (d, *J* = 8.6 Hz, 2H, **19**), 6.53 (d, *J* = 8.6 Hz, 2H, **11**), 5.02 (s, 2H, **17**), 4.76 - 4.68 (m, 6H, **14**+**7**+**23**), 4.52 (dd, *J* = 6.8, 3.2 Hz, 4H, **8**+**22**), 4.20 (t, *J* = 5.1 Hz, 2H, **13**), 4.14 - 4.03 (m, 16H, ***d***), 3.83 - 3.68 (m, 16H, ***e***), 3.66 - 3.43 (m, 16H, ***f***), 1.20 (s, 36H, **1**+**29**). ^{13}C NMR (126 MHz, Methylene Chloride-d_2) δ 159.33 (**18**), 158.80 (**12**), 151.94 (**3** or **26**), 151.90 (**26** or **3**), 147.88 and 147.82 (***c***), 143.77 (**16**), 131.85 (**6**+**24**), 131.23 (**10** or **20**), 131.21 (**20** or **10**), 124.83 (**15**), 124.48 (**9** or **21**), 124.10 (**21** or **9**), 123.96 (**5** or **25**), 123.92 (**25** or **5**), 123.71 (**4**+**27**), 121.94 and 121.86 (***a***), 114.86 (**19**), 114.59 (**11**), 112.93 and 112.85 (***b***), 71.01 and 70.98 (***f***), 70.61 and 70.60 (***e***), 68.36 and 68.28 (***d***), 66.54 (**13**), 61.91 (**17**), 53.22 (**7**+**23**), 52.70 and 52.60 (**8**+**22**), 50.01

(**14**), 35.15 and 35.14 (**2**+**28**), 31.46 and 31.45 (**1**+**29**). ^{19}F NMR (470 MHz, acetonitrile-d_3) δ –72.89 (d, J = 706.5 Hz, 12F). HRMS-ESI (m/z): calcd for [$C_{97}H_{133}N_5O_{18}$], 828.4862; found 828.9901 [**10**+H]$^{2+}$.

Tricationic [3]rotaxane, RotH_2^{3+}

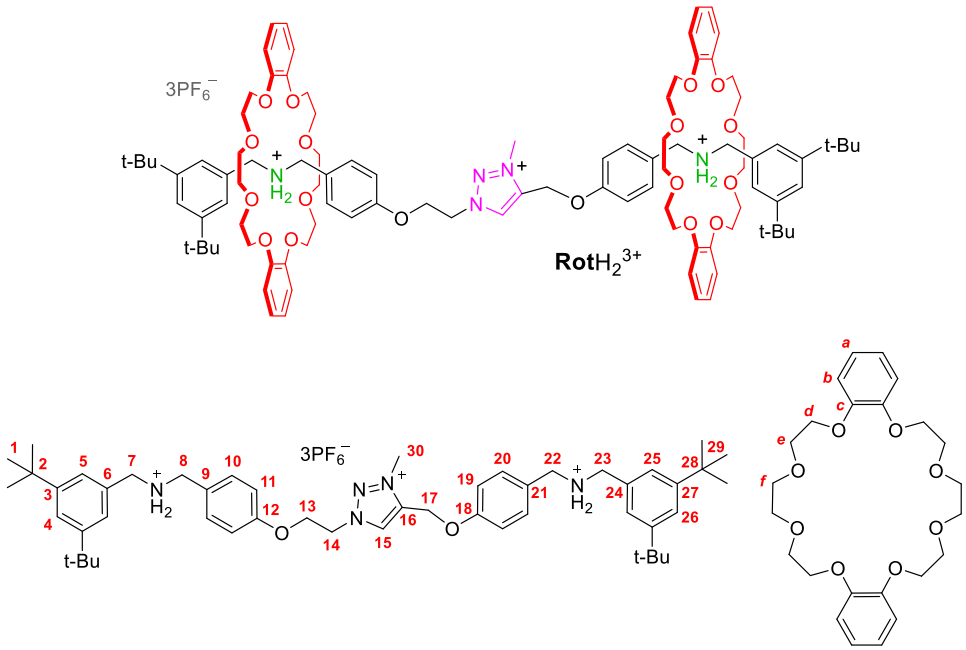

Under a dinitrogen atmosphere, compound **10** (254 mg, 0.13 mmol) was dissolved in iodomethane (13 mL) and the resulting solution was stirred for 48 h at room temperature under exclusion of light. Upon reaction completion, the solvent was removed under reduced pressure providing a yellow solid, which was dissolved in the minimum amount of acetonitrile. Addition of a saturated aqueous solution of ammonium hexafluorophosphate led to the precipitation of a yellow solid, which was isolated, dissolved in dichloromethane and washed with a saturated aqueous solution of ammonium hexafluorophosphate (3×5 mL) and water (3×5 mL) and dried over $MgSO_4$. Filtration and removal of the solvent under reduced pressure provided the product **Rot**H_2^{3+} as a yellow solid (246 mg, 91%). ^{1}H NMR (500 MHz, methylene chloride-d_2) δ 8.59 (s, 1H, **15**), 7.58 (s, 4H, NH_2), 7.41 (d, J = 6.9 Hz, 2H, **4**+**26**), 7.35 - 7.27 (m, 4H, **5**+**25**), 7.20 (d, J = 8.6 Hz, 2H, **20**), 7.14 (d, J = 8.6 Hz, 2H, **10**), 6.85 (m, 16H, ***a***+***b***), 6.69 (d, J = 8.6 Hz, 2H, **19**), 6.61 (d, J = 8.6 Hz, 2H, **11**), 5.19 (s, 2H, **17**), 4.99 - 4.93 (t, J = 5.1 Hz, 2H, **14**), 4.75 - 4.68 (m, 4H, **7**+**23**), 4.61 - 4.50 (m, 4H, **8**+**22**), 4.36 (s, 3H, **30**), 4.34 - 4.30 (t, J = 5.1 Hz, 2H, **13**), 4.10 (dtd, J = 15.9, 10.9, 6.3 Hz, 16H, ***d***), 3.77 (ddt, J = 41.8, 11.7, 6.1 Hz, 16H, ***e***), 3.68 - 3.44 (m, 16H, ***f***), 1.21 (d, J = 4.5 Hz, 36H, **1**+**29**). ^{13}C NMR (126 MHz, methylene chloride-d_2) δ 158.23 (**12**), 157.75 (**18**), 151.95 (**3** or **26**), 151.90 (**26** or **3**), 147.84 (***c***), 140.31 (**16**), 131.79 (**6**+**24**), 131.53 (**20**), 131.29 (**10**), 130.49 (**15**), 125.74 (**21**), 125.06 (**9**), 123.96 (**5** or **25**), 123.92 (**25** or **5**), 123.71 (**4**+**27**), 121.89 (***a***), 114.93 (**11**), 114.84 (**19**), 112.93 (***b***), 70.98 (***f***), 70.60 (***e***), 68.30 (***d***), 64.96 (**13**), 58.31 (**17**), 53.97 (**14**), 53.25 (**7**+**23**), 52.57 (**8**), 52.48 (**22**), 39.24 (**30**),

35.14 (**2**+**28**), 31.45 (**1**+**29**). ^{19}F NMR (470 MHz, acetonitrile-d_3) δ –72.83 (d, J = 706.6 Hz, 18F). HRMS-ESI (m/z): calcd for [$C_{98}H_{136}N_5O_{18}P_2F_{12}$], 1960.9164; found 1960.9164 [(**Rot**H_2)$(PF_6)_2]^+$.

General procedure for the stepwise deprotonation of compound **Rot**H_2^{3+}

A solution of **Rot**H_2^{3+} (38 mg, 0.018 mmol) in methylene chloride-d_2 (500 µL) was reacted with the phosphazene base **B1** (20 mg) inside an NMR tube. The suspension was mixed for fixed time intervals and the reaction progress monitored by ^{1}H NMR spectroscopy. Upon disappearance of the peaks of **Rot**H_2^{3+}, the mixture was filtered through a pad of Celite to isolate the solution containing the dicationic compounds **Rot**H_2^+-I and **Rot**H_2^+-II. An analogous protocol, comprising the addition of the base **B1** to the solution containing the intermediates **Rot**H_2^+-I and **Rot**H_2^+-II, agitation and filtration provided the monocation **Rot**$^+$.

Monocationic [3]rotaxane **Rot**$^+$

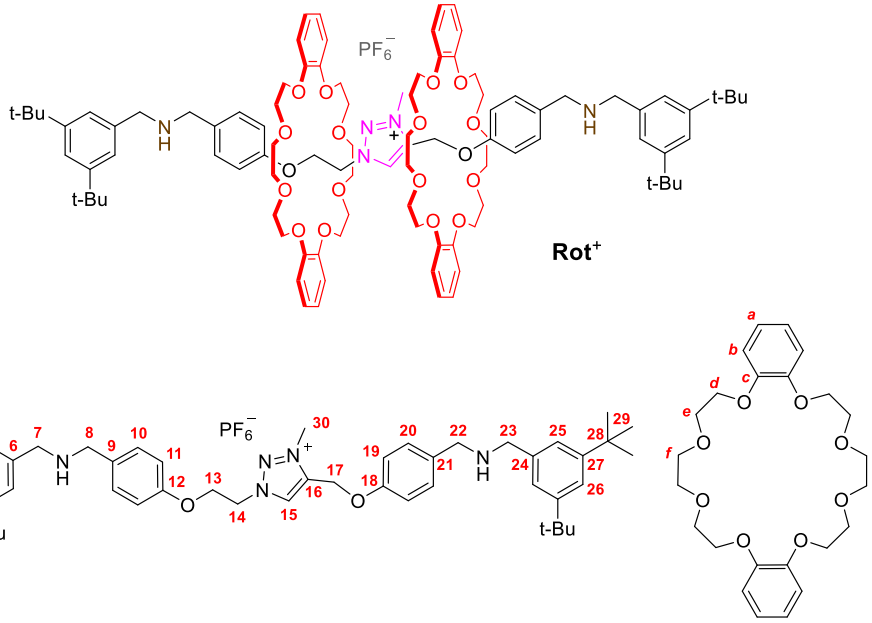

Yield: 33 mg, quantitative. ^{1}H NMR (500 MHz, methylene chloride-d_2) δ 8.63 (s, 1H, **15**), 7.51 (d, J = 8.5 Hz, 2H, **19**), 7.32 (m, 2H, **4**+**26**), 7.24 (d, J = 8.3 Hz, 2H, **20**), 7.16 (m, 6H, **5**+**25**+**10**), 6.88 (m, 10H, ***a***+**11**), 6.72 (m, 8H, ***b***), 5.65 (s, 2H, **17**), 5.42 (t, J = 8.1 Hz, 2H, **14**), 4.77 (t, J = 8.1 Hz, 2H, **13**), 3.98 - 3.84 (m, 16H, ***d***), 3.79 - 3.67 (m, 16H, **8**+**22**+**7**+**23**+***e***), 3.57 - 3.44 (m, 15H, **30**+***e***+***f***), 3.36 (ddt, J = 14.2, 5.8, 3.5 Hz, 8H, ***e***+***f***), 3.04 (tt, J = 6.5, 3.3 Hz, 4H, ***f***), 1.31 (d, J = 2.3 Hz, 36H, **1**+**29**). ^{13}C NMR (126 MHz, methylene chloride-d_2) δ 158.23 (**12**), 158.06 (**18**), 151.17 (**3** or **26**), 151.15 (**26** or **3**), 148.68 (***c***), 148.58 (***c***), 140.22 (**6** or **24**), 140.18 (**24** or **6**), 139.05 (**16**), 133.15 (**9**), 133.08 (**21**),

132.55 (**15**), 129.56 (**10**), 128.63 (**20**), 122.80 (**5** or **25**), 122.68 (**25** or **5**), 121.49 (**a** or **b**), 121.47 (**a** or **b**), 121.23 (**4** or **27**), 121.19 (**27** or **4**), 116.71 (**19**), 114.73 (**11**), 112.86 (**b** or **a**), 112.49 (**b** or **a**), 71.51 (***f***), 71.25 (***f***), 70.66 (***e***), 70.37 (***e***), 69.00 (***d***), 68.89 (***d***), 65.02 (**13**), 56.82 (**17**), 54.15 (**7**+**23**), 53.26 (**22**), 53.20 (**8**), 52.12 (**14**), 37.35 (**30**), 35.08 (**2**+**28**), 31.65 (**1**+**29**). ^{19}F NMR (470 MHz, acetonitrile-d_3) δ –2.91 (d, J = 706.6 Hz, 6F). HRMS-ESI (m/z): calcd for [$C_{98}H_{135}N_5O_{18}$], 1669.9802; found 1669.9802 [**Rot**]$^+$.

Protected neutral axle, 11

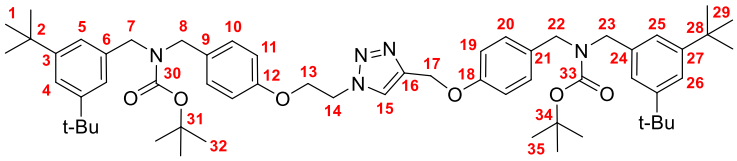

Compound **5** (110 mg, 0.30 mmol), compound **8** (113 mg, 0.30 mmol) and [Cu(MeCN)$_4$][PF$_6$] (224 mg, 0.60 mmol) were dissolved in dry dichloromethane (20 mL) and stirred at room temperature for 48 h. The mixture was then diluted with dichloromethane (50 mL) and washed with sodium ethylenediaminotetraacetate (0.1 M in H_2O, 3×25 mL), water (3×25 mL) and dried over $MgSO_4$. Filtration and removal of the solvent under reduced pressure provided a pale-yellow solid which was purified by Flash Chromatography (chloroform, R_f = 0.2) to obtain the product **11** as a colourless solid (241 mg, 84%). ^{1}H NMR (500 MHz, methylene mhloride-d_2) δ 7.90 (s, 1H, **15**), 7.38 - 7.33 (m, 2H, **4**+**26**), 7.21 (bs, 4H, **5**+**25**), 7.08 (m, 4H, **10**+**20**), 7.00 (d, J = 8.5 Hz, 2H, **19**), 6.89 (d, J = 8.5 Hz, 2H, **11**), 5.21 (s, 2H, **17**), 4.79 (d, J = 5.0 Hz, 2H, **14**), 4.45 - 4.30 (m, 10H, **13**+**7**+**8**+**22**+**23**), 1.53 (d, J = 3.9 Hz, 18H, **32**+**35**), 1.35 (d, J = 6.1 Hz, 36H, **1**+**29**). ^{13}C NMR (126 MHz, methylene chloride-d_2) δ 158.03, 157.56, 156.19, 156.18, 151.32, 144.41, 137.91, 132.07, 131.54, 129.77, 129.67, 129.47, 124.41, 122.29, 122.26, 121.46, 115.11, 114.92, 80.01, 66.92, 62.38, 54.24, 50.52, 50.25, 50.05, 49.62, 49.06, 35.11, 35.10, 31.69, 31.68, 28.68.

Tricationic axle, 12

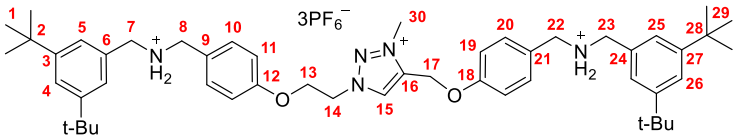

Under a dinitrogen atmosphere, compound **11** (241 mg, 0.25 mmol) was dissolved in iodomethane (15 mL) and the resulting solution was stirred for 48 h at room temperature under exclusion of light. Upon reaction completion, the solvent was removed under reduced pressure providing a yellow solid, which was dissolved in dichloromethane (30 mL) and washed with $KPF_{6(aq)}$ (3×15 mL). The organic fraction was isolated, the solvent removed under reduced pressure and the residue dissolved in trifluoroacetic acid (10 mL) and stirred at room temperature for 16 h. The acid was removed under

reduced pressure and the crude product suspended in ethyl acetate (30 mL) and washed with $Na_2CO_{3(aq)}$ (3×30 mL). Removal of the solvent from the organic fraction provided a solid that was dissolved in the minimum volume of methanol (1 mL) and reacted with 37% HCl (few drops). Addition of a saturated methanol solution of $(H_4N)PF_6$ (3 mL), followed by precipitation through dropwise addition of water provided a colourless solid which was filtered and purified by sonication in diethyl ether to obtain the product **12** as a colourless solid (124 mg, 41%). ^{1}H NMR (500 MHz, acetonitrile-d_3) δ 8.57 (s, 1H, **15**), 7.53 (m, 2H, **4**+**26**), 7.50 - 7.45 (d, *J* = 8.3 Hz, 2H, **20**), 7.44 - 7.39 (d, *J* = 8.3 Hz, 2H, **10**), 7.30 (m, 4H, **5**+**25**), 7.15 - 7.09 (d, *J* = 8.3 Hz, 2H, **19**), 7.08 - 6.81 (m, 6H, **NH₂**+**11**), 5.33 (s, 2H, **17**), 4.98 (t, *J* = 4.9 Hz, 2H, **14**), 4.47 (t, *J* = 4.9 Hz, 2H, **13**), 4.27 (d, *J* = 1.0 Hz, 3H, **30**), 4.22 - 4.13 (m, 8H, **7**+**8**+**22**+**23**), 1.32 (s, 36H, **1**+**29**). ^{13}C NMR (126 MHz, acetonitrile-d_3) δ 159.66, 159.18, 152.85, 152.84, 140.49, 133.20, 133.09, 131.39, 130.75, 125.35, 125.21, 124.69, 124.67, 124.50, 116.17, 115.98, 66.08, 59.09, 54.46, 52.81, 52.75, 51.83, 51.78, 39.62, 35.65, 31.55. ^{19}F NMR (470 MHz, acetonitrile-d_3) δ –72.89 (dd, J = 705.9, 4.9 Hz, 18F). HRMS-ESI (*m*/*z*): calcd for $[C_{50}H_{73}N_5O_2P_2F_{12}]$, 1065.5048; found 1064.4969 $[(\mathbf{12}–H)(PF_6)_2]^+$.

Monocationic axle, 13

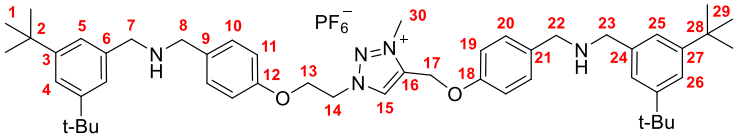

A solution of **12** (124 mg, 0.10 mmol) in dichloromethane (30 mL) was washed with $Na_2CO_{3(aq)}$ (3×30 mL) and dried over $MgSO_4$. Filtration and removal of the solvent under reduced pressure provided the product **13** as a crystalline colourless solid (90 mg, 96%). ^{1}H NMR (500 MHz, acetonitrile-d_3) δ 8.55 (s, 1H, **15**), 7.45 - 7.41 (m, 2H, **4**+**26**), 7.36 (m, 4H, **20**+**10**), 7.24 (s, 4H, **5**+**25**), 7.04 (d, *J* = 8.7 Hz, 2H, **19**), 6.92 (d, *J* = 8.6 Hz, 2H, **11**), 5.32 (s, 2H, **17**), 4.98 - 4.92 (t, *J* = 4.9 Hz, 2H, **14**), 4.46 - 4.41 (t, *J* = 4.9 Hz, 2H, **13**), 4.26 (s, 3H, **30**), 3.94 - 3.88 (m, 8H, **7**+**8**+**22**+**23**), 1.31 (s, 36H, **1**+**29**). ^{13}C NMR (126 MHz, acetonitrile-d_3) δ 158.66, 157.96, 152.30, 152.22, 140.71, 131.86, 131.75, 131.35, 124.38, 124.22, 123.30, 123.08, 115.93, 115.71, 66.10, 59.11, 54.51, 53.48, 53.34, 52.34, 52.32, 39.60, 35.55, 31.66, 31.64. ^{19}F NMR (470 MHz, acetonitrile-d_3) δ –72.89 (d, *J* = 706.5 Hz, 6F). HRMS-ESI (*m*/*z*): calcd for $[C_{50}H_{71}N_5O_2]$, 773.5608; found 772.5530 $[\mathbf{13}–H]^+$.

NMR spectra

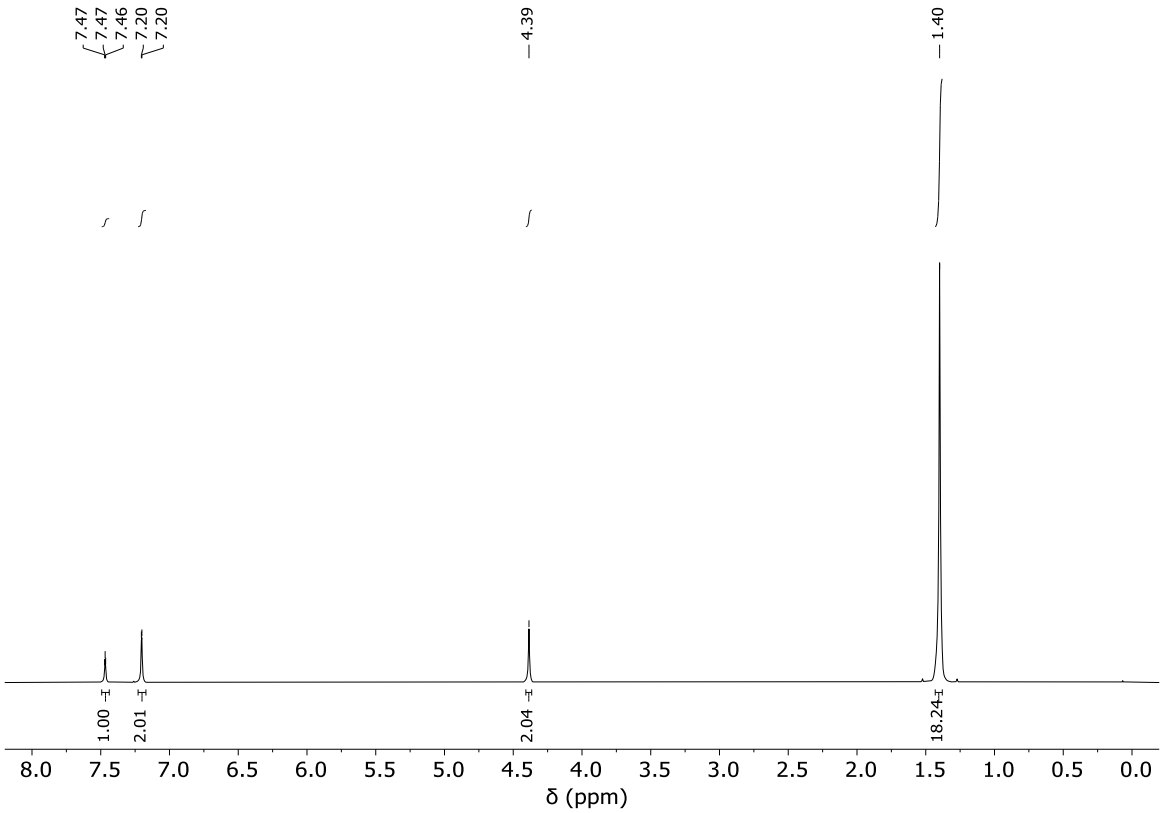

Figure S1. ^{1}H NMR spectrum of **1** (chloroform-*d*, 298 K, 400 MHz).

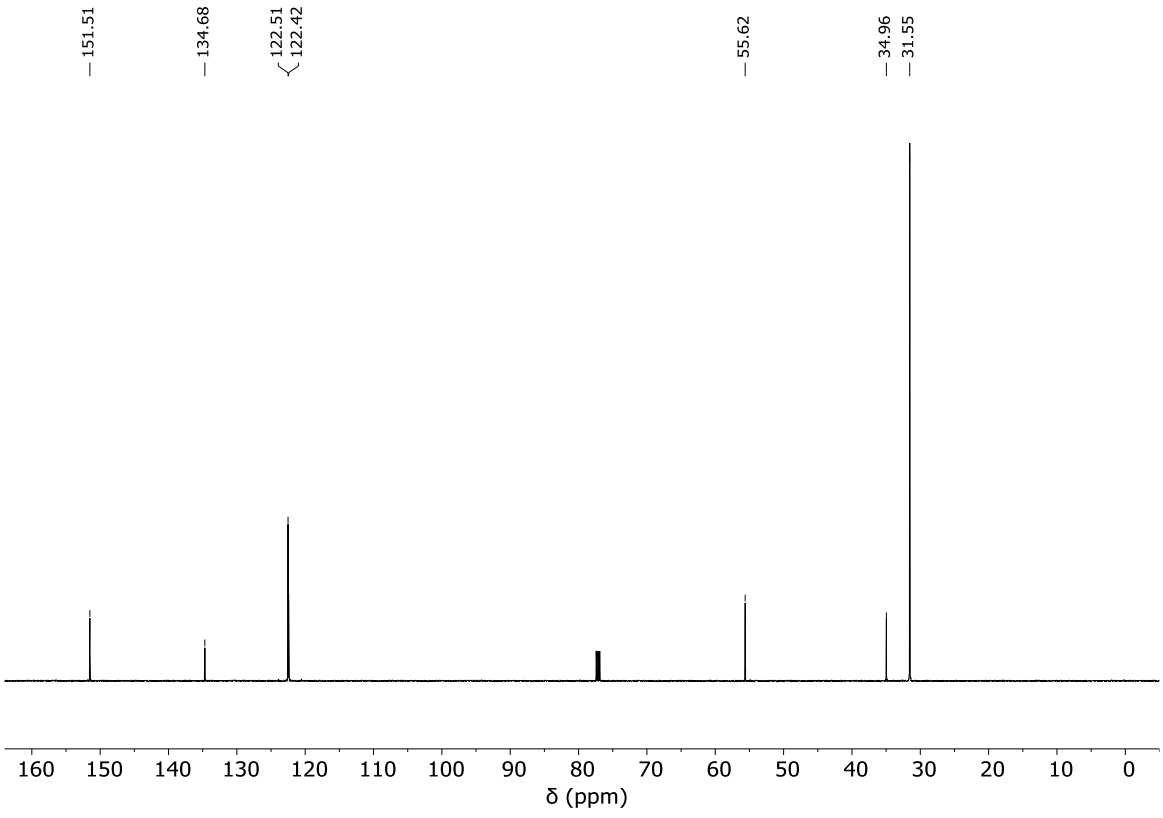

Figure S2. ^{13}C NMR spectrum of **1**(chloroform-*d*, 298 K, 101 MHz).

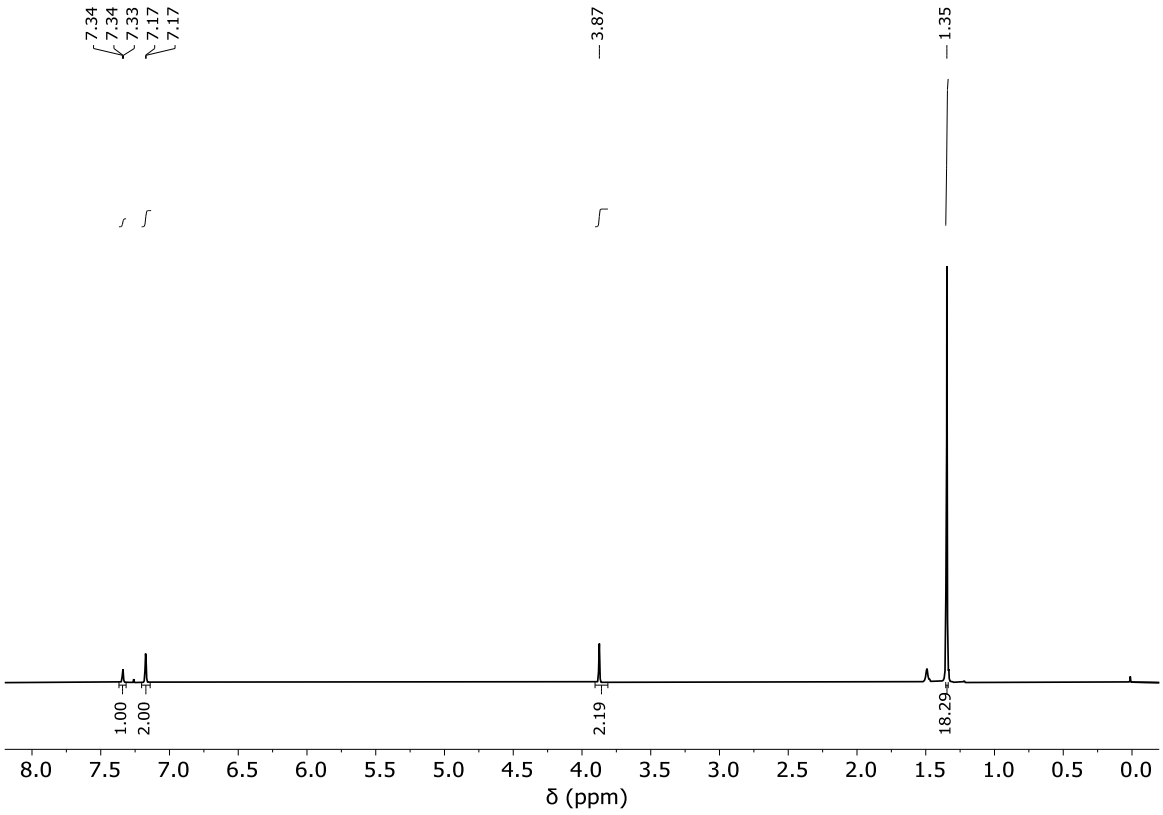

Figure S3. ^{1}H NMR spectrum of **2** (chloroform-*d*, 298 K, 400 MHz).

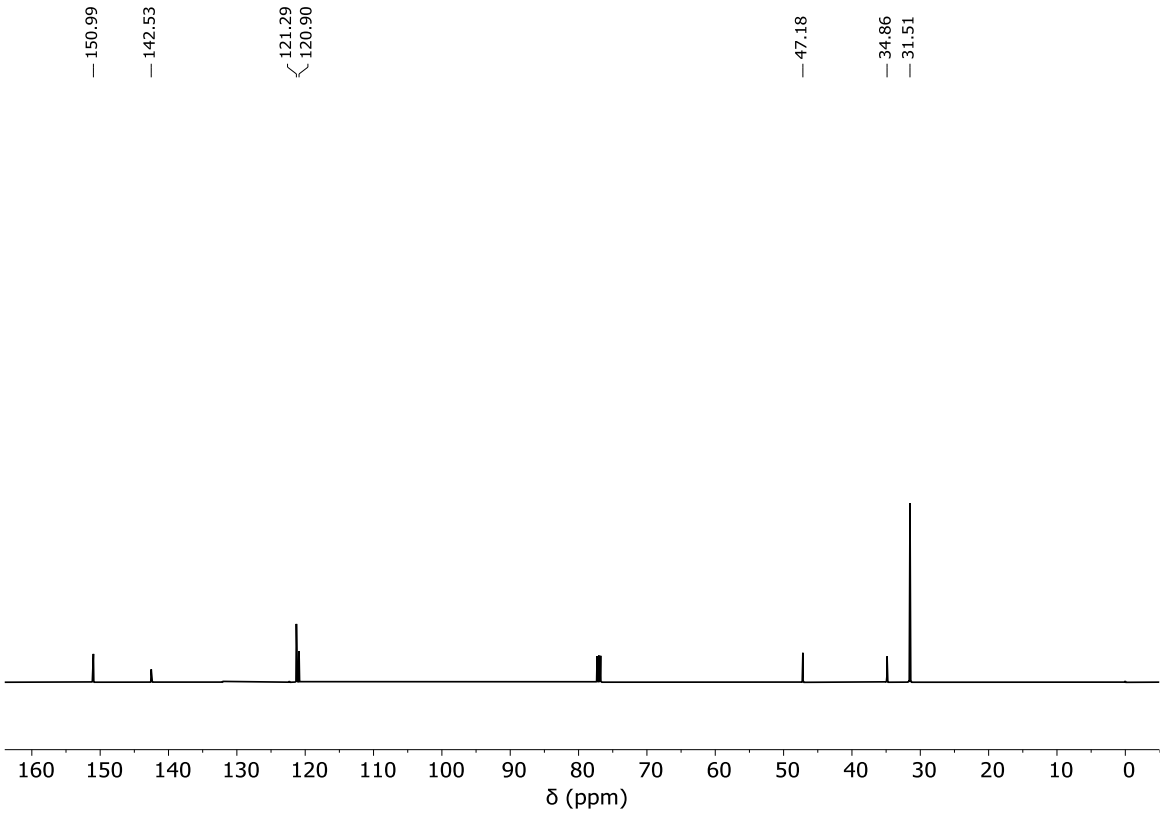

Figure S4. ^{13}C NMR spectrum of **2** (chloroform-*d*, 298 K, 101 MHz).

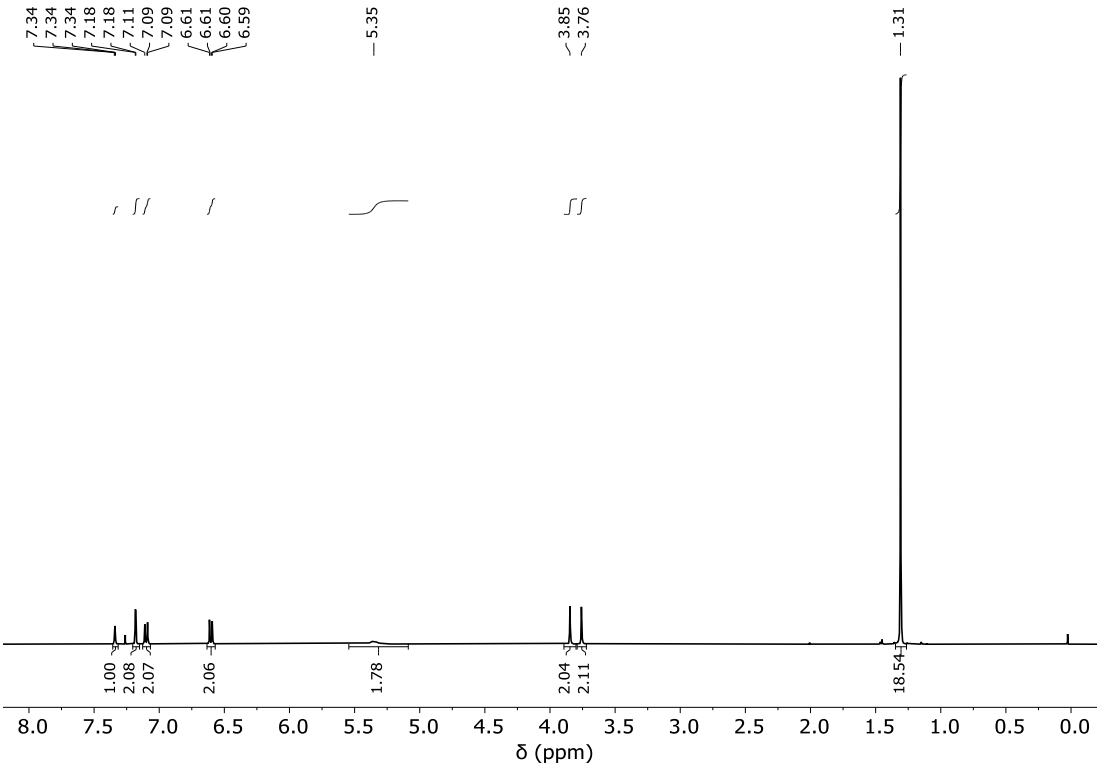

Figure S5. ^{1}H NMR spectrum of **3** (chloroform-*d*, 298 K, 400 MHz).

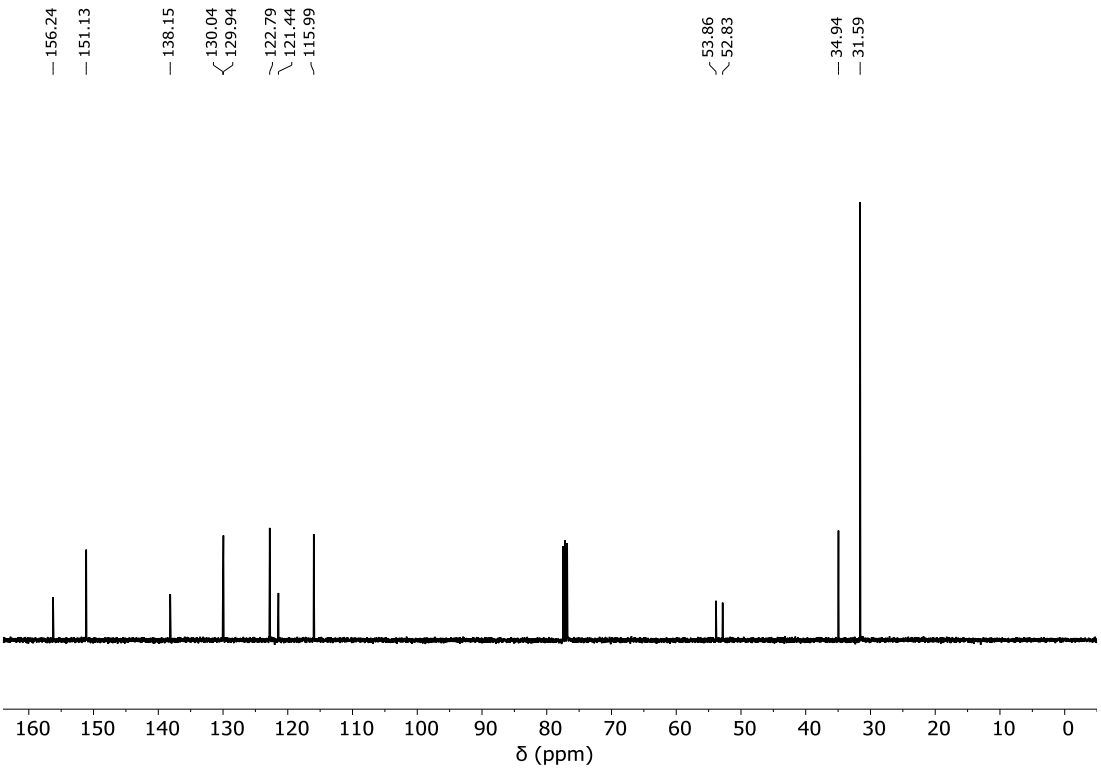

Figure S6. ^{13}C NMR spectrum of **3** (chloroform-*d*, 298 K, 101 MHz).

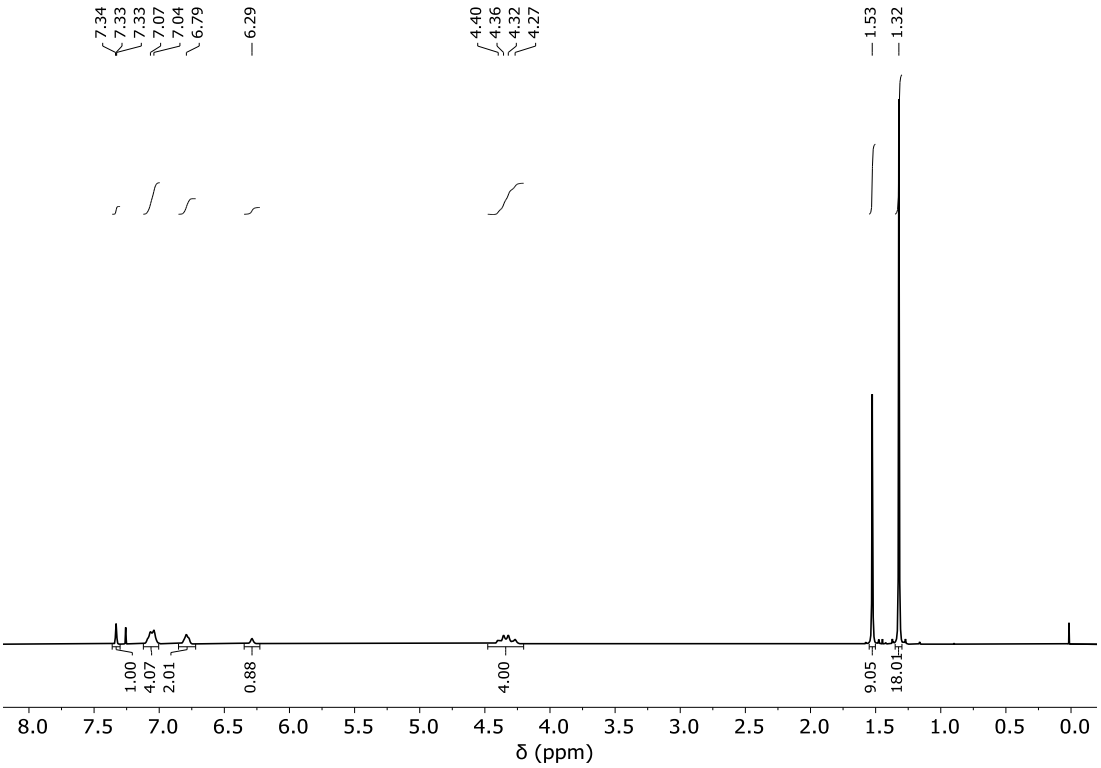

Figure S7. ^{1}H NMR spectrum of **4** (chloroform-*d*, 298 K, 400 MHz).

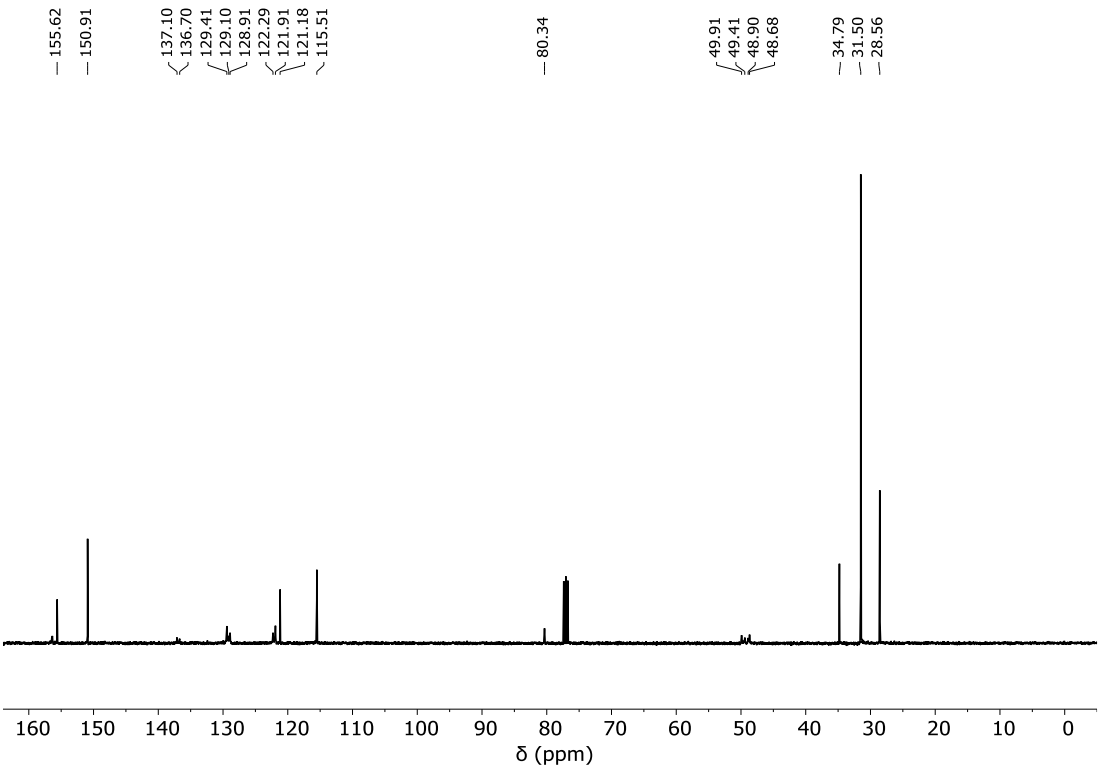

Figure S8. ^{13}C NMR spectrum of **4** (chloroform-*d*, 298 K, 101 MHz).

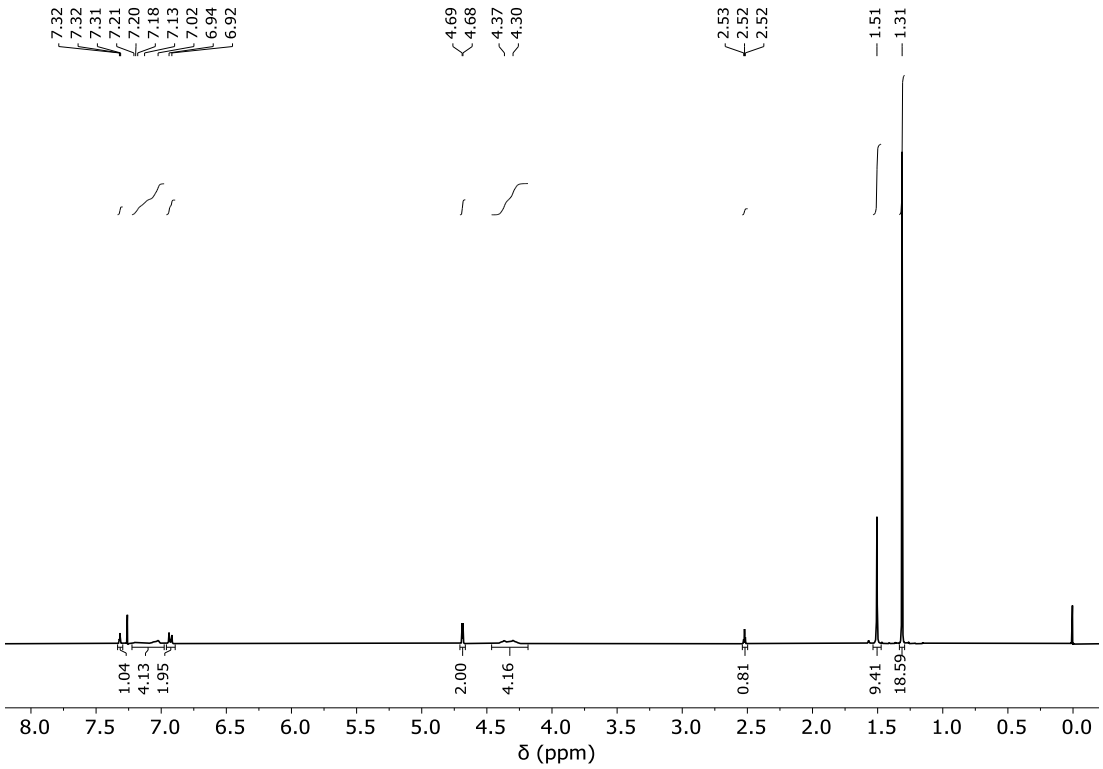

Figure S9. ^{1}H NMR spectrum of **5** (chloroform-*d*, 298 K, 400 MHz).

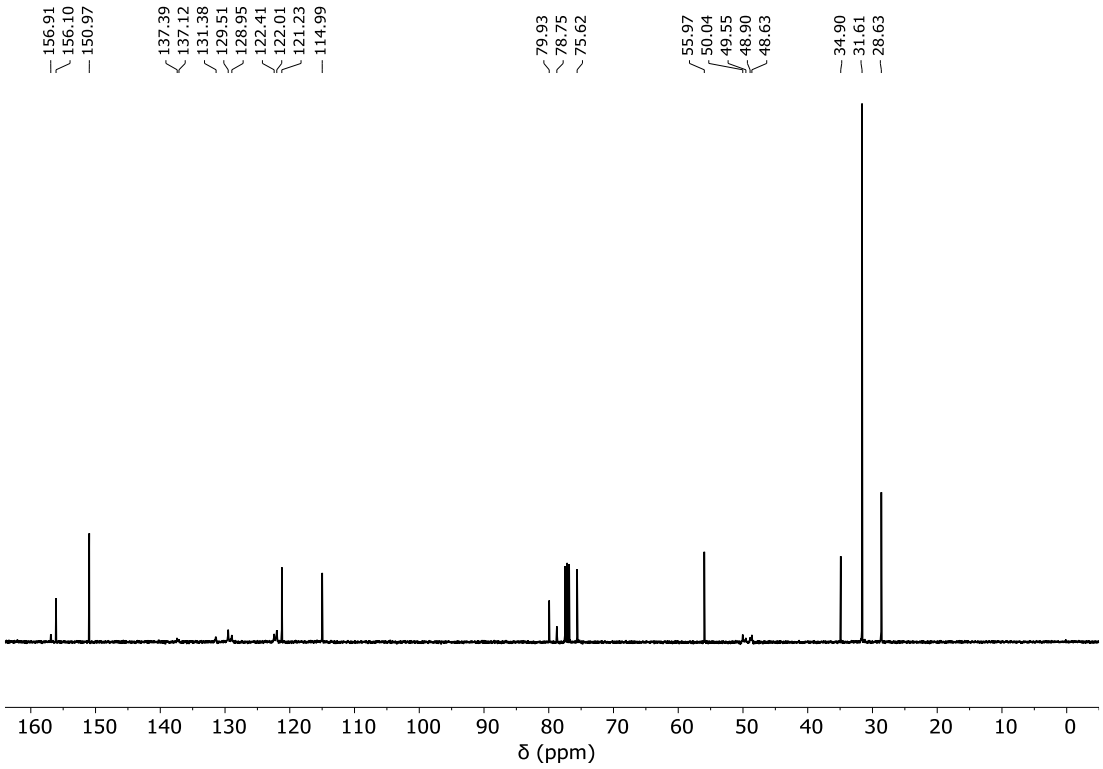

Figure S10. ^{13}C NMR spectrum of **5** (chloroform-*d*, 298 K, 101 MHz).

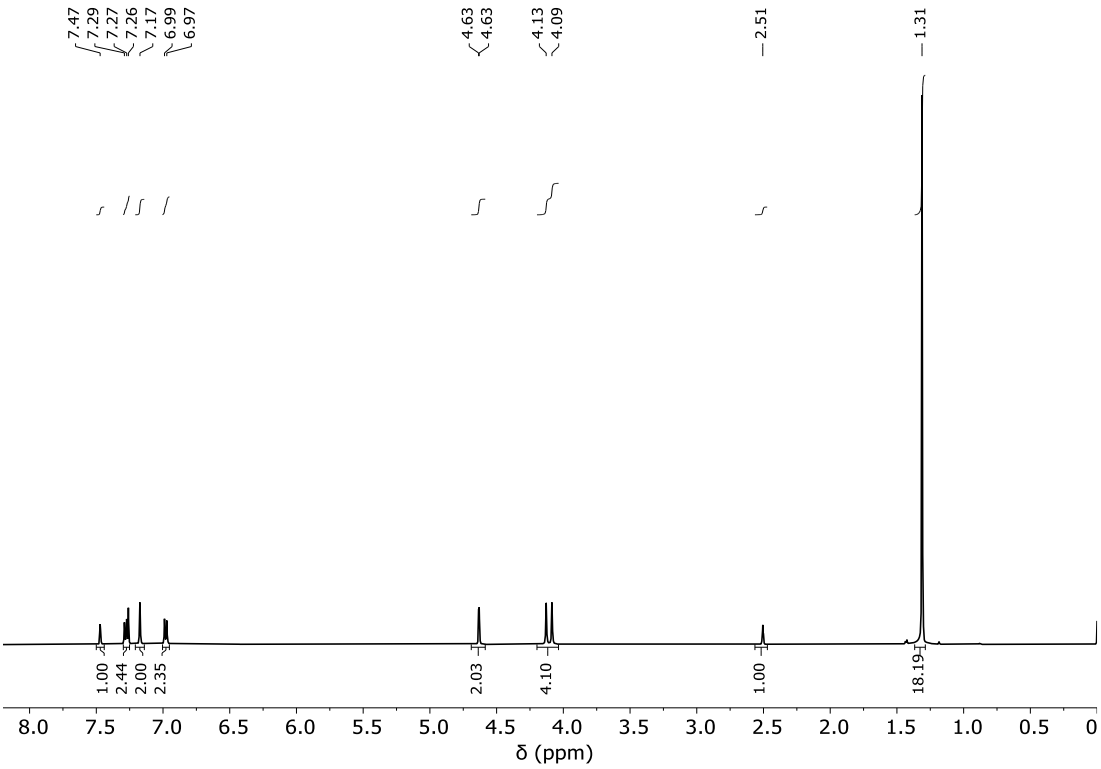

Figure S11. ^{1}H NMR spectrum of **6** (chloroform-*d*, 298 K, 400 MHz).

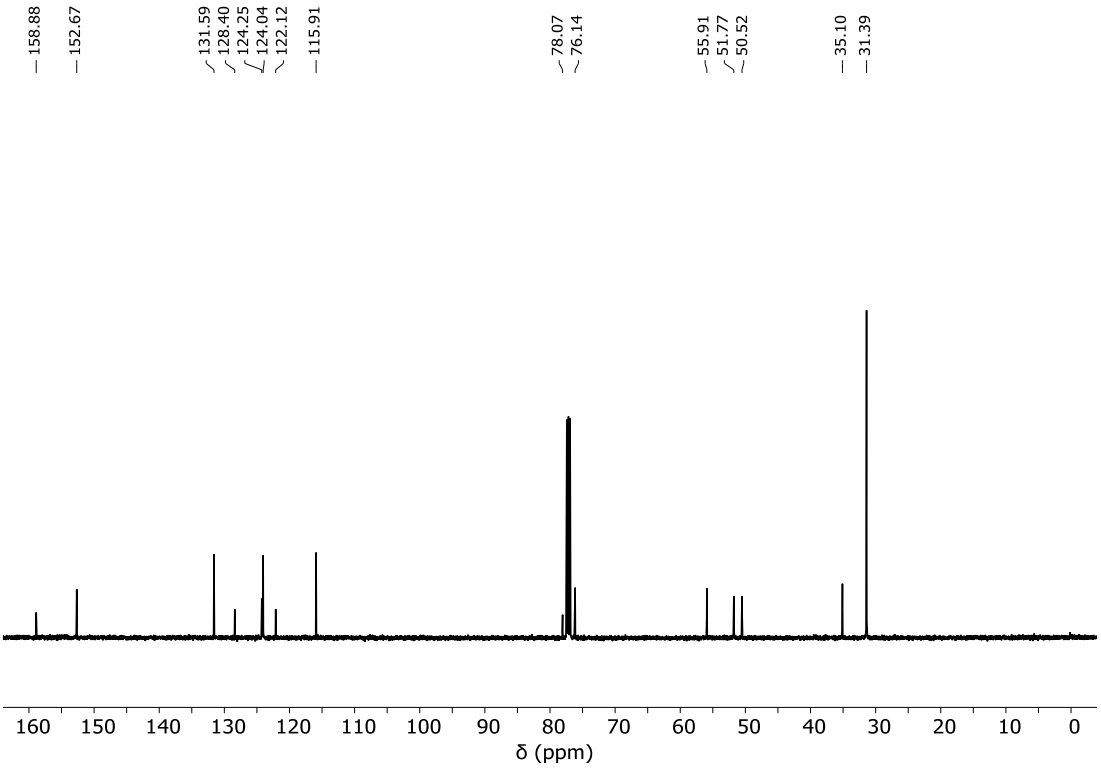

Figure S12. ^{13}C NMR spectrum of **6** (chloroform-*d*, 298 K, 126 MHz).

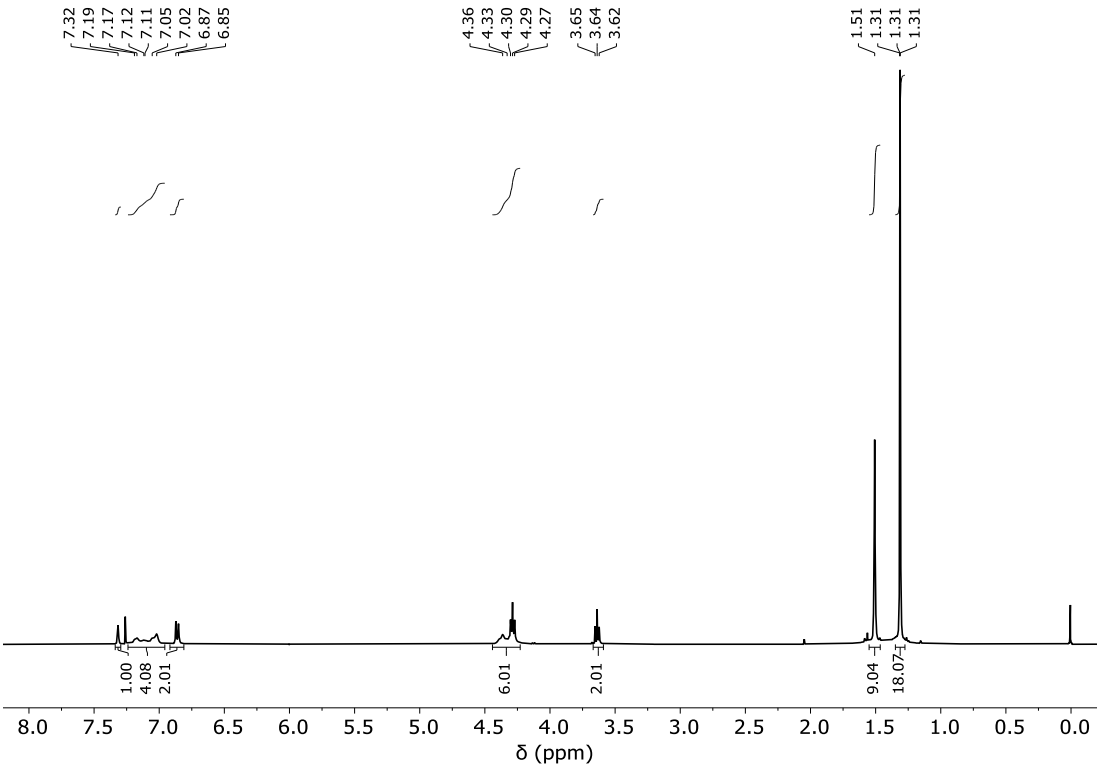

Figure S13. ^{1}H NMR spectrum of **7** (chloroform-*d*, 298 K, 400 MHz).

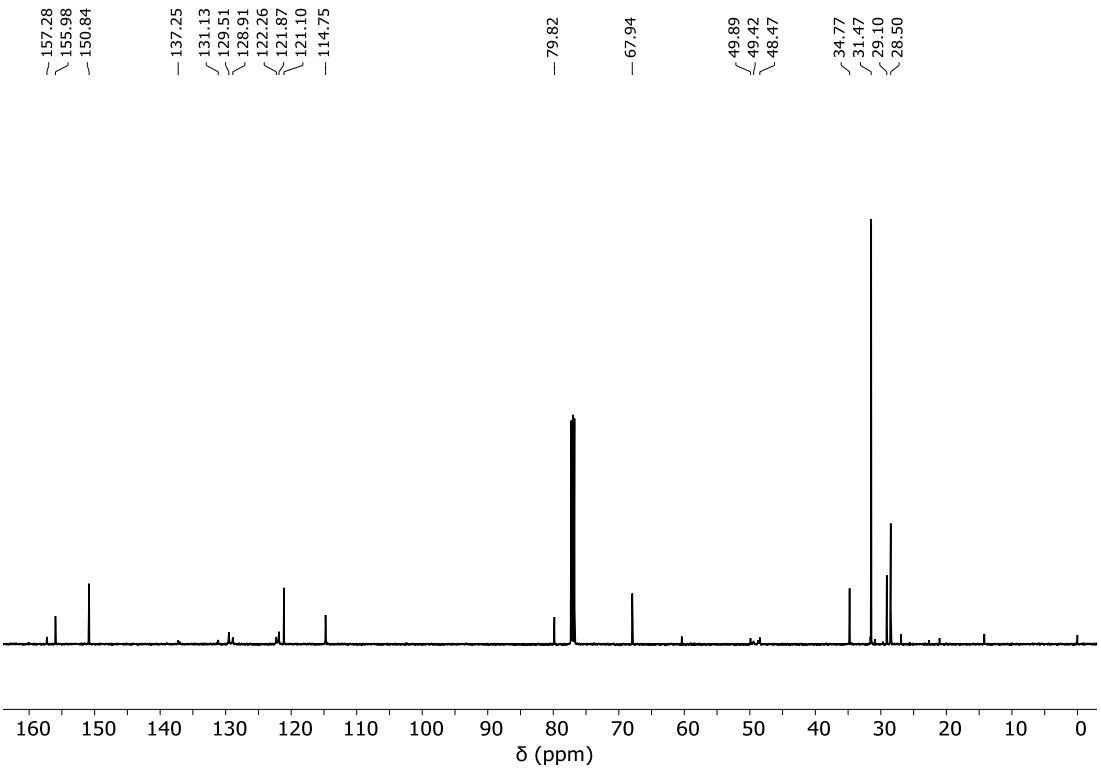

Figure S14. ^{13}C NMR spectrum of **7** (chloroform-*d*, 298 K, 126 MHz).

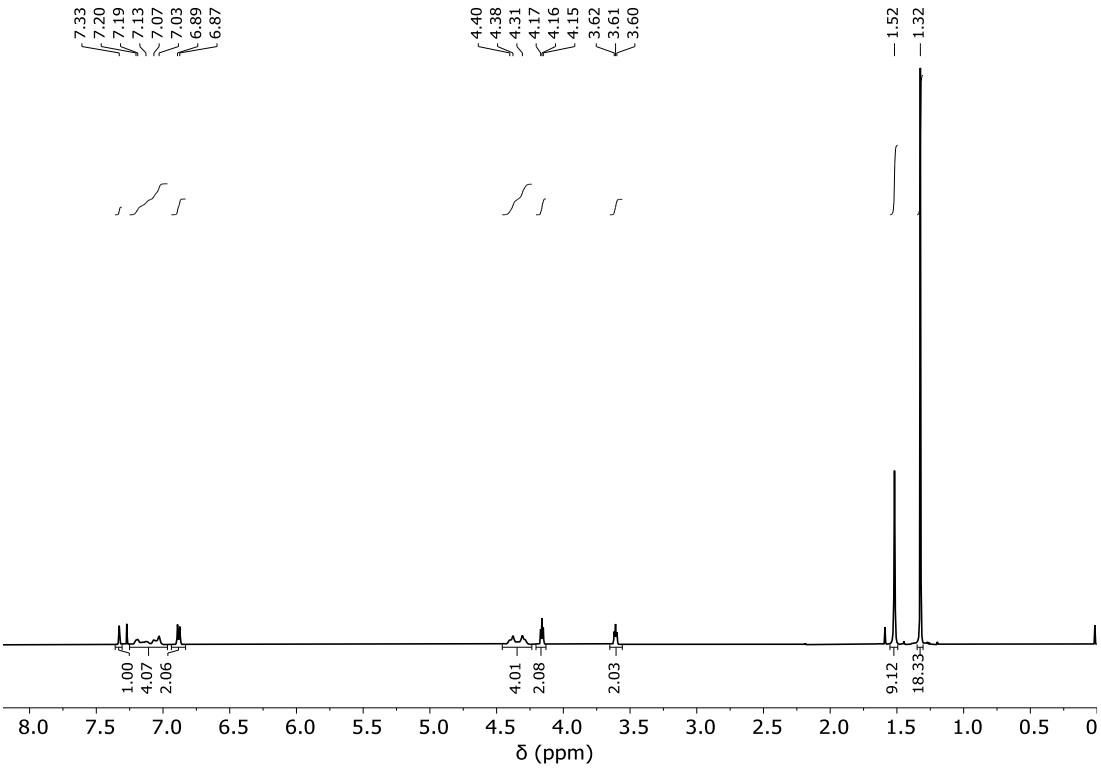

Figure S15. ^{1}H NMR spectrum of **8** (chloroform-*d*, 298 K, 400 MHz).

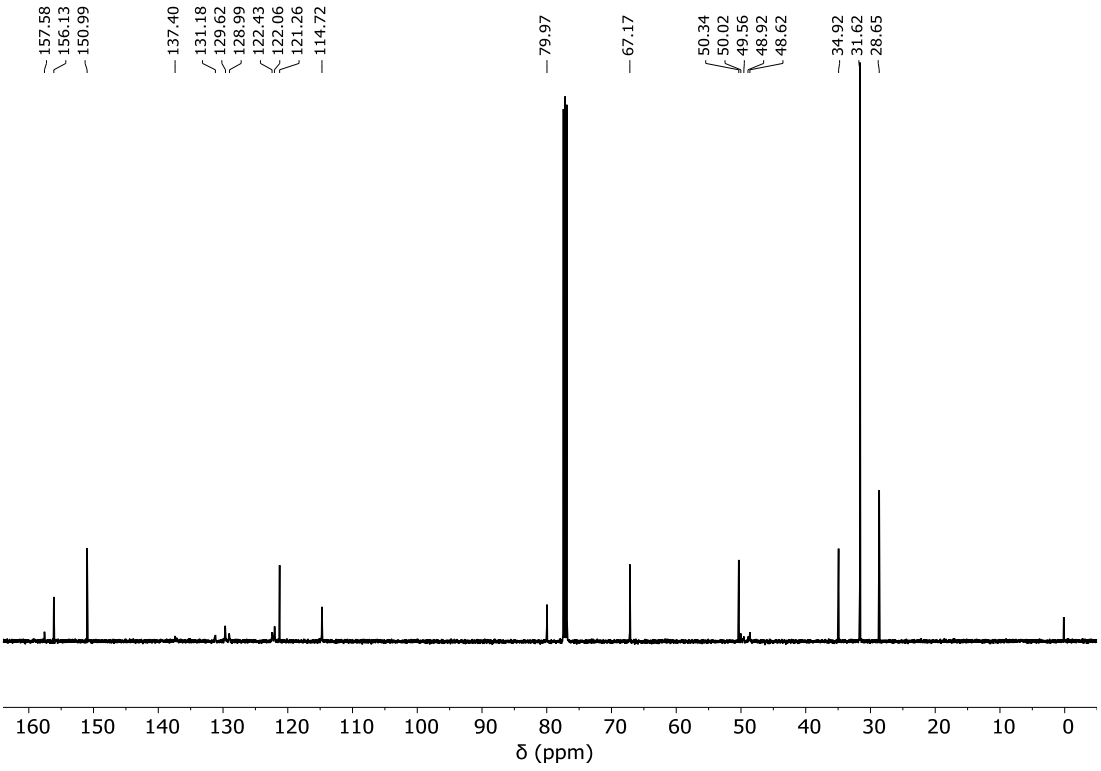

Figure S16. ^{13}C NMR spectrum of **8** (chloroform-*d*, 298 K, 101 MHz).

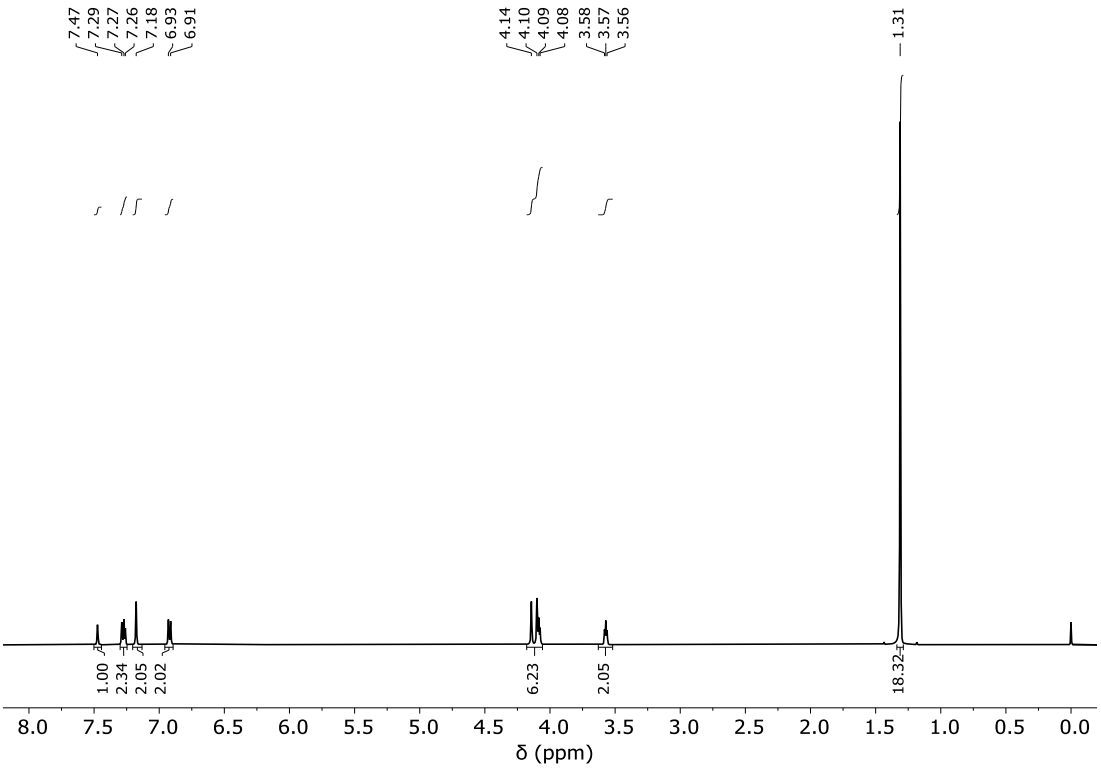

Figure S17. ^{1}H NMR spectrum of **9** (chloroform-*d*, 298 K, 400 MHz).

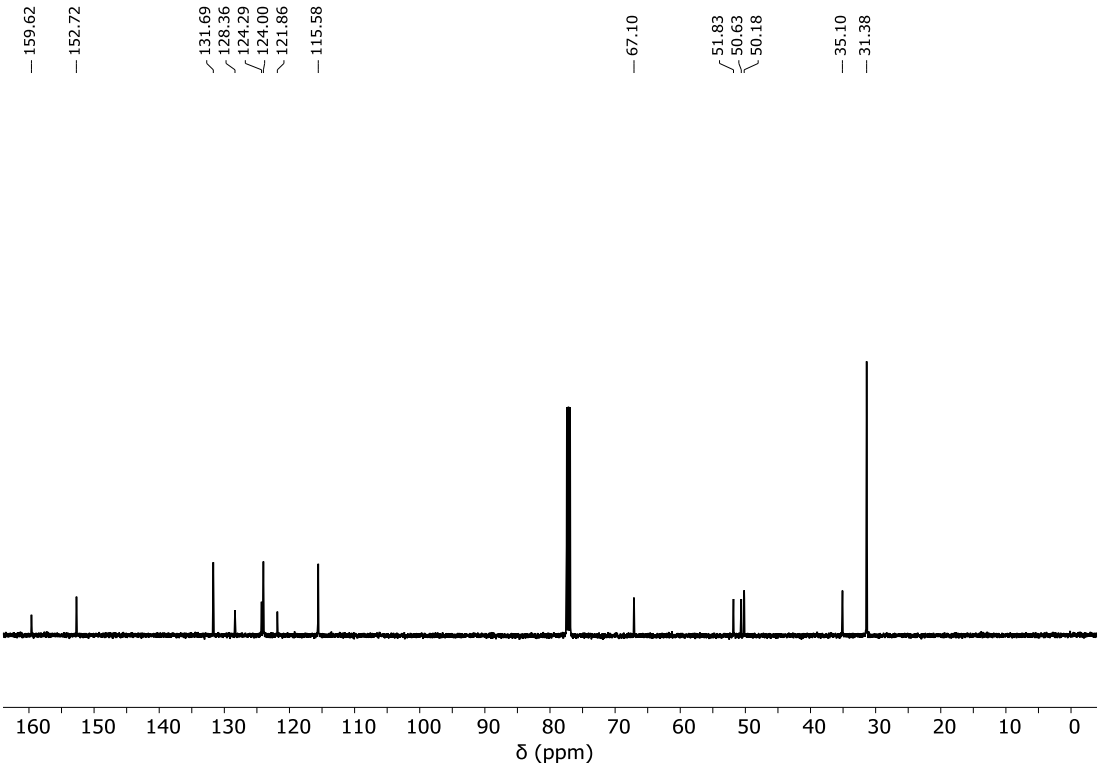

Figure S18. ^{13}C NMR spectrum of **9** (chloroform-*d*, 298 K, 126 MHz).

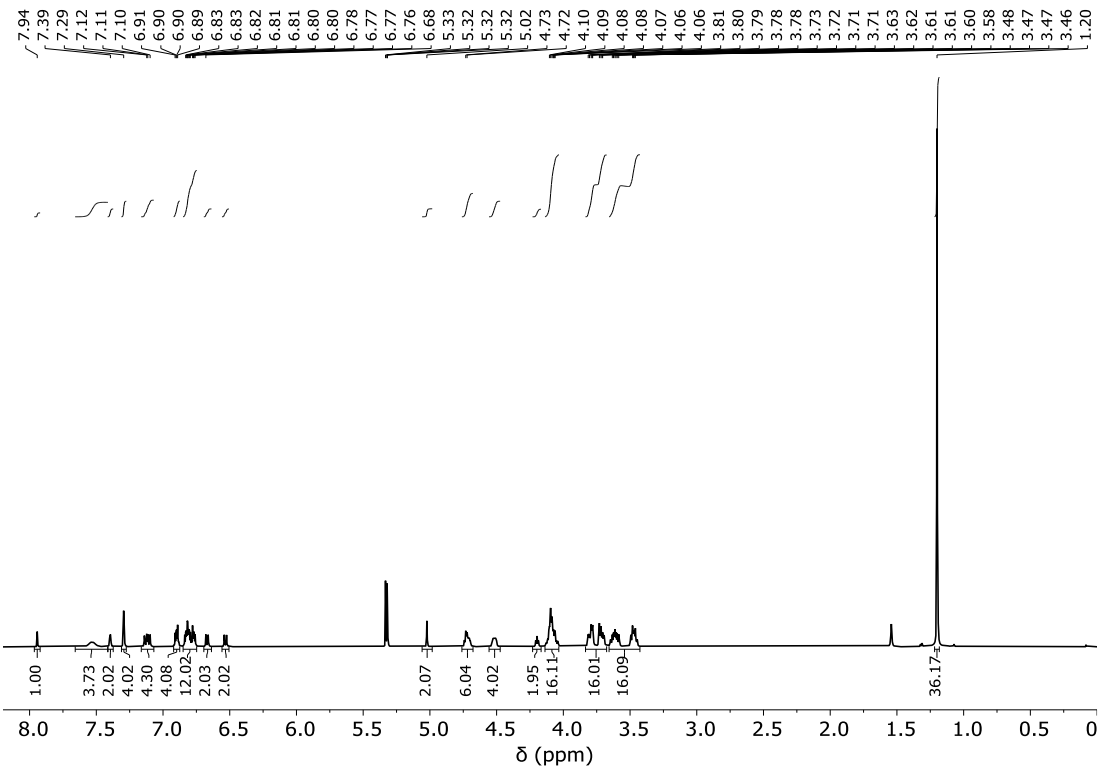

Figure S19. ^{1}H NMR spectrum of **10** (methylene chloride-d_2, 298 K, 500 MHz).

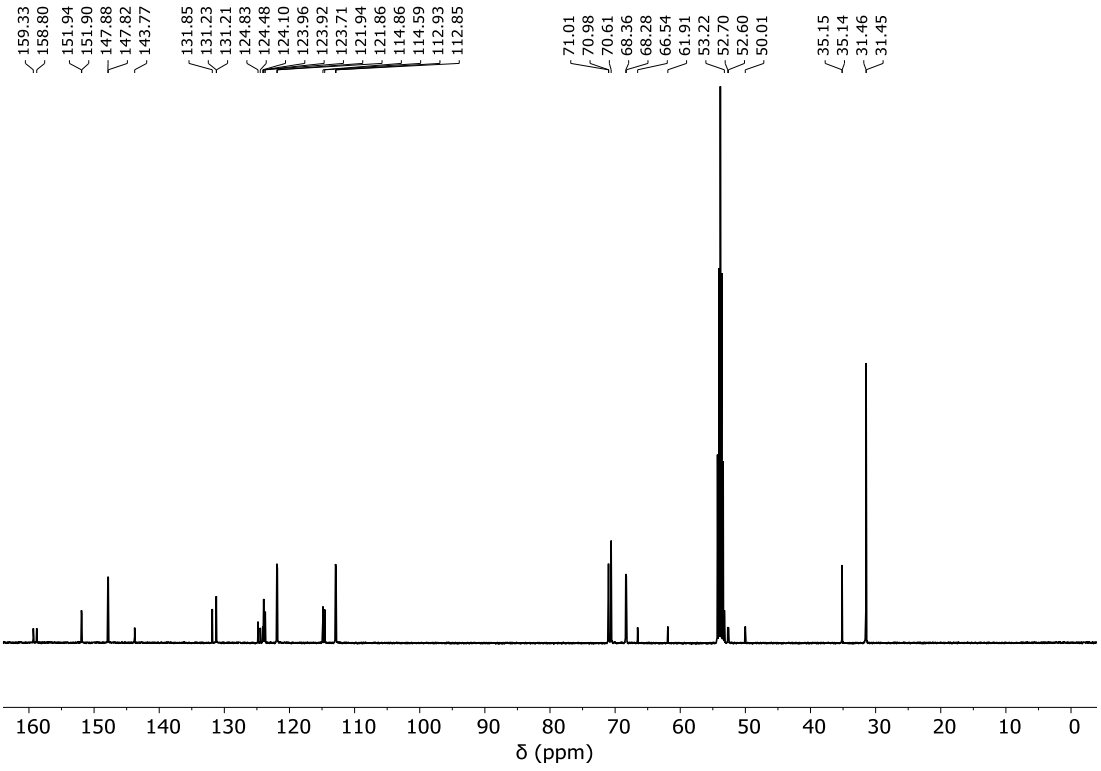

Figure S20. ^{13}C NMR spectrum of **10** (methylene chloride-d_2, 298 K, 126 MHz).

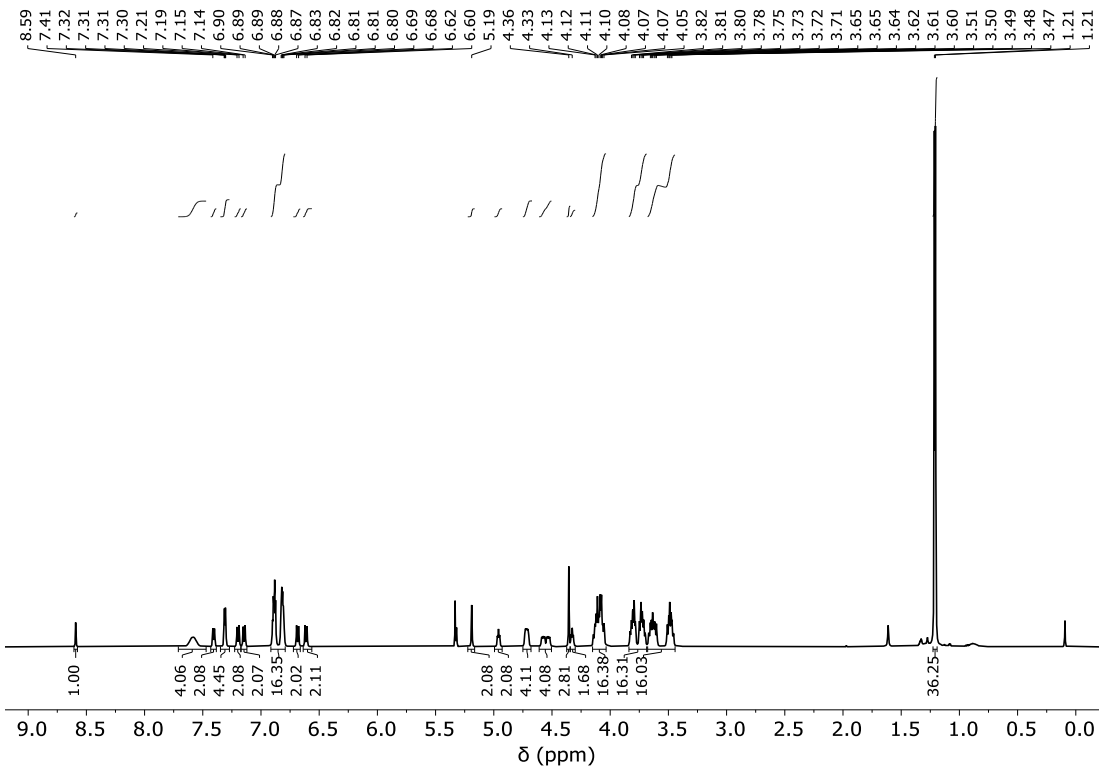

Figure S21. ^{1}H NMR spectrum of **Rot**H_2^{3+} (methylene chloride-d_2, 298 K, 500 MHz).

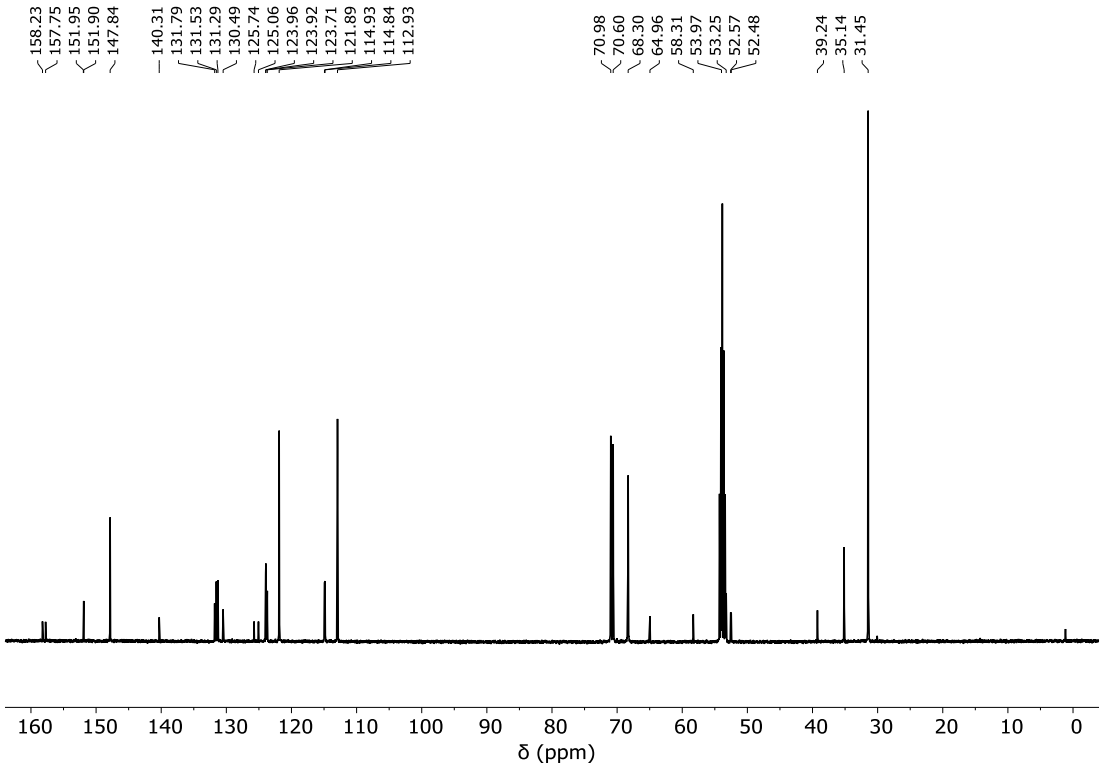

Figure S22. ^{13}C NMR spectrum of **Rot**H_2^{3+} (methylene chloride-d_2, 298 K, 126 MHz).

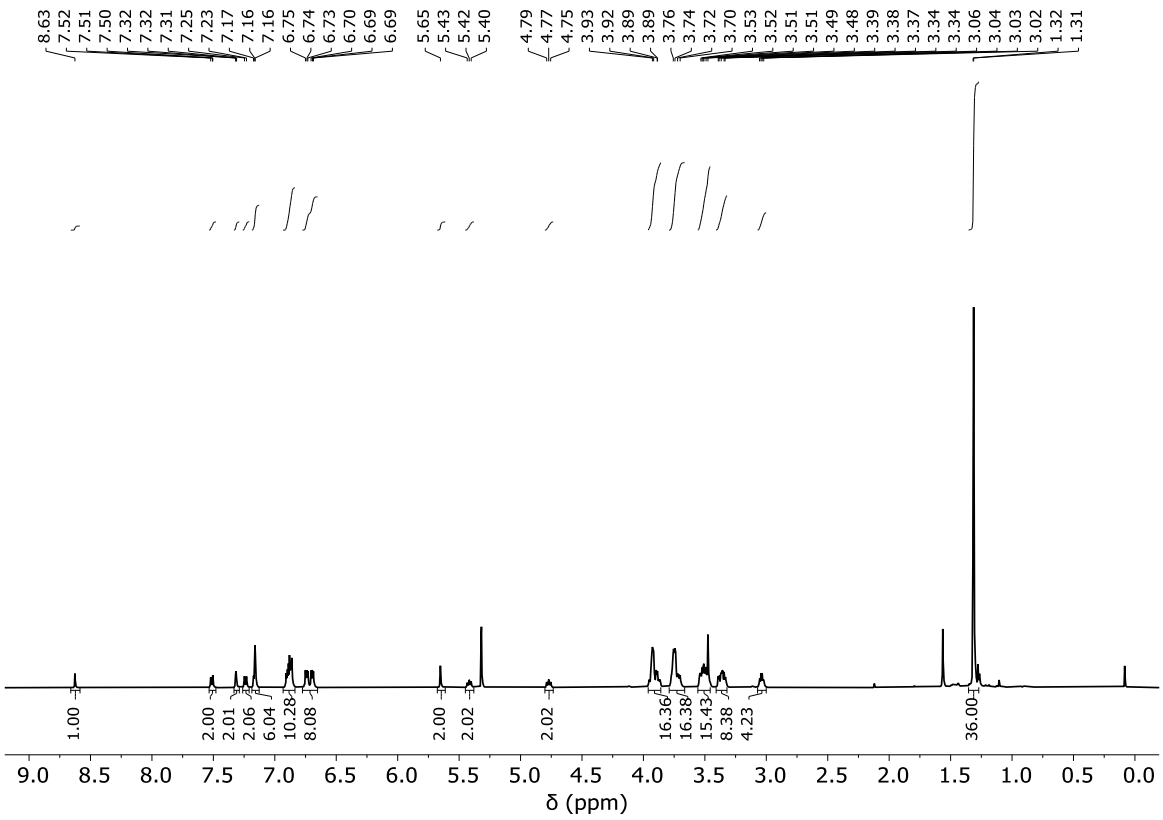

Figure S23. ^{1}H NMR spectrum of **Rot**$^{+}$ (methylene chloride-d_2, 298 K, 500 MHz).

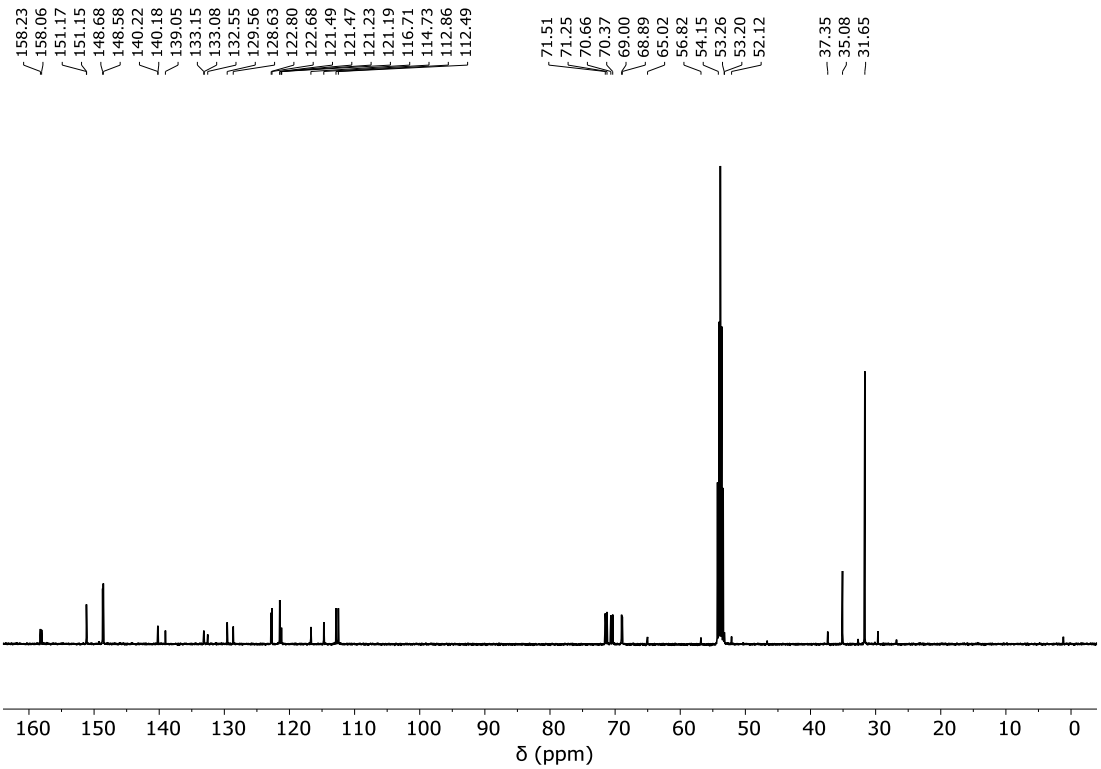

Figure S24. ^{13}C NMR spectrum of **Rot**$^{+}$ (methylene chloride-d_2, 298 K, 126 MHz).

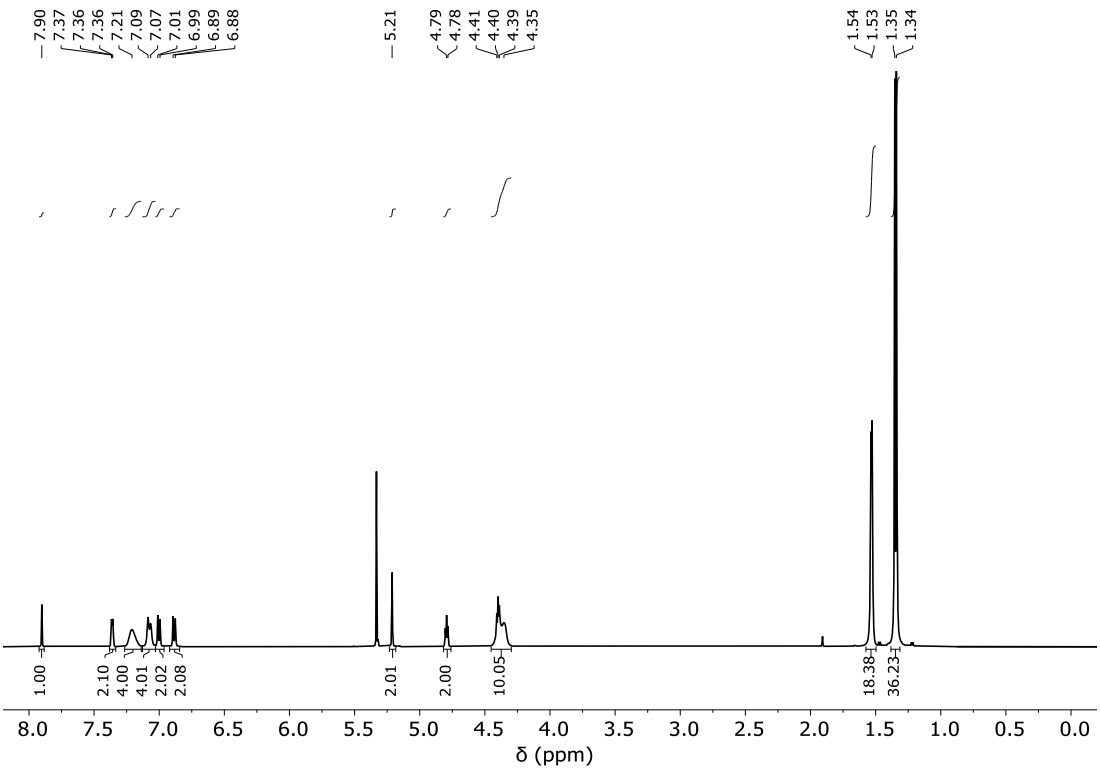

Figure S25. ^{1}H NMR spectrum of **11** (methylene chloride-d_2, 298 K, 500 MHz).

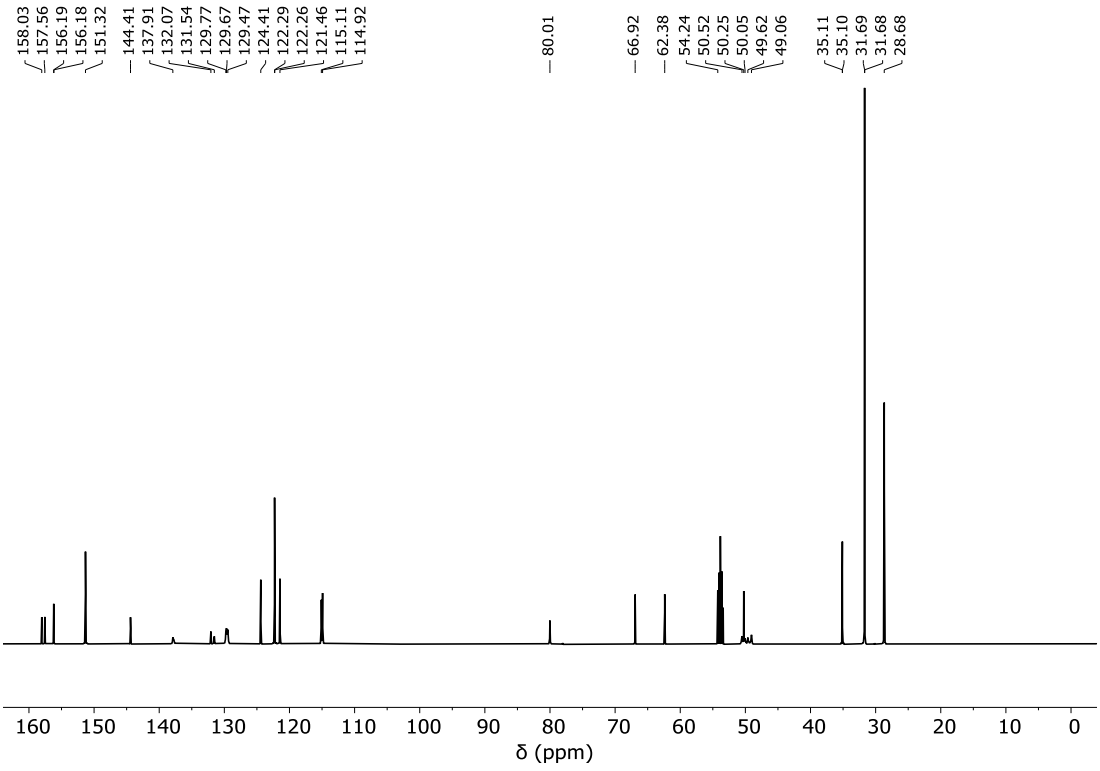

Figure S26. ^{13}C NMR spectrum of **11** (methylene chloride-d_2, 298 K, 126 MHz).

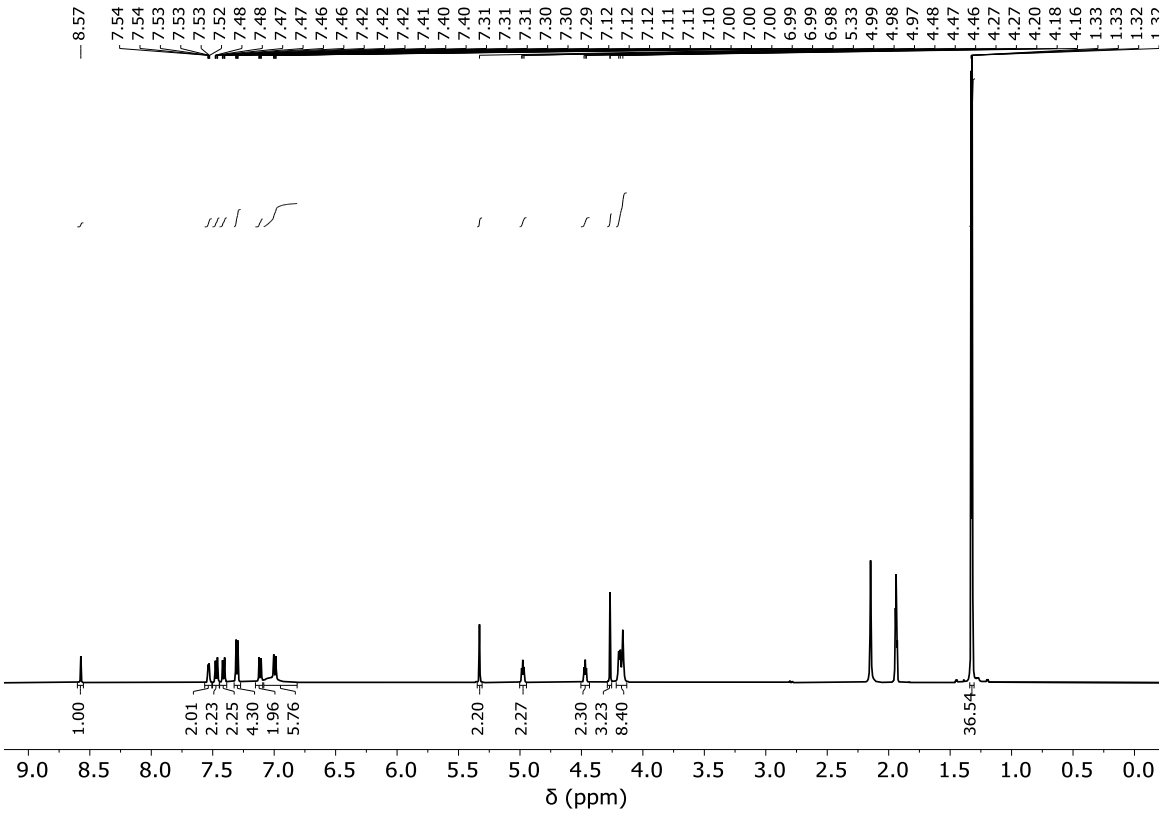

Figure S27. ^{1}H NMR spectrum of **12** (acetonitrile-d_3, 298 K, 400 MHz).

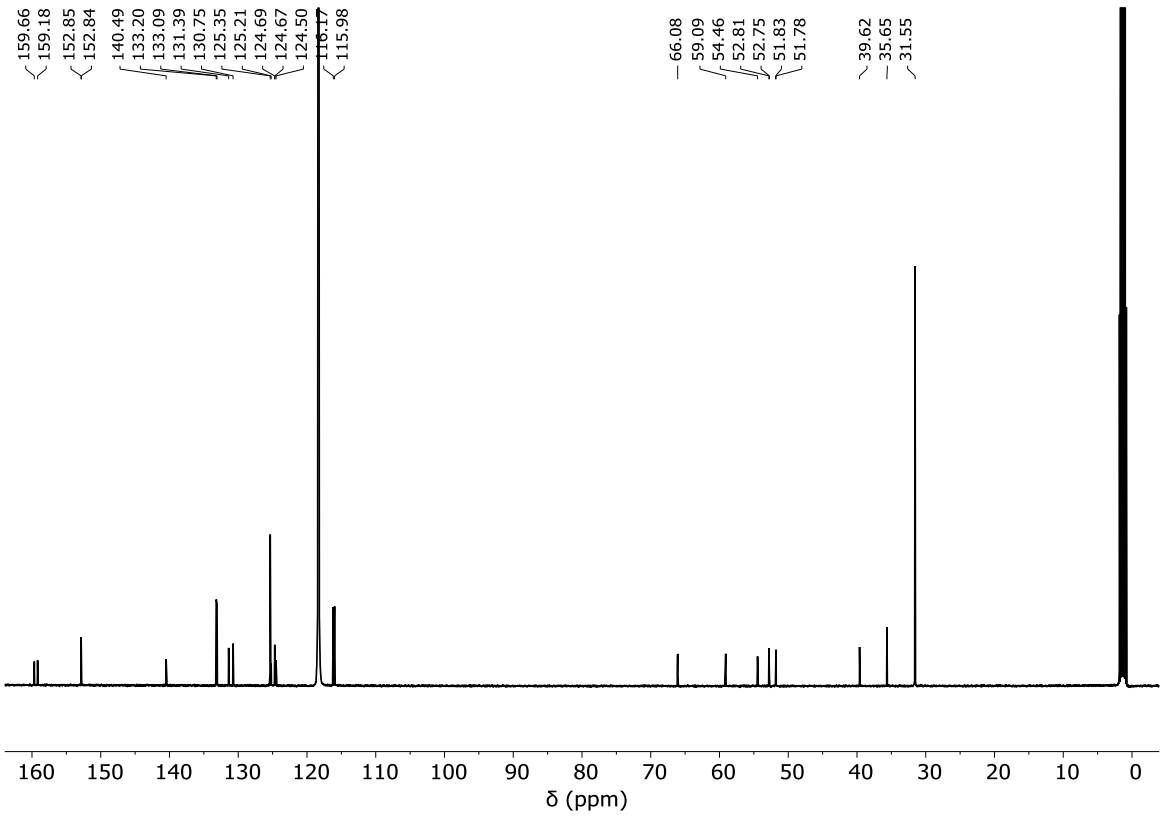

Figure S28. ^{13}C NMR spectrum of **12** (acetonitrile-d_3, 298 K, 126 MHz).

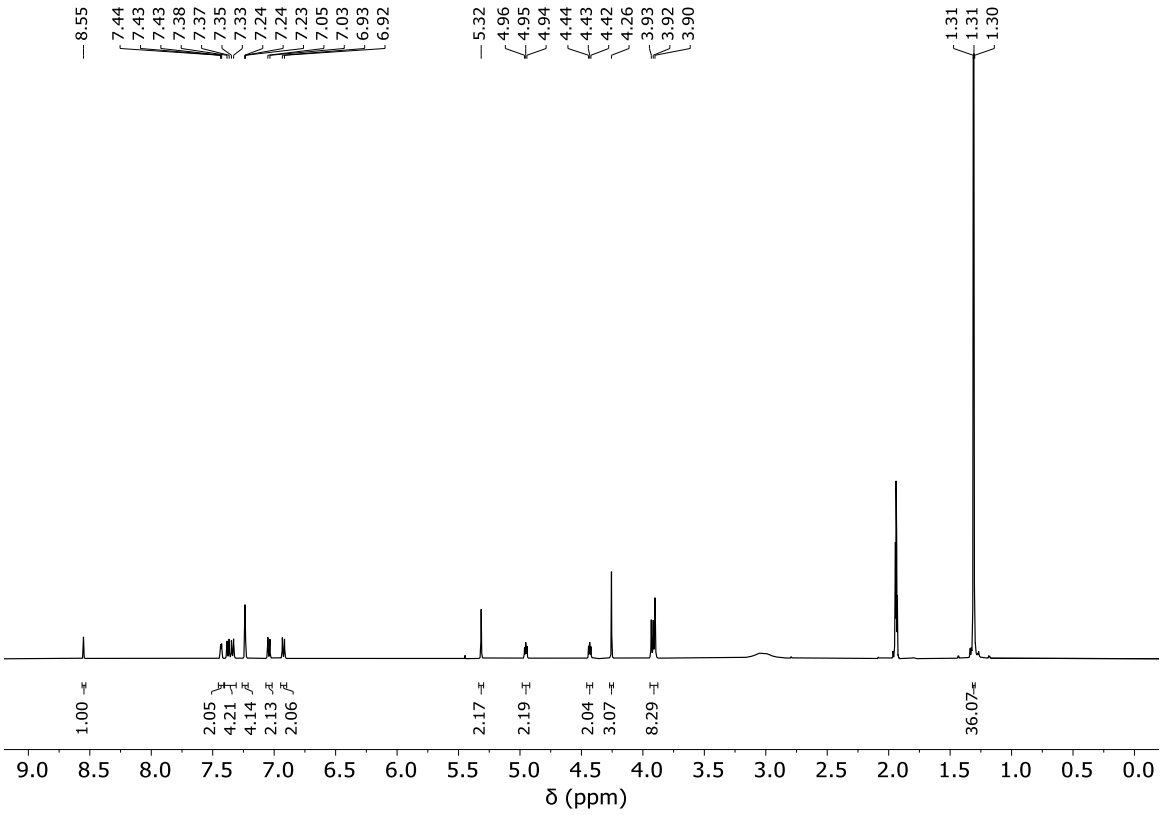

Figure S29. ^{1}H NMR spectrum of **13** (acetonitrile-d_3, 298 K, 400 MHz).

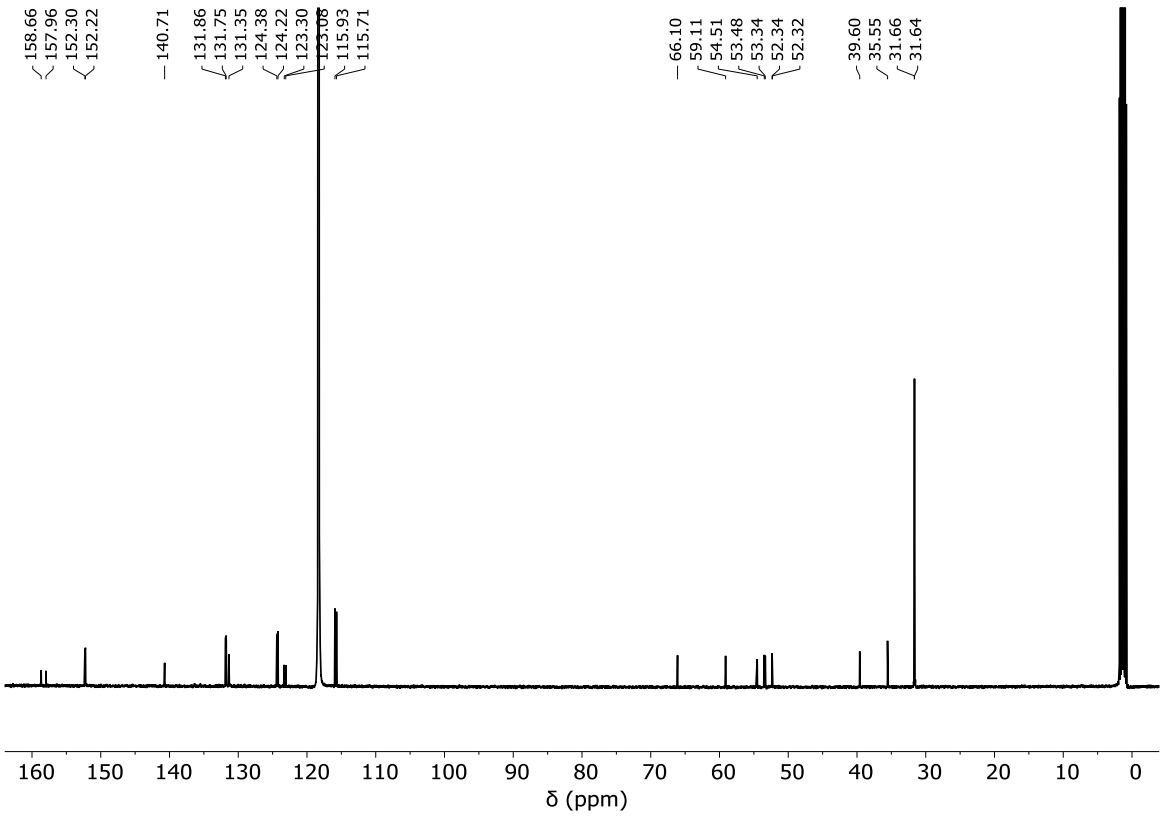

Figure S30. ^{13}C NMR spectrum of **13** (acetonitrile-d_3, 298 K, 126 MHz).

[1] Erbas-Cakmak, S.; Leigh, D. A.; McTernan, C. T.; Nussbaumer, A. L., *Chem. Rev*., **2015**, 115, 10081.

[2] Kassem, S.; Van Leeuwen, T.; Lubbe, A. S.; Wilson, M. R.; Feringa, B. L.; Leigh, D. A, *Chem. Soc. Rev*., **2017**, 46, 2592.

[3] Zhou, H.-Y.; Han, Y.; Chen, C.-F., *Mater. Chem. Front*., **2020**, 4, 12.

[4] Lewis, J. E. M.; Galli, M.; Goldup, S. M., *Chem. Commun*., **2017**, 53, 298.

[5] Jamieson, E. M. G.; Modicom, F.; Goldup, S. M., *Chem. Soc. Rev*., **2018**, 47, 5266.

[6] Mena-Hernando, S.; Pérez, E. M., *Chem. Soc. Rev*., **2019**, 48, 5016.

[7] Baroncini, M.; Silvi, S.; Credi, A., *Chem. Rev*., **2020**, 120, 200.

[8] Dattler, D.; Fuks, G.; Heiser, J.; Moulin, E.; Perrot, A.; Yao, X.; Giuseppone, N., *Chem. Rev*., **2020**, 120, 310.

[9] Moulin, E.; Faour, L.; Carmona-Vargas, C. C.; Giuseppone, N., Adv. Mater., **2019**, 32, 20, 1906036

[10] Sauvage, J.-P.; Dietrich-Buchecker, C. Molecular Catenanes, Ro-taxanes and Knots; Wiley: New York, **1999**.

[11] Bruns, C. J.; Stoddart, J. F. The Nature of the Mechanical Bond: From Molecules to Machines; Wiley: Hoboken, **2016**.

[12] Oku, T.; Furusho, Y.; Takata, T. A Concept for Recyclable Cross-Linked Polymers: Topologically Networked Polyrotaxane Capable of Undergoing Reversible Assembly and Disassembly. *Angew. Chem. Int. Ed.* **2004**, *43*, 966-969.

[13] Denis, M.; Goldup, S. M. The Active Template Approach to Interlocked Molecules. *Nat. Rev. Chem.* **2017**, *1*, 0061.

[14] Corra, S.; de Vet, C.; Groppi, J.; La Rosa, M.; Silvi, S.; Baroncini, M.; Credi, A. Chemical On/Off Switching of Mechanically Planar Chirality and Chiral Anion Recognition in a [2]Rotaxane Molecular Shuttle. *J. Am. Chem. Soc.* **2019**, *141*, 9129-9133.

[15] Chen, S.; Wang, Y.; Nie, T.; Bao, C.; Wang, C.; Xu, T.; Lin, Q.; Qu, D.-H.; Gong, X.; Yang, Y.; Zhu, L.; Tian, H. An Artificial Molecular Shuttle Operates in Lipid Bilayers for Ion Transport. *J. Am. Chem. Soc.* **2018**, *140*, 17992-17998.

[16] Dommaschk, M.; Echavarren, J.; Leigh, D. A.; Marcos, V.; Singleton, T. A. Dynamic Control of Chiral Space Through Local Symmetry Breaking in a Rotaxane Organocatalyst. *Angew. Chem. Int. Ed.* **2019**, *58*, 14955-14958.

[17] Green, J. E. et al. A 160-Kilobit Molecular Electronic Memory Patterned at 10^{11} Bits per Square Centimetre. *Nature* **2007**, *445*, 414-417.

[18] Schroder, H. V.; Schalley, C. A. Electrochemically Switchable Rotaxanes: Recent Strides in New Directions. *Chem. Sci.* **2019**, *10*, 9626-9639.

[19] Goujon, A.; Lang, T.; Mariani, G.; Moulin, E.; Fuks, G.; Raya, J.; Buhler, E.; Giuseppone, N. Bistable [c2] Daisy Chain Rotaxanes as Reversible Muscle-like Actuators in Mechanically Active Gels. *J. Am. Chem. Soc.* **2017**, *139*, 14825-14828.

[20] Zhang, Q.; Rao, S.-J.; Xie, T.; Li, X.; Xu, T.-Y.; Li, D.-W.; Qu, D.-H.; Long, Y.-T.; Tian, H. Muscle-like Artificial Molecular Actuators for Nanoparticles. *Chem* **2018**, *4*, 2670-2684.

[21] Ambrogio, M. W.; Thomas, C. R.; Zhao, Y.-L.; Zink, J. I.; Stoddart, J. F. Mechanized Silica Nanoparticles: A New Frontier in Theranostic Nanomedicine. *Acc. Chem. Res.* **2011**, *44*, 903-913.

[22] Nakazono, K.; Takata, T. Neutralization of a sec-Ammonium Group Unusually Stabilized by the "Rotaxane Effect": Synthesis, Structure, and Dynamic Nature of a "Free" sec-Amine/Crown Ether-Type Rotaxane. *Chem. Eur. J.* **2010**, *16*, 13783-13794.

[23] Matsuoka, Y.; Mutoh, Y.; Azumaya, I.; Kikkawa, S.; Kasama, T.; Saito, S. Synthesis and Shuttling Behavior of [2]Rotaxanes with a Pyrrole Moiety. *J. Org. Chem.* **2016**, *81*, 3479-3487.

[24] Riss-Yaw, B.; Clavel, C.; Laurent, P.; Waelès, P.; Coutrot, F. The Importance of Length and Flexibility of Macrocycle-Containing Molecular Translocators for the Synthesis of Improbable [2]Rotaxanes. *Chem. Eur. J.* **2018**, *24*, 13659-13666.

[25] Echavarren, J.; Gall, M. A. Y.; Haertsch, A.; Leigh, D. A.; Marcos, V.; Tetlow, D. J. Active Template Rotaxane Synthesis Through the Ni-Catalyzed Cross-Coupling of Alkylzinc Reagents with Redox-Active Esters. *Chem. Sci.* **2019**, *10*, 7269-7273.

[26] Segawa, Y.; Kuwayama, M.; Hijikata, Y.; Fushimi, M.; Nishihara, T.; Pirillo, J.; Shirasaki, J.; Kubota, N.; Itami, K. Topological Molecular Nanocarbons: All-Benzene Catenane and Trefoil Knot. *Science* **2019**, *365*, 272-276.

[27] Sakata, Y.; Ogura, T.; Akine, S. Efficient Formation of [3]Pseudorotaxane Based on Cooperative Complexation of Dibenzo-24-Crown-8 with Diphenylviologen Axle. *Chem. Commun.* **2020**, *56*, 8735-8738.

[28] Altmann, P. J.; Pöthig, A. A pH-Dependent, Mechanically Interlocked Switch: Organometallic [2]Rotaxane vs. Organic [3]Rotaxane. *Angew. Chem. Int. Ed.* **2017**, *56*, 15733-15736.

[29] Zheng, L.-S.; Cui, J.-S.; Jiang, W. Biomimetic Synchronized Motion of Two Interacting Macrocycles in [3]Rotaxane-Based Molecular Shuttles. *Angew. Chem. Int. Ed.* **2019**, *58*, 15136-15141.

[30] Inamori, D.; Masai, H.; Tamaki, T.; Terao, J. Macroscopic Change in Luminescent Color by Thermally Driven Sliding Motion in [3]Rotaxanes. *Chem. Eur. J.* **2020**, *26*, 3385-3389.

[31] Baroncini, M.; Silvi, S.; Venturi, M.; Credi, A. Reversible Photoswitching of Rotaxane Character and Interplay of Thermodynamic Stability and Kinetic Lability in a Self-Assembling Ring–Axle Molecular System. *Chem. Eur. J.* **2010**, *16*, 11580-11587.

[32] Romuald, C.; Busseron, E.; Coutrot, F. Very Contracted to Extended co-Conformations with or without Oscillations in Two- and Three-Station [c2]Daisy Chains. *J. Org. Chem.* **2010**, *75*, 6516-6531.

[33] Ma, Y.-X.; Meng, Z.; Chen, C.-F. A Novel Pentiptycene Bis(crown ether)-Based [2](2)Rotaxane Whose Two DB24C8 Rings Act as Flapping Wings of a Butterfly. *Org. Lett.* **2014**, *16*, 1860-1863.

[34] Waelès, P.; Fournel-Marotte, K.; Coutrot, F. Distinguishing Two Ammonium and Triazolium Sites of Interaction in a Three-Station [2]Rotaxane Molecular Shuttle. *Chem. Eur. J.* **2017**, *23*, 11529-11539.

[35] Kihara, N.; Tachibana, Y.; Kawasaki, H.; Takata, T. Unusually Lowered Acidity of Ammonium Group Surrounded by Crown Ether in a Rotaxane System and Its Acylative Neutralization. *Chem. Lett.* **2000**, *29*, 506-507.

[36] Ragazzon, G.; Credi, A.; Colasson, B. Thermodynamic Insights on a Bistable Acid-Base Switchable Molecular Shuttle with Strongly Shifted Co-conformational Equilibria. *Chem. Eur. J.* **2017**, *23*, 2149-2156.

[37] Ragazzon, G.; Schaefer, C.; Franchi, P.; Silvi, S.; Colasson, B.; Lucarini, M.; Credi, A. Remote Electrochemical Modulation of pK_a in a Rotaxane by Co-conformational Allostery. *Proc. Natl. Acad. Sci. U. S. A.* **2018**, *115*, 9385-9390.

[38] Groppi, J.; Casimiro, L.; Canton, M.; Corra, S.; Jafari-Nasab, M.; Tabacchi, G.; Cavallo, L.; Baroncini, M.; Silvi, S.; Fois, E.; Credi, A. Precision Molecular Threading/Dethreading. *Angew. Chem. Int. Ed.* **2020**, *59*, 14825-14834.

[39] Dunning, T. H. Gaussian Basis Sets for Use in Correlated Molecular Calculations. I. The Atoms Boron through Neon and Hydrogen. *J. Chem. Phys*. **1989**, 90, 1007-1023.

[40] Chai, J.-D.; Head-Gordon, M. Long-Range Corrected Hybrid Density Functionals with Damped Atom–Atom Dispersion Corrections. *Phys. Chem. Chem. Phys*. **2008**, 10, 6615.

[41] Gauss, J. Effects of Electron Correlation in the Calculation of Nuclear Magnetic Resonance Chemical Shifts. *J. Chem. Phys*. **1993**, 99, 3629-3643.

[42] Woon, D. E.; Dunning, T. H. Gaussian Basis Sets for Use in Correlated Molecular Calculations. III. The Atoms Aluminum through Argon. *J. Chem. Phys*. **1993**, 98, 1358-1371.

[43] Jain, R.; Bally, T.; Rablen, P. R. Calculating Accurate Proton Chemical Shifts of Organic Molecules with Density Functional Methods and Modest Basis Sets. *J. Org. Chem*. **2009**, 74, 4017-4023.

[44] Frisch, M. J.; Trucks, G. W.; Schlegel, H. B.; Scuseria, G. E.; Robb, M. A.; Cheeseman, J. R.; Scalmani, G.; Barone, V.; Mennucci, B.; Petersson, G. A.; Nakatsuji, H.; Caricato, M.; Li, X.; Hratchian, H. P.; Izmaylov, A. F.; Bloino, J.; Zheng, G.; Sonnenb, D. J. Gaussian 09, Revision E.01,. Gaussian, Inc.: Wallingford CT 2009.

[45] Tomasi, J.; Mennucci, B.; Cammi, R. Quantum Mechanical Continuum Solvation Models. *Chem. Rev*. **2005**, 105, 2999-3094.

[46] Car, R.; Parrinello, M. Unified Approach for Molecular Dynamics and Density-Functional Theory. *Phys. Rev. Lett*. **1985**, 55, 2471-2474.

[47] Laio, A.; Parrinello, M. Escaping Free-Energy Minima. Proc. Natl. Acad. Sci. U. S. A. **2002**, 99, 12562 12566.

[48] Iannuzzi, M.; Laio, A.; Parrinello, M. Efficient Exploration of Reactive Potential Energy Surfaces Using Car-Parrinello Molecular Dynamics. *Phys. Rev. Lett*. **2003**, 90, 4.

[49] Perdew, J. P.; Burke, K.; Ernzerhof, M. Generalized Gradient Approximation Made Simple. *Phys. Rev. Lett.* **1996**, 77, 3865-3868.

[50] Grimme, S. Semiempirical GGA-Type Density Functional Constructed with a Long-Range Dispersion Correction. *J. Comput. Chem*. **2006**, 27, 1787-1799.

[51] Vanderbilt, D. Soft Self-Consistent Pseudopotentials in a Generalized Eigenvalue Formalism. *Phys. Rev. B* **1990**, 41, 7892-7895.

[52] Nosé, S. A Unified Formulation of the Constant Temperature Molecular Dynamics Methods. *J. Chem. Phys.* **1984**, 81, 511-519.

[53] Hoover, W. G. Canonical Dynamics: Equilibrium Phase-Space Distributions. *Phys. Rev. A* **1985**, 31, 1695-1697.

[54] Marx, D.; Hutter, J. Ab Initio Molecular Dynamics; Cambridge University Press: Cambridge, **2009**.

[55] IBM Corp. 1990–2017; MPI für Festkörperforschung Stuttgart 1997–2001. CPMD: Car Parrinello Molecular Dynamics. **2017**.

Ringraziamenti

Questo lavoro non sarebbe stato possibile senza il supporto scientifico del Prof. Alberto Credi, che mi ha dato l'opportunità di far parte del suo bellissimo gruppo, a lui va un immenso grazie !

Ringrazio di cuore la Prof. Serena Silvi per avermi guidata e supportata in questi tre anni di continue sfide, a lei tutta la mia gratitudine.

Un grande ringraziamento va anche al Prof. Massimo Baroncini.

Ringrazio Lorenzo, Martina, Jessica, Stefano, Chiara, Leonardo, Antonio, Brian, Nina e Marina per il loro importante aiuto e la loro disponibilità.

Last but not least, uno speciale ringraziamento va ai miei grandi amici e colleghi Max e Fede per tutto quello che abbiamo condiviso scientificamente e umanamente. Grazie per esserci sempre stati !